Submillimeter Wave Harmonic Gyrotron

by

Susan Spira Hakkarainen

B.S., Cornell University (1982)
M.Eng., Cornell University (1983)

Submitted to the Department of Nuclear Engineering
in partial fulfillment of the requirements for the degree of

Doctor of Philosophy

in

Applied Plasma Physics

at the

MASSACHUSETTS INSTITUTE OF TECHNOLOGY

September 1989

Signature of Author . . . .
Department of Nuclear Engineering
June 13, 1989

Certified by . . . .
Doctor Richard J. Temkin
Thesis Supervisor

Certified by . . . .
Doctor Kenneth E. Kreischer
Thesis Supervisor

Certified by . . . .
Professor Lawrence M. Lidsky
Thesis Reader

Accepted by . . . .
Professor Allen F. Henry
Chairman, Departmental Committee on Graduate Students

Submillimeter Wave Harmonic Gyrotron

by

Susan Spira Hakkarainen

Submitted to the Department of Nuclear Engineering
on June 13, 1989, in partial fulfillment of the
requirements for the degree of
Doctor of Philosophy
in
Applied Plasma Physics

Abstract

This thesis reports a theoretical and experimental investigation of the operation at submillimeter wavelengths of a harmonic gyrotron, $\omega = n\omega_c$, where ω is the emission frequency, n is an integer, and ω_c is the electron cyclotron frequency. Research was conducted using a 65 - 75 kV, up to 10 A electron gun which produced a helical electron beam in a uniform magnetic field of up to 14 Tesla. Output powers of up to 22 kW were attained in 1 - 1.5 μsec pulses at frequencies between 300 and 500 GHz. These results represent the first operation of a high power harmonic gyrotron in the submillimeter region.

In this thesis several basic physics issues were addressed, including mode competition, and the agreement between the theoretical and measured efficiencies and starting currents. Mode competition between the fundamental and second harmonic modes can occur as well as competition between second harmonic modes. In order to obtain operation in second harmonic modes, techniques for suppression of fundamental modes were investigated. Three different cavity configurations were explored to obtain harmonic operation: a tapered cavity, a cavity with axial slots, and a cavity with an iris at the output end of the straight section. Also, a motheye window was used to provide external feedback to the second harmonic mode.

With the tapered cavity configuration, only low frequency, weak second harmonic modes were observed. The next experiment involved positioning large axial slots in the cavity at minima of the second harmonic electric field to generate large leakage losses for the fundamental modes. The slotted cavity configuration did not generate harmonics, however, almost continuously tunable emission was observed at kilowatt power levels in the frequency range 186.3 - 200.6 GHz. This may prove useful as a tunable, millimeter wave source.

The strongest harmonic emission was obtained when a cavity with an iris was used. The iris significantly increased the Q of second harmonic modes, while increasing the Q of fundamental modes only a small amount. With this cavity, fourteen different second harmonic modes were observed with frequencies between 301 - 503 GHz and output powers of 1 - 22 kW. A 15 MHz emission frequency bandwidth was observed for these modes. The highest output power was 22 kW with a total efficiency of 3.5 % at 467 GHz, and an output power of 15 kW with a 6% efficiency was obtained at 417 GHz. A variety of diagnostics that were used to discriminate between fundamental and second harmonic emission will be discussed.

Thesis Supervisor: Richard J. Temkin
Title: Senior Research Scientist, Physics Department

Thesis Supervisor: Kenneth E. Kreischer
Title: Research Scientist, Plasma Fusion Center

Thesis Reader: Lawrence M. Lidsky
Title: Professor of Nuclear Engineering

Table of Contents

To my loving parents and husband

Acknowledgments

I owe a large debt to Dr. Ken Kreischer for the guidance and support he provided during this thesis. Both he and Dr. Rick Temkin gave me a better understanding of the rigor needed to approach scientific problems properly. I appreciate the many stimulating conversations I shared with them. I would like to express my gratitude to Professor Lidsky for being my reader and for the guidance he gave me. I would also like to thank Arnie Fliflet, Bruce Danly, Shien-Chi Chen, Bill Guss, Chun-Yi Wang, Hiro Saito, Minh Tran, Jeff Casey, Bill Mulligan, Bob Childs, Paul Woskov, Steve Evangelides, Phil Lentini for their generosity in providing technical advice and assistance. Also important to this thesis were the high quality products provided by Mr. Emory Horvath and Mr. Ted Kozul, the measurements made by Dr. Afsar and the generosity with magnet time of Mr. Larry Rubin.

I would like to thank my fellow graduate students, Tak-Sum Chu, Arnold Mobius, Ken Pendergast, Terry Grimm, Anita Li and others for many important discussions.

I thank my parents for their understanding and for believing I could do it even when I didn't, and also my parents in law, Mauno and Kaisu Hakkarainen. I also owe a debt to my brother in law and his fiancee, Mikko Hakkarainen and Gloria Chen and my sisters, Lily and Juno Spira for their support.

Finally, I thank my husband Pekka for his support and encouragement and help in the laboratory as well as with computer work. Without his support this thesis would not have been possible.

CHAPTER 1

INTRODUCTION

The demand for high frequency high power microwave sources has increased recently. In plasma applications, these sources can be used for electron cyclotron resonance heating and plasma diagnostics. In electron cyclotron resonance heating of plasmas, frequencies above 100 GHz are needed (Granatstein (1987)) when the magnetic field strength is above 3.5 Tesla. Plasma diagnostics applications require frequencies above the plasma frequency (> 300 GHz) (Woskov (1987)) in order that the radiation will not be absorbed or refracted by the plasma. High frequency devices are also important for applications such as a space based radar system, communications systems and material science applications. Space based radar systems require stable coherent sources that are not excessively large. With higher frequencies a more directional beam can be achieved with a given antenna size and if frequencies that correspond to water absorption lines are used false returns and jamming from radars on the ground are prevented (Granatstein (1987)). In communications applications, frequencies corresponding to transmission windows, such as 35, 94, 140, 220 GHz are used. Atmospheric attenuation and losses are relatively low in the transmission windows, compared to optical and infrared frequencies (Granatstein (1987), Bhartia (1984)). For good resolution a narrow linewidth, stable source is required. Finally, in the material science applications, such as isotope separation and spectroscopy, narrow linewidth and stability are necessary, to utilize the high level of resolution that can be achieved by operating with small wavelengths.

Gyrotrons fill a gap between conventional microwave devices (klystron, magnetrons, triodes, etc) and lasers. As frequency increases, the level of power attainable with a conventional microwave device decreases. This decrease is due to the fact that conventional microwave devices operate in the fundamental mode, and therefore, the cavity dimensions must be on the order of the wavelength of the radiation. At higher frequencies, the cavity size decreases. Not only does this make the cavity harder to fabricate, but the power density constraints of a smaller cavity do not allow the maximum output power to be as high as for a larger cavity. In a laser, the power decreases as the frequency decreases. When an electron makes a transition to a lower energy level, a photon is released with energy δE given by

$$\delta E = \hbar f \qquad 1.0.1$$

where δE is the difference between the energy levels, $\hbar$ is Planck's constant, and f is the frequency of the photon. From equation 1.0.1, one can see that as frequency decreases, a smaller difference in energy levels is needed. Since the smaller energy levels correspond to higher excitation states, the power needed to excite the electrons to these states increases and thus the theoretical efficiency of a laser decreases.

Gyrotrons have advantages over other devices that operate in this regime. Devices such as free electron lasers (FEL) (Elias (1985), Marshall (1985), Benson (1986), Orzechowski (1986)) and cyclotron resonance masers (CARM) (Botvinnik (1982a), Botvinnik (1982b), Bekefi (1989), McDermott (1989)) are large devices that require high voltage sources (> 500 kV). Since gyrotrons are weakly relativistic devices, lower voltage (60 - 100 kV) supplies can be used. Cherenkov sources (Marshall (1988), Didenko (1983), Kuzelev (1982)) also operate in this regime, but are low efficiency devices. A gyrotron is capable of achieving efficiencies in excess of 25 % at high power (> 500 kW) and high frequency (> 100 GHz) (Kreischer (1987)).

The term gyrotron, created by Gapanov, refers to a cyclotron resonance maser (CRM) that has an electron beam which loses energy to an RF wave by passing through a resonator near cutoff. To produce the electron beam, a magnetron injection gun is typically used. The frequency ω of the emitted coherent radiation is approximately given by

$$\omega = n\omega_c + k_{\parallel}v_{\parallel} \qquad 1.0.2$$

where n is the harmonic number, ω_c is the cyclotron frequency, $k_{\parallel}$ is the parallel component of the wavenumber and $v_{\parallel}$ is the parallel electron velocity. Since the resonator is near cutoff, $k_{\parallel}v_{\parallel} \ll n\omega_c$, and therefore $\omega \simeq n\omega_c$.

In a gyrotron, a relativistic effect leads to the transfer of energy from the electrons to the RF wave. This is due to the relativistic dependence of the cyclotron frequency (through the electron mass) on the electron energy. When the beam interacts with the RF field, bunching in phase space occurs because some of the electrons gain energy and some lose energy. Gain is possible, if the phase of the bunched electrons with respect to the RF field is appropriate.

The basic configuration of the gyrotron is shown in Figure 1.0.1. An electron beam that propagates to the left is created by a magnetron injection gun. The electrons then travel through a resonant cavity, where energy is transferred to an RF wave and finally the electrons are deposited on the collector. A magnetic field in the z direction, created by a superconducting or Bitter magnet has a fairly flat profile in the resonator region as indicated in Figure 1.0.1. To accelerate the electrons, an electric field is created by applying a voltage to the anodes. After emission from the cathode, the electrons are guided by the magnetic field and enter a region of magnetic compression. The purpose of the compression is to increase the perpendicular velocity, since the electron energy obeys the adiabatic invariant $v_{\perp}^2/B_o$ is a constant, where B_o is the main magnetic field, and $v_{\perp}$ is the perpendicular electron energy. In the resonant cavity, the electrons lose energy to a resonant RF wave. After leaving the resonator, the electrons enter a region of lower magnetic field, and the electron beam follows the magnetic field lines which cause it to be deposited on the copper collector. The microwaves, created in the resonant cavity, leave the vacuum region through a quartz output window.

The experiment discussed in this thesis was established to achieve high power, submillimeter emission. To attain frequencies in the submillimeter region using fundamental mode operation magnetic fields above 12 T would be required. The advantage of using harmonic operation is that lower magnetic fields are needed for second harmonic than fundamental operation. To operate at 300 GHz using a second harmonic mode requires just 6 T, instead of 12 T required by a fundamental mode. Steady-state magnetic fields below 10 T can be produced by NbTi superconducting magnets and fields up to 15 T can be produced by Nb_3Sn superconducting magnets. Although pulsed magnets at higher fields are available, this is not an attractive alternative for several reasons. Firstly, due to the high stresses caused by pulsed operation, the total number of times a magnet

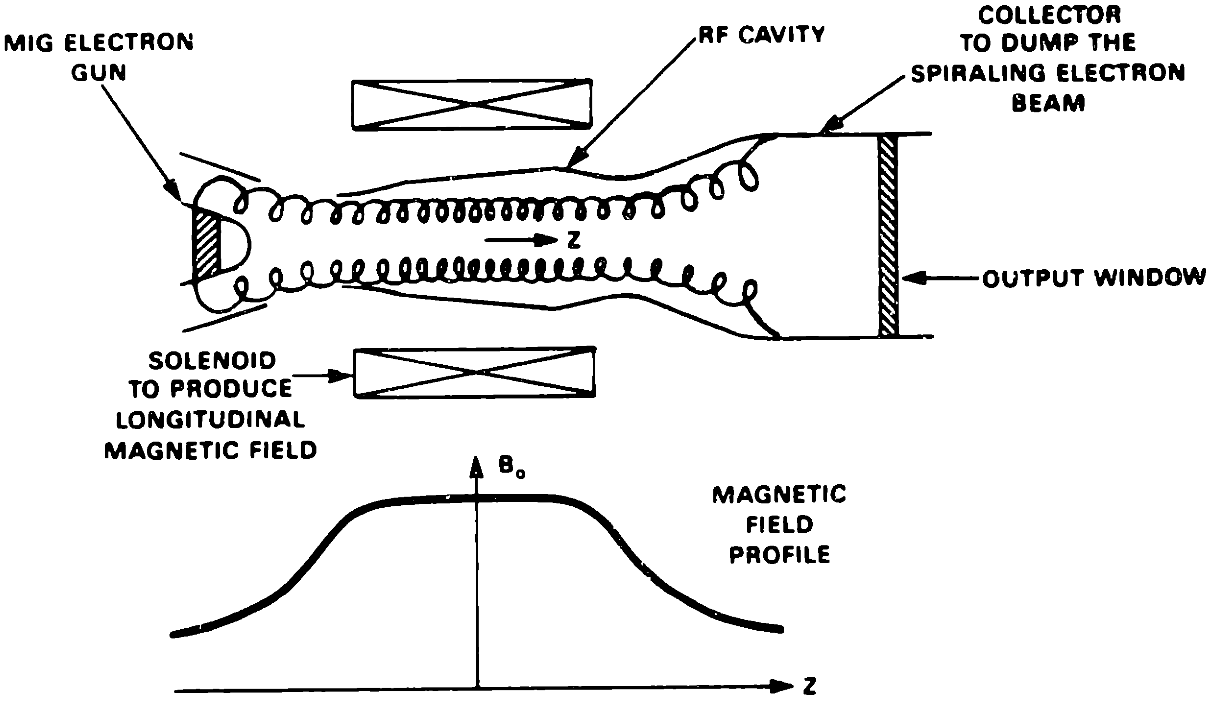

Figure 1.0.1 Schematic of the gyrotron configuration (Granatstein (1987))

can be pulsed is limited by metal fatigue (Dolan (1982), Stacey (1984)). Also, if the magnetic field varies, the frequency of the gyrotron emission may shift, the efficiency may be degraded or the operating mode may become unstable. In a pulsed system, it can be difficult to eliminate pulse to pulse fluctuations of the magnetic field. Finally, in a pulsed system, component failure is a larger problem than in a non pulsed system (Dolan (1982)).

The nonlinear theory discussed in Chapter 2 predicts that perpendicular efficiencies up to 70 %, which is comparable to the maximum efficiencies for fundamental modes, are attainable in second harmonic operation. The objective is to obtain high efficiency operation, and therefore only low harmonics (n=2,3) are considered. Third harmonic emission is less efficient than second harmonic emission, but a search for third harmonic modes was conducted in this work. Past second harmonic results show that efficient second harmonic emission is experimentally possible at high frequencies and powers. Soviet physicists conducted many second harmonic experiments in the 1970's. Kisel (1974) produced 10 kW cw power and 30 kW with pulsed operation at 34 GHz. At 154 GHz, 7 kW was produced with pulsed operation and with cw operation, 2.4 kW at 157 GHz and 1.5 kW at 326 GHz was observed (Zaytsev (1974)). Experiments were also conducted with a stepped cavity profile. At 25 GHz, 500 kW of power was emitted (Zapevalov (1979)). More recently, Zapevalov (1983) reported a second harmonic mode at 34 GHz with an output power of 150 kW and a third harmonic mode at 55 GHz and 100 kW, where both experiments were conducted with pulsed operation. An efficiency of 10 % was measured for the third harmonic mode, which indicates that high efficiency harmonic operation is possible.

Other investigations have been conducted outside the Soviet Union. At M.I.T. Byerly (1984) observed stable, very narrow bandwidth second harmonic emission ranging from 209 to 302 GHz, with a peak power of 25 kW at 241.0 GHz. A joint project between the Naval Research Laboratory (NRL) and Harry diamond Laboratories yielded 50 W at 240 GHz (Silverstein (1981)). Using a solid beam Pierce gun, instead of the usual magnetron injection gun, Hirshfield (1983) generated emission ranging from 8 mm to less than 1 mm at harmonics up to the ninth harmonic. Varian conducted a second harmonic gyrotron experiment at 106 GHz (Shively (1987)) and observed 100 kW of power using a complex cavity configuration. In the People's Republic of China (Guo (1981)) 30 kW of power was measured for a second harmonic mode at 37 GHz. The Thompson - CSF second harmonic gyrotron has produced 30 kW at 70 GHz (Boulanger (1982)).

A device similar to a gyrotron, called the peniotron, has also produced harmonic emission. At harmonics as high as the tenth harmonic (3 GHz), power levels of 2 kW (McDermott (1983)) have been observed. Similar power levels have been generated at higher frequencies at the third (25 GHz) and the fourth (32 GHz) harmonics (McDermott (1983)). Power levels of 600 kW were reported for a fifth harmonic mode at 11.3 GHz (Furuno (1988)). Harmonic operation has also been achieved with a cusptron, a device that has a vaned cavity and also uses an axis encircling beam. At sixth harmonic (6.0 GHz) 10.4 kW of power has been generated (Namkung (1988)) using this device.

In comparison, the power levels produced by conventional microwave devices especially in the submillimeter region have been much lower. At 500 GHz, Travelling-wave tube amplifiers, backward wave oscillators, and crossed field amplifiers have power levels of 0.1 - 10 watts (Bhartia (1984)). CO_2 lasers can emit up to 30 kW at 600 GHz (Shirai (1989)). However the the efficiency is less that 0.1 %.

When conducting a second harmonic experiment the basic physics issues must be studied in order to understand how to optimize the design of a second harmonic gyrotron. A major issue is mode competition between fundamental and second harmonic modes as well as competition between two or more harmonic modes. The mode competition between the fundamental and harmonic modes, however, is the dominant issue. Second harmonic modes are difficult to excite for several reasons. Firstly, their starting currents are often higher than those of the fundamental modes. As a result, the fundamental modes get excited first, and then suppress the second harmonic modes. Secondly, the severe mode competition from the q=1 (q is the axial index of a $TE_{m,p,q}$ mode) fundamental modes, the higher order fundamental modes (q=2,3) and other second harmonic modes can stifle the desired second harmonic mode. The highly overmoded cavities used to reduce ohmic losses also make mode competition more severe. Mode density increases as the cavity size becomes larger, thereby making mode competition more severe. Finally, the thick beam produced by our gun further aggravates the mode competition problem, because the beam can couple to several modes simultaneously. Another area that will be studied is agreement between the theoretical efficiency and gain and the experimental values.

In this thesis we discuss a second harmonic, submillimeter gyrotron experiment. Since the fundamental modes tend to have lower starting currents, the fundamental modes will get excited first and suppress the harmonic modes. To successfully excite second harmonic modes, the fundamental modes must be suppressed and therefore a study of five different fundamental mode suppression techniques was undertaken. The first technique uses the fact that the fundamental mode spectrum is uneven and clumpings around certain frequencies or mode indices (ν_{mp}) tend to occur (Figure 4.0.1) and one observes large gaps in the fundamental mode spectrum. Since a given mode is only excited over a limited region of magnetic field, the frequency gap can translate into a gap in the magnetic field. Therefore, it is desirable to select a second harmonic mode that exists in the magnetic field that corresponds to a gap in the fundamental spectrum. The second technique involves placing the beam in a position where the coupling to fundamental modes is weak. Another technique is to operate with a higher perpendicular electron velocity, $\beta_\perp$. At higher values of $\beta_\perp$ the ratio of fundamental to second harmonic starting current, I_{st1}/I_{st2} increases. Therefore at a high enough value of $\beta_\perp$, the second harmonic mode is excited first. The fourth technique is to manipulate the cavity Q, so as suppress the fundamental modes. This manipulation can be accomplished by two different methods. Either an electromagnetic structure where the fundamental modes are highly perturbed and the second harmonic modes are unperturbed (slotted cavity) or a structure with better feedback to the second harmonic modes (cavity with an iris) than to the fundamental can be used. Lastly, discrimination against the fundamental modes can be facilitated by providing external feedback to only the second harmonic mode.

When the second and third techniques were used with cavity which had an iris at the output end of the straight section to implement the fourth technique and a motheye window to provide external feedback to the second harmonic mode, 14 second harmonic modes were observed, with frequencies from 301 - 502 GHz and output powers of 1 - 22 kW and a 12 MHz frequency bandwidth. The highest output power was 22 kW at 467 GHz with an efficiency of 3.5%. Furthermore, an output power of 15 kW with 6% was obtained at a frequency of 417 GHz. These results represent the highest frequency high power second harmonic emission observed. To discriminate between fundamental emission and to estimate the fraction of second harmonic emission present, various diagnostic devices, such as filter horns were developed and will also be discussed in this thesis.

SUMMARY

This thesis discusses a study of a variety of methods to excite submillimeter second harmonic radiation and suppress fundamental emission with an M.I.T. gyrotron. As will be discussed in Chapter 6, the fourth technique when implemented with a cavity that has an iris, was the most effective technique. In this study, three types of resonators were explored, a standard tapered cavity, a cavity with axial slots cut along its length, and a cavity with an iris on the output end of the straight section, which will be referred to as a straight cavity, a slotted cavity, and an iris cavity respectively. Chapter 2 outlines the linear and nonlinear theory of harmonic gyrotrons and demonstrates how to apply them to predict which modes will be excited as well as their efficiencies. The diagnostics and experimental setup used in this these experiments are described in Chapter 3. Chapter 4 details the design procedure, experimental results, and analysis of the experimental results of the straight cavity experiment. In Chapter 5 the slotted cavity experiments are discussed. The iris cavity experiments are presented in Chapter 6. Chapter 7 contains the summary and recommendations for further study.

Chapter 2

Theory

In this chapter we discuss the theory of the gyrotron interaction. We start with the electron equation of motion, including the Lorentz force for the electron dynamics and Maxwell's equations to model the electromagnetic fields. A complete solution of these equations which accounts for specific device geometries is unwieldy. Even if numerical methods are used approximations are needed. Various theories differ in the assumptions made and the degree of completeness. The treatment in this thesis uses the slow time scaling assumption which involves averaging over the Larmor orbit of the electrons. The assumption of slow time scale implies that the quantities of interest, such as the electron energy, do not very change much over a Larmor orbit, so time steps that are large with respect to the period of the Larmor gyration (ω_c^{-1}) can be used without creating a large error. When the slow time scale theory is compared with the fast time scale treatment, that considers the motion of the electrons as they trace out their orbits, the agreement is found to be quite good (Schutkeker (1985)). The advantage of making the slow time scale approximation is a simpler analytic theory. In the section on the linear theory, the slow time scaling will be discussed in more detail. The linear theory is used to determine the conditions where the start of oscillation occurs. To predict the output power and efficiency a nonlinear theory is required.

In this chapter the gyrotron linear and nonlinear theory will be detailed as well as the method for applying these theories to design gyrotron resonators. In Chapters 3, 4, and 5, a more detailed description of design procedure that is specific to the type of resonator (slotted etc.) is provided.

2.1 Description of the Gyrotron Mechanism

Electron beam devices, which include gyrotrons, use an electromagnetic field to extract energy from an electron beam produced at the cathode. To simplify the analysis we assume that the electron beam is monoenergetic. In a gyrotron tube the electron beam is immersed in a steady state magnetic field and is accelerated by an electric field, making the electrons trace out helical paths. Inside the resonator the mildly relativistic electrons, excite and interact with the transverse electric field of a TE mode whose frequency is close to the cyclotron frequency of the electrons multiplied by n, where n is the harmonic number. Field is assumed to be in the azimuthal direction and vary as $E_o \cos \omega t$, where ω is the RF wave frequency. The electromagnetic wave gains energy from the electrons and a fraction of this energy is diffracted out of the cavity.

The interaction can be understood more clearly by studying the effects of the field on a beamlet containing 8 electrons which have nearly the same guiding center and a constant Larmor radius, r_L given by

$$r_L = \frac{v_\perp}{\omega_c} \qquad 2.1.1$$

where $\omega_c = eB/\gamma m$ is the relativistic cyclotron frequency, e is the electron charge, B the magnetic field, m the electron mass, $\gamma = (1 - v^2/c^2)^{-1/2}$ is the relativistic factor and v the electron velocity. At the beginning of the interaction region the phase of the electrons is random as shown in Figure 2.1.1a. The figure shows the representative positions of the electrons in the beamlet with respect to the RF electric field $E_o \cos \omega t$ labelled as **E** and represented by arrows. In the frame of reference of the electrons the RF electric field in the resonator is approximately steady-state. First, the fundamental mode case will be discussed and variations in the electric field across the Larmor orbit will be ignored. In the interaction region, the transverse electric field will accelerate some electrons and decelerate others. In Figure 2.1.1b (RF field frame of reference) electrons 2, 3, 4 are decelerated, electrons 6, 7, 8 are accelerated and electrons 1, 5 are unchanged, since the force exerted on the electrons by the electric field **E**, $F_e = -q\mathbf{E}$. The circle with a broken line represents the new positions immediately after the change in energy. When an electron gains energy the relativistic factor γ increases which decreases ω_c and increases r_L. Conversely, when an electron loses energy, γ decreases, increasing ω_c and decreasing r_L shown by the broken line circle. After a few periods of revolution, the electrons that gain energy begin to slip in phase and the electrons that lose energy advance in phase. Eventually a bunch is formed (Figure 2.1.1c). If the frequency of the electric field ω is equal to the cyclotron frequency (Figure 2.1.1c), the bunch does not gain or lose energy. To gain energy, ω must be slightly greater than the cyclotron frequency. If ω is slightly less than the cyclotron frequency, the wave loses energy to the electrons. For the wave to gain energy, $\omega > \omega_c$ but to maintain the wave particle resonance, $\omega \simeq \omega_c$.

To have a harmonic interaction the electric field must vary across the Larmor radius. The RF field can be written as a series in a coordinate system whose origin is the electron gyrocenter. The terms in the series correspond to the electric fields of the different spacial harmonics. If the RF field does not vary across the Larmor orbit only the fundamental interaction term will be nonzero. In this analysis, we are not considering multimoding, therefore the strongest term in the series of electric fields determines which harmonic will be excited. Figure 2.1.2 shows the quadrapole electric field required for a second harmonic interaction. A third harmonic interaction would require a hexapole field and so on. The regions where the electrons gain ($\dot{\gamma} > 0$) and lose energy ($\dot{\gamma} < 0$) are shown in Figure 2.1.2. It is possible but not necessary to form two bunches during a second harmonic interaction. Just the fact that the RF electric field is a quadrapole field determines that it is a second harmonic interaction. When operating at the n^{th} harmonic, up to n bunches may be formed. The modified gain and resonance condition are $\omega > n\omega_c$ and $\omega \simeq n\omega_c$ respectively for operation at the $\mathrm{n^{th}}$ harmonic.

As described above, in order to excite a second harmonic interaction the electron beam must experience a stronger second harmonic electric field than fundamental electric field. This can be accomplished by two methods. Firstly, the beam can be placed in a position which has stronger coupling to the second harmonic electric field. If, however, the coupling to the second harmonic and fundamental electric fields is similar, then a stronger second harmonic electric field is needed. To understand how a second harmonic electric field becomes stronger than a fundamental field we consider the expression for the RF fields for an n^{th} harmonic interaction in the electron frame of reference. The electric field is given by

$$\mathbf{E} = (E_{rn}\mathbf{r} + E_{\phi n}\phi)e^{i(\omega t+\psi)} \qquad 2.1.2a$$

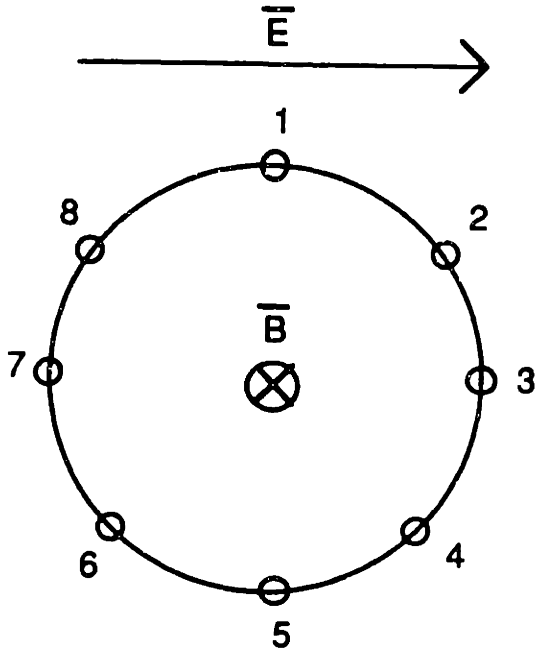

Figure 2.1.1a Gyrotron phase bunching — Initial condition, where the electrons are uniformly distributed on a beamlet.

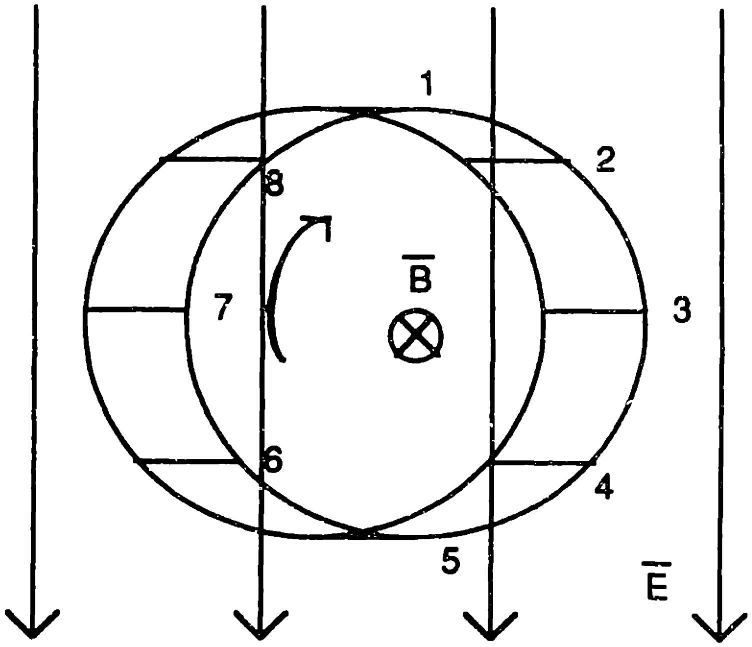

Figure 2.1.1b Gyrotron phase bunching — New positions of the electrons immediately after the change in energy.

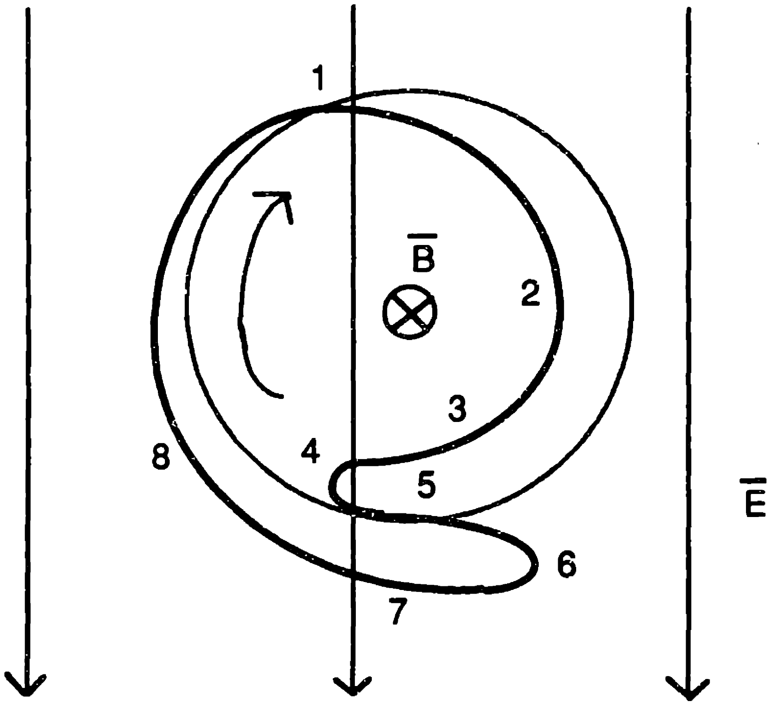

Figure 2.1.1c Gyrotron phase bunching — Formation of the electron bunch.

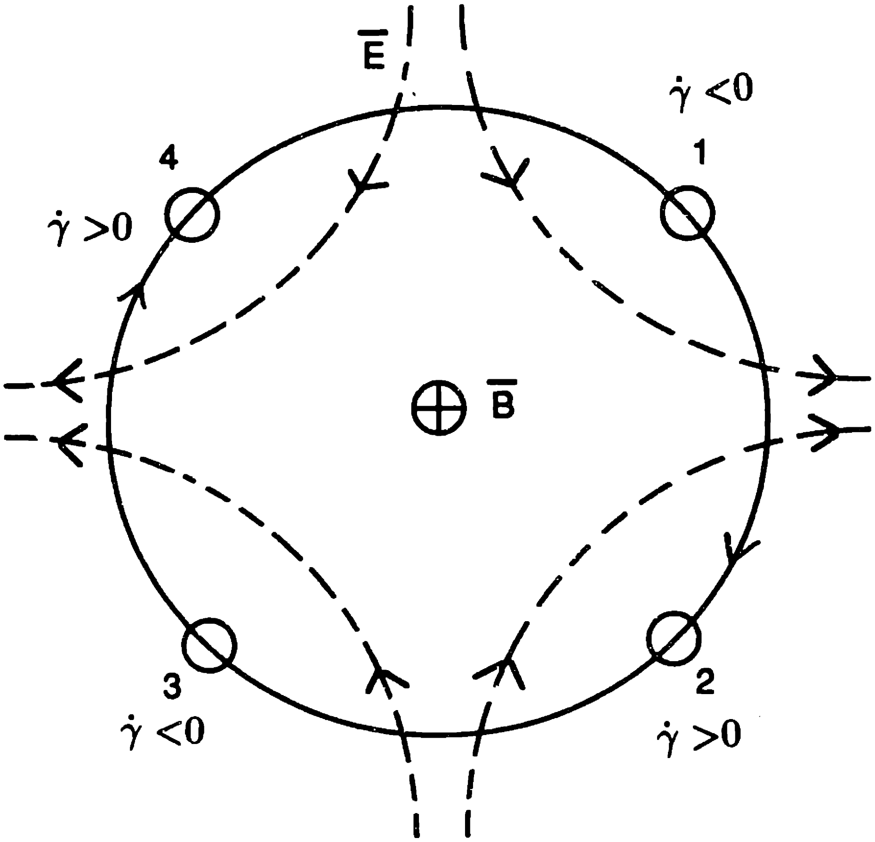

Figure 2.1.2 Regions of energy gain ($\dot\gamma > 0$) and energy loss ($\dot\gamma < 0$) for a second harmonic interaction. The electric field is represented by dashed lines.

$$E_{rn} = i\frac{n}{k_\perp r}E_0 f(z)J_{m\pm n}(k_\perp R_e)J_n(k_\perp r)e^{-im\phi_0}e^{in(\phi-\phi_0)} \qquad 2.1.2b$$

$$E_{\phi n} = E_0 f(z)J_{m\pm n}(k_\perp R_e)J_n'(k_\perp r)e^{-im\phi_0}e^{in(\phi-\phi_0)} \qquad 2.1.2c$$

where n is the harmonic number, $k_\perp = \nu_{mp}/R_o$, ν_{mp} is the p$^{\text{th}}$ root of $J_m' = 0$, R_o is the cavity radius, R_e is the radial position of the electron beam, f(z) is the axial field profile of the RF electric field in the cavity, E_o is the field amplitude, $r = v_\perp/\omega_c$ is the radius of the electron's Larmor gyration, $J_{m\pm n}(k_\perp R_e)$ is the beam - RF field coupling term, and the term $J_n(k_\perp r)$ represents the variation of the RF field across the larmor orbit. As will be discussed further in section 2.2, the following assumptions can be made for the fundamental and harmonic modes, which are denoted by the subscripts 1 and n respectively: for modes with large m, $J_{m\pm n}(k_\perp R_e) \simeq J_{m\pm 1}(k_\perp R_e)$ for the position corresponding to the innermost radial maximum of $J_{m\pm n}(k_\perp R_e)$, $\nu_{mp,n} \simeq n\nu_{mp,1}$, and $f_1(z) \simeq f_n(z)$. Using these assumptions the following relations can be obtained for the the harmonic to fundamental ratios of r and ϕ components of the RF electric fields

$$E_{rn}/E_{r1} \simeq \frac{J_n(k_\perp r_L)}{J_1(k_\perp r_L)} \qquad 2.1.3a$$

$$E_{\phi n}/E_{\phi 1} \simeq \frac{J_n'(k_\perp r_L)}{J_1'(k_\perp r_L)} \qquad 2.1.3b$$

The finite Larmor radius term $J_n(k_\perp r)$ can be approximated (when $k_\perp r \ll 1$) by

$$J_n(k_\perp r) \simeq \frac{n^n\beta_\perp^n}{2^n n!} \qquad 2.1.4$$

where $\beta_\perp = v_\perp/c$. With this approximation the ratio of the nth harmonic to fundamental total RF field can be written

$$\frac{E_n}{E_1} = \frac{n^n\beta_\perp^{n-1}}{n!2^{n-1}} \qquad 2.1.5$$

From equation 2.1.5, it can be seen that by increasing $\beta_\perp$ the harmonic field strength gets stronger. As $\beta_\perp$ increases, the Larmor radius increases, and therefore the electron experiences a larger RF field gradient. With a stronger gradient, the harmonic components of the field are larger. Therefore to reinforce the harmonic modes, one would like to operate with the largest $\beta_\perp$ possible.

The cyclotron resonance interaction described above is entirely caused by azimuthal bunching and is the gain mechanism in a gyrotron. However, axial bunching caused by a Lorentz force interaction between electrons and the RF magnetic field, known as the Weibel instability (Weibel (1959)), can occur. The Weibel instability and the cyclotron resonance interaction compete with each other (Chu (1978)). In a fast wave interaction the cyclotron resonance interaction dominates (Hirshfield (1965)). Gyrotrons operate near cutoff, and therefore $k_\perp \gg k_{||}$, where $k_\perp$ and $k_{||}$ are respectively the components of the wave number, k, perpendicular and parallel to the steady state magnetic field. Since $k_{||}v_{||}$ is small, the fast wave condition

$$v_\phi = \omega/k_{||} \gg c \tag{2.1.6}$$

is satisfied. The RF magnetic field B_{RF} is small compared to the RF electric field, E. The approximate scaling can be obtained from Faraday's law ($\mathbf{B_{rf}} = c/\omega \mathbf{k} \times \mathbf{E}$), yielding $E \simeq v_\phi B_{RF}/c$ and in a fast wave device, the phase velocity, v_ϕ is greater than the speed of light. For that reason axial bunching is not included when analyzing a gyrotron interaction. Transverse magnetic modes are ignored because the transverse electric field, $E_\perp$ scales as $k_{||}/k_\perp$ and therefore the TM mode RF-electron beam interaction will be weaker than that of the TE modes.

The modes excited in a gyrotron waveguide cavity are the transverse electric mode ($TE_{m,p,q}$) solutions to the wave equation. The subscripts m, p, q are the azimuthal, radial, and longitudinal indices, respectively, of the mode. This mode will oscillate at a frequency ω determined by

$$\frac{\omega^2}{c^2} = k^2 = k_\perp^2 + k_{||}^2 \tag{2.1.7}$$

where $k = 2\pi/\lambda$, λ is the wavelength and $k_{||}$, the axial wavenumber, is the qth eigenmode of the axial wave equation. The condition for exciting the cyclotron instability is

$$\omega - k_{||}\beta_{||}c = n\omega_{co}/\gamma \tag{2.1.8}$$

with the cyclotron frequency $\omega_{co} = eB_o/m$, $\gamma^{-2} = (1 - \beta^2)$, the total normalized beam velocity $\beta = v/c$ and where $\beta_\perp$ and $\beta_\parallel$ are the perpendicular and parallel components of the normalized velocity with respect to the main field B_o. Since $k_\perp \gg k_\parallel$ we also have $\omega \simeq \nu_{mp}/R_o \simeq \omega_c$. A mode of frequency ω can only oscillate over a small region in B_o. When the magnetic field is varied it is possible to excite a sequence of discrete modes with different ν_{mp}, which accounts for the many frequencies generated in the gyrotron resonator as the magnetic field is varied.

2.2 Linear Theory

Equations of Motion

The first step in developing a linear and nonlinear theory is to derive a set of equations that model the electron dynamics and incorporate the gyrotron beam geometry (Danly (1985)). A set of equations of motion known as the Yulpatov or pendulum equations (Flyagin (1977), Nusinovich (1972), Fliflet (1982), Bratman (1981)) provide a method of analyzing the electron dynamics. These equations can be condensed into fairly compact and physically transparent form. In this section the Yulpatov equations will be derived and a discussion of the assumptions made in the standard derivation with regard to harmonic ($n > 1$) interactions is presented.

To derive the Yulpatov equations we consider the electron dynamics. In the interaction region, the electron experiences a static magnetic field that is perpendicular to an RF electric field generated in the cavity. The equations for the electron energy ε and momentum, **p**, are

$$\frac{d\varepsilon}{dt} = -e\mathbf{v} \cdot \mathbf{E} \qquad 2.2.1a$$

and

$$\frac{d\mathbf{p}}{dt} = -e\mathbf{E} - \frac{e}{c}\mathbf{v} \times \mathbf{B} \qquad 2.2.1b$$

with $\varepsilon = \gamma m_e c^2$, $\gamma = (1 - \beta_\perp^2 - \beta_\parallel^2)^{-1/2}$ is the relativistic factor, $\beta^2 = \beta_\perp^2 + \beta_\parallel^2$, $\beta = v/c$ is the normalized beam velocity, $|\mathbf{p}| = \gamma\beta m_e c$, m_e is the electron mass, $\mathbf{E}$ is the RF electric field vector, and $\mathbf{B}$ is the static axial magnetic field vector. We make the following assumptions to simplify these equations. First, the axial RF field profile, $f(z) = e^{-(k_{\|}z)^2}$, where $\mathbf{E} \propto f(z)$ and z is the axial position, is an axially fixed Gaussian, so that we may write $k_{\|} = 2/L_{EFF}$ where L_{EFF} is the axial interaction length of the RF field in the cavity. The assumption of an axially fixed Gaussian is reasonable for a cavity with a high diffractive Q, (Gapanov (1981), Zaytsev (1974)) $Q_D \gg Q_{Dmin}$, where $Q_{Dmin} = 4\pi\left(\frac{L_{eff}}{\lambda}\right)^2$ is the minimum diffractive Q of the cavity. The electric field is however, permitted to rotate azimuthally. Fixing the mode axially allows it to be modeled as a cylindrical TE mode. The electric field is assumed to correspond to only one cylindrical TE resonator mode. As a result, this treatment does not describe the case where two modes are simultaneously excited. Since gyrotrons operate near cutoff, we have $k_{\|} << k_{\perp}$, so that the resultant RF magnetic field has very little effect as discussed in Chapter 1. To simplify the analysis, energy and velocity spread effects will be ignored and a single particle theory will be used. In addition to the assumptions listed above, we introduce two normalized variables. The normalized energy, w, and the normalized length, Z, are defined as $w = 1 - \gamma/\gamma_o$ and $Z = \omega z / c\beta_{o\|}$, where the subscript o refers to quantities at the entrance of the cavity and ω is the frequency of oscillation.

At this point we have made no assumptions about the beam geometry in the energy and phase equations. To incorporate the cylindrical geometry of the annular beam and model the electron's motion, a transformation to the frame of reference whose origin is at the center of an electron gyro orbit as shown in Figure 2.2.1, is needed. Using the complex momentum in the form $\mathbf{p} = \mathbf{p_x} + i\mathbf{p_y} = |\mathbf{p}_+|e^{i\alpha}$, and electric field $\mathbf{E} = \mathbf{E_x} + i\mathbf{E_y} = |\mathbf{E}_+|e^{i(\omega t+\psi)}$, where α is defined in Figure 2.2.1 as the angle that the momentum vector $\mathbf{p}$ traces out in the electron frame of reference and ψ is the angle between the electron and the wave, the energy equation can be rewritten as

$$\frac{dw}{dz} = \frac{e}{m^2c^2\omega}\frac{\beta_{\|o}}{\gamma\gamma_o\beta_{\|}}Re(\mathbf{p}_+\mathbf{E}_+) \qquad 2.2.2$$

and the momentum equation reduces to the phase equation for α

$$\frac{d\alpha}{dZ} = \frac{\beta_{\|o}\omega_c}{\beta_{\|}\omega} - \frac{e\beta_{\|o}}{\omega\beta_{\|}|\mathbf{p}_+|}Im(\mathbf{p}_+\mathbf{E}_+) \qquad 2.2.3$$

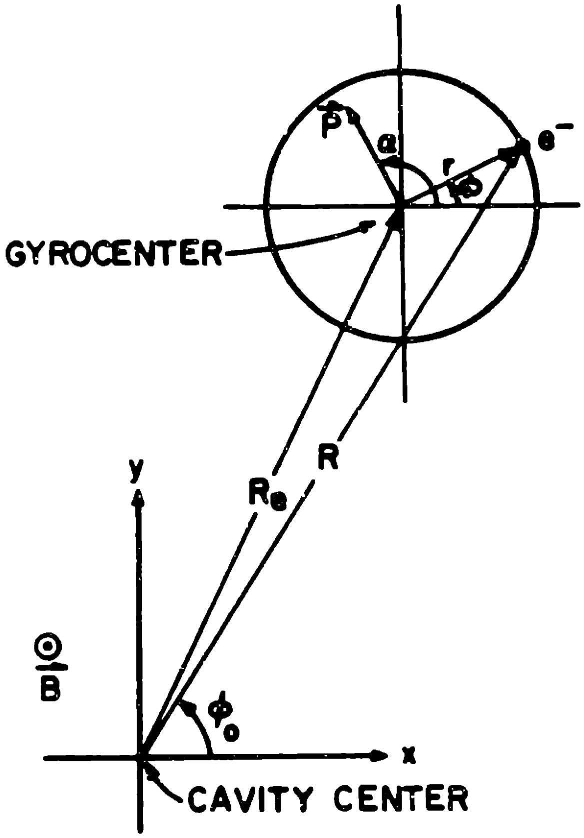

Figure 2.2.1 Coordinate system and definition of variables used in the derivation of the pendulum equations (Danly (1985))

where Re and Im refer to the real and imaginary parts of the bracketed quantities.

In a cavity with a circular cross section the electric field of a TE_{mp} mode near cutoff ($k_\perp >> k_\parallel$) is given by

$$\mathbf{E} = (E_R \tilde{R} + E_{\phi_o} \tilde{\phi}_o) e^{i(\omega t + \psi)} \tag{2.2.4a}$$

$$E_R = \frac{im}{k_\perp R} E_o f(z) J_m(k_\perp R) e^{-im\phi_o} \tag{2.2.4b}$$

$$E_{\phi o} = E_o f(z) J'_m e^{im\phi_o} \tag{2.2.4c}$$

where (R, ϕ_o) are the coordinates of the system with the origin at the center of the cavity, $\tilde{R}$ and $\tilde{\phi}_o$ are unit vectors in the radial and azimuthal directions respectively, E_o is the field amplitude, and $f(z)$ is the axial field distribution as a function of axial position z normalized to unity. The electric fields also need to be transformed to the electron's frame of reference. To accomplish this transformation, Graf's formula is used to express the Bessel functions as an infinite series (Haldar (1979)), representing a summation of the electric fields synchronous with all the harmonics. Since this theory is a single mode theory the electric field is represented by only the RF field synchronous with the electron for an n^{th} order cyclotron resonance ($\omega = n\omega_c$) and the representation is then

$$\mathbf{E} = (E_{rn} \tilde{r} + E_{\phi n} \tilde{\phi}) e^{i(\omega t + \psi)} \tag{2.2.5a}$$

$$E_{rn} = i \frac{n}{k_\perp r} E_o f(z) J_{m \pm n}(k_\perp R_e) J_n(k_\perp r) e^{-im\phi_o} e^{in(\phi - \phi_o)} \tag{2.2.5b}$$

$$E_{\phi n} = E_o f(z) J_{m \pm n}(k_\perp R_e) J'_n(k_\perp r) e^{-im\phi_o} e^{in(\phi - \phi_o)} \tag{2.2.5c}$$

The term $J_n(k_\perp r)$ represents the variation of the RF field across the Larmor orbit. After the introduction of the slow time variable, $\theta = \omega t - n\phi$, where the electron phase ϕ is related to α by $\alpha = \phi + \pi/2$, and a magnetic field detuning parameter, $\delta_o = 1 - n\omega_{co}/\omega$ the equations of motion become

$$\frac{dw}{dZ} = \frac{E_\phi}{nB_o} p'_\perp \sin\theta \tag{2.2.6a}$$

and

$$\frac{d\theta}{dZ} = \delta_o - w + \frac{E_r}{B_o}\frac{1-w}{p'_\perp}\cos\theta \qquad 2.2.6b$$

where $p'_\perp = \frac{|p_\perp|}{\gamma_o m_e c} = (\beta^2_{\perp o} - 2w - w^2)^{1/2}$, $E_r = |E_{rn}|$ and $E_\phi = |E_{\phi n}|$. Since at the entrance to the cavity no bunching has yet occurred ψ is arbitrary. In this analysis ψ is assumed to be constant throughout the interaction region, and we set $\psi - (m-n)\phi_o = \pi/2$.

We next introduce a renormalized energy variable, u, and a renormalized axial position variable, ξ, given by

$$u = \frac{2}{\beta^2_{\perp o}} w = \frac{2}{\beta^2_{\perp o}}(1 - \frac{\gamma}{\gamma_o}) \qquad 2.2.7a$$

$$\xi = \frac{\beta^2_{\perp o}}{2} Z = \frac{\pi\beta^2_{\perp o}}{\beta_{\| o}}\frac{z}{\lambda} \qquad 2.2.7b$$

Finally, the normalized interaction length μ is defined as

$$\mu = \frac{\pi\beta^2_{\perp o}}{\beta_{\| o}}\frac{L}{\lambda} \qquad 2.2.8$$

With the new variables, the equations of motion become

$$\frac{du}{d\xi} = \frac{4}{\beta^4_{\perp o}}\frac{E_\phi}{nB_o} p'_\perp \sin\theta \qquad 2.2.9a$$

$$\frac{d\theta}{d\xi} = \Delta - u - \frac{2}{\beta^2_{\perp o}}\frac{E_r}{B_o p'_\perp}\cos\theta \qquad 2.2.9b$$

where $\Delta = 2\delta_o/\beta^2_{\perp o}$ and $(1-w) \simeq 1$.

All of the above approximations and assumptions made are appropriate for the fundamental as well as harmonic interactions. However, at this point the standard derivations of the Yulpatov Equations (Danly (1985), Nusinovich (1972)) make the following assumption for the finite Larmor radius term, $J_n(k_\perp r)$

$$J'_n(k_\perp r) \simeq J'_n(n\beta_\perp) \simeq \frac{n^n \beta^{n-1}_\perp}{2^n n!} \qquad 2.2.10$$

This approximation is valid if $k_\perp r << 1$, where r is the electron gyro radius. To examine this assumption, we note that $r = \frac{v_\perp}{\omega_c}$ and use the approximations $k_\perp \simeq k$ and $n\omega_c \simeq \omega$

to get $k_\perp r \simeq n\beta_\perp$. For our electron gun, $\beta_\perp \simeq 0.4$, and therefore for the fundamental interaction ($n = 1$), the small argument approximation of the Bessel function is valid. In the case of the second harmonic, the approximation is worse, but for the purposes of our present analysis, adequate. A bigger error will be introduced when calculating the starting current and nonlinear efficiency than for the fundamental mode, because

$$\frac{J_n'(k_\perp r)/n^n\beta_\perp^{n-1}}{2^n n!} \simeq 0.9$$

for the second harmonic design mode of the iris cavity, compared to a typical fundamental mode for which the ratio is 0.94. The approximation becomes worse when the third harmonic interaction is considered.

Previously we have made the approximation $k_\perp r \simeq n\beta_\perp$. However, a better approximation is that $k_\perp r \simeq np'_\perp$, where we recall that $p'_\perp = \gamma\beta_\perp/\gamma_o = (\beta_{\perp o}^2 - 2w + w^2)^{1/2}$. Using the approximations for $k_\perp r$, retaining the J_n' term, and defining a normalized field amplitude F' as

$$F' = \frac{2E_o}{nB_o}\beta_{\perp o}^{-3} J_n'(np'_\perp) J_{m\pm n}(k_\perp R_e) \qquad 2.2.11$$

the equations of motion can be written as

$$\frac{du}{d\xi} = 2F' f(\xi)(1-u)^{1/2}\sin\theta \qquad 2.2.12a$$

$$\frac{d\theta}{d\xi} = \Delta - u - \frac{nf(\xi)F'}{\beta_{\perp o}(1-u)}\frac{J_n(np'_\perp)}{J_n'(np'_\perp)}\cos\theta \qquad 2.2.12b$$

where we have made the following approximation for $p'_\perp$. For a weakly relativistic beam $n\beta_{\perp o}^2/2 \ll 1$ is valid up to the fifth harmonic when $\beta_{\perp o} = 0.4$. Using this assumption we then make the approximation (Bratman (1981))

$$p'_\perp \simeq (\beta_{\perp o}^2 - 2w)^{1/2} = \beta_{\perp o}(1-u)^{1/2} \qquad 2.2.13$$

which has been used to give equations 2.2.12a and 2.2.12b.

To put these equations in a form similar to the standard Soviet form, we define

$$p = \frac{\gamma\beta_\perp}{\gamma_0\beta_{\perp o}} = \frac{p'_\perp}{\beta_{\perp o}} \qquad 2.2.14a$$

$$\theta = n\phi - \omega t_o + \pi/2 \tag{2.2.14b}$$

where t_o is the time when the electrons enter the interaction region. The equations of motion then become

$$\frac{dp}{d\xi} = -F' f(\xi)\sin\theta \tag{2.2.15a}$$

$$\frac{d\theta}{d\xi} = -(\Delta + p^2 - 1) - \frac{n}{\beta_{\perp o} p^2} F' f(\xi) \frac{J_n(n\beta_{\perp o} p)}{J_n'(n\beta_{\perp o} p)} \cos\theta \tag{2.2.15b}$$

To recover the standard form of the Yulpatov equations, the approximation given by equation 2.2.10 is made for the J_n' and J_n term. A slightly different form of the normalized field amplitude, F, given by

$$F = \frac{E_o}{B_o}\beta_{\perp o}^{n-4}\left(\frac{n^{n-1}}{n!2^{n-1}}\right) J_{m\pm n}(k_\perp R_e) \tag{2.2.16}$$

is used to yield

$$\frac{dp}{d\xi} = -F f(\xi) p^{n-1}\sin\theta \tag{2.2.17a}$$

$$\frac{d\theta}{d\xi} = -(\Delta + p^2 - 1) - nF f(\xi) p^{n-2}\cos\theta \tag{2.2.17b}$$

which are the standard forms of the equations.

With these normalizations, $f(\xi)$ becomes

$$f(z) = e^{-(k_\parallel z)^2} = e^{-(2\xi/\mu)^2} \tag{2.2.18}$$

These equations are used in the linear and nonlinear theory to analyse the electron dynamics.

As the harmonic number increases, the error introduced by the approximation made in equation 2.2.10 becomes larger. However, as will be shown later, a simple correction can be made so equations 2.2.15 and 2.2.12 yield efficiencies whose difference is less than 1%, even up to the third harmonic. Therefore for convenience, equations 2.2.12a and 2.2.12b will be used to derive the equilibrium equation and an analytic expression for the starting current in the following section.

Starting Current

We next derive an analytic expression for the starting current. The energy balance equation can be expressed in a form that relates the normalized field amplitude F to the normalized beam current I given by

$$F^2 = \eta_\perp I \tag{2.2.19}$$

where I is the normalized beam current. The linear efficiency, $\eta_{\perp lin}$, can then be calculated from the linearized Yulpatov equations. Using equation 2.2.19 with the linear efficiency, an analytic expression can then be calculated for the starting current. Since the linear efficiency is valid only for the small signal regime (small F), the expression thus obtained is valid only at beam currents close to the starting current. In this section, we first manipulate the energy balance equation to yield the form given by equation 2.2.19 and then derive an expression for the linear efficiency. Finally we calculate an analytic expression for the starting current that is valid for analyzing fundamental and second harmonic interactions.

The energy balance equation involves the definition of the cavity Q. Power is lost by two mechanisms, diffraction and ohmic losses to the walls. For the diffractive losses the cavity Q is defined as

$$Q_D = \frac{\omega U}{P_{diff}} \tag{2.2.20}$$

where U is the stored energy, ω is the RF wave frequency, and P_{diff} is the power that is diffracted out of the cavity. The ohmic losses in the cavity walls are similarly expressed in terms of the ohmic Q. The two Q factors can be combined in the total Q, Q_T by

$$\frac{1}{Q_T} = \frac{1}{Q_D} + \frac{1}{Q_{oh}} \tag{2.2.21}$$

where the ohmic Q is given by $Q_{oh} = R_o(f\mu_0\sigma\pi)^{1/2}(1 - \frac{m^2}{\nu_{mp}^2})$, μ_0 is the permittivity of vacuum and σ the conductivity of the cavity wall.

The power lost by the two mechanisms can be combined in a term P_{loss} which represents the power that leaves the resonator by diffraction (P_{out}) and ohmically heating the walls. The power lost by diffraction, P_{out} is what is measured experimentally and will be defined later in equation 2.3.1b. Therefore the energy balance equation can be written as

$$Q_T = \frac{\omega U}{P_{loss}} \qquad 2.2.22$$

and

$$P_{loss} = \eta P_{in} = \eta V I_a = \eta_{el}\eta_{\perp} V I_a, \qquad 2.2.23$$

where V is the cathode voltage in volts and I_a is the beam current in amperes. The perpendicular efficiency, $\eta_{\perp}$ accounts for the fact that only the perpendicular velocity contributes to the beam-RF interaction. The ohmic losses and the power diffracted out of the cavity are represented by the electrical efficiency, $\eta_{el} = \beta_{\perp o}^2/2(1-\gamma^{-1})$, which represents the losses of the system independent of the mechanism. Using this definition of η_{el} the quantity P_{loss} can be re-expressed as

$$P_{loss} = \frac{mc^2}{e}\frac{\gamma_o \beta_{\perp o}^2}{2}\eta_{\perp} I_a \qquad 2.2.24$$

where $\gamma_o = 1 + V/511 \times 10^6$. In a cylindrical cavity with a cylindrical beam and a fixed Gaussian RF profile, the stored energy, U can be written ((S.N. Vlasov (1969), Temkin (1984))

$$U = \epsilon_0 E_o^2 (\pi/2)^{1.5}(L/2k_{\perp}^2)(\nu_{mp}^2 - m^2)J_m^2(\nu_{mp}) \qquad 2.2.25$$

Substituting equations 2.2.24 and 2.2.25 into 2.2.22 yields an energy balance equation of the form 2.2.19 with I given by

$$I = 0.239 \times 10^{-3}\frac{Q_T I_a}{\gamma_o}\beta_{\perp}^{2(n-3)}\left(\frac{\lambda}{L}\right)\left(\frac{n^n}{2^n n!}\right)^2 \frac{J_{m\pm n}^2(k_{\perp}R_e)}{(\nu_{mp}^2 - m^2)J_m^2(\nu_{mp})} \qquad 2.2.26$$

An expression for the linear efficiency is used to obtain an analytic form of the normalized current I in the small signal regime ($I = I_{st}$, where I_{st} is the current required for start of oscillation) from the energy balance equation. To derive an expression for the linear efficiency, with the linearized Yulpatov equations, one makes use of an expansion in $\epsilon \ll 1$ of equations 2.2.17a and b. We then obtain the following expressions (Tran (1985))

$$F = \epsilon F_1 \tag{2.2.27a}$$

$$\theta = (\theta_0 - \Delta\xi) + \epsilon\theta_1 + ... \tag{2.2.27b}$$

$$p_\perp = 1 + \epsilon p_1 + \epsilon^2 p_2 \tag{2.2.27c}$$

$$p_1^2 = 1 + 2\epsilon p_1 + \epsilon^2(p_1^2 + 2p_1) \tag{2.2.27d}$$

$$p^{n-1} \simeq 1 + \epsilon(n-1)p_1 \tag{2.2.27e}$$

$$F/p = \epsilon F_1 - \epsilon^2 p_1 F_1 \tag{2.2.27f}$$

$$\sin\theta = \sin[(\theta_0 - \Delta\xi)] + \epsilon\theta_1 \cos[(\theta_0 - \Delta\xi)] \tag{2.2.27g}$$

$$\cos\theta = \cos[(\theta_0 - \Delta\xi)] - \epsilon\theta_1 \sin[(\theta_0 - \Delta\xi)] \tag{2.2.27h}$$

After substituting these expressions into equations 2.2.17, we obtain a series of equations in orders of ϵ. These are solved separately up to order ϵ^2. This procedure yields equations for p_1', p_2' and θ', where $'$ represents the derivative with respect to ξ. These equations are integrated from $+\infty$ to $-\infty$ giving expressions for p_1 and p_2. The perpendicular efficiency, $\eta_\perp$ is defined by

$$\eta_\perp = 1 - < w > \tag{2.2.28}$$

where $<>= 1/2\pi \int_0^{2\pi} d\theta_o$ and

$$< w >= \frac{1}{2\pi} \int_0^{2\pi} d\theta_0 w(\theta_0, \xi = +\infty) = 1 + < p_1^2 > +2 < p_2 > \tag{2.2.29}$$

where we have used $w = 1 + 2p_1 + p_1^2 + 2p_2$ and $< p_1 >= 0$. Using the expression for $< p_1^2 >$ and $< p_2 >$ the linear efficiency is obtained, after a short calculation, in the form

$$\eta_{\perp lin} = \frac{\pi}{4} F^2 \mu^2 e^{\frac{-\Delta^2\mu^2}{8}} [\frac{\mu^2\Delta}{4} - n] \tag{2.2.30}$$

The starting current can now be obtained from the energy balance equation in the small signal or linear regime, with the expression 2.2.30 for the linear efficiency $\eta_{\perp lin}$. The normalized starting current I_{st} becomes (Kreischer (1980))

$$I_{st} = \frac{4}{\pi\mu^2} \frac{e^{2x^2}}{\mu x - n} \tag{2.2.31}$$

where $x = \mu\Delta/4$. As can be seen in Figure 2.2.2, which shows the starting current for the second harmonic design mode of the tapered cavity ($TE_{8,5,1}$) the starting current is a function of the magnetic field through the detuning parameter, Δ. The minimum starting current is obtained by minimizing with respect to Δ, and this occurs at

$$x = x_{min} = \frac{1}{2}\left(\frac{n}{\mu} + \left(\frac{n^2}{\mu^2} + 1\right)^{1/2}\right) \tag{2.2.32}$$

The starting current corresponding to x_{min} is the minimum starting current shown in Figure 2.2.2.

Starting Current Calculation

We now calculate numerically the starting current as a function of magnetic field for a specific mode. This involves the calculation of I_{st} at different values of Δ or magnetic field. Since I_{st} is the normalized starting current, equation 2.2.26, which defines the beam current normalization, is then used to give the current in amperes. In this section we discuss two codes, CAVRF and LINEAR, that are used to calculate the starting current.

As can be seen from equations 2.2.26 and 2.2.31 the diffractive Q, which gives the total Q, and the effective interaction length need to be calculated numerically. These quantities are calculated with a code, CAVRF (Fliflet (1981)), that solves for the eigenmodes of a weakly irregular gyrotron cavity without the presence of an electron beam. Specifically, the code solves the axial wave equation:

$$\frac{d^2 f(z)}{dz^2} + k_{\parallel}^2 f(z) = 0 \tag{2.2.33}$$

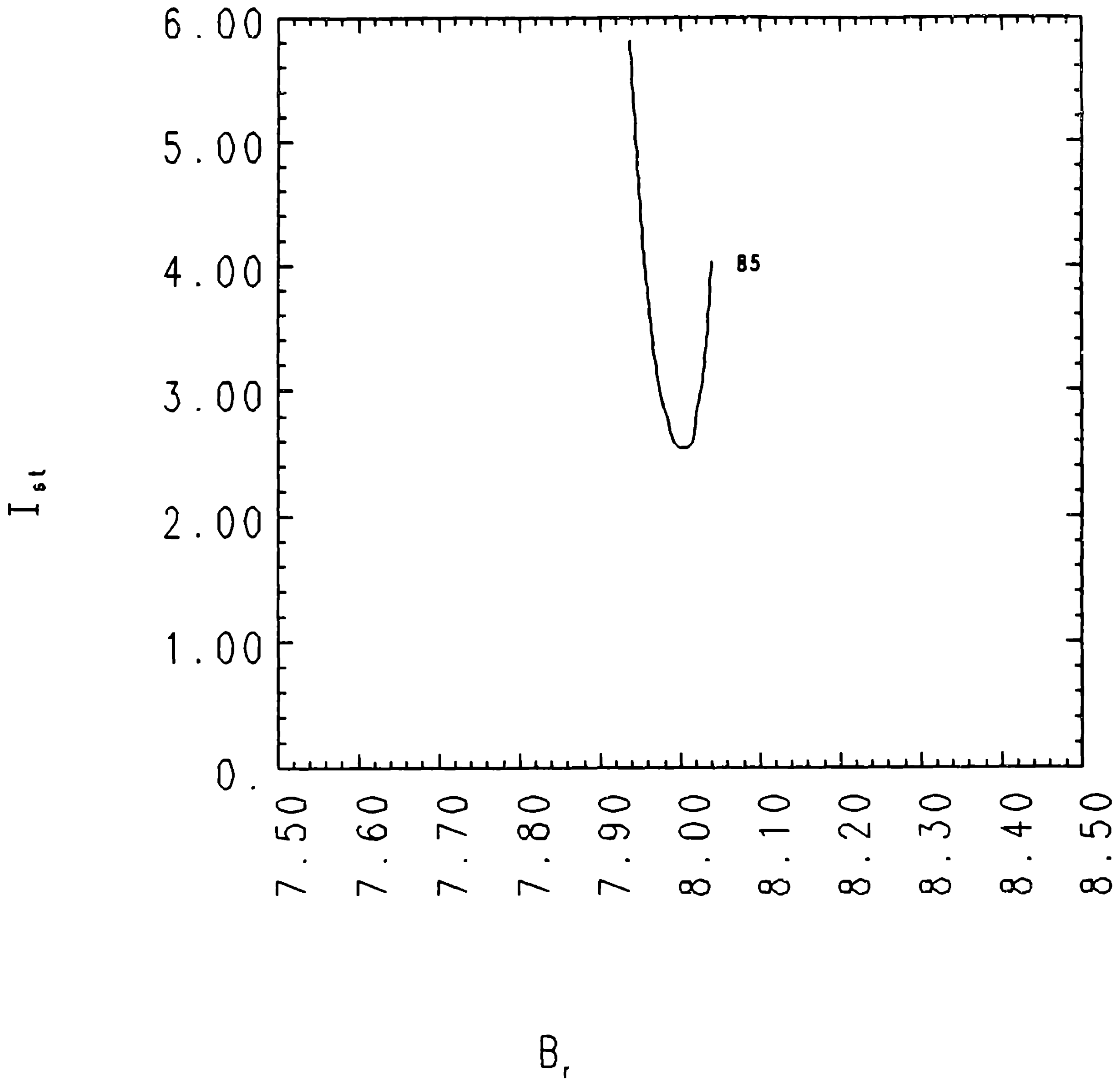

Figure 2.2.2 Starting Current as a function of magnetic field for the design second harmonic mode ($TE_{8,5,1}$) in the tapered cavity experiment.

where

$$k_{\parallel}^2(z) = (\omega/c)^2 - k_{\perp}^2(z) \qquad 2.2.33b$$

and $k_{\parallel}$ is the parallel wavenumber and $k_{\perp}$ is the transverse wave number. This code uses the initial boundary conditions:

$$\left[\frac{df(z)}{dz} - ik_{\parallel}f(z)\right]_{z=z_1} = 0 \qquad 2.2.34a$$

and

$$\left[\frac{df(z)}{dz} + ik_{\parallel}f(z)\right]_{z=z_2} = 0 \qquad 2.2.34b$$

with z_1 the axial position of the cavity input and z_2 the axial position of the cavity output. The result of the calculation is an estimated value of the eigenfrequency. The diffractive Q, Q_D is calculated by the code using $Q_D = Re(\omega)/2iIm(\omega)$. Before discussing the method of calculating the effective interaction length, we need to determine how this length should be defined. In the previous derivations the RF axial profile was assumed to be a fixed Gaussian, and the effective interaction length was defined by equation 2.2.33b with $k_{\parallel} = 2/L_{eff}$. Using equation 2.2.33b with the frequency calculated by CAVRF, one finds for the iris cavity, agreement between the parallel wavenumber calculated by the wave equation and that obtained with the effective effective interaction length of the RF axial profile calculated by CAVRF is very good. With the tapered cavity, agreement is not as good, but is adequate for that experiment. Therefore one can assume that the cold cavity RF field profile calculated by CAVRF can be approximated by a fixed Gaussian profile. To further check the Gaussian profile assumption, a self consistent nonlinear code (Fliflet (1987)) was used to calculate and plot the nonlinear efficiency and the RF field profile as a function of axial position. By observing the axial distance in the cavity, where the efficiency is not excessively small (ie. the effective interaction length), one can check whether this length corresponds to the length predicted for a Gaussian axial profile. From these two plots, which were done for several fundamental modes, it could be seen that when the field amplitude dropped by a factor of e (2.718) the beam-wave efficiency became small. Therefore the effective interaction length can be defined as the axial distance where the RF field amplitude is greater than (1/e) x maximum RF field amplitude, as shown in Figure 2.2.3, where the maximum amplitude of the RF field profile has been normalized to unity. This is the definition of the effective interaction length of a Gaussian profile. So the effective interaction length is estimated from the graphical output of the axial RF field profile, f(z) using the definition discussed above.

Using the total Q calculated from the diffractive Q and the effective interaction length determined by CAVRF, the starting current can be calculated by the code LINEAR (Kreischer (1982)) LINEAR is a code that calculates the starting current for a Gaussian, sine or an arbitrary axial RF field profile in a cylindrical open resonator. If the Gaussian profile is assumed the starting current equation used by LINEAR is equivalent to the combination of equations 2.2.26 and 2.2.31, without the approximation for the harmonic term (equation 2.2.9). As will be discussed in the nonlinear theory section, the substitution of the proper harmonic term $J'_n(k_\perp r_L)$, into the normalized current to replace the approximation made in equation 2.2.10 is the only change necessary to obtain an analytic expression for the starting current that accounts for the harmonic term. The code LINEAR assumes that adiabatic field theory is valid in the gun region, and that we have a monoenergetic, annular azimuthally symmetric electron beam that has no thickness or velocity spread. In order to calculate the starting current we need to specify the cathode voltage, the ratio of perpendicular to parallel velocity $(\beta_\perp/\beta_\parallel)$, the cavity and cathode magnetic fields, mode, cavity radius and effective length, cathode to anode distance, the total Q of the mode, the cathode radius, the RF field profile and finally the harmonic number. Using this data, both the J_{m+n} and J_{m-n} rotations of the starting current are calculated as a function of magnetic field. This method of numerically calculating the starting current will be used in all the analyses of starting currents of the various experiments described in this thesis.

Challenges in Exciting the Second Harmonic

When examining the gyrotron linear theory, it becomes obvious why the second

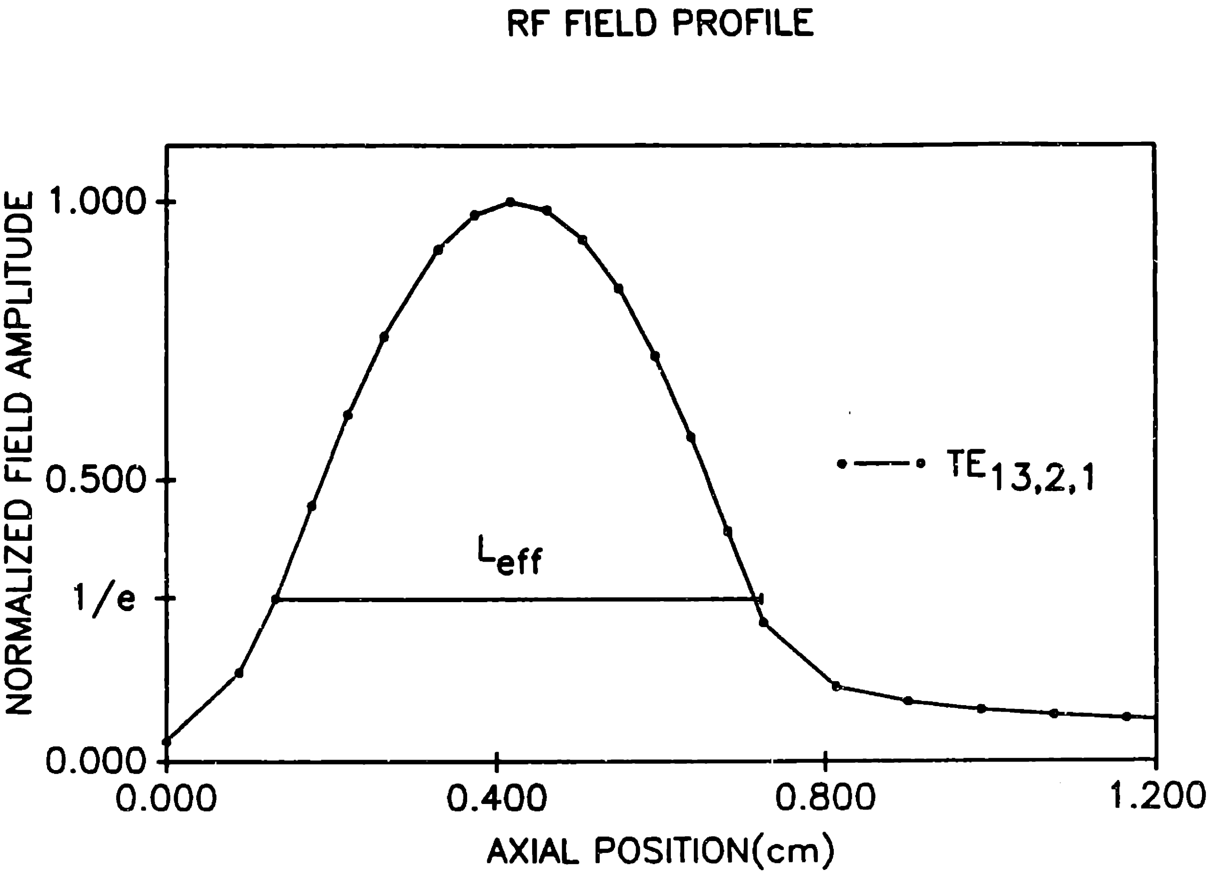

Figure 2.2.3 Normalized RF field profile of the second harmonic $TE_{13,2,1}$ mode where the effective interaction length L_{eff} is shown

harmonic is hard to excite. The most important issue is that the starting current of the second harmonic is higher than that of the fundamental modes and therefore the fundamental modes are usually excited first and suppress the harmonic modes. At lower frequencies harmonic modes are occasionally observed (Byerly (1984)), when there is a gap in the fundamental spectrum. However, at frequencies above 300 GHz, the fundamental spectrum becomes very dense and, before this experiment, high power second harmonic modes above 300 GHz have not been observed.

To further illustrate this point it is useful to calculate an approximate ratio of second harmonic to fundamental mode starting currents for a standard cylindrical cavity with a Gaussian RF field profile. We start with the normalized starting current equations equations 2.2.31 and 2.2.32, and make the following approximations. Since μ is on the order of 5 or 6 for the fundamental modes, and 10 to 15 for second harmonic modes, one can assume that $\mu \gg n$ and $x \simeq 1/2$, giving

$$I_{st} \propto \frac{1}{\mu^3} \qquad 2.2.35$$

In equation 2.2.26 we note that for modes where $m \gg 1$ and p is small (whispering gallery modes) which tend to be the most easily excited harmonic modes, and for strong fundamental modes, $J_{m\pm n}(k_\perp R_e) \simeq J_m(\nu_{mp})$ if the beam is positioned on the innermost peak of $J_{m\pm n}(k_\perp R_e)$. To make a worst case scenario comparison, we assume that the beam is positioned at the best position for not only the second harmonic modes, but also for the fundamental. This turns out to be a reasonable assumption due to beam spread and misalignment effects, which will be discussed later. In the other part of the coupling term (C_{mp}) given by

$$C_{mp}^2 = \frac{J_{m\pm n}^2(k_\perp R_e)}{J_m^2(\nu_{mp})(\nu_{mp}^2 - m^2)} \qquad 2.2.36$$

$\nu_{mp}^2 \gg m^2$ and so $C_{mp} \simeq 1/\nu_{mp}^2$. Furthermore, $\nu_{mp} \propto k = 2\pi/\lambda$ so that $C_{mp} \propto \lambda^2$. We therefore obtain from equation 2.2.26

$$I \propto Q_T I_a \beta_\perp^{2(n-3)} (\lambda/L)\, \lambda^2 \qquad 2.2.37$$

Combining equations 2.2.35 and 2.2.37 and using equation 2.2.8 (for μ) one gets the following expression

$$I_a \propto \frac{\beta_{\|o}^3 \beta_\perp^{-2n}}{L^2 Q_T} \qquad 2.2.38$$

Using equation 2.2.38 and assuming that for the n^{th} harmonic $\beta_{\perp,\|o\;n} \simeq \beta_{\perp,\|o\;1}$, $L_1 \simeq L_n$, $Q_T \simeq Q_{Dmin} = 4\pi(L/\lambda)^2$ (this assumption was made to simplify the calculation, but in an actual cavity, high efficiency operation requires a high Q cavity, $Q_T \gg Q_{Dmin}$) and $\lambda_n \simeq \frac{1}{n}\lambda_1$, where the subscripts 1 and n refer to fundamental and n^{th} harmonic quantities, yields an expression for the starting current ratio given by

$$\frac{I_{a\;n}}{I_{a\;1}} \simeq \frac{Q_{T\;1}\beta_{\perp o}^{2(1-n)}}{Q_{T\;n}} \simeq \frac{\beta_{\perp o}^{2(1-n)}}{n^2} \qquad 2.2.39$$

What this expression means physically is that there are two factors determining the starting current: the gain, which is lower by $\beta_{\perp o}^2$ at the second harmonic, and the cavity Q, which is higher by about a factor of 4 at the second harmonic. Therefore, the second harmonic starting current is comparable to that of the fundamental. For the electron gun used in this experiment $\beta_{\perp o} \simeq 0.4$. From this analysis we conclude that the starting current of a second harmonic mode is larger than that of a fundamental mode by at least a factor of 1.6, for typical fundamental and second harmonic modes. However, even though the second harmonic starting current is typically only slightly higher than the fundamental starting current, it is difficult to excite high frequency second harmonic modes, due to the dense fundamental spectrum. After a mode is excited, a nonlinear effect (Dialitis (1983), Zarnitsina (1974), and Nusinovich (1977)) raises the starting currents of the surrounding modes. Therefore to excite a second harmonic mode, that mode must have the lowest starting current, so it can be excited first. One can also see from equation 2.2.39, that either the total Q ratio $Q_{T\;2}/Q_{T\;1}$ or the value of the normalized perpendicular velocity $\beta_{\perp o}$ must be increased to improve the starting current ratio and lessen the difficulty of exciting high frequency harmonic modes. Since an existing gun was used for the set of experiments discussed in this paper, increasing $\beta_{\perp o}$ was not possible. Operating with a higher total Q ratio was a more practical solution and as discussed in Chapter 5, proved to be a successful method for exciting high frequency second harmonic modes.

The above analysis does not include the beam spread effects on the second harmonic starting current. Due to the fact that the beam has a finite thickness not all the electrons are in the radial position corresponding to the maximum beam-RF coupling, and we can therefore expect the second harmonic starting current to be higher than predicted in this analysis.

Another difficulty is presented by the fact that thick beams can couple to several different modes simultaneously, as can be seen in Figures 2.2.4a and 2.2.4b. The beam thickness, or spread of the guiding centers normalized by the Larmor radius, δ/r_L, is given by (Felch (1982))

$$\frac{\delta}{r_L} = \frac{2\pi I_a \sin\theta}{n\beta_\perp \alpha \lambda^2 \nu_{m\pm n} J_k} \qquad 3.2.40$$

where I_a is the beam current, θ is the angle of the cathode, n is the harmonic number, α is the ratio of the main magnetic field to the magnetic field at the gun, $\nu_{m\pm n}$ is the root of the equation $J'_{m\pm n} = 0$ that is closest to the beam position, and J_k is the cathode emission density. When we use the value of the magnetic field at which the iris cavity is designed to operate, we find that the guiding center spread is 2.0 r_L, where the Larmor radius is given by $r_L = v_\perp/\omega_c$, with the cyclotron frequency $\omega_c = eB/\gamma m$, and $v_\perp$ is the component of the beam velocity perpendicular to the main field. As an example, in Figures 2.2.4a and 2.2.4b, $J^2_{m\pm n}(k_\perp R_e)$, which is the part of the coupling coefficient C_{mp} that varies with beam radius, is plotted against normalized beam radius r_L/R_o, where R_o is the cavity radius, for the $TE_{4,3,1}$ mode (Figure 2.2.4a) and the $TE_{6,2,1}$ mode (Figure 2.2.4b), which were the two strongest fundamental modes in the tapered cavity experiment. The corresponding plot for the desired second harmonic mode, the $TE_{8,5,1}$ is shown in Figure 2.2.4c. From equation 2.2.26 we note that the starting current is inversely proportional to the quantity $J_{m\pm n}(k_\perp R_e)$. The double peaked structures correspond to the two rotations, J_{m+n} and J_{m-n}. The shaded area corresponds to the electron beam. Since the starting currents of fundamental modes are lower than those of

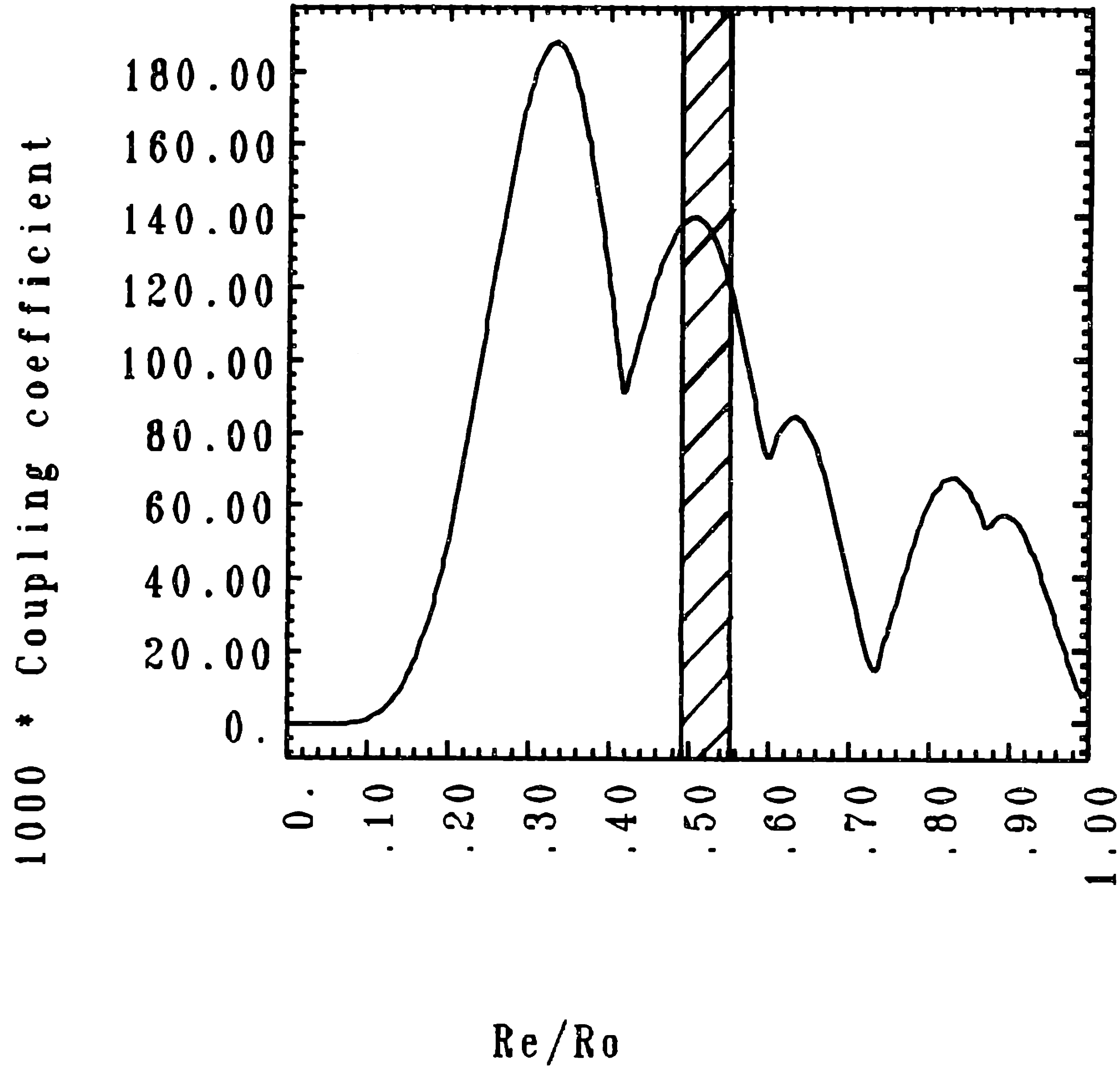

Figure 2.2.4a The harmonic factor of the coupling coefficient $J^2_{m\pm n}(k_\perp R_e)$ plotted as a function of the normalized beam position R_e/R_o for the fundamental $TE_{4,3,1}$ mode

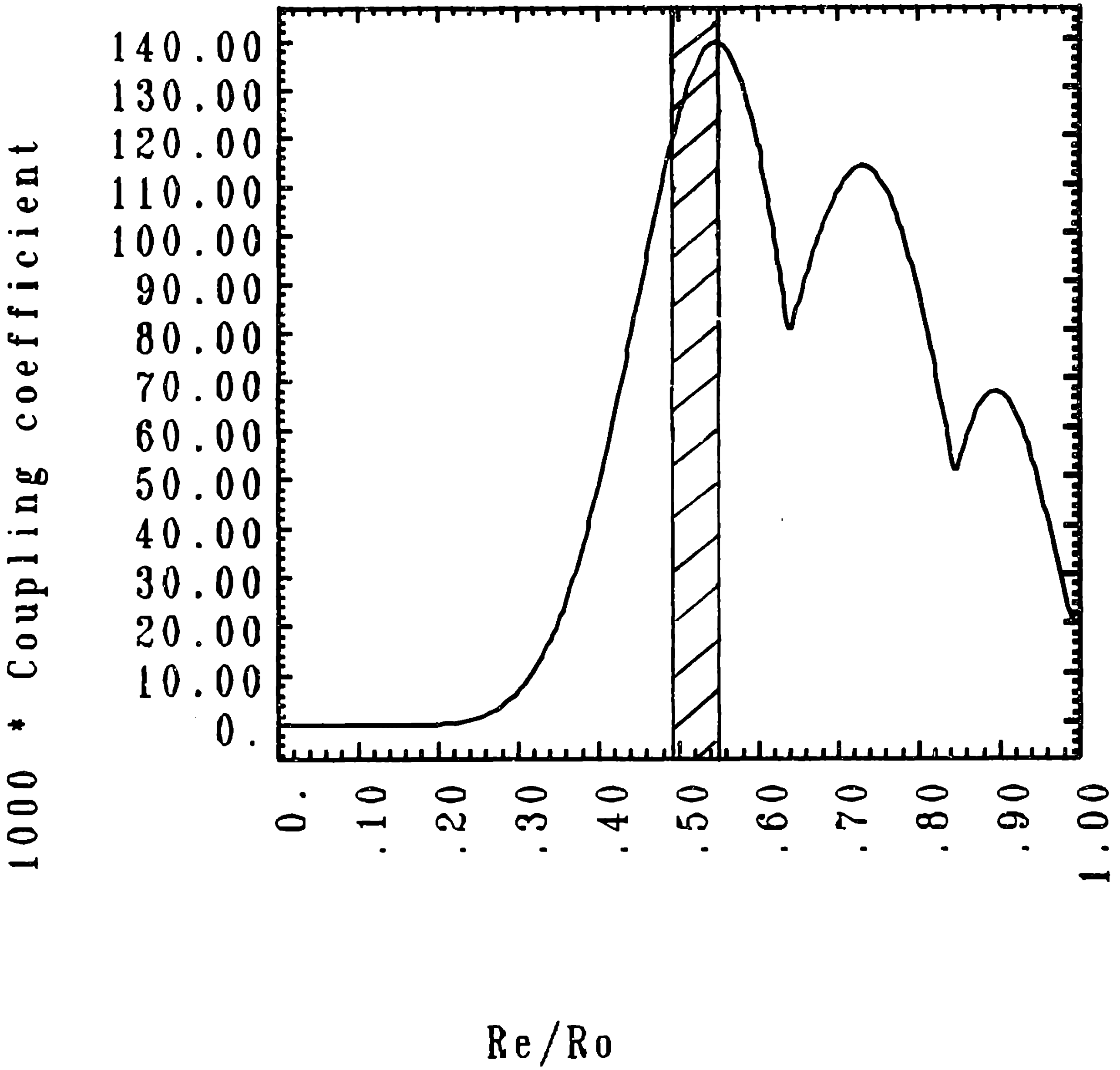

Figure 2.2.4b The harmonic factor of the coupling coefficient $J^2_{m\pm n}(k_\perp R_e)$ plotted for the fundamental $TE_{6,2,1}$ mode as a function of normalized beam position R_e/R_o.

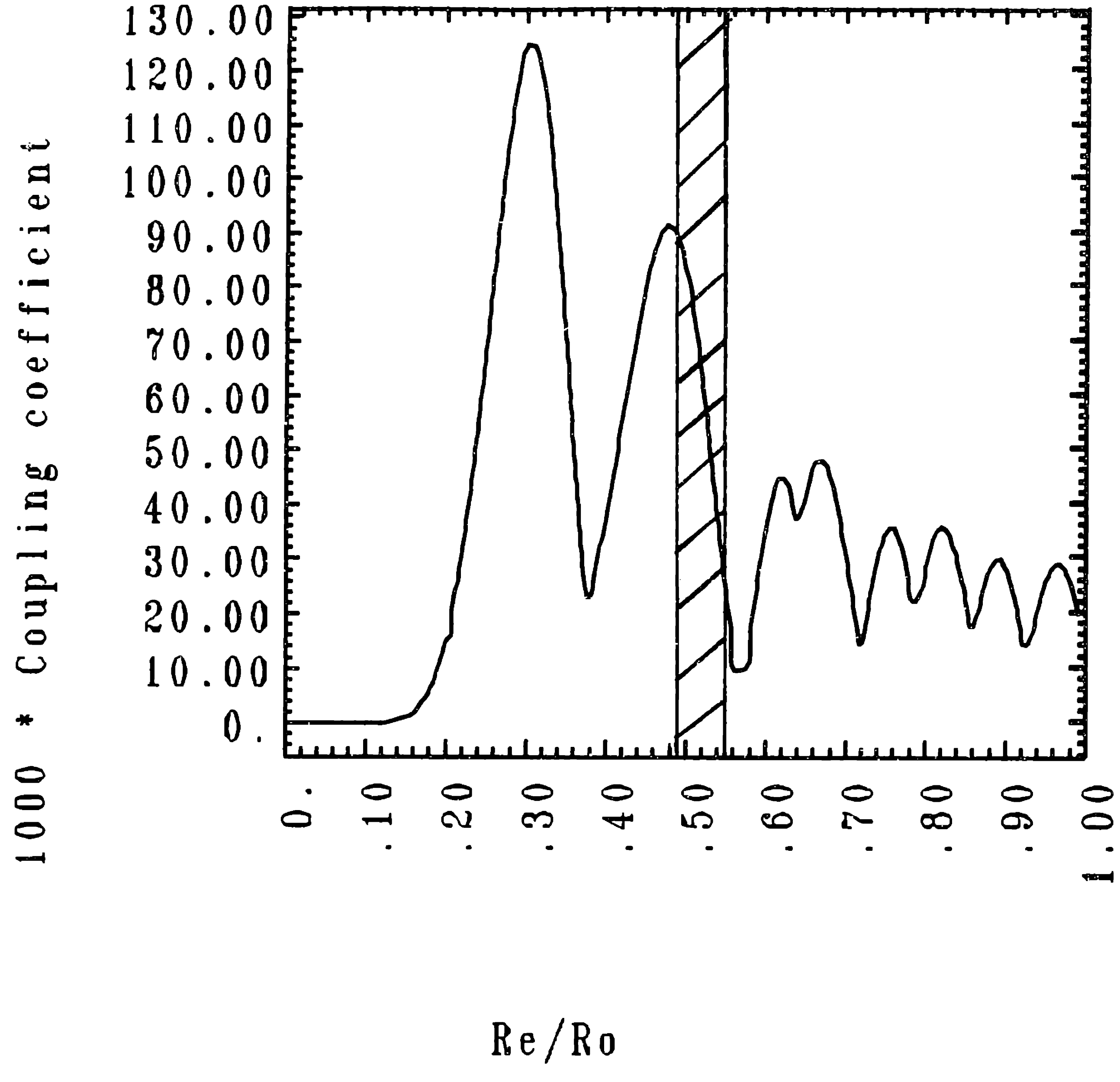

Figure 2.2.4c The harmonic factor of the coupling coefficient $J^2_{m\pm n}(k_\perp R_e)$ plotted as a function of normalized beam position R_e/R_o for the second harmonic $TE_{8,5,1}$ mode.

second harmonic modes, only the fundamental mode spectrum needs to be considered in a fundamental mode experiment. Even a thick beam will couple well to just one or two fundamental modes. However, when operating with a second harmonic mode a thick beam typically couples not only to the design mode but also to one or two fundamental modes and possibly to several other harmonic modes. Only an infinitely thin beam could be placed in a position that provides strong coupling to the desired second harmonic mode and no other. We conclude that the initial simplified analysis assuming a thin beam is not valid. One has to assume that even if the beam is centered at a position where the fundamental is weak, strong coupling to the fundamental will occur due to beam thickness or misalignment. As the frequency increases this problem becomes worse, because the cavity size decreases and the radial extent corresponding to the beamspread occupies a larger fraction of the cavity.

Starting currents can also be affected by misalignment, which can position the beam in a non optimal position. Misalignment effects may be more severe than beam spread effects. Whereas beamspread tends to be an averaging of areas with strong and weak effects, misalignment may cause the beam to be centered on an area of weak coupling to the harmonic modes or strong coupling to fundamental modes creating a larger increase in the starting current ratio, I_{st2}/I_{st1}.

The conclusion is that in order to excite a second harmonic mode the fundamental modes need to be suppressed. In this thesis three different methods which have been used to try to suppress the fundamental modes are discussed. In the first experiment, the straight cavity, a second harmonic mode was chosen that existed in a frequency gap in the fundamental spectrum. This experiment suffered from the thick beam effects described above. In the second experiment we tried to selectively perturb and thereby suppress the fundamental modes, by attempting a slotted cavity experiment with axial slots cut in the cavity wall designed to accomplish this purpose. In the third experiment, an iris at the output end of the resonator's straight section selectively trapped the second harmonic modes more than the fundamental modes and allowed second harmonic modes to be excited before the fundamental modes.

2.3 Nonlinear Theory

In this section the full Pendulum equations will be used with the energy balance equation in the form given by equation 2.2.19, to calculate the nonlinear or large signal perpendicular efficiency and the output power, P_{out}. In the linear analysis, expansions of quantities such as the perpendicular momentum and the slow time scale variable, θ, were made and the higher order terms were disregarded as small. In a nonlinear analysis, these terms are no longer small, and therefore must be kept. For this reason a simple analytic expression for the perpendicular efficiency cannot be obtained and it must be calculated numerically. The perpendicular efficiency is defined by equation 2.2.28. The quantity $< w >$ is calculated numerically using a code developed at MIT by Danly, which numerically integrates the pendulum equations with a Gaussian axial field profile, yielding a value of w for a specified value of F. To get an ensemble average, 32 electrons uniformly distributed in space were used to give an approximation to $< w >$ and therefore $\eta_\perp$. The efficiency calculated by this code is also optimized with respect to the detuning, Δ. A contour plot has been generated by calculating the optimized efficiency for a large number of values of F and μ where the contours are those of isoefficiency as shown in Figure 2.3.1 for the second harmonic. For a fixed value of μ the F - μ plot gives the efficiency, $\eta_\perp$, for a specific value of F. To determine the proper pair of F, $\eta_\perp$ values the energy balance equation 2.2.19, which shows the relationship between F, I, and $\eta_\perp$, must be satisfied.

To develop an energy balance equation that does not use the normalized beam current we substitute equations 2.2.23 and 2.2.25 into 2.2.22 and rewrite the resulting equation in terms of F, μ and Δ as shown below

$$\mu = \frac{2155 \times 10^6 F^2}{8P_{out}}(1 - R_2)\gamma_o^2 \alpha \beta^{-(2n-9)}(1 - 0.5\beta_{\perp o}^2 \Delta)^2 \left(\frac{2^n n!}{n^n}\right)^2 \frac{J_m(\nu_{mp})^2(\nu_{mp}^2 - m^2)}{J_{m\pm n}(k_\perp R_e)} \qquad 2.3.1a$$

where we have used

$$P_{out} = P_{loss}\eta_{oh} = \eta_\perp \eta_{el} \eta_{oh} V(volts) I(amps) \qquad 2.3.1b$$

$$\eta_{oh} = \frac{Q_{ch}}{Q_D + Q_{oh}} \qquad 2.3.1c$$

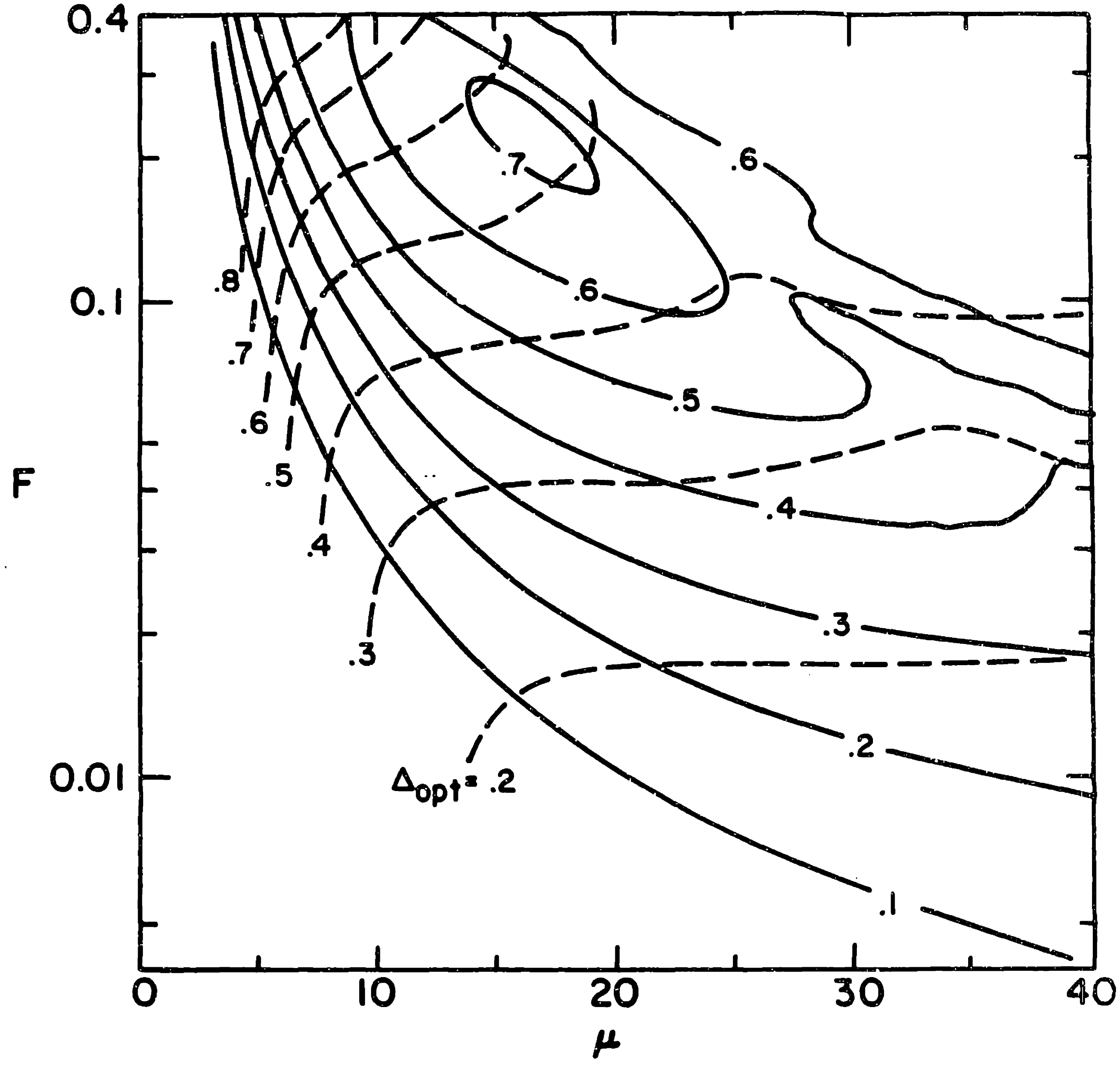

Figure 2.3.1 Plot of the transverse efficiency $\eta_{\perp}$ and the optimum magnetic field Δ_{opt} (dashed lines) as functions of normalized field amplitude F and normalized effective interaction length μ for the second harmonic interaction (Danly (1985))

$$Q_D = \frac{4\pi}{(1 - R_2)} \left(\frac{L}{\lambda}\right)^2 \qquad 2.3.1d$$

In the above R_2 refers to the reflection coefficient at the output end of the resonator. The reflection coefficient at the input end is assumed to be unity, which is a reasonable assumption for an actual gyrotron system where large amounts of power cannot be allowed to travel towards the electron gun and cause damage. There is a unique point on Figure 2.3.1 that satisfies equation 2.3.1a and thereby specifies F and $\eta_\perp$ for a specific μ. After the perpendicular efficiency has been determined, the output power is calculated using equation 2.3.1b.

A study was conducted to determine whether the approximation for the harmonic Larmor radius term $J_n'(k_\perp r_L)$ given in equation 2.2.10 introduced a large error into the efficiency calculation. Using the high power mode, the $TE_{12,3,1}$ in the "high Q" output iris cavity experiment discussed in Chapter 5, it was found that the error was less than 10 %. Also, modifying the energy balance expression of equation 2.3.1a, reduces the error in the efficiency calculation introduced by using the uncorrected equations of motion (equations 2.2.17a and 2.2.17b) to less than 1.4%, even at third harmonic. This correction is equivalent to modifying the normalized beam current expression given in equation 2.2.26 by using the actual finite Larmor radius term, $J_n'(k_\perp r_L)$ instead of the approximation. Cases were run at small beam current to check the expression for the starting current, which is calculated from the linear efficiency. Even in these cases, the error was less than 1.4%, showing that that the code ISTART, which uses an analytic expression for the starting current with the proper finite Larmor radius term, will calculate the starting current with reasonable accuracy. Much larger errors and corrections are caused by other effects such as window losses and misalignment.

As mentioned in the linear theory section, the beam spread effects need to be considered in an accurate analysis of harmonic interactions. In the nonlinear theory, the beam spread effects lower the perpendicular efficiency since not all the electrons are in the radial position of strongest beam-RF interaction or most efficient energy transfer. However, since the beamspread for the experiments described in this thesis is only 2 Larmor radii, the decrease in efficiency is small.

Summary

In this chapter a linear and nonlinear theory for the gyrotron interaction has been developed. To simplify the analytic theory, a slow time scale, which only considers the motion of the guiding centers, was used. The linear theory was used to develop an analytic expression for the starting current and the efficiency and output power were derived from the nonlinear theory. The first sections of chapters 3, 4 and 5 will deal with the design philosophy and list the starting currents and efficiencies for each experiment calculated with the methods that have just been described.

CHAPTER 3

Experimental System

3.1 Experimental Setup

The experiments described in this chapter were conducted with a gyrotron tube that has been in operation since 1982 at the Francis Bitter National Magnet Laboratory. The design of the system is described in detail by Temkin (1982). A schematic of the system is shown in Figure 3.1.1. On the far left side is the electron gun, which produces an annular electron beam. The beam moves to the right into a region of magnetic compression. In the region where the beam is compressed to increase its perpendicular velocity, the beam passes through a beam tunnel. After leaving the resonator, which is in a constant high magnetic field, the beam follows the magnetic field lines which cause it to be deposited on a copper collector. The collector also acts as an overmoded waveguide for the RF radiation generated by the resonator. The microwaves leave the vacuum region by passing through a fused quartz window.

The electron beam is generated by a magnetron injection type gun built by Varian Associates (Felch (1982)) that produces a nonlaminar flow of electrons. The gun was designed to have a perpendicular to parallel velocity ratio ($v_\perp/v_{||}$) of 1.49. Beam cathode voltages of up to 80 kV have been used and a maximum current of 15 A has been observed. The gun is operated in pulsed mode with a pulse length of 1-2 μsec and a repetition rate of 4 Hz.

A beam tunnel is needed to transport the beam through vacuum for the distance of the field gradient before the cavity and prevent spurious oscillations. If no beam tunnel is used mirroring could occur due to voltage depression of the beam. Voltage depression causes the kinetic energy of the beam to be changed into potential energy, thereby becoming unavailable for the beam-rf interaction. The beam tunnel acts as a ground plane near the beam and decreases voltage depression ΔV given by

$$\Delta V = \frac{30IG(R_e, \Delta_b)}{\beta_{||}} \qquad 3.1.1a$$

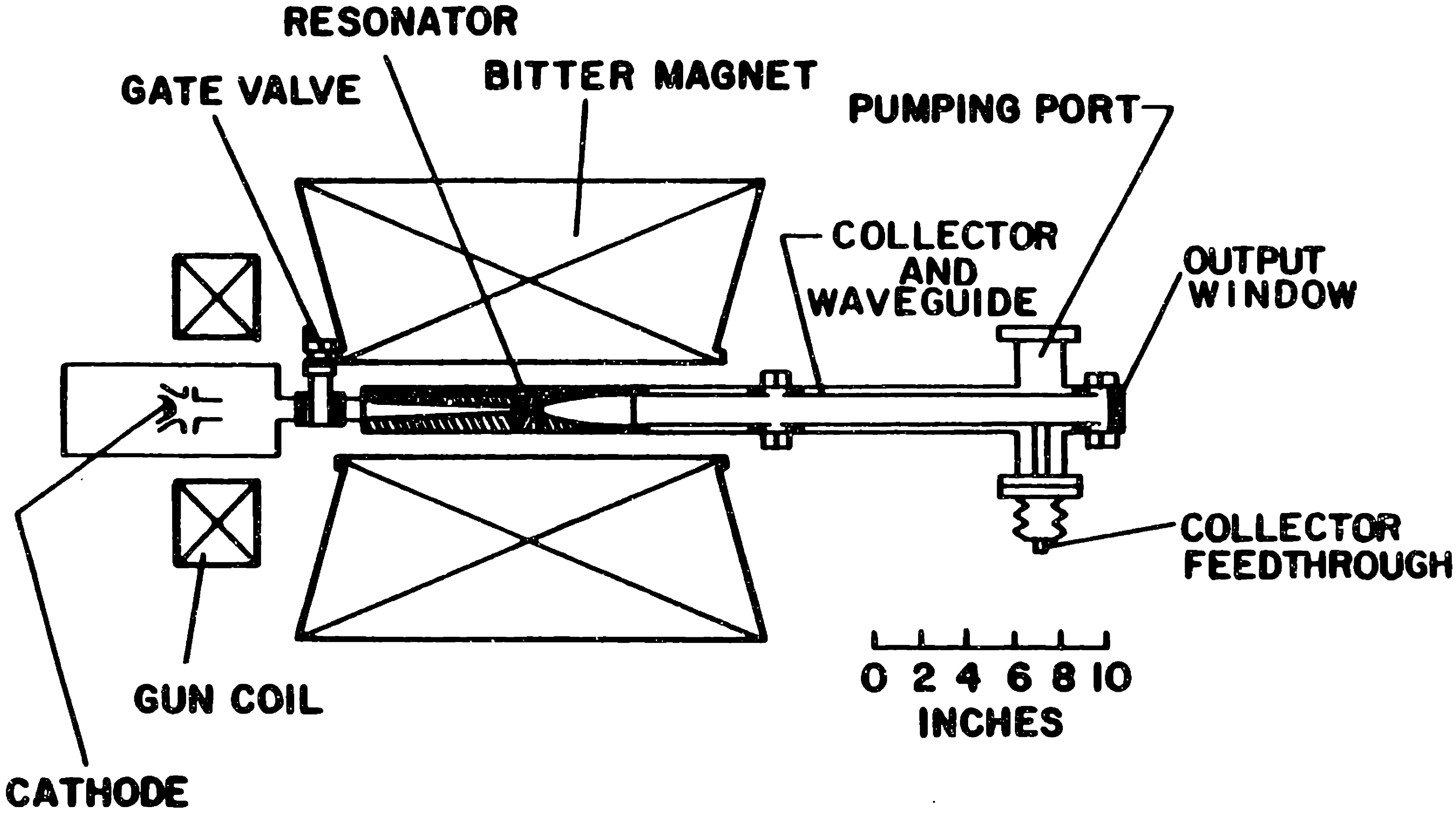

Figure 3.1.1 Schematic Diagram of the Second Harmonic Gyrotron (Byerly (1984))

with the quantity G given by

$$G(R_e, \Delta_b) \simeq 0.75\left(\frac{\Delta_b}{R_e}\right) + 2ln\left(\frac{R_o}{R_e + \Delta_b/2}\right) \qquad 3.1.1b$$

where $\Delta_b = 2r_L + \Delta_g$ is the beam spread, Δ_g is the radial spread of the guiding centers, r_L is the Larmor radius, I is the beam current, R_e is the beam radius, and R_o is the cavity radius or radius of the conducting surface nearest to the beam. The first term in G represents the voltage drop from R_e to the beam's edge and the second term is the drop from the outer edge of the beam to the nearest conductor. The second term in G is minimized by bringing a conductor as close as possible to the edge of the beam, without perturbing the beam. The beam tunnel minimizes the voltage depression in the compression region by making the second term in G as small as possible. At the gun end the inner radius of the tunnel is the largest. The radius decreases towards the cavity following the compression of the beam. Instead of using a solid copper piece for the ground plane, it consists of copper discs separated by discs of lossy dielectric to absorb any RF radiation generated by the copper. The copper discs have a slanted profile for two reasons. The first is to prevent these discs from acting as small resonators. Secondly, by extending the copper radially inward further than the dielectric, the copper discs act as beam scrapers and save the dielectric from beam damage.

The main magnetic field is produced by a Bitter magnet that generates a solenoidal field. Bitter magnets are water cooled copper magnets that are capable of producing high dc magnetic fields. In the tapered harmonic cavity, the slotted cavity experiments, and part of the iris cavity experiments, a 10 T Bitter magnet was used. In the later part of the iris cavity experiment, a 14 T Bitter magnet was used.

A small coil centered over the cathode, capable of generating .2 T is used to vary the magnetic field compression ratio, B_M/B_g where B_M is the field at the cavity and the field at the gun, B_g is given by

$$B_g = B_{Mg} \pm .00046 I_g \qquad 3.1.2$$

and B_{Mg} is the strength of the main field at the cathode and I_g is the current in the gun coil. The negative sign in equation 3.1.2 refers to the case where the field in the gun coil is opposing the main field, and the plus sign indicates that the field is adding to the main field. Electron guns are designed to operate at a specific value of B_M/B_g. If operating below the designed main field a field at the cathode adding to the main field is needed so that the electron beam is not mirrored back to the cathode.

3.2 DIAGNOSTICS

In this chapter, the diagnostics used for the set of experiments covered by this thesis will be discussed. Diagnostics were required for three types of measurements: signal strength, power and frequency. Since second harmonic experiments were conducted, methods were needed to filter out the fundamental signal and to estimate the percentage of second harmonic radiation present. This chapter will be divided into three sections. First the signal strength diagnostics will be discussed, followed by the power measurement diagnostics and lastly the frequency system. The methods of filtering out the fundamental modes and estimating the fundamental-second harmonic mixture will be covered in the section where that method was used.

Signal Strength Measurements

The signal strength of a mode is measured by video diodes as shown in Figure 3.2.1. To measure the second harmonic and fundamental signals separately, two different systems were used, referred to here as the fundamental and the second harmonic system. It is important to be able to monitor the experiment so that one can vary the system parameters, such as magnetic field or cathode voltage, in a systematic fashion, so as to maximize the second harmonic signal and minimize the fundamental signal.

The fundamental system used a WR - 6 size waveguide. Although the operational frequency range for the WR - 6 waveguide is 110 - 170 GHz, higher frequencies will also propagate in this guide. An Aerowave video diode detector was used to rectify the RF emission so that the pulse envelope can be observed on an oscilloscope. A Hughes model 45728H-1000 calibrated dial attenuator was used to limit the signal strength to a level that would not damage the diode element. A Hughes standing wave ratio (SWR)

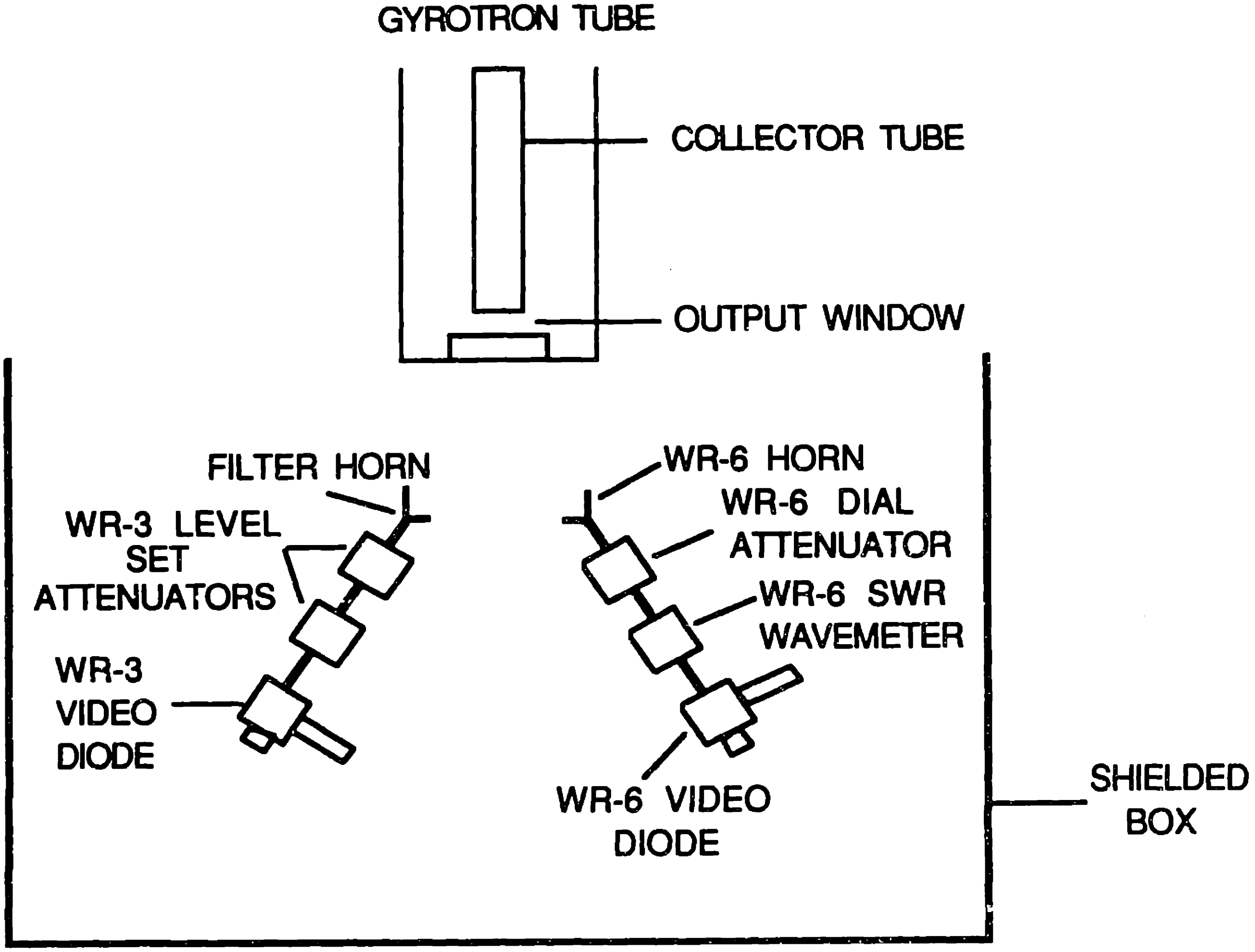

Figure 3.2.1 Schematic of the system used for signal strength measurements.

wavemeter (model 45718H-1000) with a 108 - 165 GHz range was also included in order to measure the frequency of signals which are in the wavemeter's frequency range. The measurements made with this detector are used as only an estimate of the fundamental mode frequency, since the accuracy of the heterodyne frequency system, which is also part of the diagnostic setup, is better than that of the wavemeter.

The second harmonic system uses a WR - 3 band waveguide where the radiation propagates in the fundamental mode of the guide for frequencies in the range of 220 - 325 GHz. Since the detector wafers are the same for the WR - 6 and WR - 3 diodes, a wafer, which is the part of the detector assembly that contains the diode, was chosen that has good sensitivity at high frequencies for high frequency measurements. To limit signal strength, two WR - 3 variable attenuators were used. In this system a filter was needed to eliminate the fundamental signal.

A study was conducted to determine the best type of filter. The optimal filter would strongly attenuate the low frequency fundamental emission and not diminish the second harmonic signal at all. Three different types of filters were studied: a pipe filter, several "small holes" filters and cutoff horns. The pipe filter, shown in Figure 3.2.2a, consists of a 0.95 cm high by 0.95 cm wide (the area of the input of a standard WR - 3 horn is 0.33 cm by 0.33cm) honeycomb of 1 cm long pipes stacked together in the densest possible manner. This filter is used by placing it in front of the WR-3 horn of the second harmonic diode system. The stainless steel pipes, which had an inner diameter of 1/40 inch have cutoff frequencies below 277 GHz, which is above the highest fundamental frequency observed in the region surrounding a 400 GHz second harmonic mode. The "small holes" filters (Figure 3.2.2b) were blocks of aluminum where a 1/2 inch by 5/16 inch grid of 1/40 inch holes were drilled as closely as possible and would also be placed in front of the WR-3 horn. One of the "small holes" filters had a thickness T of 0.16 cm and the other was 0.95 cm thick. The high frequency attenuation of these two types of filters was measured by using a CH_3F far infrared laser (Evangelides (1989)) as a pulsed 604 GHz source and a Laser Precision pyroelectric detector to measure the power with and without the filter in front of the source. In Table 3.2.1, the results of this measurement are summarized. Due to a pulse to pulse power variation an average was taken over 10 shots for each measurement. The uncertainty introduced by the power variation in the attenuation is on the order of ± 1 dB. It was found that the pipe filter has a lower attenuation than either of the "small hole" filters. Since the pipe filter and the thick "small holes" filter have the same thickness, the attenuations can be expected to be very similar. The lower value of signal attenuation in the pipe filter may be due to the fact that the pipes can be packed to give a higher fill factor (more empty space). Within the error bars, the attenuation of the two "small holes" filters is similar, indicating that the filter thickness is not as significant as the fill factor. The thickness is significant only in terms of the ohmic losses, and these losses may cause a smaller variation in attenuation than the error bars. The pipe filter, which had the lowest attenuation, was tested with the WR-3 Even when a strong harmonic mode was excited, no signal was detected when the pipe filter was placed in front of the input horn. Although the signal strength was attenuated by the pipe filter, some signal should have been detected. The problem may be caused by a radiation pattern mismatch, since the pipes have a broad radiation pattern and the horn has straight very directional pattern. Therefore a focussing lens may be needed to remedy this problem. system, by placing the filter in front of the input WR-3 horn.

By using a horn that can be attached to the input waveguide as a filtering device, one has a simpler system. A filter horn can be made that has a lower high frequency attenuation by virtue of a very smooth interior surface plated with a high conductivity material such as gold or copper and a sufficiently short cutoff section. The filter horn assembly that was used in this work (Figure 3.2.2c) has a standard WR - 3 screw connector attached to the section of WR - 3 waveguide, which tapers down to a cutoff section. At the other end of the cutoff section is a standard gain (25 dB) WR - 3 horn. Three custom made filter horns were made with cutoff frequencies of 280 GHz, 300 GHz and 400 GHz. Since the attenuation of the high frequency second harmonic modes that were not cutoff increases with the horns cutoff frequency, due to the decreasing size of the cutoff section, one should use the cutoff horn with the lowest cutoff frequency

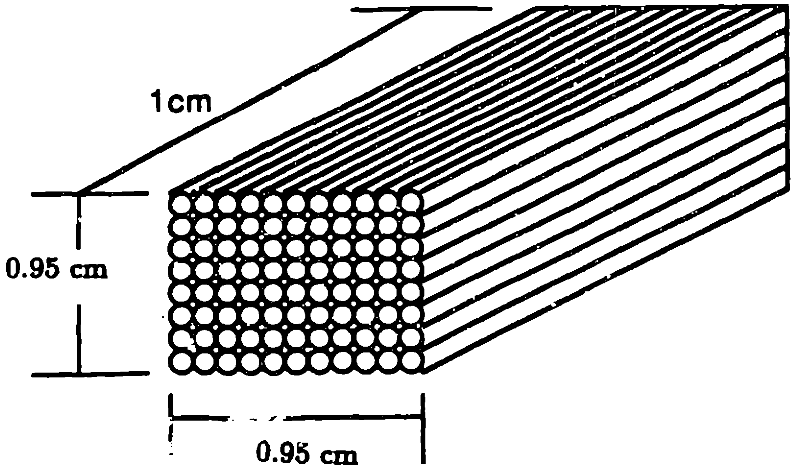

Figure 3.2.2a High pass filter constructed from densely packed thin walled stainless steel pipes

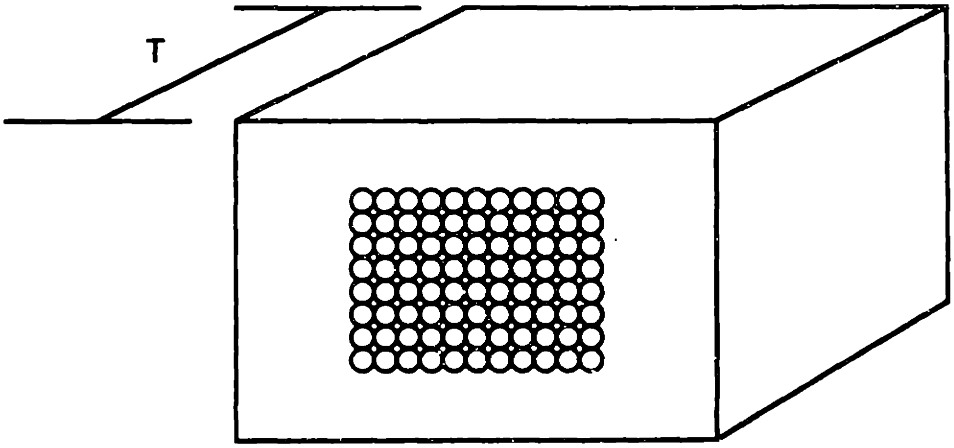

Figure 3.2.2b 'Small Holes" Filter — 1/40 inch diameter holes were drilled in a rectangular grid into small blocks of aluminum of different thicknesses, T.

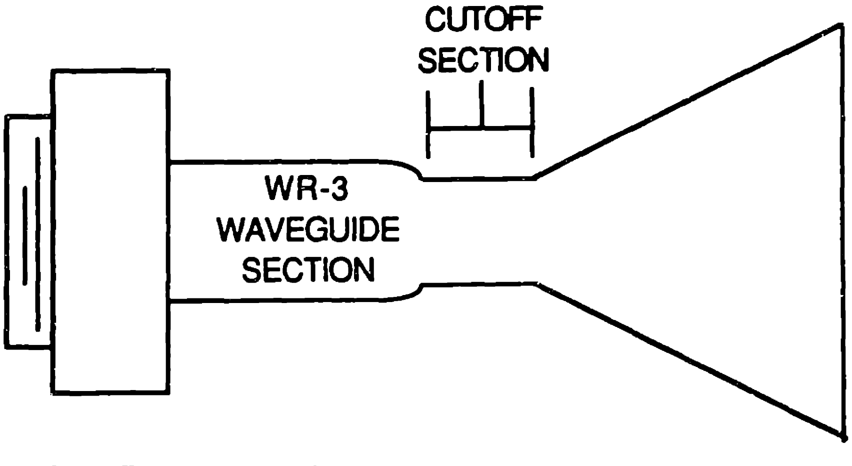

Figure 3.2.2c Cutoff horn assembly

TABLE 3.2.1

Measured Attenuations for Various Cutoff Filters at 604 GHz

TYPE OF FILTER	ATTENUATION (dB)
Pipe Filter	8.94
Thin ‘small holes’ filter	11.3
Thick ‘small holes filter	12.4

that still filtered out the fundamental modes. The filter horn with a cutoff frequency of 400 GHz was needed when the frequency of the second harmonic emission is around 500 GHz, since the fundamental modes tended to leak through the horn with a 300 GHz cutoff frequency. Fundamental leakage is caused by the fact that signals with frequencies below cutoff have an attenuation that increases as frequency decreases, so strong signals with frequencies 30 - 50 GHz below the horn cutoff frequency can be seen by the diode. Two methods were used to check that only second harmonic signal was being detected by the diode. The input of the horn was covered with foil, to make sure that the signal was propagating through the horn and not bypassing it. Secondly, a piece of plexiglass was put between the detector and the gyrotron to check that the signal is second harmonic emission. Since the attenuation in plexiglass increases with frequency, as will be discussed in the next section, a second harmonic signal will be much more attenuated that a fundamental signal. In this fashion, the fundamental and second harmonic signals can be measured separately.

Power Measurements

To measure power a modified Scientech thermoelectric disc calorimeter (Blaney (1984) and Kreischer (1984)), model 36 - 0401 with a 10 cm aluminum plate absorbing surface was used. An array of thermoelectric elements connects the aluminum plate to a heat sink and senses temperature rises in the plate. To improve the absorption of the 10 cm aluminum plate for frequencies in the millimeter regime, a uniform layer of 3M Nextel paint was applied with roughly a 0.3 mm thickness. A measurement of reflectivity as a function of frequency (Figure 3.2.3) was made for the calorimeter from 100 - 400 GHz with a dispersive Fourier transform spectrometer (Afsar (1984)). As shown in Figure 3.2.3, we note that the calorimeter is quite a good absorber down to frequencies of 100 GHz. A photographic record was made of the video diode signal, which showed the pulse shape. Since the calorimeter measures only average power, pulse shape information is necessary to calculate the peak power.

With second harmonic mode power measurements, it is necessary to be able to esti-

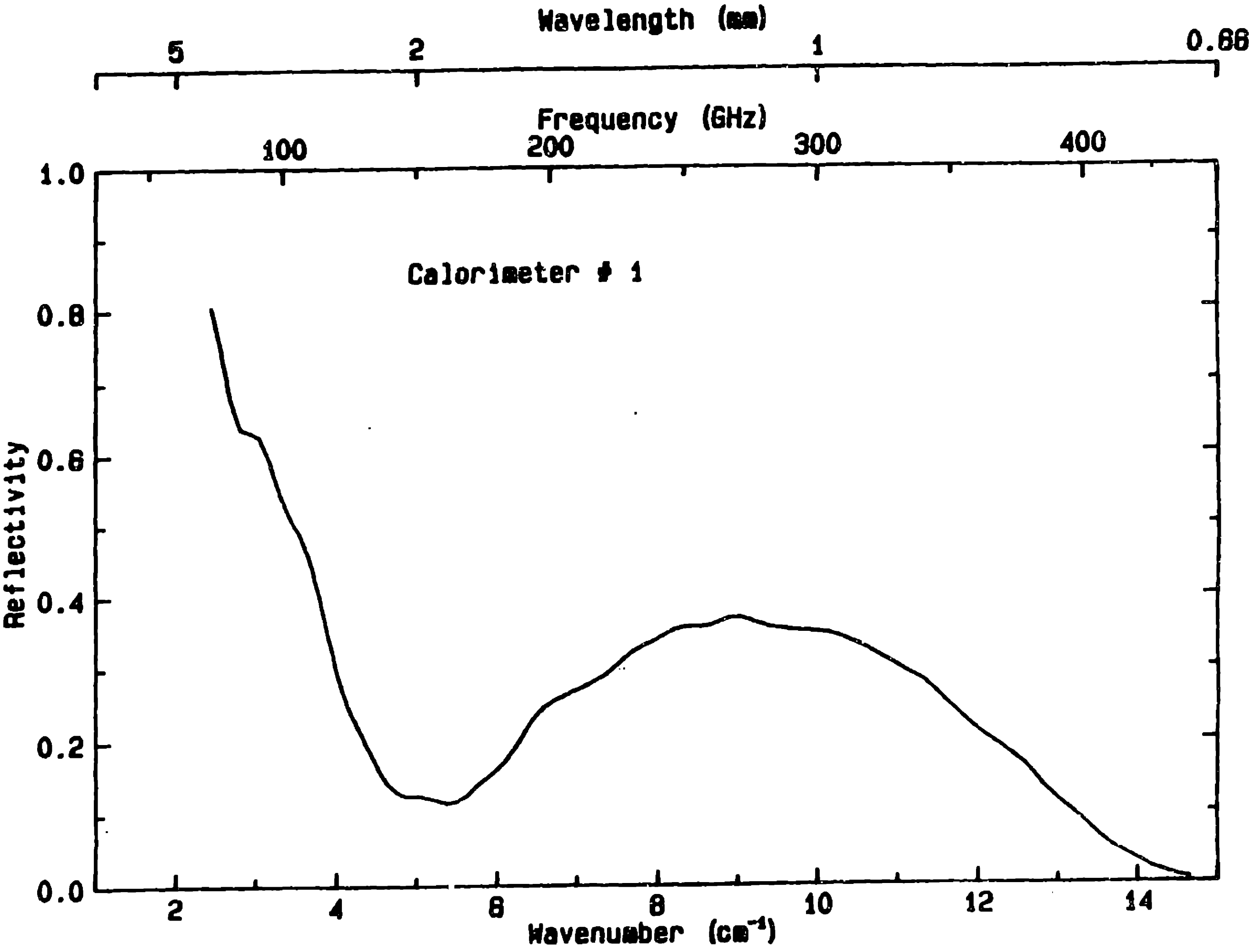

Figure 3.2.3 Reflectivity as a function of frequency for the laser calorimeter (Afsar (1984b)).

mate the fraction of second harmonic and the fraction of fundamental emission present. This can be accomplished by using a sheet of plexiglass, which is a material whose attenuation coefficient α' increases approximately as ω^2 for frequencies in the millimeter regime (reference Mon and Sievers (1975), Strom (1974) and Afsar(1987)), where

$$P_{plexi} = P_o e^{-\alpha'(\omega^2)t} \qquad 3.2.1$$

and P_o is the total power, P_{plexi} is the power that is transmitted through the plexiglass sheet, t is the the sheet thickness, and ω is the frequency of the signal. Since the absorption in plexiglass is not uniform between different manufacturers and sometimes even different batches from the same manufacturers, it was necessary to measure the attenuation of the plexiglass we had bought (Acrylite GP manufactured by Cyro Industries) and compare the measured value of α' with the values quoted in the literature for a frequency of 141 GHz. The experimental setup for this measurement is shown in Figure 3.2.4. A Hughes (model 47178H-1102) IMPATT diode was used to provide the 141 GHz signal whose frequency was measured by a Hughes SWR wavemeter. A variable frequency light fan chopper (EG and G Princeton Applied Research model 192) and a Ithaco dynatrac model 393 lock-in amplifier, synchronous power detector were used to allow for greater sensitivity, and a Hughes calibrated WR - 6 dial attenuator was included to limit the input power. The attenuation α' was measured for sheets of plexiglass varying from 1/2 inch to 3 inches in 1/2 inch intervals at a fixed frequency. It was important that the plexiglass was placed perpendicular to both horns, so as to minimize the effects of the reflections at the two surfaces of the plexiglass. The variations in attenuation at certain thicknesses may have been caused by these reflection effects. Figure 3.2.5 shows the attenuation in dB as a function of plexiglass thickness for various frequencies. The line in Figure 3.2.5 identified by the open circles is the data taken at 141 GHz. From that data we obtain a value of $\alpha' = 0.48 \pm 0.05$ which is close to the result obtained by Mon and Sievers. This can be seen in Table 3.2.2, which lists the value of α' we obtained and the values obtained by Afsar, Strom et al, and Mon and Sievers. The variation between the values of α' may be caused by outer surface reflection effects or by using plexiglass from different manufacturers. The attenuation curves for the other frequencies in Figure 3.2.5 were calculated assuming that $\alpha' \propto \omega^2$. With this graph one can now calculate the attenuation of a sheet of our Acrylite GP if the thickness of the sheet and the frequency of the signal is specified.

To estimate the mixture of fundamental and second harmonic signal present, two power measurements are taken with the calorimeter. The first one, taken without the plexiglass sheet measures P_o, where

$$P_o = \Gamma_1 P_1 + \Gamma_2 P_2 \tag{3.2.2}$$

and P_1 and P_2 are the values of power in the fundamental and second harmonic modes respectively. Γ, which is estimated from Figure 3.2.3, refers to the absorption coefficient of the calorimeter at a specific frequency, and the subscripts 1 and 2 refer to the fundamental and second harmonic modes respectively. In the next power measurement a sheet of plexiglass is placed between the calorimeter and the output waveguide of the gyrotron window. This measurement gives P_{plexi} where

$$P_{plexi} = \Upsilon'_1 \Gamma_1 P_1 + \Upsilon'_2 \Gamma_2 P_2 \tag{3.2.3}$$

and $\alpha'(dB) = 10 log_{10} \Upsilon'$, where α'_1 and α'_2 which can be obtained from Figure 3.2.5, are the attenuations of the fundamental and the second harmonic modes in the plexiglass. From equations 3.2.2 and 3.2.3 the fraction of fundamental and second harmonic emission present can be estimated where

$$P_1 = \frac{P_o \Upsilon'_2 - P_{plexi}}{\Gamma_1(\Upsilon'_2 - \Upsilon'_1)} \tag{3.3.4a}$$

$$P_2 = \frac{P_{plexi} - \Upsilon'_1 P_o}{\Gamma_2(\Upsilon'_2 - \Upsilon'_1)} \tag{3.3.4b}$$

In these measurements 1/2 inch thick sheet of the calibrated plexiglass was used. A thicker piece of plexiglass causes the second harmonic modes to be too attenuated and at smaller thicknesses the surface reflection effects can cause the transmitted power to be too sensitive to the orientation of the plexiglass. For the second harmonic modes measured at 417 GHz and 467 GHz discussed in Chapter 6, the error bars on the percent

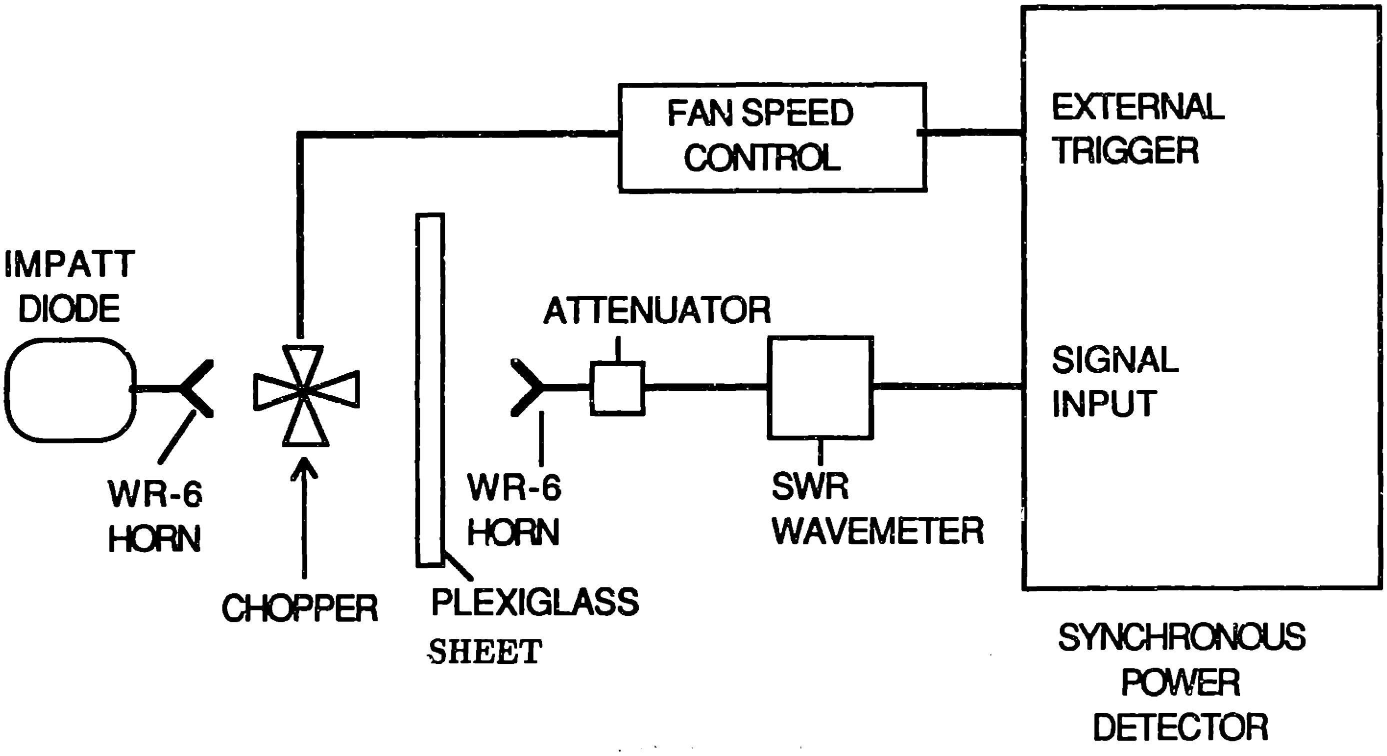

Figure 3.2.4 Schematic of the system used for measuring the attenuation of plexiglass at a fixed frequency.

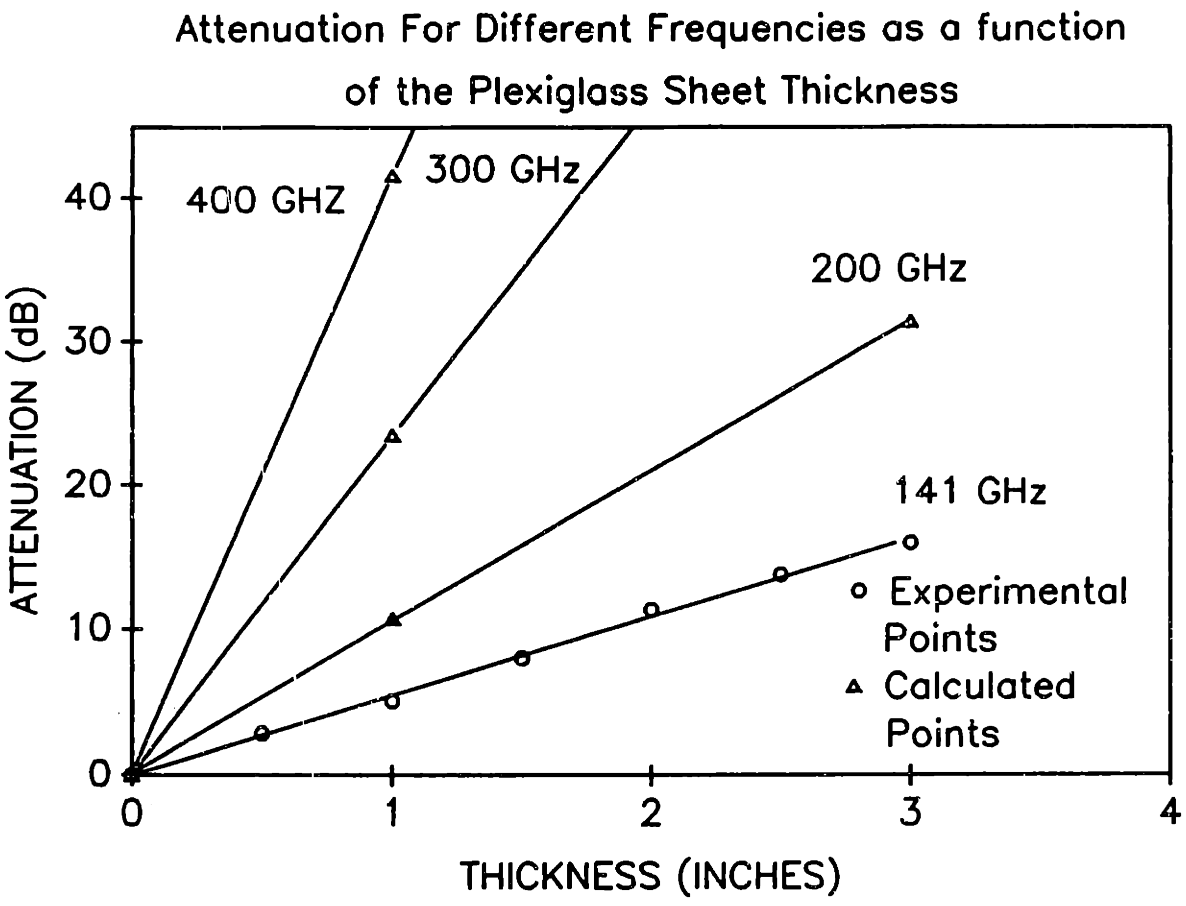

Figure 3.2.5 Attenuation at different frequencies of microwaves propagating through a sheet of acrylite GP as a function of the thickness of the plexiglass sheet.

TABLE 3.2.2

Attenuation of Plexiglass at 141 GHz

REFERENCE	ATTENUATION (neper/cm)
Afsar	0.4
Mon and Sievers	0.46
Strom et al.	0.37
This thesis	0.48

of fundamental emission present in these measurement are taken to be 8 % where the power levels for the 417 GHz and 467 GHz modes were 15 kW and 22 kW respectively. At these frequencies for power levels of 15 - 22 kW, the power transmitted through the plexiglass is too small to be measured by the calorimeter, and a small amount of fundamental emission may also be present that would not be detected by the calorimeter. Therefore, the error bars are based on the largest amount of fundamental mode power that will be undetected by the calorimeter and so one can only claim mode purity to within 8%.

Frequency Measurements

Although the Hughes wavemeter can be used to make approximate measurements of the lower frequency fundamental modes, other methods of measurements are needed for the fundamental modes above 170 GHz and the second harmonic modes. A Fabry-Perot interferometer can be used, but even the most sensitive interferometers can only measure the frequency to within 0.5% accuracy. At 400 GHZ, this corresponds to an uncertainty of 2 GHz. To get better accuracy a heterodyne receiver was used. With a heterodyne receiver, measurements to within one part in 10^5 can be made. The resolution of the lineshape measurement is 10 MHz, which is approximately a factor of ten better than a Fabry-Perot interferometer. Another advantage provided by the heterodyne receiver is the fact that the data can be collected in the duration of a single pulse, so the lineshape of a single shot can be recorded. The high resolution and single shot capability were a result of using a SAW (surface acoustic wave) delay line as the IF spectrum analyser. The range of the receiver can be as large as 60 - 780 GHz. However, since in this experiment, a Hughes D band harmonic (model 47448H-1002) mixer diode was used, it is difficult to detect frequencies above 500 GHz, as will be discussed later.

Operation

The schematic of the heterodyne mixer system (Evangelides (1989)) used in the experiments discussed in this thesis is shown in Figure 3.2.6. The gyrotron emission is detected by the Hughes harmonic mixer diode. The mixer diode is also driven by a local oscillator (LO), which is a narrow linewidth stable source. An Avantek (model AV-26040) YIG tuned FET oscillator with a 26.5 - 40 GHz frequency range and a -3 dB linewidth of 5 kHz was selected as the source. Before the LO signal enters the mixer, 4% of the signal is diverted to a counter that measure the frequency of the LO signal. To maintain the high level of accuracy of this measurement technique, the counter must be very stable. Therefore an HP (model 5352a) microwave counter with a temperature stabilized crystal oscillator was used. When the diode was driven with the LO, harmonics of the LO frequency were generated due to the highly nonlinear nature of the mixer diode. These harmonics then combine with the LO signal to generate sum and difference frequencies. Since a SAW device with a 1 GHz center frequency and a 500 MHz bandwidth was used, only the difference frequencies were analysed, and tunability in the LO source was needed to insure that the difference was in the operating range of the SAW device. At the next step the difference frequency, also known as the IF, is amplified. To decrease the level of electronic noise, the IF is gated and filtered. The filtered signal is separated into its different Fourier components by the SAW device (Evangelides (1989)).

The SAW device acts as a linear dispersive delay line. If the IF signal frequency is in the bandwidth of the SAW device, the transit time of the signal is linearly inversely proportional to the IF frequency. In the SAW device shown in Figure 3.2.7, a piezoelectric transducer converts the IF signal electromagnetic wave into an acoustic signal of the same frequency. This acoustic wave travels along a surface etched with an acoustic grating with gradually increasing spacing. The wave travels through this grating until the spacing of the groove satisfies the Bragg condition for a wavelength contained in the signal. At this point, the fraction of the signal corresponding to that specific wavelength is reflected 90° and is reflected 90° once again by a grating with the same spacing on the other side of the symmetric series of grooves shown in Figure 3.2.7. The reflected signal travels down a path parallel to the original path and is converted back into an electromagnetic wave by a second piezoelectric transducer. Since the Bragg condition is

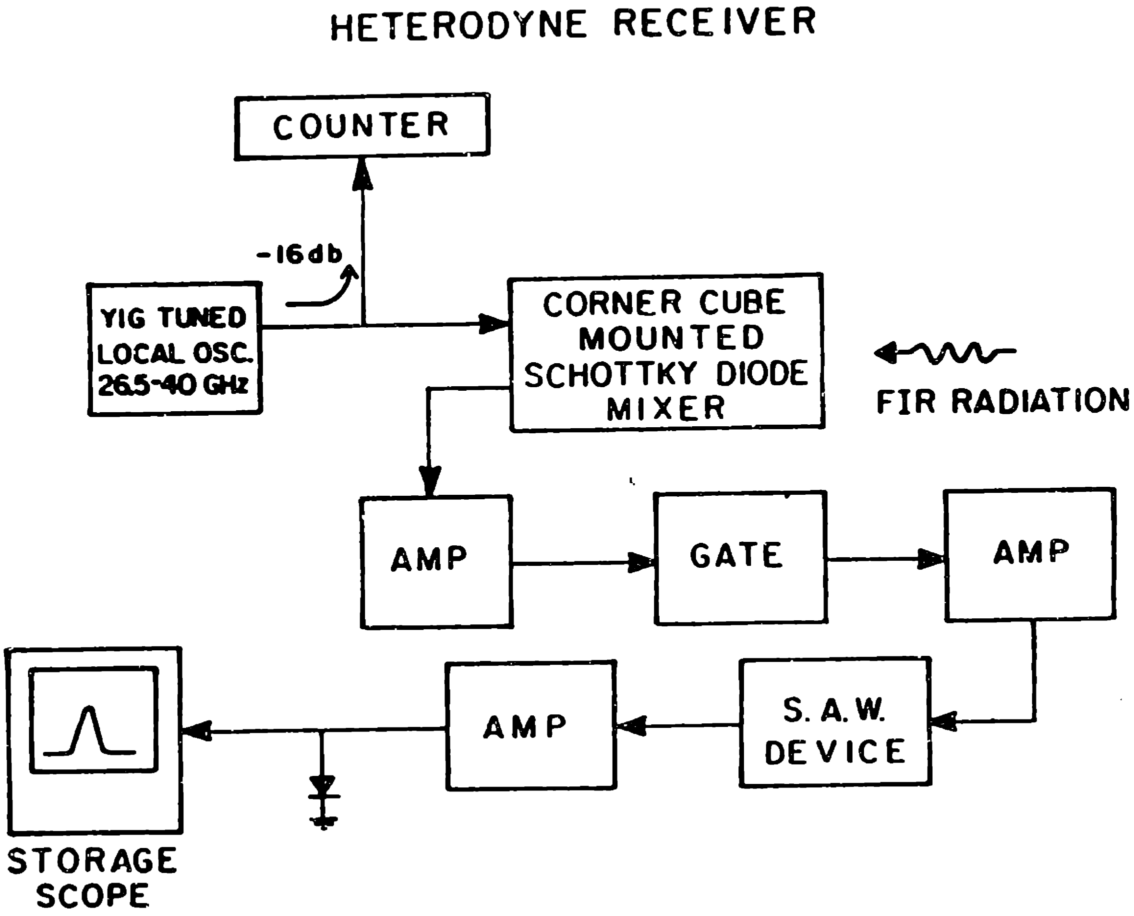

Figure 3.2.6 Schematic diagram of the heterodyne receiver system (Evangelides (1989).

frequency dependent, the transit time increases for signals with lower frequencies that are reflected by the gratings with larger spacings. In this fashion, the SAW device behaves as a linear dispersive delay line.

The output from the SAW device is amplified and then rectified by a video diode. A storage oscilloscope is then used to display the rectified signal and allow one to see the lineshape as well as the frequency. To measure the frequency, the LO must be tuned to a frequency where the IF is within the bandwidth of the SAW device. Since the IF frequency, ν_{IF}, is given by

$$|n\nu_{LO} - \nu_{RF}| = \nu_{IF} \tag{3.2.4}$$

where ν_{LO} is the frequency generated by the local oscillator, n is the harmonic of the local oscillator signal that is being mixed with the RF signal, and ν_{RF} is the frequency of the RF signal, two local oscillator frequencies will produce a IF frequency corresponding to the SAW device center band frequency (1 GHZ for the system described in this thesis). These two frequencies are called the upper (ν_{LO}^{usb}) and lower (ν_{LO}^{lsb}) sidebands, where $\nu_{LO}^{usb} > \nu_{LO}^{lsb}$. When the upper and lower sideband frequencies are known, the RF frequency and the harmonic number n can be determined from the relation

$$\frac{2\nu_{IF}}{|\nu_{LO}^{usb} - \nu_{LO}^{lsb}|} = n \tag{3.2.5}$$

and equation 3.2.4. The existence of two sideband frequencies for each mode that are 2 GHz apart allows one to distinguish between actual signals and electronic noise or to differentiate signals, if more than one frequency is present.

In Figure 3.2.8 the experimental setup for the frequency measurements is shown. A 1/2 inch diameter copper pipe was used as an over moded guide to couple the radiation out of the shielded box and into the harmonic mixer diode. Since the mixer will be damaged by more than 100 mW of combined RF and LO power, two Hughes WR-6 level set attenuators (model 45738H-1200) were used in front of the mixer diode. When using a heterodyne receiver to measure frequency, it is not necessary to use a harmonic mixer diode. Other devices, such as a Schottky diode can be also used. The harmonic mixer, however, has a definite advantage when conducting second harmonic experiments,

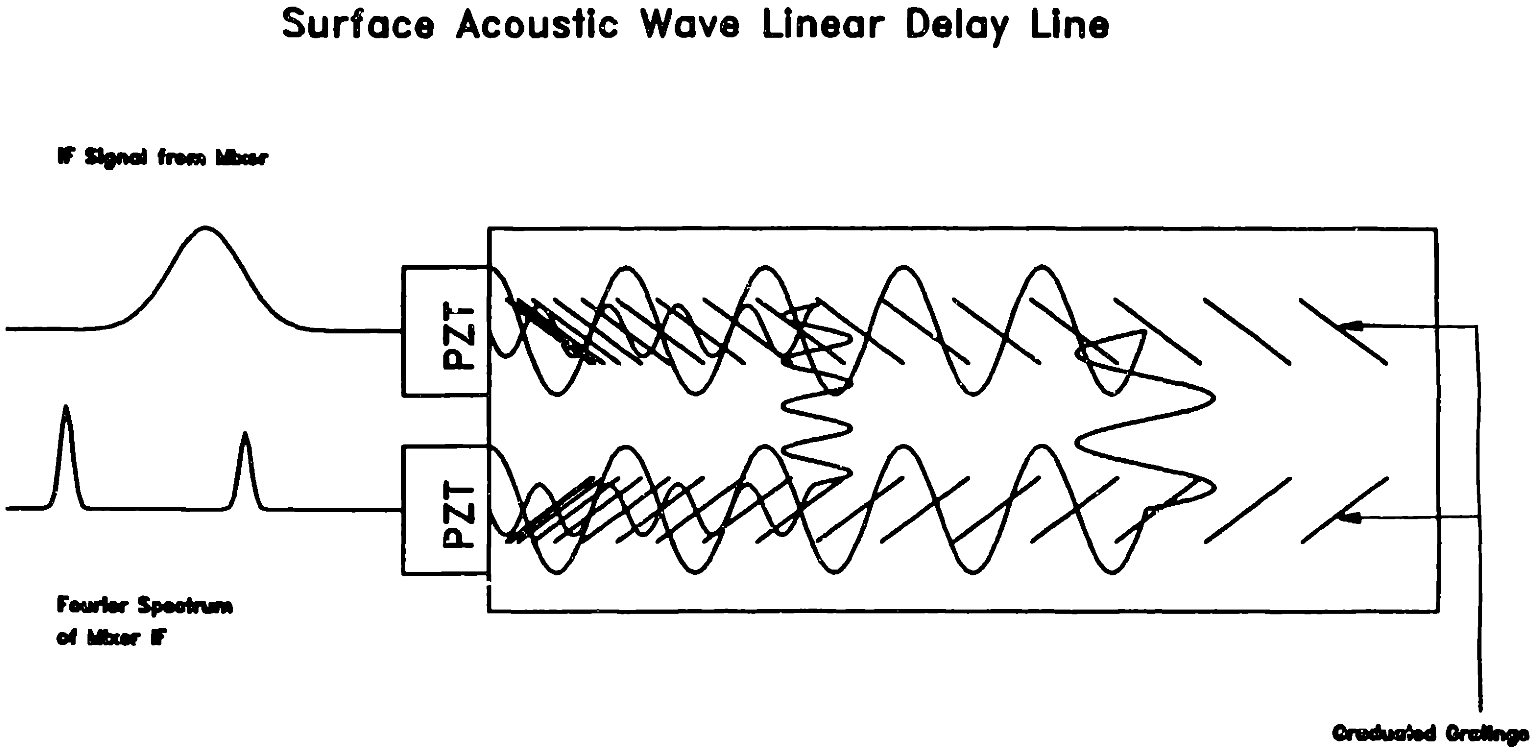

Figure 3.2.7 Schematic showing the surface acoustic device operation.

since the RF signal enters through a waveguide structure, rather than an open structure (Schottky diode), where the RF signal directly illuminates the diode detector element. With a waveguide structure, a filter horn can be attached to filter out the fundamental signals. This is important, because, the amplitude of the harmonics that the mixer diode generates are roughly given by the Fourier components. The higher frequencies of the second harmonic modes require higher mixer harmonics which have less power. The combined LO and RF power comprise the signal strength of the IF signal, so by increasing the level of RF power, one can compensate the decrease in LO power to some extent, but not completely. This decrease in combined signal strength can be observed in the signals that are very high frequency, such as the $TE_{17,2,1}$ (503 GHZ), which were so weak that they were hard to distinguish from the noise, even when the attenuation in front of the mixer diode was decreased. Therefore, since the fundamental RF signals are sometimes stronger than the second harmonic RF signals and the fundamental IF signal strength is often stronger than that of the second harmonic, a second harmonic signal might go undetected, because the fundamental signal is saturating the frequency system. For this reason it is very useful to have the capability of attaching a filter horn to eliminate the fundamental signals. Also, when using a filter horn, one has an extra test as to whether the observed signal is second harmonic emission.

With this diagnostic system information about the lineshape as well as the frequency can be obtained on a shot to shot basis. To illustrate this capability, some data from the experiment discussed in Chapter 6, is used. Figure 3.2.9a shows the frequency spectrum of a typical shot for the $TE_{13,2,1}$ second harmonic mode taken with a digitized storage scope. Data was taken for this mode at three other operating points where this second harmonic mode is excited and no fundamental modes were present. The frequency spectrum of these other data points was very similar to Figure 3.2.9a. The width of the pulse is approximately 0.12 μsec and the delay on the storage scope is set so that 1μsec represents 100 MHz. Thus the linewidth, or spread in frequency, is 12 MHz for the mode with a frequency of 467 GHz. Similarly, the frequency spectrum for the $TE_{17,2,1}$ (Figure 3.2.9b), which oscillated at 503 GHz showed that this mode had roughly a 12

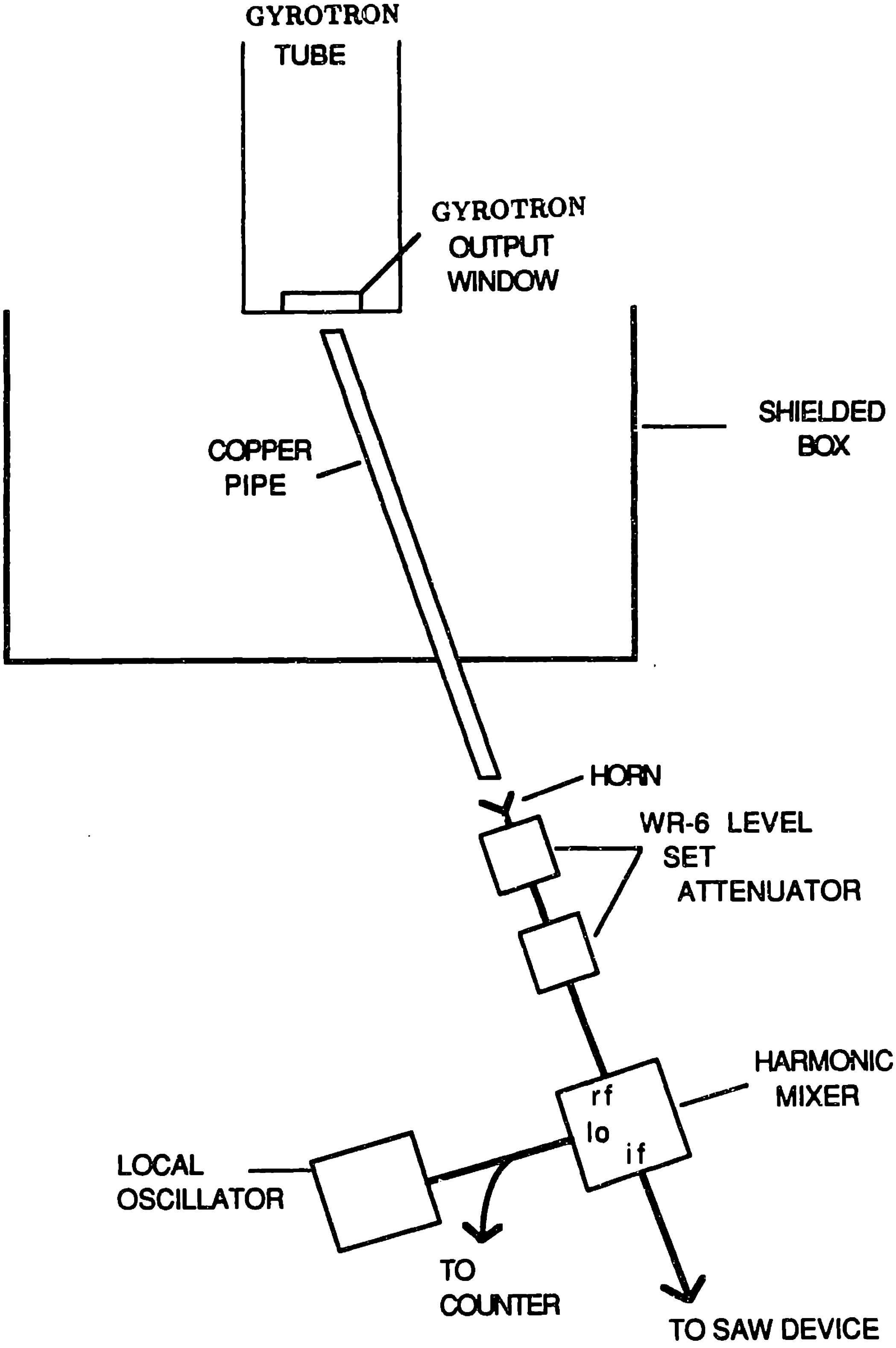

Figure 3.2.8 Schematic of the system used for the frequency measurements made by the heterodyne receiver.

MHz bandwidth. However, the sensitivity of the bandwidth measurement is limited by the resolution of the SAW device (Evangelides (1989)), which is 10 MHz. Therefore, since the measured bandwidth is so close to the limit of the SAW device sensitivity, the actual bandwidth may be slightly less than 12 MHz.

SUMMARY

In the set of experiments described in this thesis, three types of measurements were made: signal strength, power and frequency. With each of these measurements the fundamental mode needed to be filtered out or the fraction of fundamental present had to be estimated. A set of filter horns were used to prevent the WR-3 diode from detecting fundamental emission in the signal strength measurement. Similarly, the filter horns were attached to the harmonic mixer, to avoid saturating the frequency system with the stronger fundamental signal. Since plexiglass is a low pass filter that can be calibrated, where the attenuation increases with frequency, using the plexiglass sheet with the calorimeter, provided a simple method of estimating the fraction of fundamental present. The plexiglass sheet also gives an easy way to check whether the observed signal is a harmonic signal, because the harmonic signals, due to their higher frequencies, are much more attenuated than the fundamental signals.

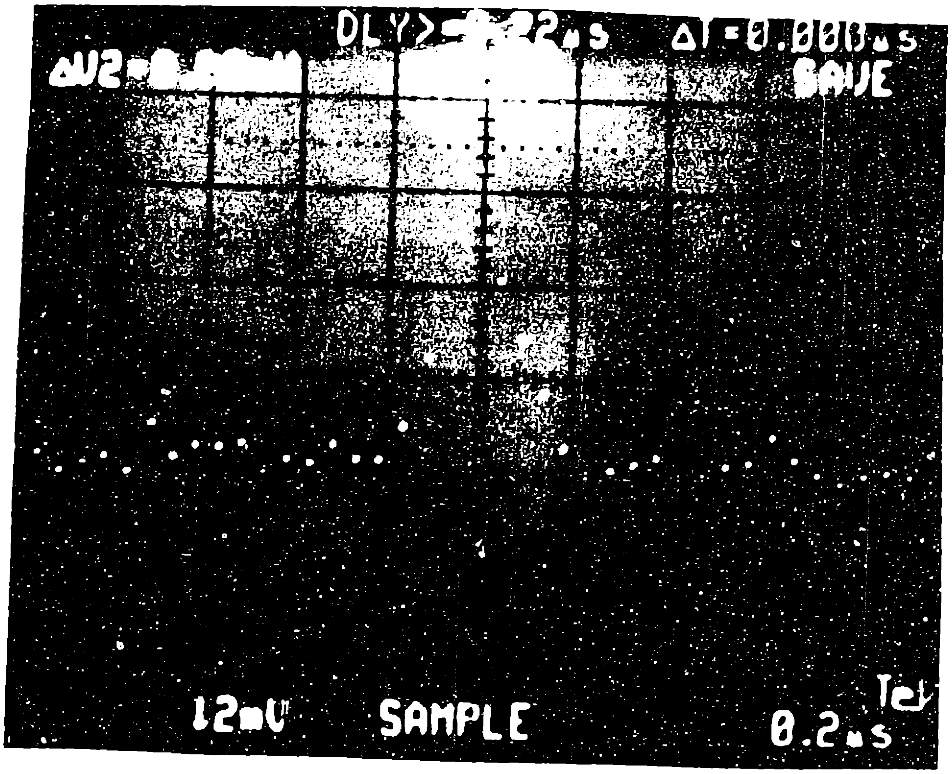

Figure 3.2.9a Frequency spectrum for the $TE_{12,3,1}$ second harmonic mode that oscillates at 467 GHz.

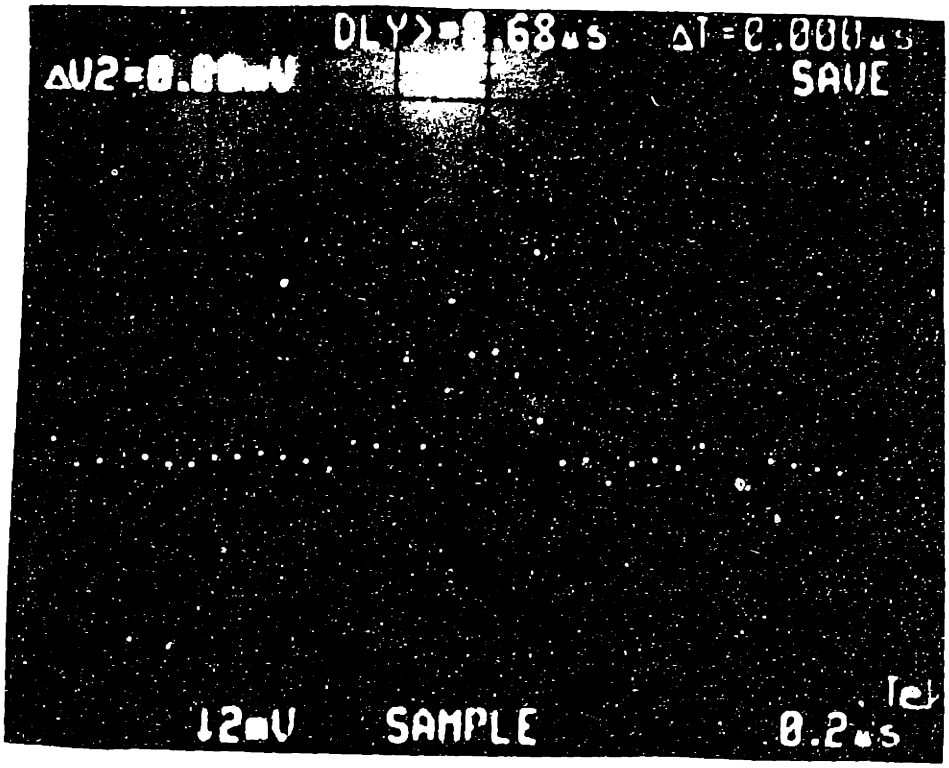

Figure 3.2.9b Frequency spectrum of the second harmonic $TE_{17,2,1}$ mode that oscillates at 503 GHz.

CHAPTER 4

TAPERED CAVITY EXPERIMENT

In this chapter we discuss the first high frequency ($> 350GHz$) harmonic experiment. A tapered cavity design was used because past experience showed that lower frequency ($< 350GHz$) second harmonic emission can be produced by tapered cavities (Byerly (1984)). As mentioned in Chapter 2, fundamental modes generally have lower starting currents than the harmonic modes, explaining why second harmonic modes are often observed in the regions of magnetic field where no fundamental modes exist. Since any given mode can be excited only over limited range of magnetic field, it was assumed that the regions of magnetic field devoid of fundamental modes are equivalent to gaps in the fundamental frequency spectrum. The relationship between the magnetic field and frequency is obtained by applying the resonance condition for a gyrotron interaction, $\omega \simeq n\omega_c$ where ω is the rf frequency, n is the harmonic number, and $\omega_c = eB/\gamma m$ is the cyclotron frequency. The frequency ω of a $TE_{m,p,q}$ mode is given by

$$\frac{\omega^2}{c^2} = k_\perp^2 + k_\parallel^2 \qquad 4.0.1$$

where $k_\perp = \nu_{mp}/R_o$, $k_\parallel = 2/L_{eff}$ for a mode with q = 1 and a Gaussian RF field profile, L_{eff} is the axial interaction length of the RF field in the cavity, the mode index, ν_{mp} is the pth root of $J'_m = 0$, and R_o is the cavity radius. For a gyrotron operating near cutoff ($k_\perp \gg k_\parallel$), the frequency, f, of a TE_{mp} mode can be approximated by

$$f = \frac{c\nu_{mp}}{2\pi R_o} \qquad 4.0.2$$

and from the resonance condition one sees that $\nu_{mp1} \simeq \frac{1}{2}\nu_{mp2}$ where the subscripts 1 and 2 refer to the fundamental and second harmonic modes respectively. Therefore, equation 4.0.2 shows that gaps in the frequency spectrum are a result of the spacing of the values of ν_{mp}, which are not evenly distributed as shown in Figure 4.0.1. To achieve the optimal isolation from fundamental modes, one would like to choose a second harmonic mode where the value of $\frac{1}{2}\nu_{mp2}$ is in the center of as large a gap as possible between consecutive values of fundamental mode index ν_{mp1}, and also satisfies the system constraints discussed in the next section. The next section will outline design procedures that are relevant to all of the resonators in this paper as well as the design of the tapered cavity. The experimental results will be presented and analysed in Section 4.2.

4.1 DESIGN PROCEDURES

The decisions to use an existing electron gun and to operate in the submillimeter regime imposed a number of constraints on the design of this experiment and the operating point. A Varian pulsed magnetron injection gun (Felch (1982)) that has a peak current of 10 A at 65 kV with a pulselength of 1 - 2 μsec was used to produce the electron beam. The cathode radius is 0.92 cm and $\beta_\perp/\beta_\parallel = 1.5$ where $\beta_\perp$ and $\beta_\parallel$ are the normalized perpendicular and parallel velocities respectively. The radius of the emitter strip and the magnetic compression, which is the ratio of the magnetic field at the cavity over the magnetic field at the gun, determine the normalized beam position, $k_\perp R_e$, where R_e is the beam radius at the cavity. Since $k_\perp \simeq k = 2\pi/\lambda$ where λ is the wavelength, the normalized beam position given by adiabatic theory is

$$k_\perp R_e = \frac{\omega}{c} R_k \sqrt{\frac{B_g}{B_o}} \qquad 4.1.1$$

where ω is the frequency, R_k is the emitter strip radius, B_o is the magnetic field at the cavity, and B_g is the magnetic field at the cathode. The magnetic field at the cavity is calculated from the resonance condition for a gyrotron

$$\omega = \omega_c + k_\parallel v_\parallel \qquad 4.1.2$$

where $k_\parallel$ is the parallel wavenumber and $v_\parallel$ is the parallel beam velocity. Therefore to operate at a frequency of 400 GHz, a magnetic field around 8 Tesla is needed. Past experience with high frequency operation (Danly (1985)) using the same gun suggests that at this operating point $B_g \simeq 0.23$ Tesla is needed for high efficiency operation. Specifying the gun and cavity magnetic fields fixes the magnetic compression, B_o/B_g, as well as the beam position, $k_\perp R_e \simeq 13.0$.

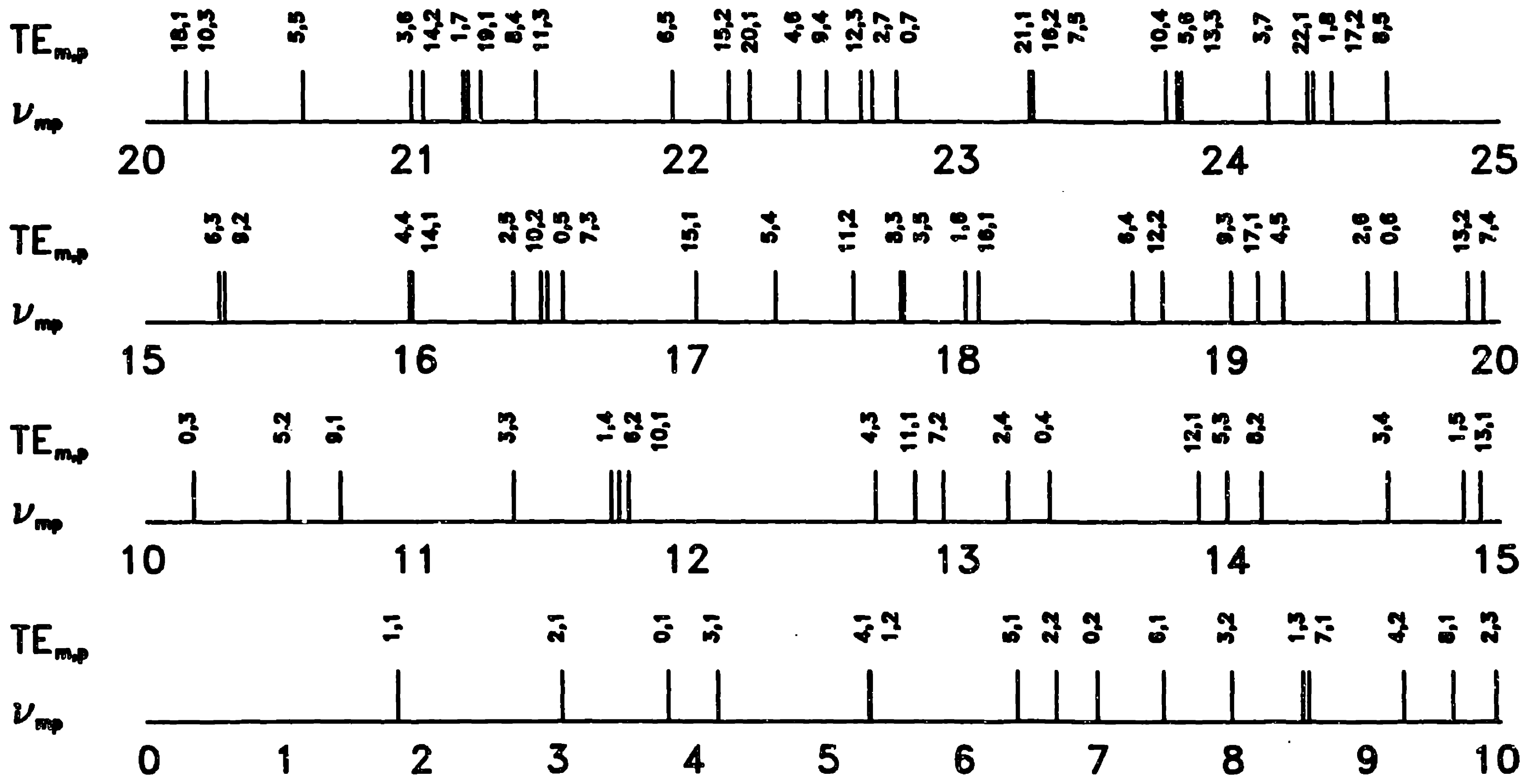

Figure 4.0.1 Chart of the *TE* mode indices up to $\nu_{mp} = 25$.

When selecting a design mode, one wants strong coupling to the preferred second harmonic mode and weak coupling to other fundamental and second harmonic modes. The coupling strength for a gyrotron interaction is given by

$$S_{mp} = \frac{J^2_{m\pm n}(k_\perp R_e)}{(\nu^2_{mp} - m^2)J^2_m(\nu_{mp})} \qquad 4.1.3$$

where n is the harmonic number and the Bessel function $J_{m\pm n}$ is a measure of the RF harmonic field content at the beam position, $k_\perp R_e$. Sign choice in the order of the Bessel function depends on the azimuthal rotation of the mode. The starting current, I_{st}, which is the current required to excite a mode in an oscillator, is proportional to S^{-1}_{mp}. Therefore, to lower the starting current of the desired mode relative to competing modes, S_{mp} of the desired mode is maximized. To minimize beam interception by the wall the beam radius was restricted to be less than 0.9 R_o.

Figure 4.0.1 shows the mode indexes, ν_{mp}, plotted for the TE modes, and one can see the frequency spacing of the different modes. For the fundamental modes that satisfy the above constraints, the largest gap in the fundamental mode index spectrum is around $\nu_{mp} = 12$, between the $TE_{10,1,1}$ and the $TE_{4,3,1}$ modes. The second harmonic $TE_{8,5,1}$ mode index is in the center of that gap ($(1/2)\ \nu_{8,5} = 12.3$), which implies fairly good isolation from fundamental modes. Additionally, there is a sparse second harmonic spectrum around the $TE_{8,5,1}$. From these considerations, the $TE_{8,5,1}$ was a logical mode to pursue, even though due to the system constraints the beam cannot be placed exactly at the radius to obtain the maximum coupling coefficient.

When the mode has been selected, the cavity radius is determined from $R_o = \nu_{mp}c/\omega$. The next step is to use linear theory to calculate the fundamental and second harmonic starting currents of a cavity for a given Q and effective interaction length (Kreischer (1983)). As discussed in Chapter 2, the diffractive Q and the effective interaction length are calculated using a cold cavity code. To prevent excessive mode conversion, the input and output taper angles were required to be less than 5°. The cavity length and taper dimensions are determined by designing a cavity with the starting currents of the fundamental modes as large as possible, and for which the desired second harmonic mode has a low starting current and a reasonable nonlinear efficiency.

The gap in the frequency spectrum did indeed translate into a region of magnetic field without fundamental modes, as can be seen in Figure 4.1.1, which shows the starting currents for the second harmonic design mode and the two strongest fundamental modes. The starting current of the second harmonic mode is significantly higher than those of the surrounding fundamental modes. However, because of the gap in the fundamental spectrum it was hoped that access to the second harmonic mode would be achieved without exciting the fundamental modes first.

The parameters for this 400 GHz, 200 kW, second harmonic experiment are listed in Table 4.1.1. At 9 Amps the total theoretical efficiency for the $TE_{8,5,1}$ mode is 34 % at a cathode voltage of 65 kV. The magnetic field of 8.0 Tesla corresponds to the magnetic field of the minimum starting current.

4.2 RESULTS

When this experiment was conducted, a gap in the fundamental spectrum was not observed. The magnetic field range corresponding to this gap, 7.6 - 8.1 Tesla, was filled in with the higher order axial modes (q = 2,3) of the $TE_{6,2,q}$ mode. Unfortunately, the higher order axial modes may have been strong enough to suppress the desired second harmonic mode, the $TE_{8,5,1}$. Using the diffractive Q calculated by the cold cavity code for the $TE_{6,2,2}$ mode, one gets a starting current for this mode of approximately 2.5 Amps. This starting current for the $TE_{6,2,2}$ is slightly lower than that of the $TE_{8,5,1}$, and the $TE_{6,2,2}$ can get excited first. Furthermore, the range of magnetic field for the fundamental q=1 modes may have been larger than predicted by linear theory, thereby limiting the region where the second harmonic mode can be excited. The starting currents shown in Figure 4.1.1 do not consider the problems of accessibility of the mode during startup. At the beginning of a voltage pulse, the higher frequency modes get excited at the lower voltages (Kreischer (1980)) and may stay excited at higher voltages if the final operating point is in the hard excitation region of the higher frequency mode.

In addition to having low starting currents, the fundamental modes have high power operation as shown in Table 4.2.1, where we list the power and efficiency observed

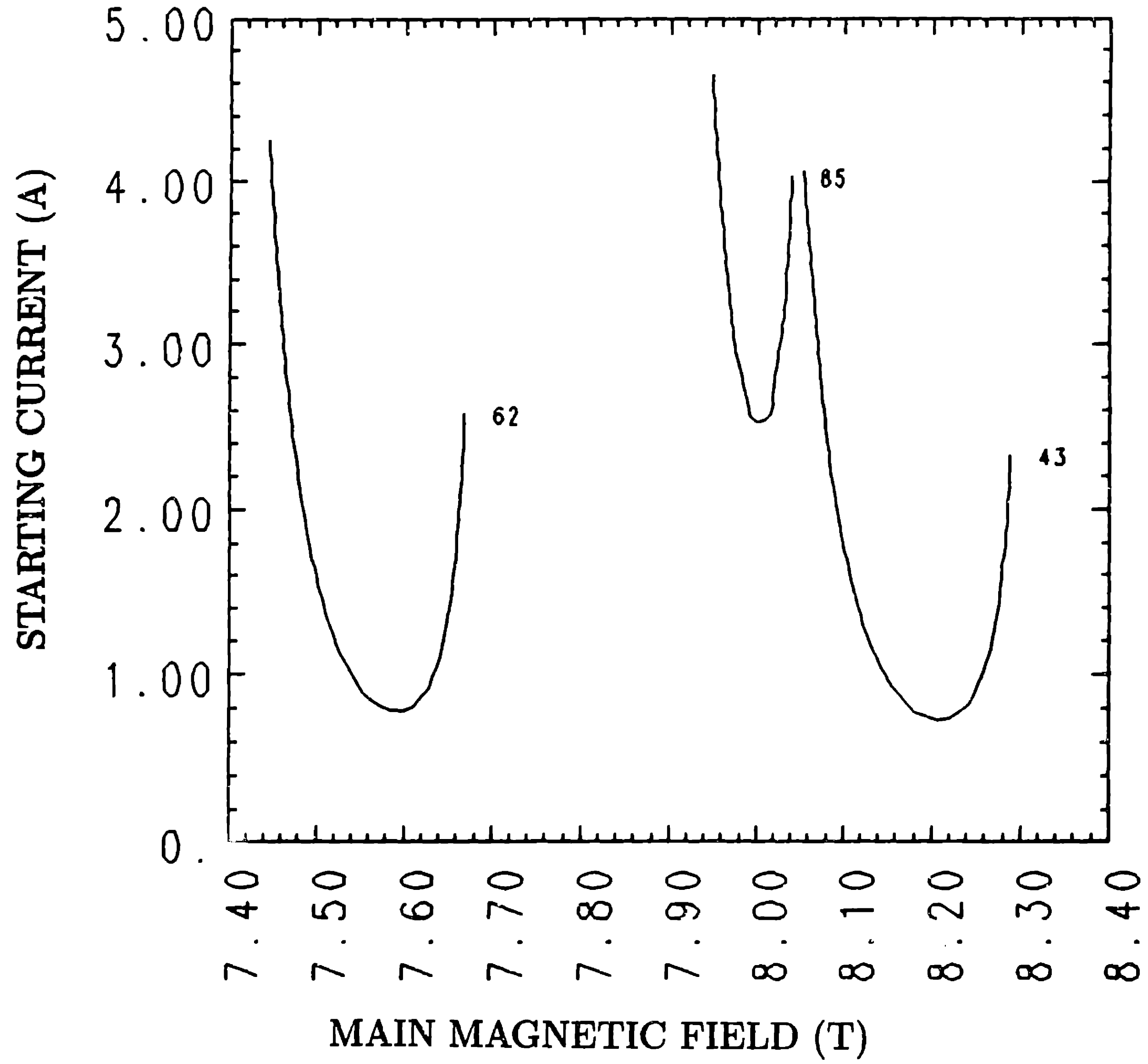

Figure 4.1.1 Starting currents for the design second harmonic mode $TE_{8,5,1}$ and the two strongest fundamental modes $TE_{4,3,1}$ and $TE_{6,2,1}$.

TABLE 4.1.1

TAPERED CAVITY DESIGN PARAMETERS

$TE_{8,5,1}$

Second Harmonic

Frequency = 400.7 GHz

Power = 200 kW

Magnetic Field = 8.0 Tesla

$\eta_{\perp} = 61.7$ %

$\eta_{el} = 65.3\%$

$Q_{D2\omega c} = 3271$

$I_{ST2\omega c} = 2.5$ Amps

Beam Current = 9 Amps

$\eta_T = 34.1$ %

Cathode Voltage = 65 kV

$\eta_{OH} = 84.7$ %

Cavity Radius = 0.293 cm

$Q_{D\omega c} = 863$ $(TE_{6,2,1})$

$I_{ST\omega c} = 0.8$ Amps $(TE_{6,2,1})$

for various modes. In three of the cases, the mode identification was done from the frequency, and in the case of the $TE_{6,2,1}$ the mode was deduced from past measurements of frequency made at that magnetic field. Since the $TE_{6,2,1}$ was observed to be a strong mode, the presence of the $TE_{6,2,2}$ and the $TE_{6,2,3}$ is not surprising.

One low frequency second harmonic mode, the $TE_{8,3,1}$ mode was observed at 290 GHz and a magnetic field of 5.7 Tesla. The diode signal was weak so a power measurement was not taken, however, the amplitude of the diode signal indicated that the mode was probably emitting roughly 1 kW of power. Since it was possible to excite the $TE_{8,3,1}$ mode, the coupling to the $TE_{8,5,1}$ was probably good, however the fundamental starting currents were too low to allow the $TE_{8,5,1}$ to be excited.

In order to excite the harmonic modes the fundamental modes need to be weakened. The higher order axial modes can be weakened by shortening the input taper until these modes are no longer cutoff. In this case, they will suffer large diffraction losses. The cutoff radius, R_c, is given by

$$R_c = \frac{c\nu_{mp}}{\omega} \qquad 4.3.1$$

where ω is calculated from equation 4.0.1. One can see that the higher frequency, q = 2, 3 modes will have a smaller cutoff radius than the q = 1 modes, since the mode index, ν_{mp} does not change for the higher order axial modes. Therefore the input taper can be shortened enough to cause large leakage losses for the higher order axial fundamental modes and keep the second harmonic losses small. All of the subsequent cavities for this reason have a shorter input taper.

However, shortening the input taper will not weaken the fundamental q = 1 modes enough to prevent them from suppressing the desired second harmonic mode, which is why a different type of mode suppression must be used. In the following chapters we discuss techniques that actively try to suppress the fundamental modes (slotted cavity) or selectively reinforce only the desired second harmonic mode (iris cavity), instead of just trying to find an operating point where the fundamental mode is weak.

SUMMARY

Table 4.2.1

Power Measurements for the Tapered Cavity

Frequency (GHz)	Magnetic Field (T)	Power (kW)	Efficiency (%)	TE Mode
140.8	5.5	46.3	9.4	$TE_{4,2,1}$
163.0	6.3	44.9	8.6	$TE_{2,3,1}$
166.5	6.5	27.8	5.3	$TE_{0,3,1}$
–	7.4	41.7	21.4	$TE_{6,2,1}$

This chapter outlines the tapered cavity experiment. This cavity was designed to operate with a beam position where coupling to the fundamental modes was weak, due to a gap in the fundamental mode spectrum. This gap was expected to translate into a region of magnetic field devoid of fundamental modes. However, the region of excitation for the fundamental modes tended to be larger than predicted by the linear theory, and the higher order axial modes also filled in this region, thereby suppressing the second harmonic $TE_{8,5,1}$ mode. Therefore this experiment shows that to excite high frequency second harmonic modes with the available electron gun, more powerful fundamental mode suppression techniques are needed.

Chapter 5

SLOTTED CAVITY EXPERIMENTS

The initial harmonic gyrotron experiment, which was discussed in the previous chapter, did not excite high frequency (> 300 GHz) second harmonic emission. For that experiment, which was done with a tapered cavity, a second harmonic mode, the $TE_{8,5,1}$, was chosen that was positioned in the center of a large gap in the fundamental frequency spectrum. Theoretically, this would place the harmonic mode into a region of magnetic field where the fundamental modes are weak or nonexistent. Due to thick beam effects and strong higher order axial ($q \geq 2$) fundamental modes, this frequency gap was not observed. Therefore the second harmonic mode was suppressed by the strong fundamental modes that occupied the region of magnetic field corresponding to where the frequency gap should have been.

To successfully excite second harmonic modes at high frequency, a technique must be found that suppresses the fundamental modes and leaves the second harmonic modes relatively unperturbed. To weaken the higher order axial modes the input taper was shortened, so that these modes are no longer cutoff and will have large leakage losses. To perturb the q=1 fundamental modes, a technique using axial slots will be explored in this chapter. In this technique axial slots are cut along the straight section of the cavity at the azimuthal positions where the second harmonic RF field has a minimum making this mode relatively unperturbed. These slots were designed to be half way between consecutive maxima. If a second harmonic mode can be found that has a different symmetry from the surrounding fundamental modes, the fundamental modes will be highly perturbed, since not all of the slots will correspond to fundamental RF field minima at the wall.

In this chapter, we discuss cavities with two different sizes of slots. These cavities had the same dimensions as the tapered cavity of the previous chapter. First a cavity, known as the small slots cavity, was designed for the second harmonic $TE_{10,4,1}$ mode. Then a large slots cavity, which used the $TE_{5,6,1}$ mode, had slots that were twice the width of the ones in the small slots cavity. When the large slots and the small slots cavity experiments were conducted, no second harmonic emission was seen. As shown in Figures 5.1.2b-5.1.2d, the slots were cut all the way through the resonator wall, so some second harmonic leakage out of the slots was suspected. To determine if leakage was occurring, the outside of the large slots cavity was wrapped with foil, to reflect back into the cavity any leakage that propagated down the slots. With the foil sheath nineteen discrete fundamental frequencies were observed, instead of the six predicted for a conventional resonator without slots. In Figure 5.1.2d, one observes, that with a foil sheath, the large slots cavity resembles a magnetron configuration, and therefore magnetron resonator theory can be used to explain some of the extra frequencies. In this chapter, the first two sections will discuss the designs of the large slots and the small slots cavities. Next, magnetron theory will be reviewed and then the data from the three experiments covered in this chapter — small slots without foil and large slots with and without foil — will be analysed. These experiments will then be compared with the unslotted case of Chapter 4.

5.1 SMALL SLOTS CAVITY

To use the axial slots technique, a mode with a different symmetry than the surrounding modes is needed. Figure 5.1.1 shows the starting currents of the strongest fundamental (q=1) and second harmonic modes. The $TE_{10,4,1}$, which has a starting current of 3.86 Amps at 7.71 Tesla and oscillates at 386.6 GHz, has a five and tenfold symmetry, which the surrounding fundamental modes, the $TE_{4,3,1}$ and the $TE_{6,2,1}$, do not have. When talking about a fivefold symmetry, we mean that the azimuthal index is 5n (ie. the mode has 10n maxima at the wall), where n is a nonzero integer, therefore a resonator with 10 slots would not perturb this mode very much. In the case of this particular mode the same is true about a 20 slots system. The $TE_{10,4,1}$ was chosen as the design mode since it had the second lowest second harmonic starting current (the $TE_{8,5,1}$ had the lowest) and a different symmetry from the surrounding modes. In this experiment, 10 slots were cut in the straight section, instead of 20 for reasons of structural integrity as shown in Figure 5.1.2b. The unslotted case with the $TE_{8,5,1}$ mode is shown in Figure 5.1.2a. Since this cavity had the same dimensions as the tapered cavity, and the slot width was chosen to be 1/3 of the distance between consecutive maxima, resulting in a slot width of 0.033 cm.

When this experiment was conducted, the fundamental modes were weakened. In the unslotted cavity case, the $TE_{6,2,1}$ which oscillated at 191.7 GHz, had an output power of 42 kW with an efficiency of 21 % at beam currents of 3.0 Amperes. When small slots had been cut into the cavity, power levels of only 5.0 - 10.8 kW with efficiencies of 1.6 - 5.2 % were observed in the frequency range of 150 - 190 GHz at beam currents of 3.0 - 5.0 Amperes, as shown in Table 5.1.1. No mode assignments have been made in Table 5.1.1, since, the slots alter the frequencies of all the modes, as will be discussed later.

Although second harmonic emission was not observed, a standing wave pattern was observed for the fundamental modes. This indicates that the slots were significantly perturbing the fundamental modes. Due to the slots, the wall currents in the azimuthal direction were interrupted, and therefore there is no azimuthal rotating $\hat{y}$ component of the RF electric field, and a standing wave pattern results.

5.2 LARGE SLOTS CAVITY

In the previous experiment, no second harmonic emission was observed, even though the fundamental modes were weakened. It was decided that a cavity with larger slots to further weaken the fundamental modes was desirable. Figure 5.1.1, shows that in the region of magnetic field between 7.6 and 8.2 Tesla, the $TE_{5,6,1}$ which also has five-fold symmetry, has the third lowest second harmonic starting current. The $TE_{5,6,1}$ has a minimum starting current of 4.0 Amps at 7.73 Tesla and oscillates at 387.3 GHz. Since this mode has 10 maxima at the wall, the same resonator can be used as in the last experiment. The slots would be made twice as wide, and were cut to a width of 0.066 cm as shown in Figure 5.1.2c.

The results of this experiment were similar to those of the previous experiment, in terms of the observed power levels, and we conclude that the wider slots are not causing

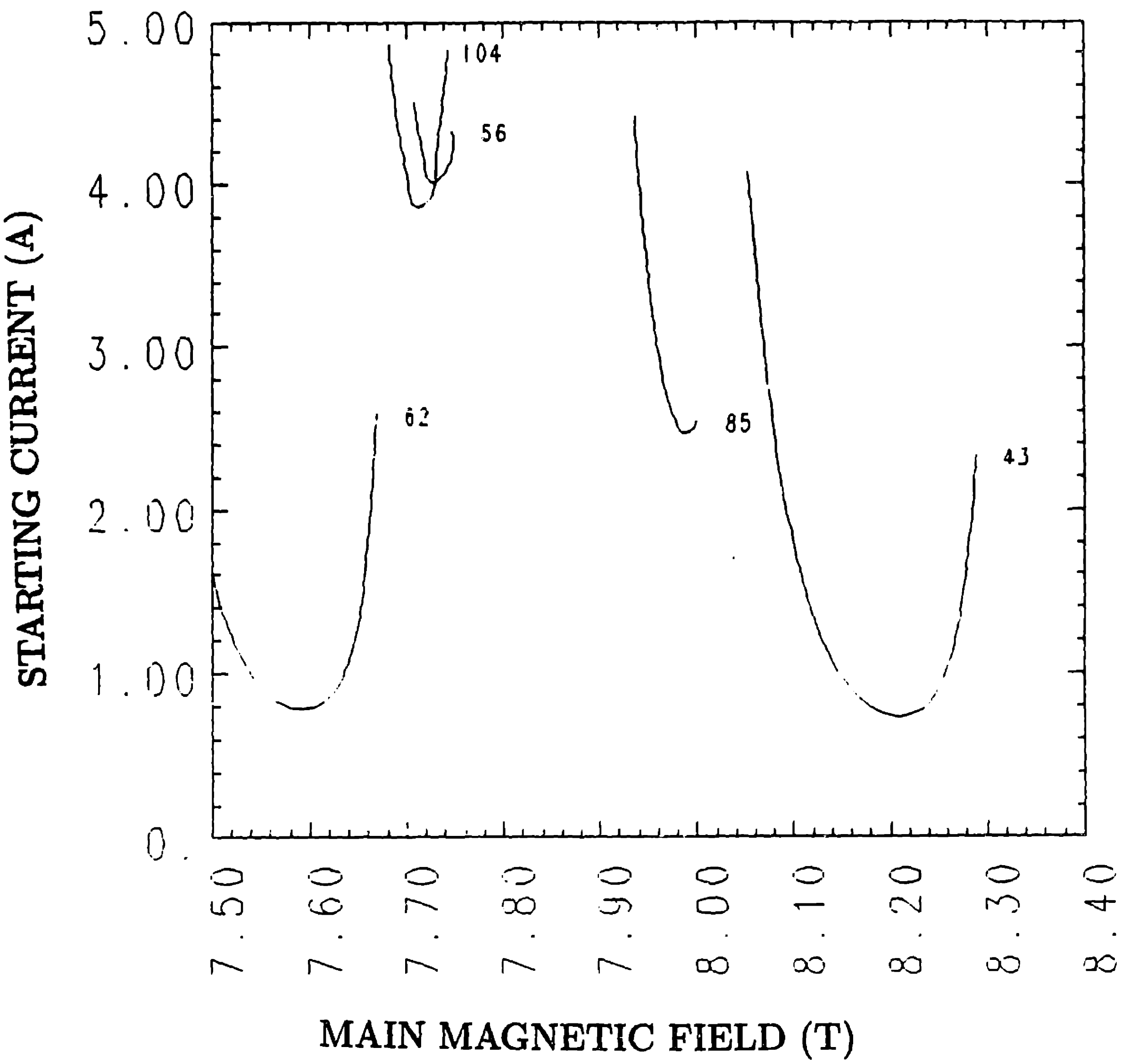

Figure 5.1.1 Starting current for the strongest fundamental and second harmonic modes.

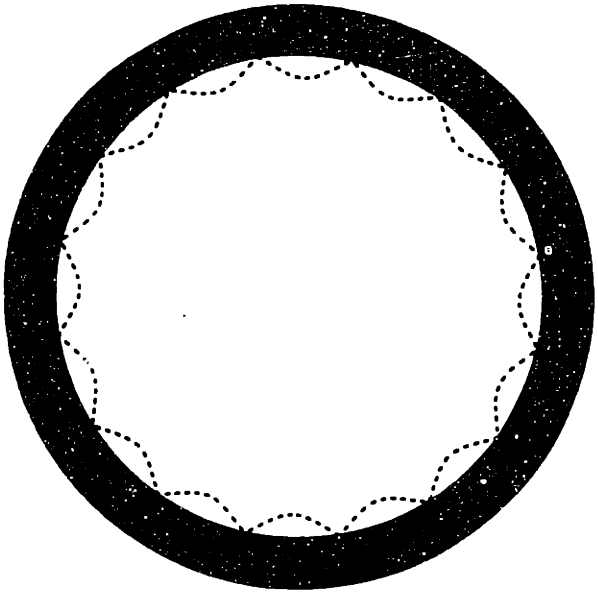

Figure 5.1.2a Unslotted cavity where the $TE_{8,5,1}$ is the design mode (dashed line).

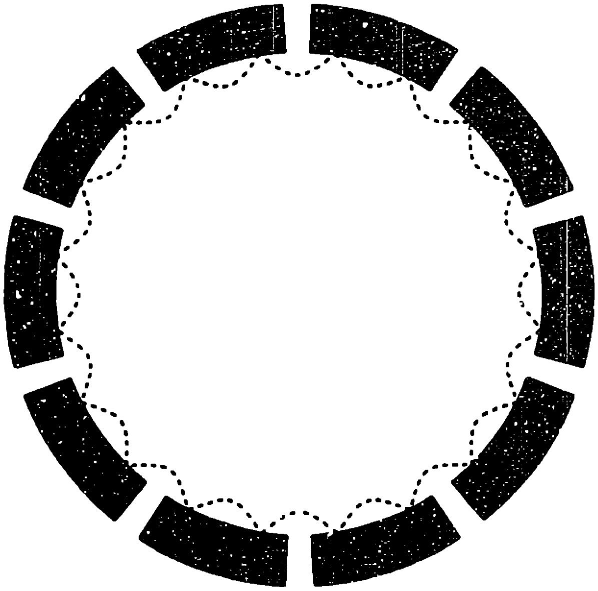

Figure 5.1.2b Small slots cavity that was designed for the $TE_{10,4,1}$ mode (dashed line).

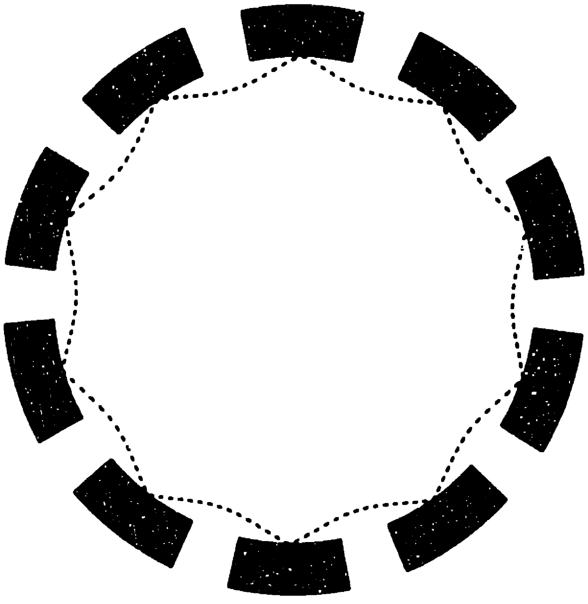

Figure 5.1.2c Large slots cavity (no foil sheath) with the $TE_{5,6,1}$ design mode (dashed line).

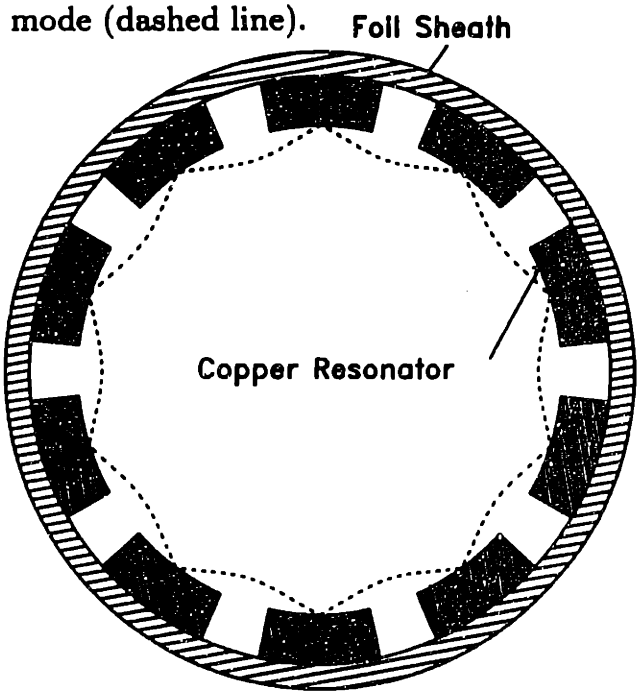

Figure 5.1.2d Large slots cavity with a foil sheath with the $TE_{5,6,1}$ mode represented by a dashed line.

TABLE 5.1.1

Fundamental Emission Observed when using the Small Slots Cavity

Magnetic Field (T)	Beam Current (A)	Power (kW)	Efficiency (%)	Frequency (GHz)
6.1	4.8	5.6	1.8	152.5
6.7	3.0	10.8	5.2	170.0
7.3	6.0	12.3	3.1	183.7
7.5	5.0	5.3	1.6	190.1

any further weakening of the fundamental modes. Again, no second harmonic mode emission was observed.

To check whether the slots were allowing excessive leakage of the second harmonic modes, and were therefore allowing the fundamental to suppress the harmonic modes, a foil sheath was wrapped around the slotted section of the resonator, as shown in Figure 5.1.2d. The foil acts as an impedance short at the end of the slots and reflects the radiation that has leaked into the slot back towards the center of the resonator. Again, after the foil sheath was installed, no second harmonic emission was observed. The absence of second harmonic emission may be explained by the fact that the slots could be significantly decreasing the second harmonic diffractive Q. Therefore the ratio of the second harmonic to fundamental total Q, Q_{T2}/Q_{T1} (the subscripts 1 and 2 refer to the fundamental and second harmonic respectively), might not have been increased enough to allow the second harmonic modes to be excited first.

However higher power levels were observed for the fundamental modes. Power levels of 15 - 19 kW with efficiencies of 5.0 - 9.3 % were observed at beam currents of 3.0 - 4.7 Amperes for modes with frequencies ranging from 170.7 - 205.7 GHz. Also, nineteen discrete frequencies were observed in the frequency range of 186.3 - 200.6 GHz. In Table 5.2.1 are listed the theoretical frequencies of the modes that would be in this frequency range for a conventional cylindrical resonator with the unslotted cavity profile. Even when the q=2 axial modes are included in the analysis, and a bit of frequency variation due to frequency pulling is assumed, the modes in Table 5.2.1 would account for only eight frequencies. Since the input taper was shortened to weaken the higher order axial modes and the slots significant lower the cavity diffractive Q, it is unlikely that the q=3 axial modes would have been excited. Therefore, conventional resonator theory cannot explain the extra frequencies. From Figure 5.1.2d, one can see that with the foil sheath the resonator resembles a magnetron configuration without a center conductor, and the frequencies of the modes may be highly distorted due to slot effects. In the next section, a theory will be developed that will model the resonator as a ten vaned magnetron — whose center conductor radius has been set to zero — and can relate the magnetron modes to gyrotron modes and show how frequency varies with slot depth.

5.3 THEORY OF A RESONATOR WITH VANES

Figure 5.3.1 shows a slotted magnetron configuration with a center conductor of radius r_c. If the center conductor is assumed to be infinitely thin, the configuration is very similar to the slotted cavity with foil sheath (Figure 5.1.2d), and vaned resonator theory (Collins (1948) and Chu (1984)) can be used to analyse this resonator.

Magnetrons have a rotating RF field with a nonsinusoidal variation around the anode. A sum of Fourier components can be used to model the spatial variation. Each component corresponds to a periodic rotating wave containing a unique number of complete periods and rotates with a distinct velocity. These components have Γ complete periods around the circumference given by

$$\Gamma = n + mN \qquad 5.3.1$$

where Γ is an integer, N is the number of slots and is an even number, n = 1,2,..,N/2 is the mode number of the harmonic component and is related to the phase shift between slots which is $2\pi n/N$. If N is an odd number, the modes corresponding to non-integer values of n do not exist. The other parameter, m = 0, ±1, ±2,... is an integer. The ± values for m account for the fact that if m is nonzero there are two counter rotating RF fields for each Fourier component. If the electrons that form the undistorted space charge have angular velocities close to that of one of the Fourier components, the effect of the RF field component will be cumulative and the space charge will be distorted to have Γ spokes.

The frequency corresponding to each value of Γ is calculated in the following fashion. The admittance of the interaction region is calculated as a function of frequency. Then we calculate the admittance of a slot as a function of frequency and apply the boundary condition that these admittances must be equal at the slot-interaction region boundary (denoted in Figure 5.3.1 as the dotted line cd). Due to the symmetry of the system, applying this procedure to any slot will give the same answer. The admittance of a slot

TABLE 5.2.1

Theoretical Frequencies for an Unslotted Cavity

TE MODE	THEORETICAL FREQUENCY (GHz)
$TE_{3,3,1}$	185.4
$TE_{1,4,1}$	191.3
$TE_{6,2,1}$	191.7
$TE_{10,1,1}$	192.3

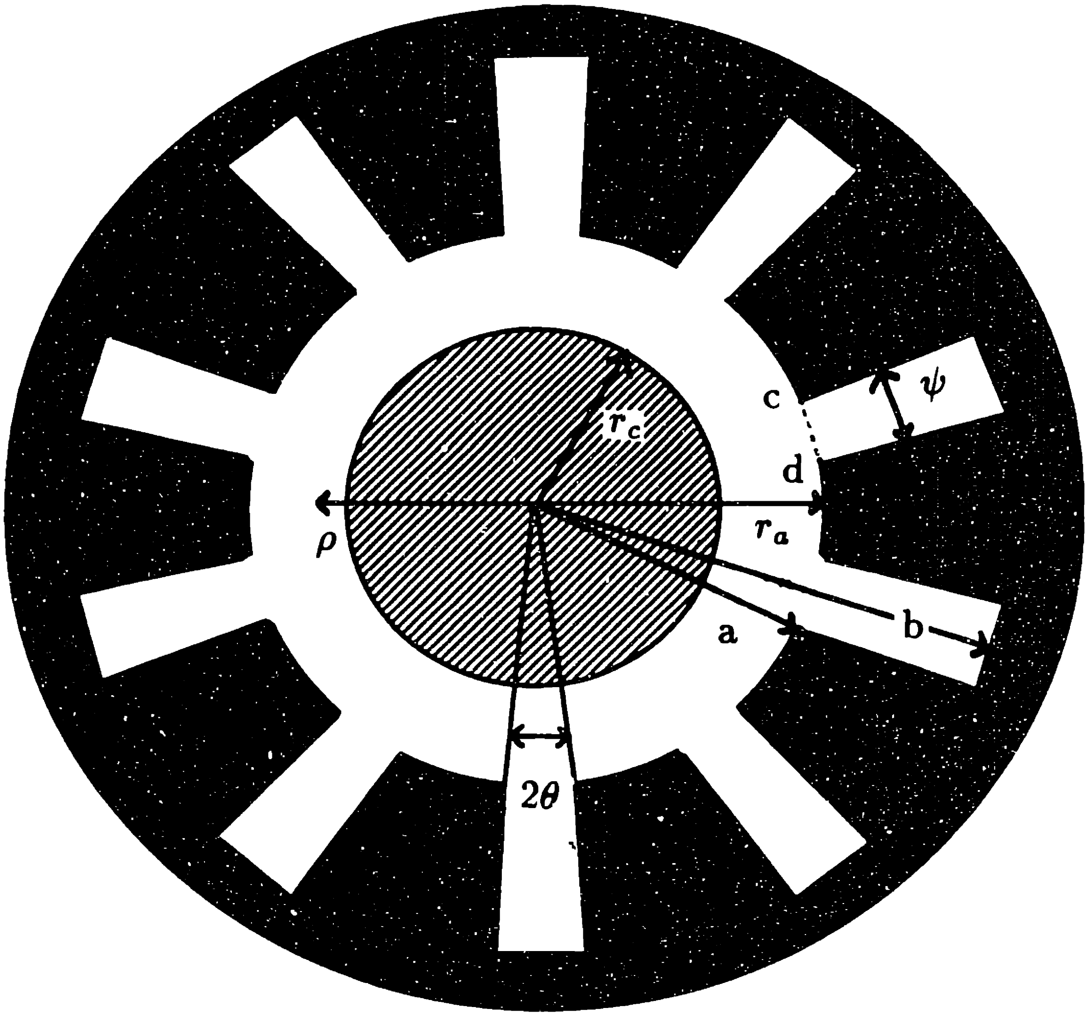

Figure 5.3.1 Cross–section of a resonator with vanes.

is given by (Collins (1948))

$$Y_{slot} = j\sqrt{\frac{\epsilon_o}{\mu_o}} \frac{h}{\psi a} \frac{J_o(ka)N_1(kb) - J_1(kb)N_o(ka)}{J_1(ka)N_1(kb) - J_1(kb)N_1(ka)} \tag{5.3.2a}$$

and the admittance of the interaction region, Y_{int}, is

$$Y_{int} = j\sqrt{\frac{\epsilon_o}{\mu_o}} \frac{Nh}{2\pi r_a} \sum_{m=-\infty}^{\infty} \left(\frac{sin\Gamma\theta}{\Gamma\theta}\right)^2 \frac{Z_\Gamma(kr_a)}{Z'_\Gamma(kr_a)} \tag{5.3.2b}$$

with

$$Z_\Gamma(k\rho) = J_\Gamma(k\rho) - \frac{J'_\Gamma(kr_c)}{N'_\Gamma(kr_c)} N_\Gamma(k\rho) \tag{5.3.2c}$$

$$Z'_\Gamma(k\rho) = J'_\Gamma(k\rho) - \frac{J'_\Gamma(kr_c)}{N'_\Gamma(kr_c)} N'_\Gamma(k\rho) \tag{5.3.2d}$$

where J_o, J_1 and N_o, N_1 are Bessel functions of the first and second kind, k is the wave number, h is the length of the anode or center conductor, r_c is the radius of the center conductor, and μ_o and ϵ_o are the permeability and permittivity of free space respectively. The parameters ρ, r_a and θ describe the geometry of the interaction region, a and b are the radii of the top and the bottom of the slot region and ψ the angular slot width. All these quantities are shown in Figure 5.3.1. The value for k is determined by setting the admittance of a slot Y_{slot} equal to that of the interaction region Y_{int} at the slot boundary ($r_a = a$). The frequency for each value of n, is then calculated from k using the free space dispersion relation.

A code, MATCH SLOT (Chen (1987)), which incorporates the admittance matching technique described above, has been used to calculate the frequency for each value of n for the dimensions of the large slots cavity foil sheath configuration. These values are plotted in the Brillouin Diagram shown in Figure 5.3.2. The horizontal axis is the mode number n. Since Y_{slot} is a periodic function, there many frequencies that correspond to a specific value of n. These other values represent the higher order radial modes. The higher order radial modes explain the presence of more than one curve in Figure 5.3.2. One notices that the values of frequency corresponding to $n > 5$ (= N/2) are symmetric with the $n < 5$ cases. This symmetry is a result of the fact that the harmonics rotating counter-clockwise have the same frequency as those rotating in the clockwise direction.

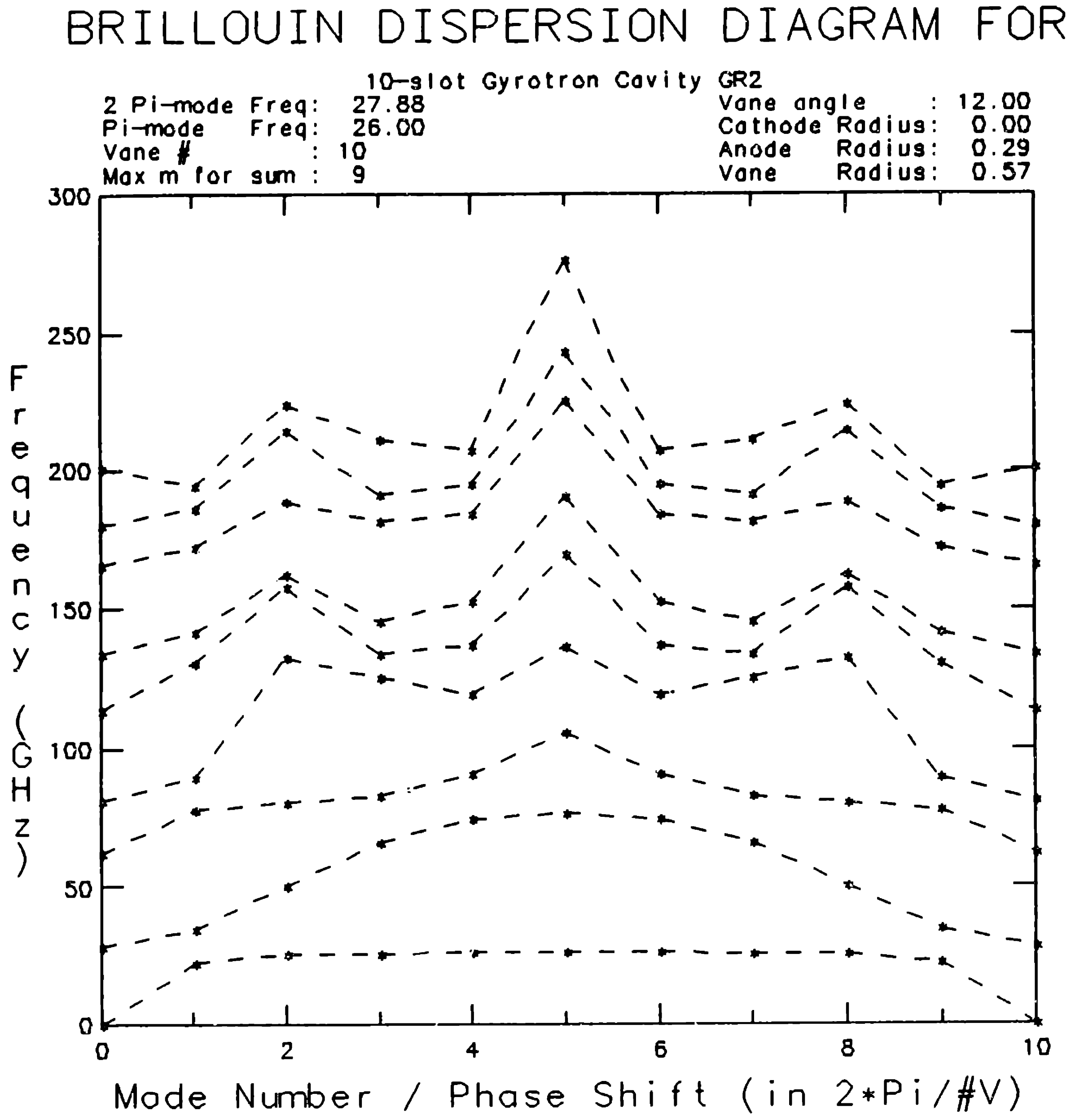

Figure 5.3.2 Frequency spectrum for the large slots case with a foil sheath.

To test for the existence of new modes, the slot depth was reduced to almost zero in the code. At zero slot depth the magnetron modes can be related to gyrotron TE modes. When the slot depth was reduced to b/a = 1.01 the agreement between the magnetron mode frequencies calculated by the code and the theoretical frequencies of the gyrotron modes for an unslotted cavity was quite good, with discrepancies that were less than 0.5 %. This result suggests that no new modes were created when the slots were added, instead, the effect of the slots was to distort the frequencies of the unslotted cavity modes.

To facilitate a better understanding of frequency changes caused by the slots, the behavior of mode frequency with increasing slot depth was studied. Figure 5.3.3 shows the frequency as a function of slot depth for the seven modes whose frequency is in the range of interest, which is 185.9 - 201 GHz (and a mode that is slightly out of this range) at the slot depth, b/a = 1.94, corresponding to the configuration of the large slots cavity with a foil sheath. Generally, the frequency of each mode decreases with slot depth, since the effective cavity radius is increasing. In certain limited regions, however, the frequency does increase with slot depth, perhaps due to slot impedance effects. Since the rate of change of the frequency is not the same for all the modes, several modes may converge to a small range of frequency at a specific slot depth. In this fashion, the seven modes listed in Table 5.3.1 have frequencies in the range of interest instead of four as predicted by conventional cylindrical resonator theory.

5.4 EXPERIMENTAL RESULTS

In this section the experimental results observed with the small slots cavity, and the large slots cavity, with and without the foil sheath will be compared with those of the unslotted cavity. To accomplish this purpose, the frequency data of each experiment is plotted as a function of magnetic field. Several trends will emerge in the data. One trend will be frequency tuning due to variation in the main magnetic field. A rough estimate of this range in magnetic field can be made from the detuning as follows. The

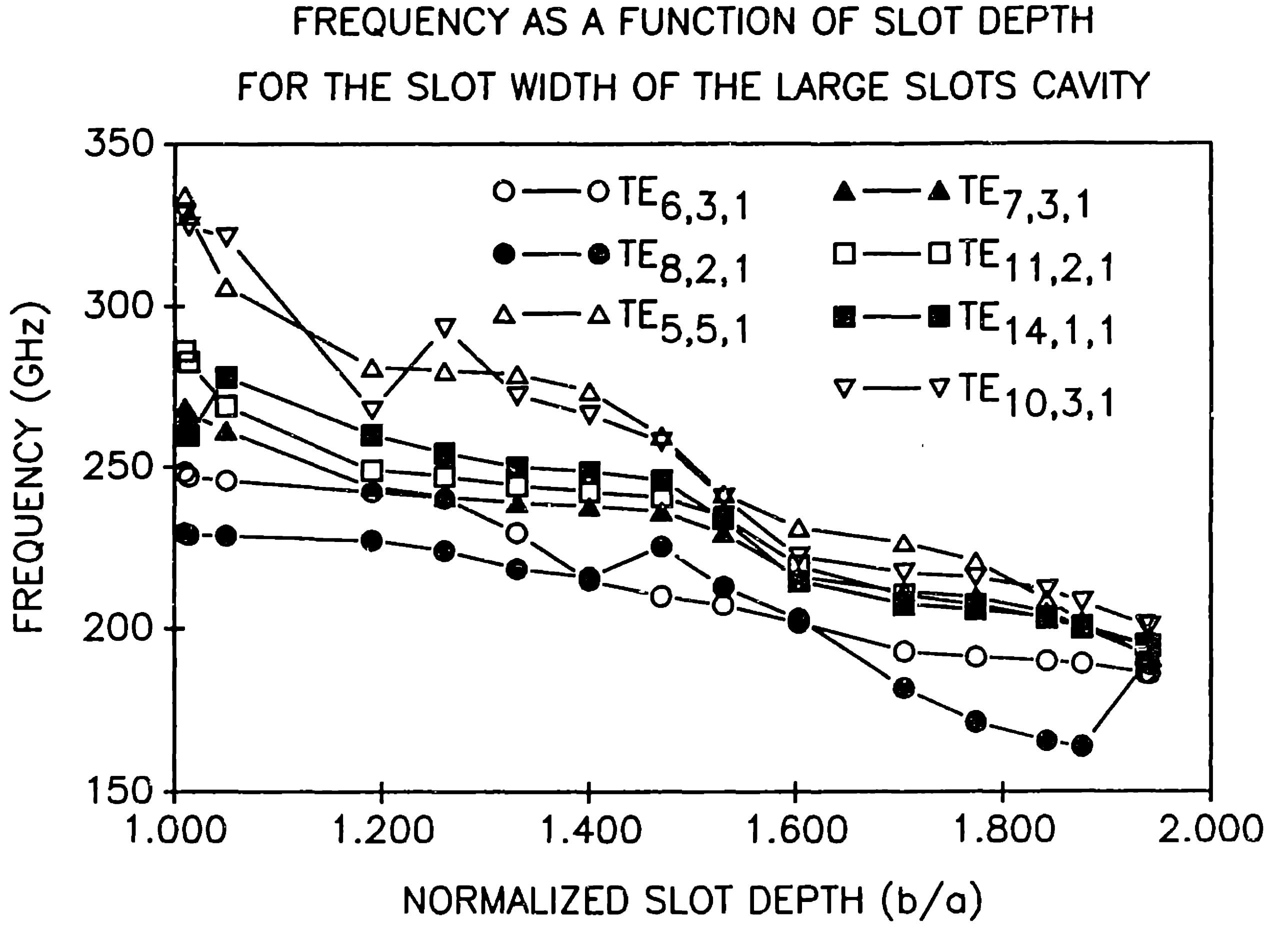

Figure 5.3.3 Frequency as a function of slot depth for a resonator with 10 slots and the same inner radius and slot width as the large slots cavity.

TABLE 5.3.1

Theoretical Frequencies Using Magnetron Theory

TE MODE	THEORETICAL FREQUENCY (GHz)
$TE_{4,4,1}$	184.12
$TE_{6,3,1}$	185.97
$TE_{8,2,1}$	188.67
$TE_{5,5,1}$	190.73
$TE_{7,3,1}$	191.35
$TE_{11,2,1}$	194.39
$TE_{14,1,1}$	194.87
$TE_{10,3,1}$	200.71

modes are assumed to operate at detunings, Δ, in a range of 0 - 0.5, where

$$\Delta = \frac{2}{{\beta_{\perp o}}^2}\left(1 - \frac{n\omega_c}{\omega}\right) \tag{5.4.1}$$

with $\omega_c = eB/\gamma m$. If the normalized perpendicular velocity $\beta_{\perp o}$ has a value of 0.384, the mode has range in magnetic field of 4%. An increase in frequency with increasing magnetic field is predicted by theory. The increase in RF frequency results from the higher cyclotron frequency, ω_{co} as seen in equation 5.4.3. When the total Q - Q_T - is high, the mode frequency has very little variation with the magnetic field because the maximum change in frequency scales as $\Delta f/f \propto Q_T^{-1}$(Kreischer (1984)).

One will also see cases where the frequency varies when the value of cathode voltage and magnetic field (and therefore, cyclotron frequency) is fixed and the cathode magnetic field is varied. This frequency pulling, which is observed with the large slots cavity with a foil sheath (Figure 5.4.4b), can be explained in terms of variation in pitch angle, α, where $\alpha = v_{\perp o}/v_{\|o}$. In general, the frequencies of modes increased as the cathode magnetic fields increased. Based on adiabatic theory, the perpendicular velocity at the entrance of the cavity, $v_{\perp o}$, is given by

$$v_{\perp o}^2 = \frac{B_o}{B_k} v_{\perp k}^2 \tag{5.4.2}$$

where $v_{\perp k} = E_k/B_k$ is the perpendicular velocity at the cathode, E_k is the electric field between the cathode and the mod anode, and B_o is the main magnetic field. Therefore as the magnetic field at the cathode increases the perpendicular velocity at the entrance of the cavity decreases. Since the cathode voltage, V_c, is not varied, the relativistic factor γ does not vary ($\gamma = 1 + V_c(kV)/511$), and as the perpendicular velocity decreases, the parallel velocity increases according to $\gamma^{-2} = 1 - (v_{\perp o}/c)^2 - (v_{\|o}/c)^2$. The condition of excitation for the cyclotron instability is given by

$$\omega - k_{\|}v_{\|o} = \omega_{co}/\gamma \tag{5.4.3}$$

where $\omega_{co} = eB_o/m$ is the cyclotron frequency, ω is the RF frequency, $k_{\|o} = 2/L_{eff}$ is the component of the wave number parallel to the main magnetic field if a Gaussian

RF profile is assumed, and L_{eff} is the effective interaction length. One can see that as $v_{\|o}$ increases the frequency increases, since all the other quantities remain constant. Therefore, the observed increase in frequency at higher cathode magnetic fields is a result of a increase in the parallel velocity, $v_{\|o}$. To calculate the change in detuning due to pitch angle tuning, the variation in magnetic field at the cathode, ΔB_k must be related to the change produced in the parallel velocity, $\Delta v_{\|o}$. Using equation 5.4.2, the relation is given by

$$\frac{\Delta v_{\perp o}}{v_{\perp o}} = -\frac{3}{2}\frac{\Delta B_k}{B_k} \qquad 5.4.4a$$

and

$$\Delta v_{\|o} = -\frac{v_{\perp o}\Delta v_{\perp o}}{v_{\|o}} = \frac{3}{2}\frac{v_{\perp o}^2}{v_{\|o}}\frac{\Delta B_k}{B_k} \qquad 5.4.4b$$

where $v_{\perp o}$ and $v_{\|o}$ are related by the definition of γ_o, and the subscripts k and o refer the the values of different variables at the cathode and at the entrance of the cavity, respectively.

An expression can be derived with the linear theory (Kreischer (1980)) to calculate the percentage change in frequency $\Delta\omega/\omega$, caused by a given percentage change in $v_{\|o}$, $\Delta v_{\|o}/v_{\|o}$ in the linear regime. The operating frequency ω is defined by (Slater(1950))

$$\frac{\omega-\omega'}{\omega} = -\frac{1}{2Q_T}\frac{D_n}{W_n} \qquad 5.4.5a$$

where ω' is the frequency of the cavity without the beam present and

$$W_n = Im(\int_0^T -e\mathbf{E}\cdot\mathbf{v}dt) \qquad 5.4.5b$$

$$D_n = Re(\int_0^T -e\mathbf{E}\cdot\mathbf{v}dt) \qquad 5.4.5c$$

and **E** is the RF electric field and **v** is the electron velocity. If a Gaussian RF field profile is assumed, equation 5.4.5a can be rewritten as (Kreischer (1984))

$$\frac{\Delta\omega}{\omega} = \frac{1}{Q_T}P(x) \qquad 5.4.6a$$

where

$$P(x) = \frac{D(x/\sqrt{2}) - 1/2s\beta_{\perp o}^2 D'(x/\sqrt{2})}{\sqrt{\pi}exp(-x^2/2)(1+1/2s\beta_{\perp o}^2 x)} \qquad 5.4.6b$$

and D(y) is Dawson's integral (Abramowitz and Stegun (1965)), $x = (\omega_c - \omega)L_{eff}/2v_{\parallel o}$ and $s = \omega_c L/2v_{\parallel o}$. To calculate the percentage of frequency variation as a function of the change in $v_{\parallel o}$, the derivative with respect to $v_{\parallel o}$ must be taken. If it is assumed that $s\beta_{\perp o} \gg 1$, which is valid for this experiment, and the minimum starting current corresponds to $x \simeq x_{min} \simeq -1$, the D' term dominates. Therefore

$$\frac{dP(x)}{dv_{\parallel o}} = \frac{dx}{dv_{\parallel o}} \frac{dP(x)}{dx} \qquad 5.4.7$$

where $dP(1/\sqrt{2})/dx \simeq D''(1/\sqrt{2}) = 1.4$ and 5.4.6a can be written as

$$\frac{\Delta\omega}{\omega} = -\frac{1.4x}{Q_T}\frac{\Delta v_{\parallel}}{v_{\parallel}} = \frac{1.4(\omega - \omega_c)L_{eff}}{2v_{\parallel o}Q_T}\left(\frac{3}{2}\left(\frac{v_{\perp o}}{v_{\parallel o}}\right)^2 \frac{\Delta B_k}{B_k}\right) \qquad 5.4.8$$

Figure 5.4.1a shows the frequency data for the q=1 modes, and one notices that certain frequencies are excited over a range of magnetic field. A more detailed graph (Figure 5.4.1b) shows a small change in frequency due to frequency pulling as seen in the mode between 210 and 215 GHz. Experimentally, a frequency variation of 0.17 Ghz was observed over a 0.21 Tesla range in magnetic field. To compare this with theory, an expression can be obtained by using the gyrotron linear theory (Kreischer (1984)) and is given by

$$\frac{(\Delta f/f)}{\Delta B/B} \simeq \frac{1.4s}{Q_T} \qquad 5.4.9$$

where $s = \omega_c L_{eff}/2v_{\parallel o}$, ω_c is the cyclotron frequency, L_{eff} is the axial interaction length of the cavity RF electric field, and $s\beta_{\perp o}^2 \gg 1$ has been assumed. Since the Q of the cavity for that mode is 860 one expects a maximum frequency variation due to frequency pulling, Δf of 0.51 GHz where $L_{eff} = 0.72cm$, B = 8.0 Tesla, $\beta_{\parallel o} = 0.256$, $\Delta B = 0.21$ and $\gamma = 1.13$. This value of frequency variation is higher than the experimental value of 0.17 GHz, however, the frequency tuning for this mode may be larger than 0.17 GHz, since a detailed study was not conducted on this mode and the data points were at beam currents ranging from 1.7 to 6.5 Amps.

Figure 5.4.2a shows the data for the small slots cavity. The modes at 190.3 GHz and 152.5 GHz show some change in frequency due to variation of the main magnetic field.

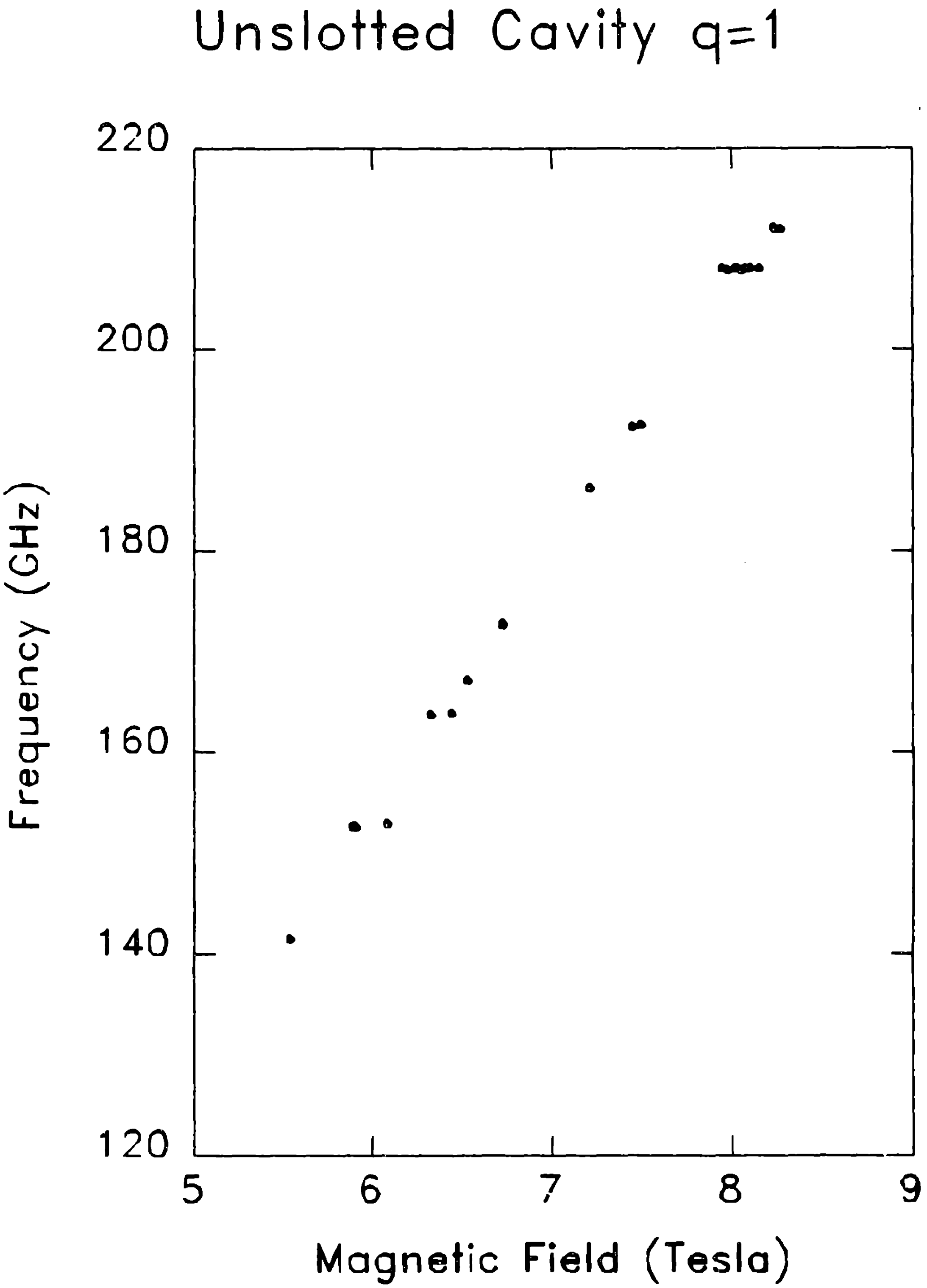

Figure 5.4.1a Frequency data for the unslotted cavity.

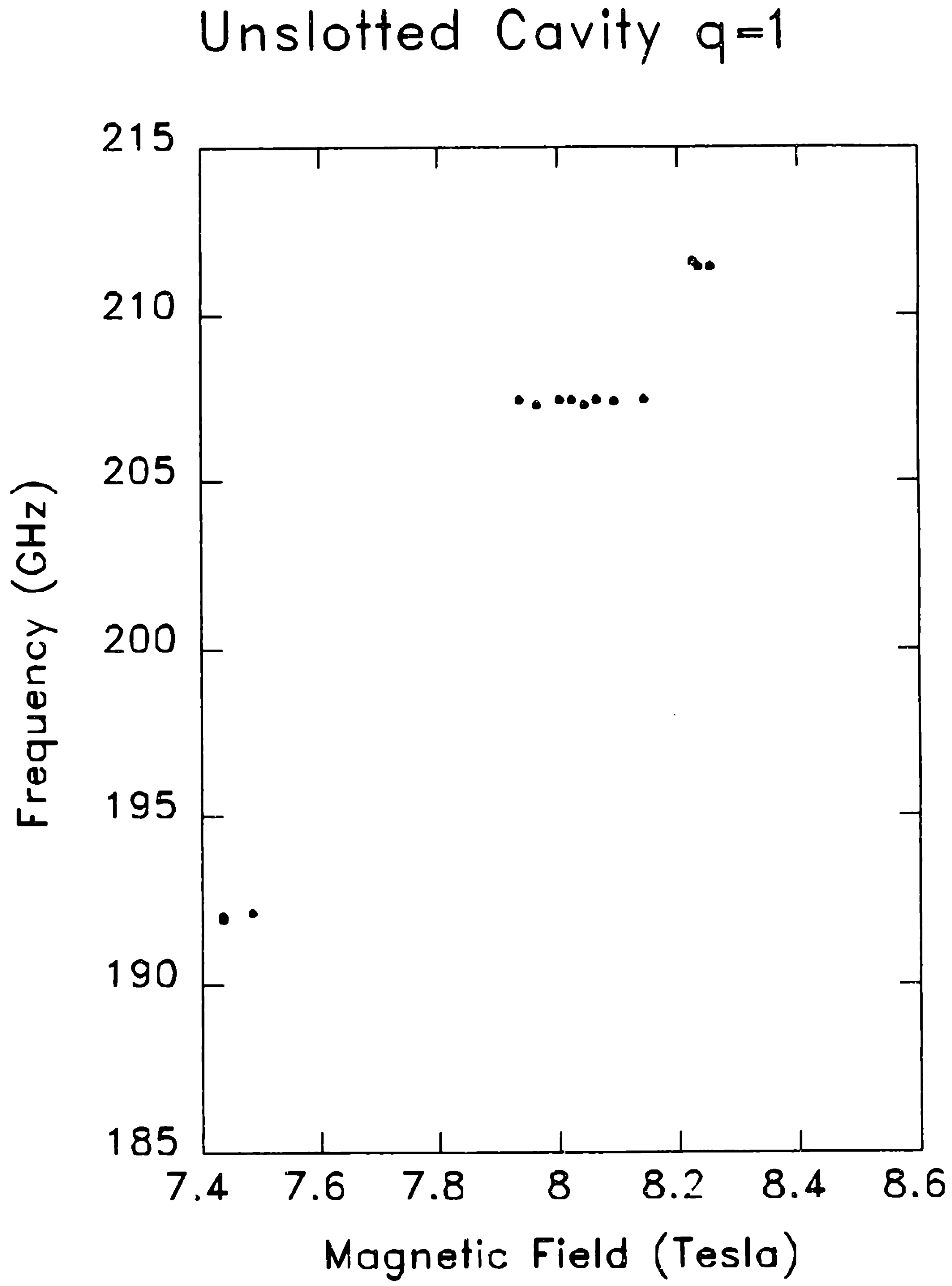

Figure 5.4.1b Expanded view of the unslotted cavity frequency data.

An expanded view of the mode at 190 GHz — see Figure 5.4.2b — shows a frequency variation of 0.082 GHz, which shows that this is a high Q mode. Again, since a careful study was not conducted on this mode, and the data points are a collection of points taken at beam currents between 2.0 to 5.0 Amps. Therefore, the frequency variation of this mode may be larger than 0.082 GHz, and is likely to be larger than the value of 0.17 GHz observed in the unslotted cavity, since the Q of this cavity will be somewhat lower due to the small slots cut in the cavity wall. The small change in frequency, shows that even with the slots, this mode still has a fairly high Q, which is in contrast with the large slots cases where the frequency variation due to frequency pulling is larger and therefore the cavity Q must be lower. One sees some examples of frequency variation at a constant magnetic field in Figures 5.4.3a and 5.4.3b showing the data for the large slots case with no foil. Some cases are also present where the frequency increased at higher magnetic fields as a result of frequency pulling due to varying the main magnetic field. When the foil sheath is used (Figure 5.4.4a and 5.4.4b) more modes are present especially in the range between 185-201 GHz. Since so many modes were present, the frequencies were measured while the magnetic field at the cathode was varied at fixed values of the main magnetic field, beam current, and cathode voltage and no data was taken at any other values of magnetic field. In this fashion one could observe how the mode frequencies vary with main field and cathode magnetic field (and $\beta_{\perp o}$). Measurements were made at nine values of magnetic field, resulting in the nine vertical lines. If data was taken at more values of magnetic field, the area between the vertical lines would probably be filled in with more frequencies. Figures 5.4.4a and 5.4.4b show a surprising result. A high density of frequencies was observed due to a large amounts of frequency pulling at a fixed value of magnetic field. In some cases the change in frequency was as large as 3 GHz. In comparison, the unslotted cavity case (Figure 5.4.1) has only a frequency variation of 0.17 GHz, and therefore fewer frequencies. Also the frequency pulling in the unslotted cavity is only caused by variations of the main magnetic field. The large amount of frequency variation in the large slots cavity with a foil sheath require a low cavity Q, which is quite possible in this case, since large slots were cut in the cavity walls.

The change in frequency at constant magnetic field, may be explained by two different mechanisms: mode hopping and frequency pulling due to pitch angle tuning. For the variation of magnetic field at the cathode experienced during the frequency tuning at a fixed value of main field, the change in frequency due to frequency pulling predicted by pitch angle tuning using adiabatic theory and equations 5.4.4b and 5.4.8 is 0.9 GHz, for a Gaussian axial RF field profile, $v_{\perp o}/v_{\parallel o} = 1.5$, $L_{eff} = 0.72cm$, $Q_T = 100$ and $\beta_{\parallel o} = v_{\parallel o}/c = 0.256$ where c is the speed of light. However the value of the effective interaction length, L_{eff} was assumed to be the straight section length. This assumption may under estimate the effective interaction length for a slotted cavity, especially for a low Q cavity where the mode is not highly trapped. With a longer effective interaction length or lower value of parallel velocity, $v_{\parallel o}$, larger frequency variations due to pitch angle tuning are possible. Also the value of the total Q, Q_T, may be lower than 100. Since no mode identification measurements were made, it is not possible to prove that only one mode was present during the tuning at a fixed value of magnetic field. Mode hopping between higher order axial modes or different transverse modes may be responsible for some of the frequency variation, especially in the set of frequencies at 6.59 Tesla, which couldn't be explained by the pitch angle tuning. Therefore, the high density of modes may be a result of the presence of more modes due to the magnetron effects that are subject to mode hopping and large amounts of frequency pulling caused by pitch angle tuning and possibly even variations in the main magnetic field.

SUMMARY

In this chapter we have discussed cavities with axial slots cut along the straight section of the cavity at positions where the RF field of the second harmonic mode has a minimum. In this manner, the fundamental modes would be weakened, without perturbing the second harmonic design mode. Initially small slots were cut. The fundamental modes were weakened, but no second harmonic emission was observed. The next step was to chose a mode that allowed the slots to be cut larger, so as to further weaken the fundamental modes. Again, no second harmonic modes were observed and it was sus-

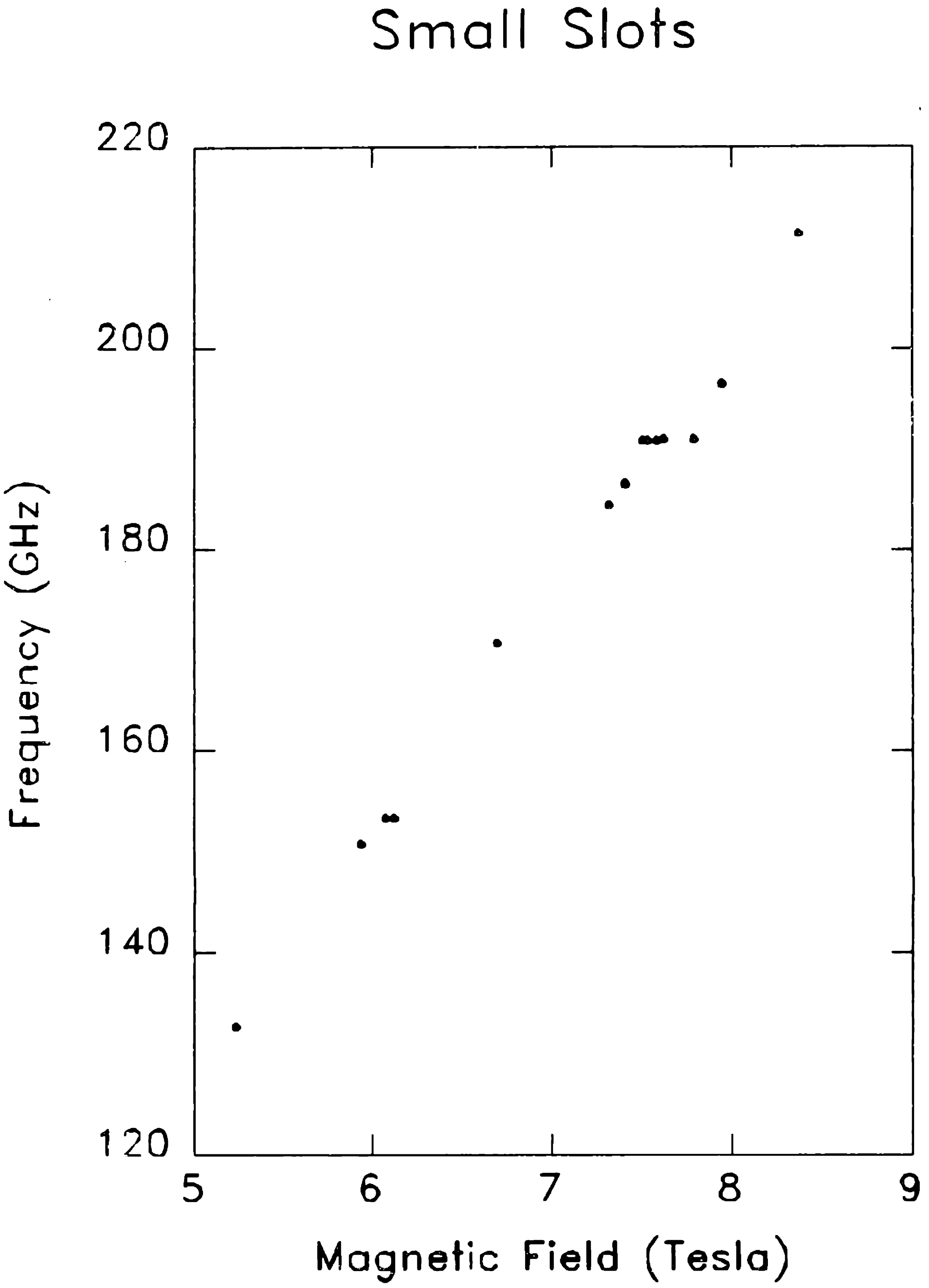

Figure 5.4.2a Frequency data for the small slots cavity.

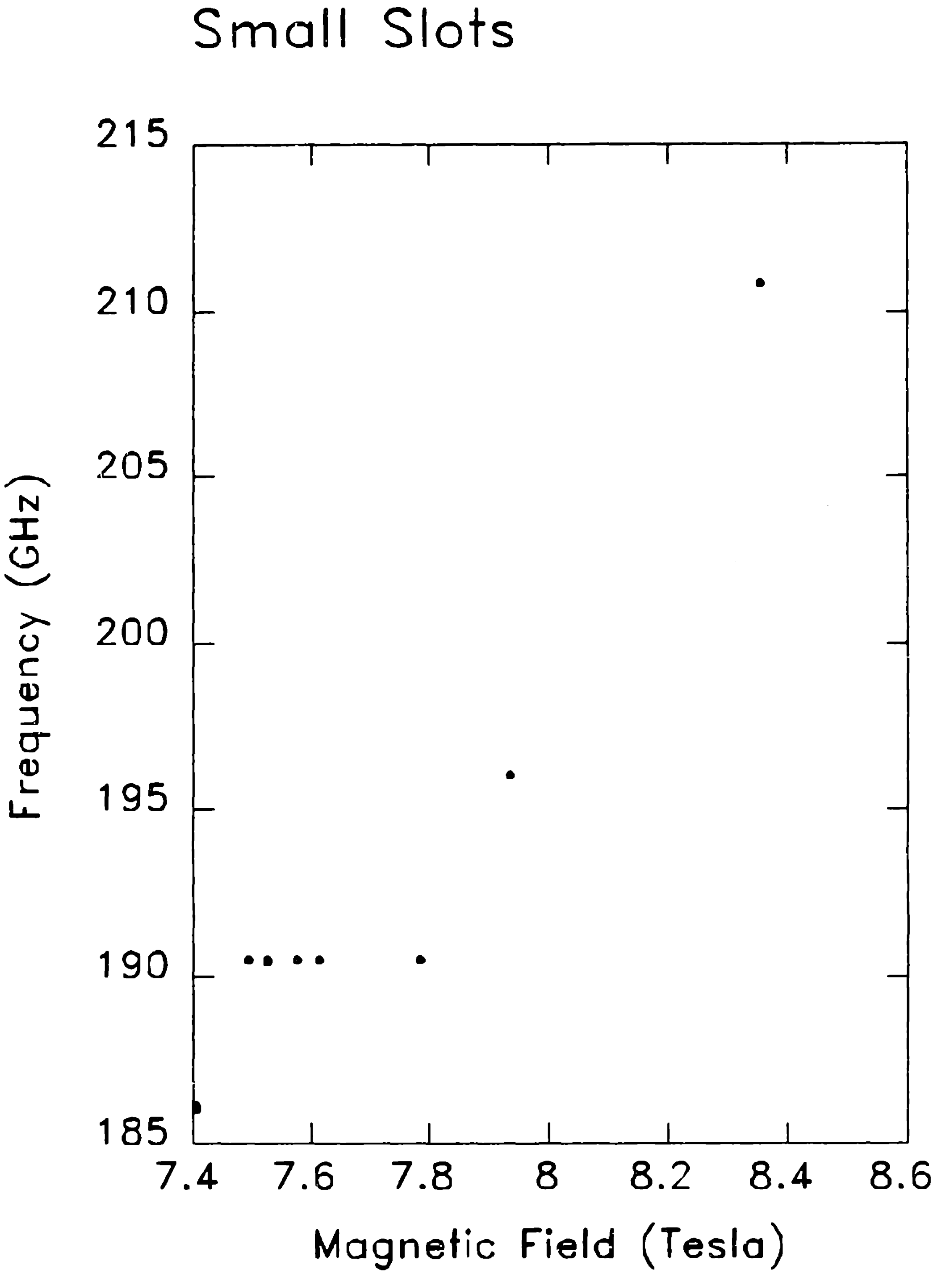

Figure 5.4.2b Expanded view of the small slots frequency data.

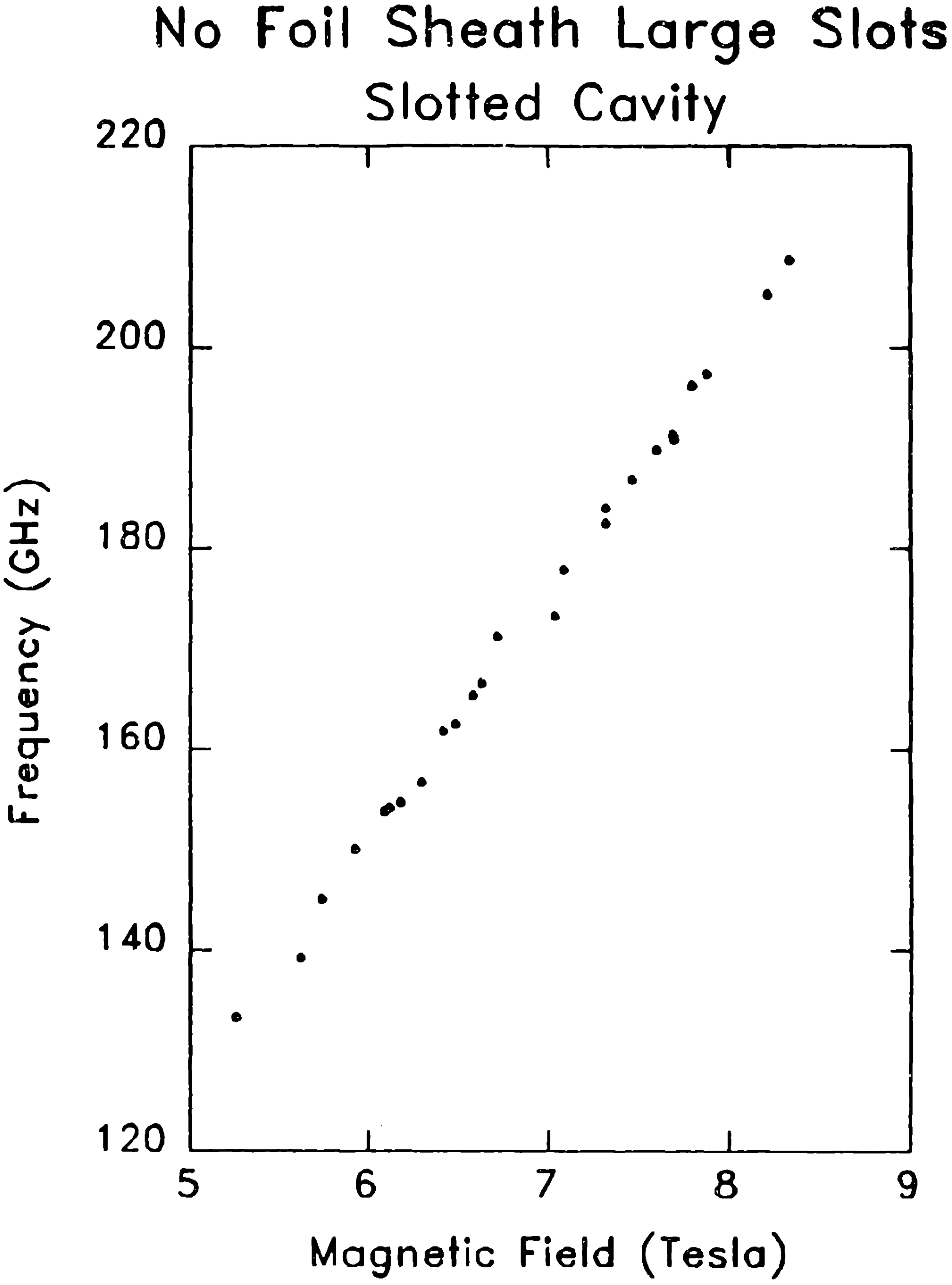

Figure 5.4.3a Frequency data for the large slots cavity with no foil.

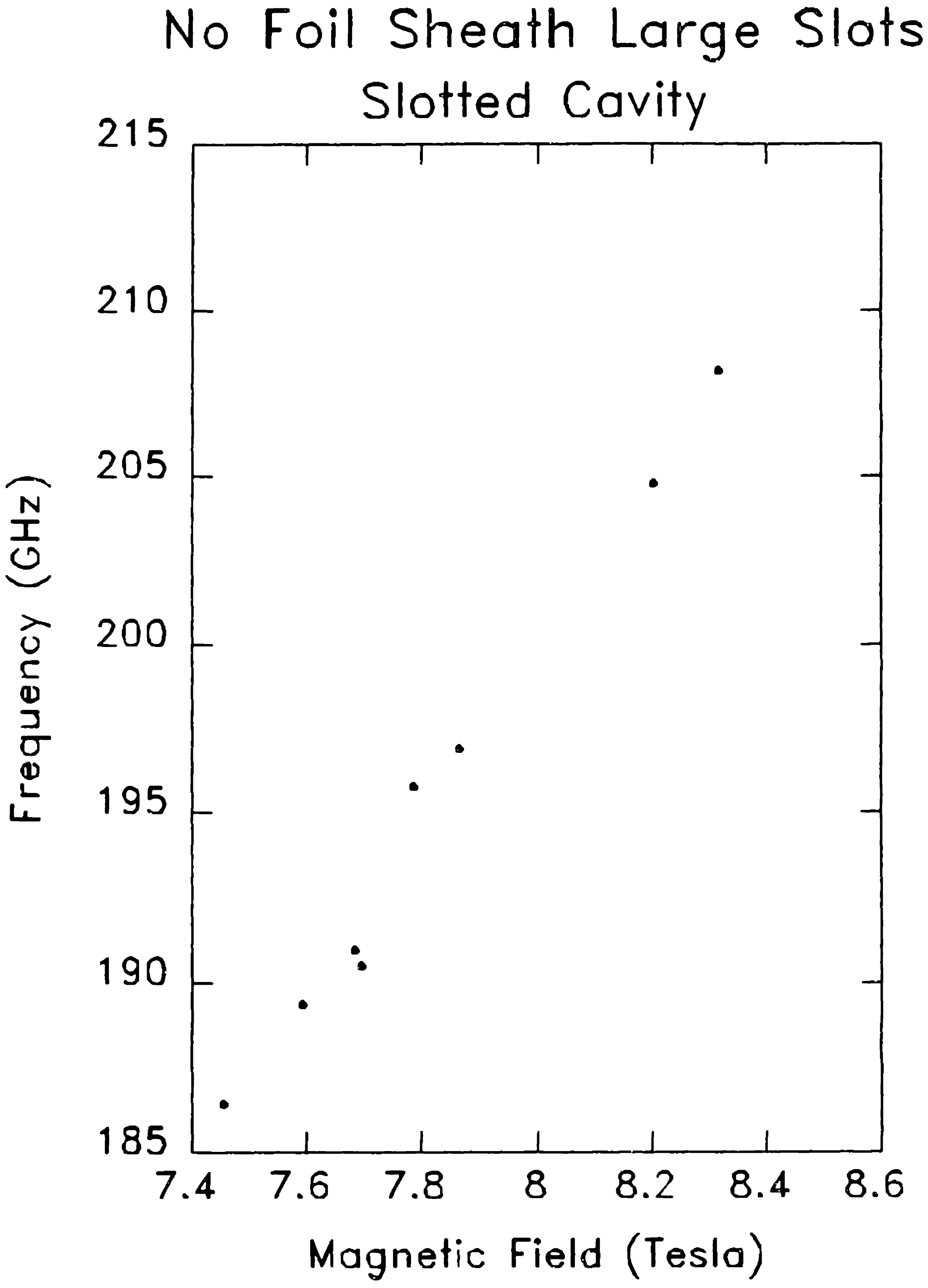

Figure 5.4.3b Expanded view of the large slots cavity (without a foil sheath) frequency data.

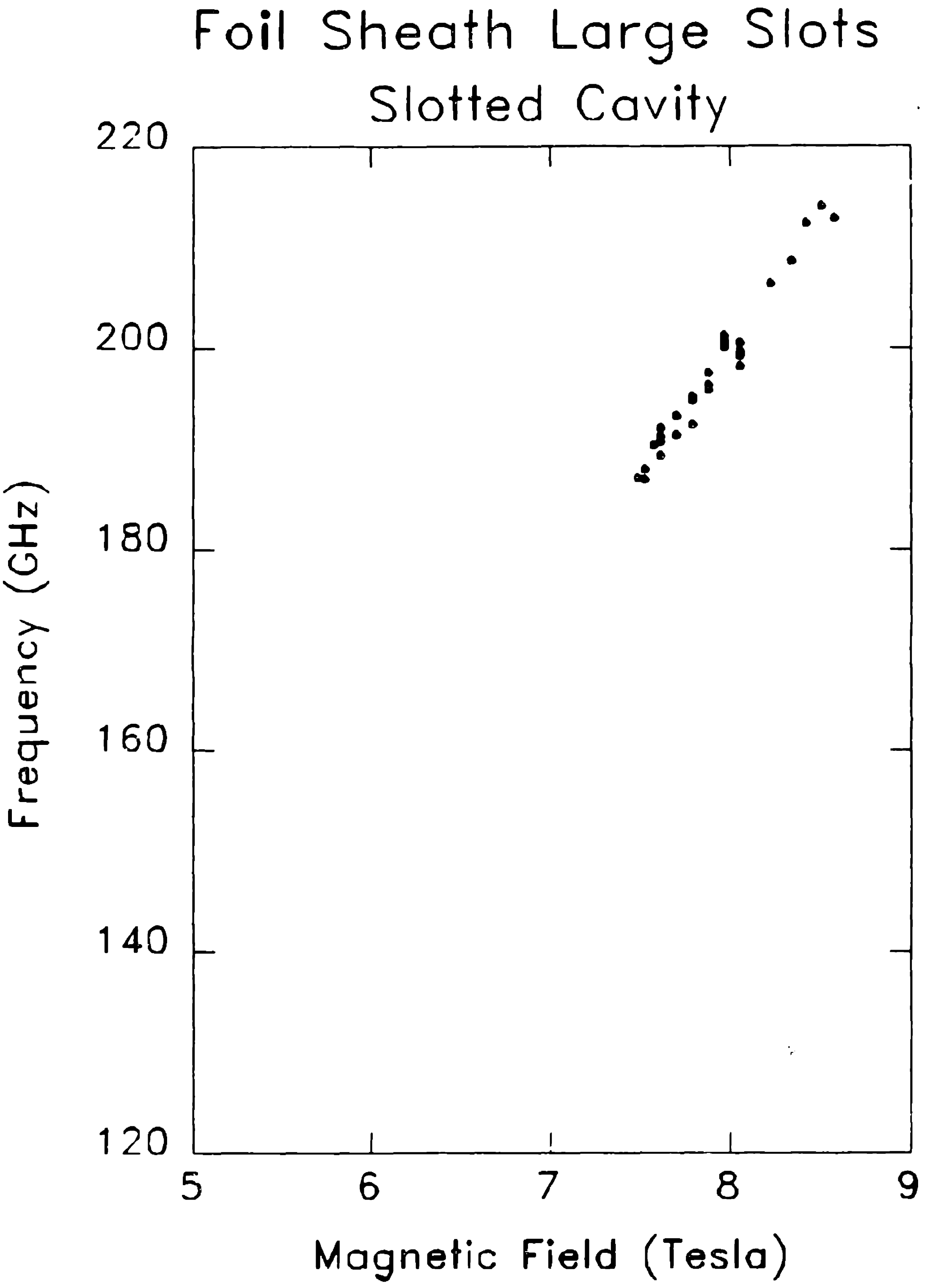

Figure 5.4.4a Large slots cavity (with foil sheath) frequency data.

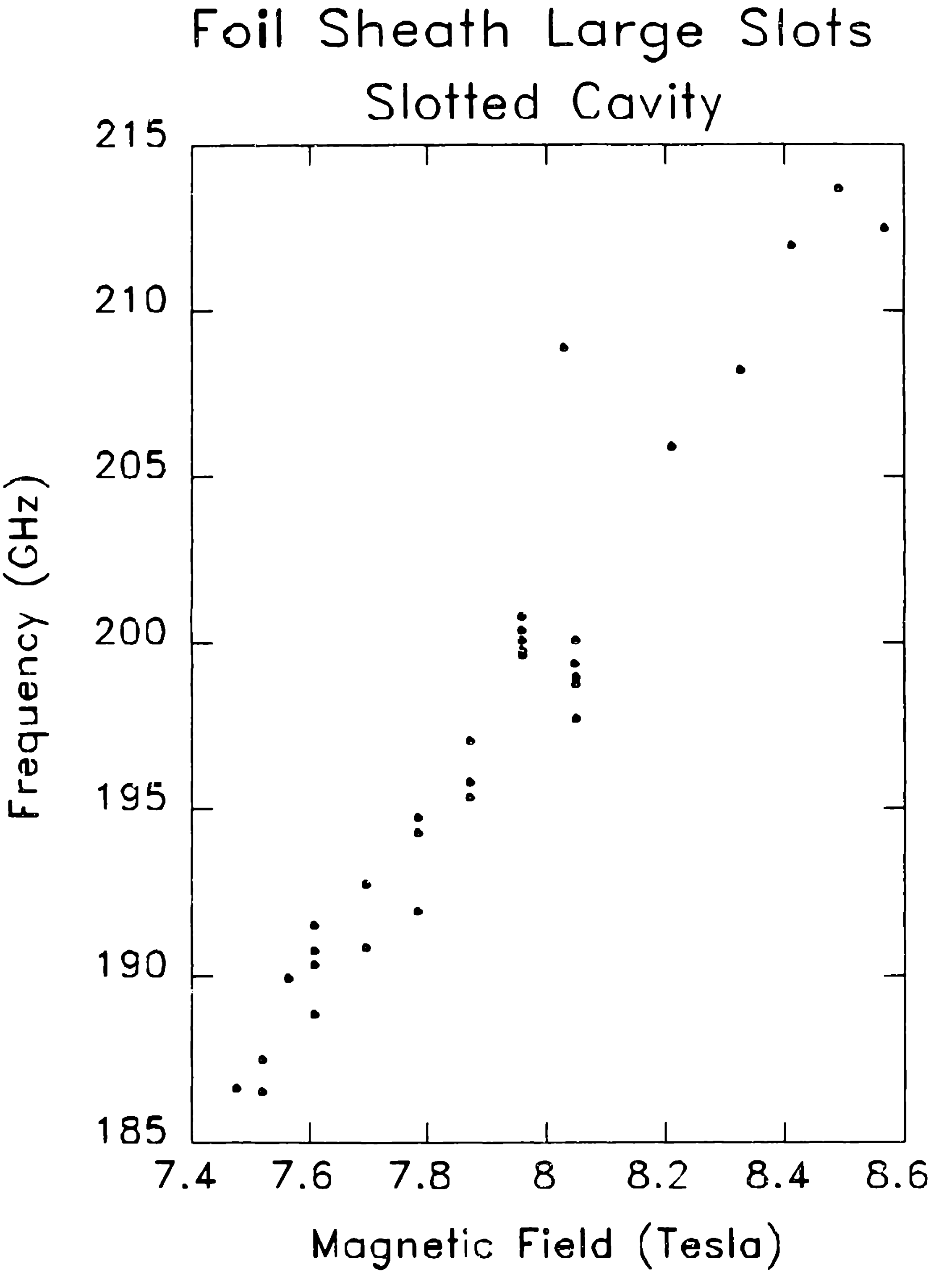

Figure 5.4.4b Expanded view of the large slots cavity (with foil sheath) frequency data.

pected that the harmonic modes were also leaking out of the slots. To reduce the second harmonic leakage, a foil sheath was wrapped around the outside of the straight section. Even with the foil sheath no second harmonic modes were observed. The absence of second harmonic modes may have resulted from the fact that cutting slots in the cavity wall can drastically reduce the Q of the cavity for the second harmonic modes and cause their starting currents to be very high. The foil sheath did have an interesting effect on the fundamental modes, since a higher density of modes was observed than would be predicted for a cavity without slots. The presence of a higher density of modes shows that the gyrotron has the potential to be developed as a tunable source for applications such as spectroscopy. The higher density of modes may be explained by two effects. First, when the foil sheath is used, the large slots cavity resembles a magnetron configuration, which has a higher density of modes than an unslotted cavity. Secondly, these frequencies could have been further changed by mode hopping and frequency pulling due to variation of the main magnetic field and pitch angle tuning.

CHAPTER 6

IRIS CAVITY EXPERIMENTS

In the previous experiments, high frequency second harmonic emission was not observed. The fundamental modes in these resonators succeeded in totally suppressing any second harmonic modes that might have been excited. Therefore, more powerful mode discrimination techniques are required. However it is instructive to briefly examine each of the earlier experiments first.

As discussed in Chapter 1, five techniques to suppress fundamental modes have been studied in this thesis. The first technique is based on the spacing of modes. In figure 4.0.1, one notes that the fundamental mode spectrum is uneven, and clumpings around certain frequencies or mode indices (ν_{mp}) tend to occur. In Chapter 4, a tapered resonator was designed with a second harmonic mode that existed in a frequency gap in the fundamental spectrum. Since a given mode is only excited over a limited region of magnetic field it was assumed that the frequency gap would translate into a magnetic field gap. However the predicted gap in magnetic field was not observed. The second technique involves placing the beam where coupling to the fundamental modes is weak. This technique combined with the first technique are not quite strong enough to fully suppress the fundamental modes as indicated by the experiment in Chapter 4 which used only these two techniques. Since the fundamental mode spectrum is denser at higher frequencies, it is difficult to find a beam position where coupling to the fundamental is sufficiently weak, so that it is possible to excite second harmonic modes. Another technique, is to use a higher value of perpendicular velocity, $\beta_\perp$. Operating at a higher cathode voltage, which increases the perpendicular velocity, $\beta_\perp$, improves the second harmonic to fundamental starting current ratio as shown in equation 6.1.4. The decrease in starting current at higher values of $\beta_\perp$ can be seen in the starting current data of this chapter (Figures 6.2.8a-c). However, since an existing 65 kV gun was used for this experiment, only a limited increase in $\beta_\perp$ was possible due to the upper limit on the cathode voltage.

The fourth mode suppression technique involves designing an electromagnetic structure where the fundamental is highly perturbed and the second harmonic is unperturbed or a structure with better feedback to the second harmonic than to the fundamental. To perturb fundamental modes, a slotted cavity configuration was tried, where axial slots were cut in the cavity wall. These slots were placed at positions corresponding to electric field minima of the second harmonic mode so as to selectively weaken the fundamental modes and leave the second harmonic modes relatively unperturbed. A small slots case and a large slots case were tried. The result of this technique for both cases was to weaken the fundamental modes but also to suppress the second harmonic modes, since the second harmonic modes were also perturbed by the slots.

In the cavities discussed in this chapter, the techniques mentioned above as well as a technique that involves actively reinforcing the second harmonic modes by enhancing the second harmonic diffractive Q and leaving the fundamental Q relatively unchanged, was used. By selectively reinforcing the second harmonic, and ensuring that it is excited first, we take advantage of the nonlinear perturbation of the beam which causes the starting currents of the neighboring second harmonic and fundamental modes to increase when a mode exists in the cavity (Dialetis (1983) Nusinovich (1977), Zarnitsina(1974)). In this manner, the problem is simplified from the tasks of suppressing the fundamental and reinforcing the harmonic mode to just the latter. To selectively raise the Q of only the second harmonic mode, an iris at the output end of the resonator was used. Another method of fundamental mode suppression, external feedback to enhance the second harmonic mode, was also used in the experiments. A motheye window which selectively increases the second harmonic diffractive Q of the system more than that of the fundamental was used to provide the external feedback.

In this chapter the iris theory will be developed. Two different iris resonators were designed. The experiments with iris cavities will be discussed after the theory section as well as the effect of the motheye window.

6.1 IRIS THEORY

The effect of the iris is to trap the second harmonic more effectively than the fundamental modes. Since gyrotrons operate near cutoff, even a very small iris ($\leq .0005in$) will extend below the cutoff radius. Extending an iris below the cutoff radius creates a region where the RF field is an evanescent wave. To facilitate a simpler analysis, a flat iris with an abrupt transition to the resonator region is considered as shown in Figure 6.1.1. The frequencies in both regions are assumed to be the same and $k_{\|}$ and $k_{\perp}$ are constant in each region. However, $k_{\|r} \neq k_{\|i}$ and $k_{\perp r} \neq k_{\perp i}$, where the subscript r refers to the resonator region and i to the iris region. A gaussian model for the cavity RF field varying as $e^{-k_{\|}^2 z^2}$ is assumed so that $k_{\|1r} \simeq k_{\|2r} \simeq 2/L_{eff}$ in the resonator region, L_{eff} being the effective axial length of the RF field in the cavity and the subscripts 1 and 2 represent the fundamental and second harmonic modes respectively. In the iris region the relation between $k_{\|}$ and $k_{\perp}$ is given by

$$k_{\|i}^2 = (\omega^2/c^2) - k_{\perp i}^2 \qquad 6.1.1$$

where $k_{\perp i} = \nu_{mp}/R_i$, and R_i is the radius of the iris region. Since $\omega_1 \simeq \frac{1}{2}\omega_2$ and $\nu_{mp1} \simeq \frac{1}{2}\nu_{mp2}$, we have $k_{\|i1}^2 \simeq \frac{1}{4}k_{\|i2}^2$. Therefore, the ratio of the second harmonic field amplitude, E_2, to that of the fundamental, E_1, in the iris region at axial distance z past the junction, is given by

$$\frac{E_2}{E_1} = \frac{e^{-ik_{\|2}^2 z^2}}{e^{-ik_{\|1}^2 z^2}} = e^{-\frac{3}{4}k_{\|i2}^2 z^2} \qquad 6.1.2$$

As an example, consider the design parameters for the first cavity listed in Table 6.2.1, where $k_{\|2} = 18/cm$. Then the ratio $E_2/E_1 = 0.55$ when $z = 0.05cm$. This is the distance that the iris extends below cutoff in the design of the first iris cavity.

The faster decay rate of the second harmonic modes result in their effective interaction length, L_{eff} being shortened more than the fundamental interaction length. Since the starting current $I_{st} \propto L_{eff}^{-4}$, the second harmonic starting currents increase with the smaller L_{eff}. The faster decay rate of the second harmonic also increases the iris's reflection coefficient more than that of the fundamental. The starting current is

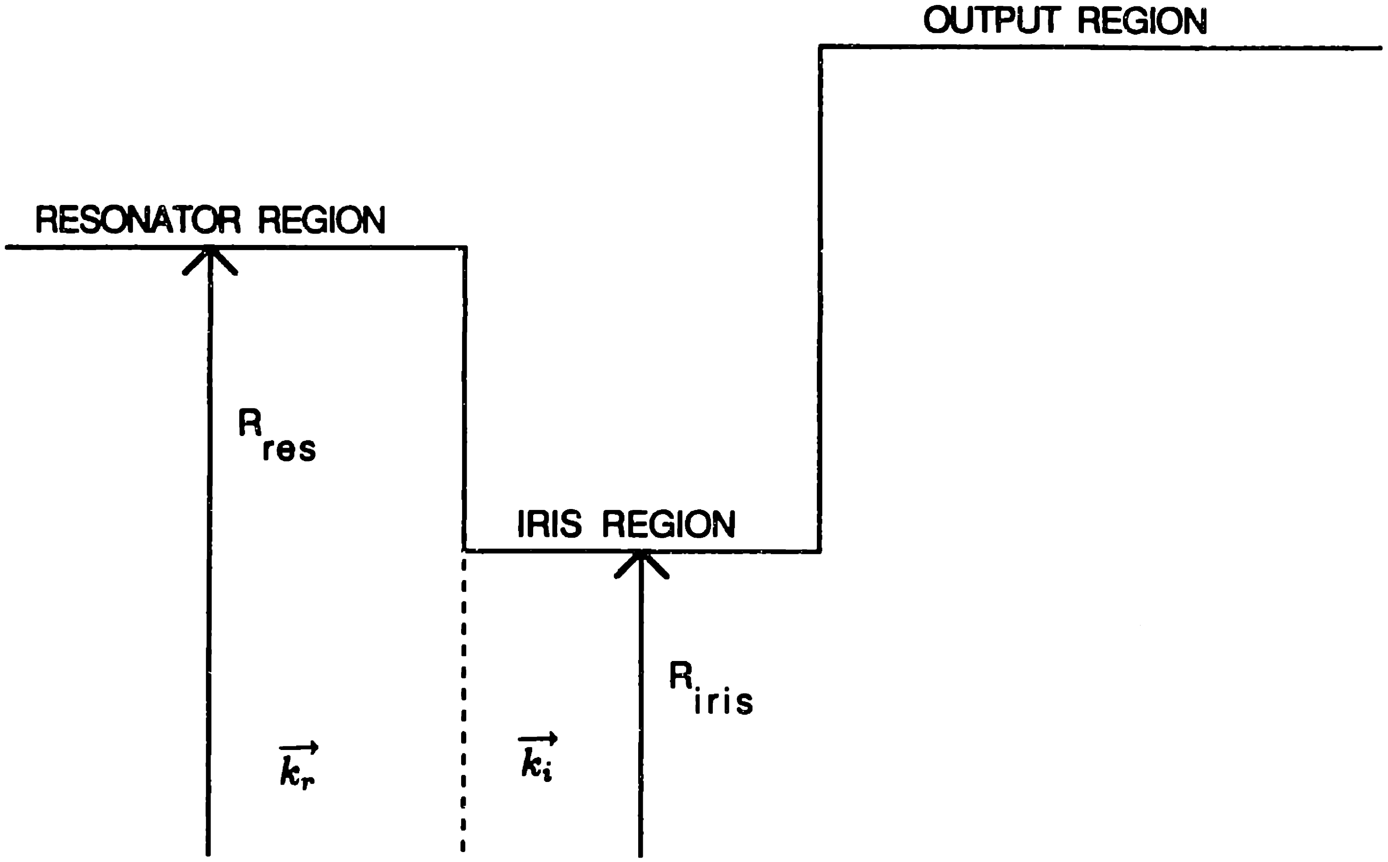

Figure 6.1.1 Schematic of a simplified resonator and iris system

inversely proportional to the total Q and the total Q increases with diffractive for values of the diffractive Q that are less than the ohmic Q, since the total Q is defined by

$$Q_T^{-1} = Q_D^{-1} + Q_{oh}^{-1} \qquad 6.1.3$$

where Q_T is the total Q, Q_D is the diffractive Q, and Q_{oh} is the ohmic Q. The diffractive Q is related to the reflection coefficient by $Q_D \propto L_{eff}^2/(1-|R|)$, where $|R|$ is approximately the reflection coefficient of the output end. The iris has a larger effect on the reflection coefficient than the effective length, as will be demonstrated below in the symmetric iris study, so the net effect is to decrease the second harmonic starting current more than that of the fundamental.

A study was conducted to determine the effect of iris shape on the ratio I_{st1}/I_{st2} and to ascertain whether if for a given diffractive Q of the second harmonic, an optimal design could be found. The ratio I_{st1}/I_{st2} is a measure of how strong the second harmonic can become before the fundamental mode is excited. To determine this ratio, numerical values are required for the diffractive Q and the effective interaction length as discussed in section 2.1, since

$$I_{st1}/I_{st2} \simeq \beta_\perp^2 \left(\frac{L_{eff2}}{L_{eff1}}\right)^2 \left(\frac{Q_{T2}}{Q_{T1}}\right) \qquad 6.1.4$$

where $\beta_\perp$ is a constant for this study, since it is unaffected by the cavity geometry. If one takes the optimum total Q ratio, $Q_{T2}/Q_{T1} = 9$ that was attained when the $TE_{13,2,1}$ was used as the second harmonic mode and the corresponding effective length ratio $L_{eff1}/L_{eff2} = 0.7$ with a typical value of $\beta_\perp = 0.38$ the starting current ratio $I_{st1}/I_{st2} = 0.93$. In comparison, if a no iris case is considered, where the same cavity dimensions and $\beta_\perp$ are used and the iris is just flattened, the total Q ratio $Q_{T2}/Q_{T1} = 3.79$, the effective length ratio $L_{eff1}/L_{eff2} = 0.78$ and the starting current ratio is $I_{st1}/I_{st2} = 0.34$. Therefore, the iris offers a definite improvement in the starting current ratio. These quantities are calculated with the code CAVRF (Fliflet (1981)) discussed in the linear theory section. This code can handle the case where the iris cuts off the RF mode at the output end of the interaction region, as long as the iris does not cause mode conversion.

A symmetric cavity design was adopted in order that the effect of the iris shape and size on the effective interaction length and the diffractive Q could be clearly determined and not be confused with an effect caused by the input taper. The second harmonic design mode, $TE_{13,2,1}$ and the strongest fundamental mode, the $TE_{5,2,1}$, were selected for this study. Since Q_D and L_{eff} depend on wavelength, rather than on the mode, any modes used would have yielded similar results. Figures 6.1.2a and 6.1.2b show the two cases that were analysed. By using two different types of symmetric iris geometries, stepped and pointy, the effects of output taper angle and iris length can be studied separately. To analyse the effect of the output taper angle, the pointy iris case, shown in Figure 6.1.2a, had a fixed inner angle, $\alpha_1 = 45°$ and the outer angle α_2 was varied keeping the iris depth, D_i, fixed. The outer angle scans were done for three different iris depths. In the stepped iris case, where the effects of the iris length (Figure 6.1.2b) were studied, the input and outer angles are fixed at $\alpha_1 = \alpha_2 = 45°$, and the iris length, L_i, was varied keeping the iris depth D_i fixed at the same values as before. As the shape was varied the effect on Q_D and L_{eff} was observed.

In the pointy iris case, shown in Figure 6.1.3a, the effective interaction length ratio, L_{eff2}/L_{eff1} varies slightly with outer angle, α_2, but not with iris depth, except for the smallest iris depth shown, 0.0051 cm, at angles below 10° where the effect of the output angle is stronger than the iris effect. When the outer taper angle is increased, the reflection coefficient at that junction increases decreasing the effective interaction length. Since the fundamental mode is less attenuated by the iris at that point the effect of the outer taper angle is stronger on the fundamental effective interaction length, causing an increase in the effective length ratio. For an optimum effective length ratio, an iris with a steep outer angle is desired. Figure 6.1.3b shows that the ratio of the fundamental and second harmonic L_{eff} does not vary significantly in the stepped iris case when the iris dimensions are varied. The optimum value of the pointy iris case is similar to that in the stepped iris case. The diffractive Q, however, is strongly effected by the iris dimensions. As the iris becomes a bigger potential barrier, by becoming thicker, deeper or having shallower inner or outer angles, the reflection coefficient increases more

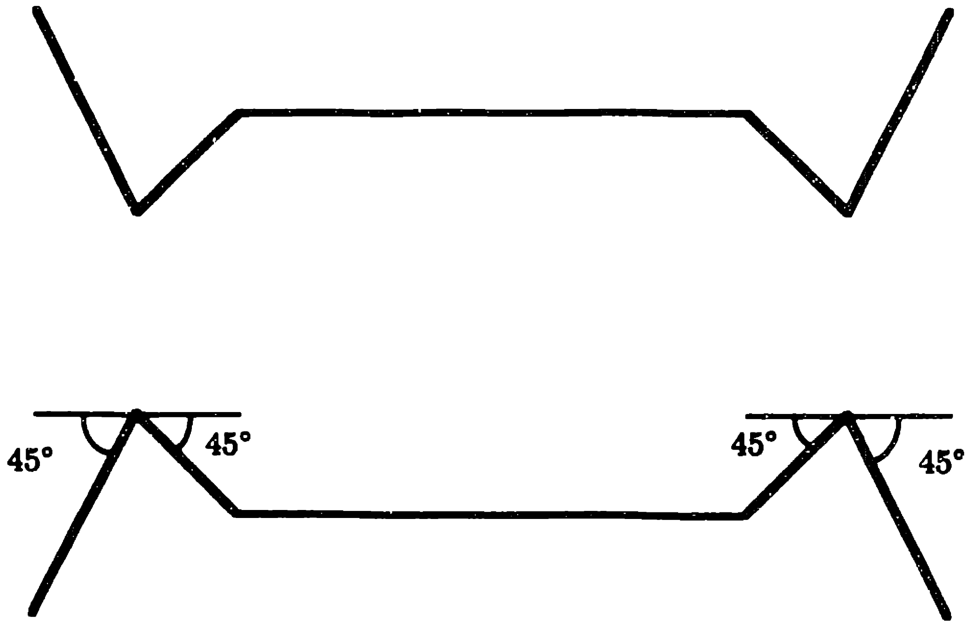

Figure 6.1.2a Schematic of the pointy iris resonator used in the symmetric iris study.

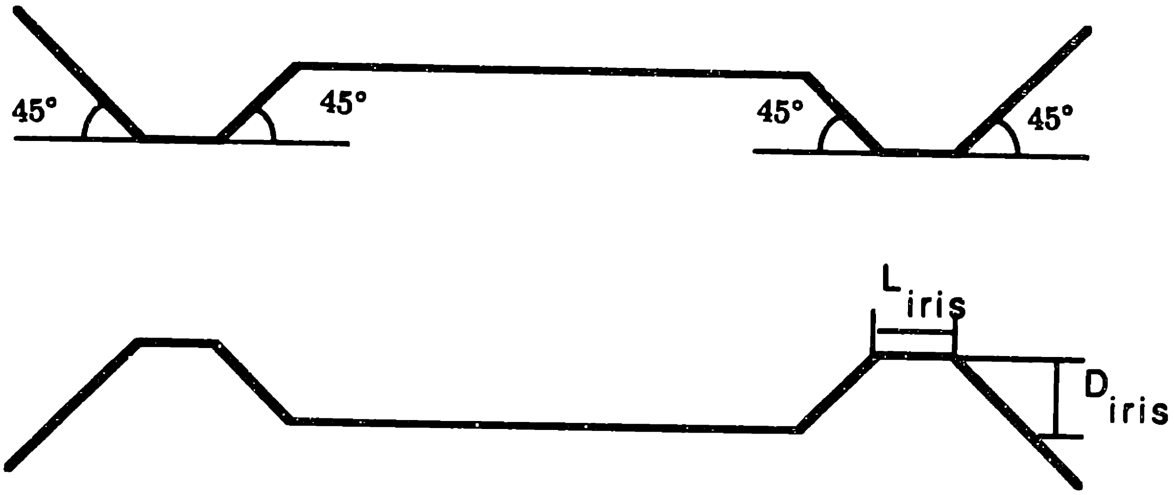

Figure 6.1.2b Schematic of the stepped iris resonator used in the symmetric iris study.

than L_{eff} decreases. Figures 6.1.4a and 6.1.4b show the diffractive Q's corresponding to different iris dimensions, with the higher values of Q_D corresponding to the deeper irises. In the pointy iris case, the diffractive Q decreases as the outer angle increases, and similarly, in the stepped iris case, the diffractive Q increases with iris length. For any given iris size and therefore second harmonic diffractive Q, we obtain an almost constant value of the fundamental Q_D as the shaping of the iris was varied from a pointy iris with a shallow outer angle to one with a steep angle or a stepped iris with long iris length to one with a short length. We conclude that the diffractive Q ratio is independent of iris shape and depends only on the iris size.

The graphs in Figures 6.1.4a and 6.1.4b show that one would like to operate at as high a second harmonic diffractive Q as possible to have the best diffractive Q ratio, Q_{D2}/Q_{D1}. However, since $I_{st} \propto 1/Q_T$, at high diffractive Q the total Q ratio saturates due to the effect of the ohmic Q. This leads to a saturation in I_{st} as a function of Q, when the value of the diffractive Q begins to approach that of the ohmic Q. The effect can be seen in Figures 6.1.5a and 6.1.5b, where at higher diffractive Q values the total Q ratio Q_{T2}/Q_{T1} peaks at a value near 10 and then starts decreasing. This optimum can be understood very simply. The ohmic Q represents the wall losses, which become significant when the stored energy increases. The degradation of the total Q ratio is gradual and for values of Q_D in the range $[0.5Q_{oh} - 1.5Q_{oh}]$ the total Q is close to the optimum value. This broad maximum shown in Figures 6.1.6a and 6.1.6b, which depict how the starting current ratio I_{st1}/I_{st2} varies with the iris dimensions for the pointy and the stepped symmetric iris cases.

The effect of the iris can be noticed by a comparison with a symmetric cavity without an iris also shown in Figure 6.1.5a. This case corresponded to a pointy iris case where the iris depth was reduced to zero, and the outer taper angle α_2 was varied. At steeper angles, where the reflection coefficient is larger, the total Q ratio saturated at a value of 4.5. Since at steep output angles the reflection coefficient saturates, the straight section was lengthened to produce a result with a second harmonic diffractive Q above 1000. However, even with a longer straight section, the value of the starting current

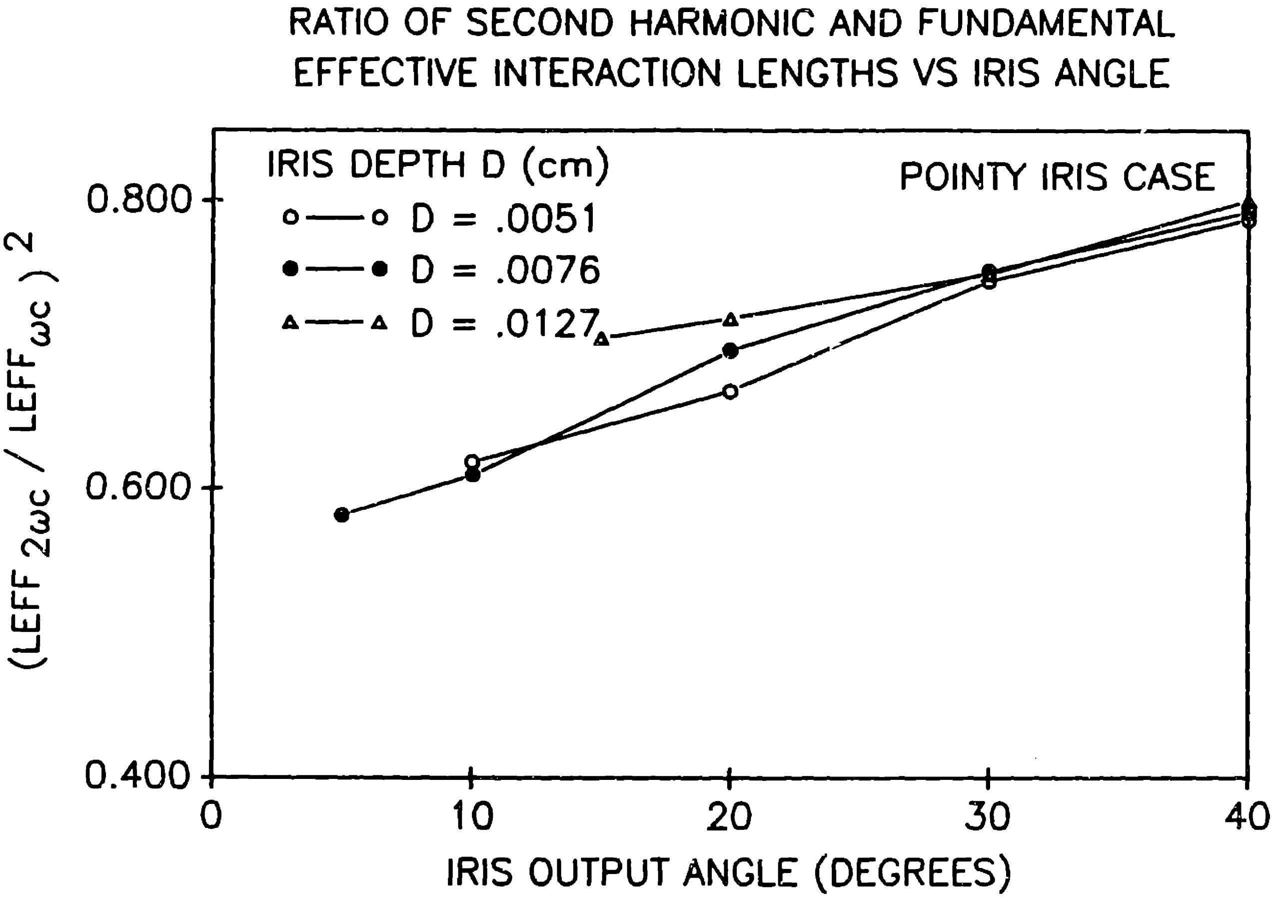

Figure 6.1.3a Ratio of the second harmonic to the fundamental effective interaction lengths as functions of angle α_2 for the pointy iris case of the symmetric iris cavity.

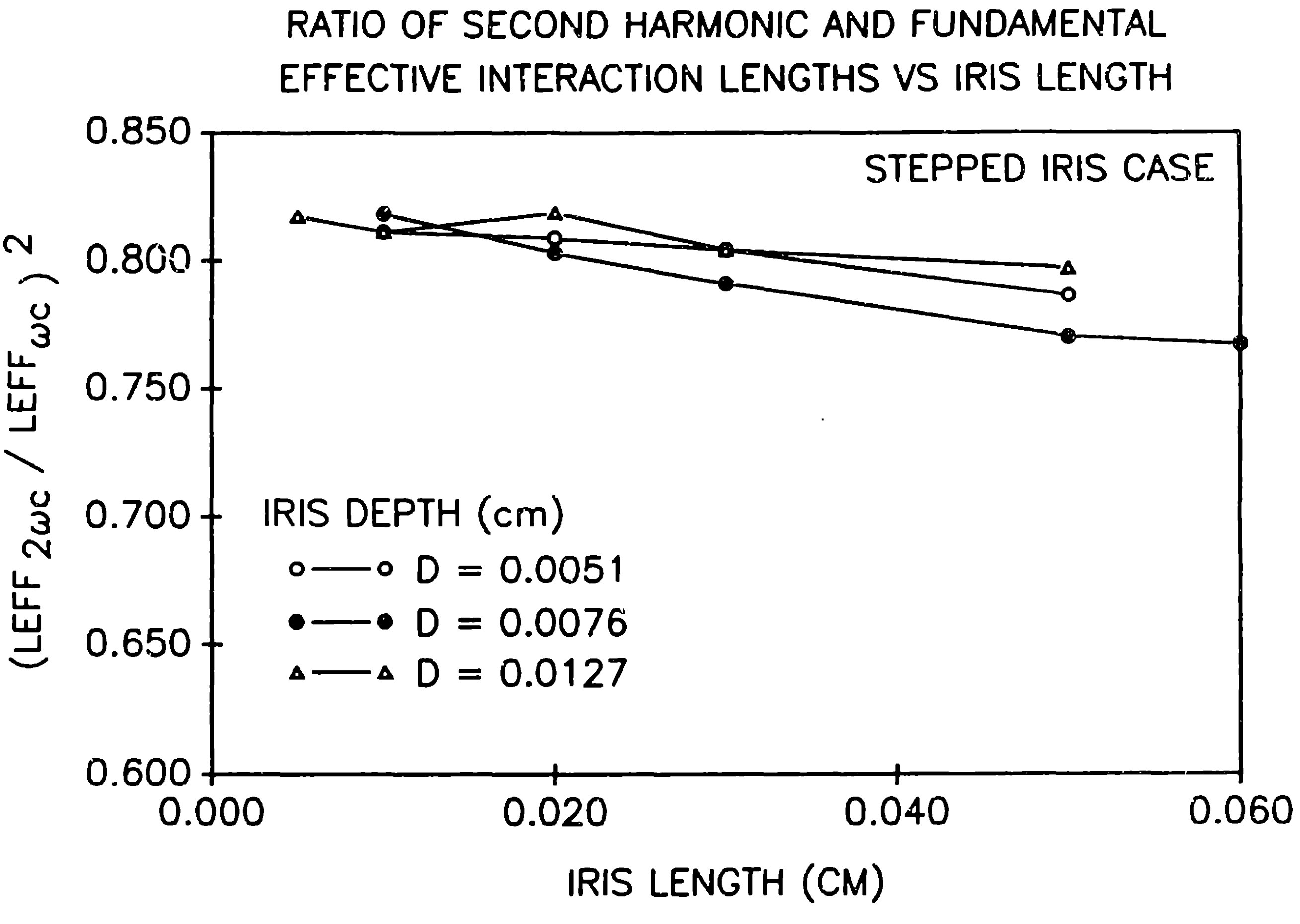

Figure 6.1.3b Ratio of the second harmonic to the fundamental effective interaction lengths as functions of iris length for the stepped iris case of the symmetric study.

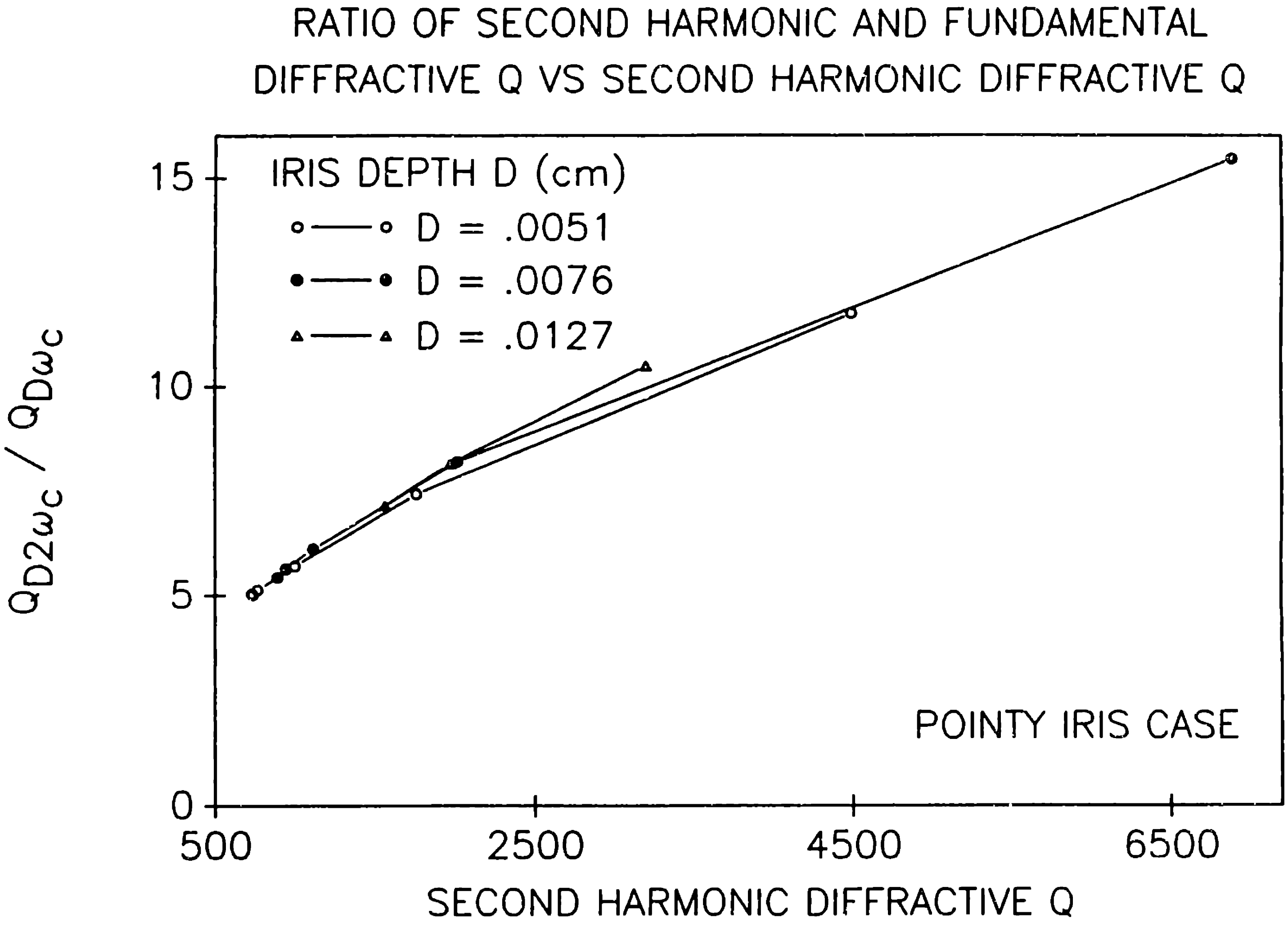

Figure 6.1.4a Ratio of the second harmonic to the fundamental diffractive Q as a function of second harmonic diffractive Q for the pointy iris case of the symmetric iris study. The higher Q values correspond to the shallower output taper angles.

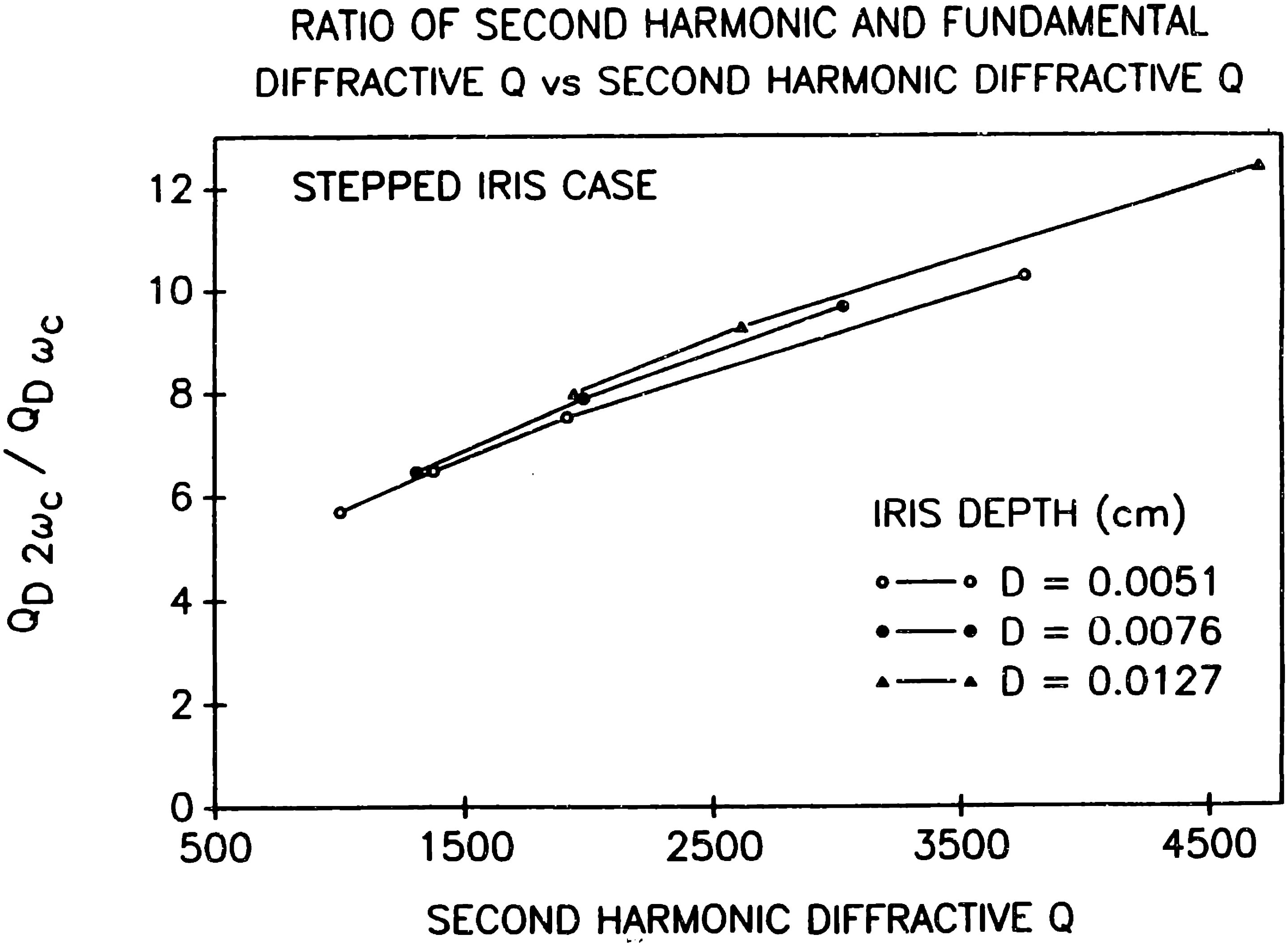

Figure 6.1.4b Ratio of the second harmonic to the fundamental diffractive Q as a function of second harmonic diffractive Q for the stepped iris case of the symmetric iris study. The higher Q values correspond to longer iris lengths.

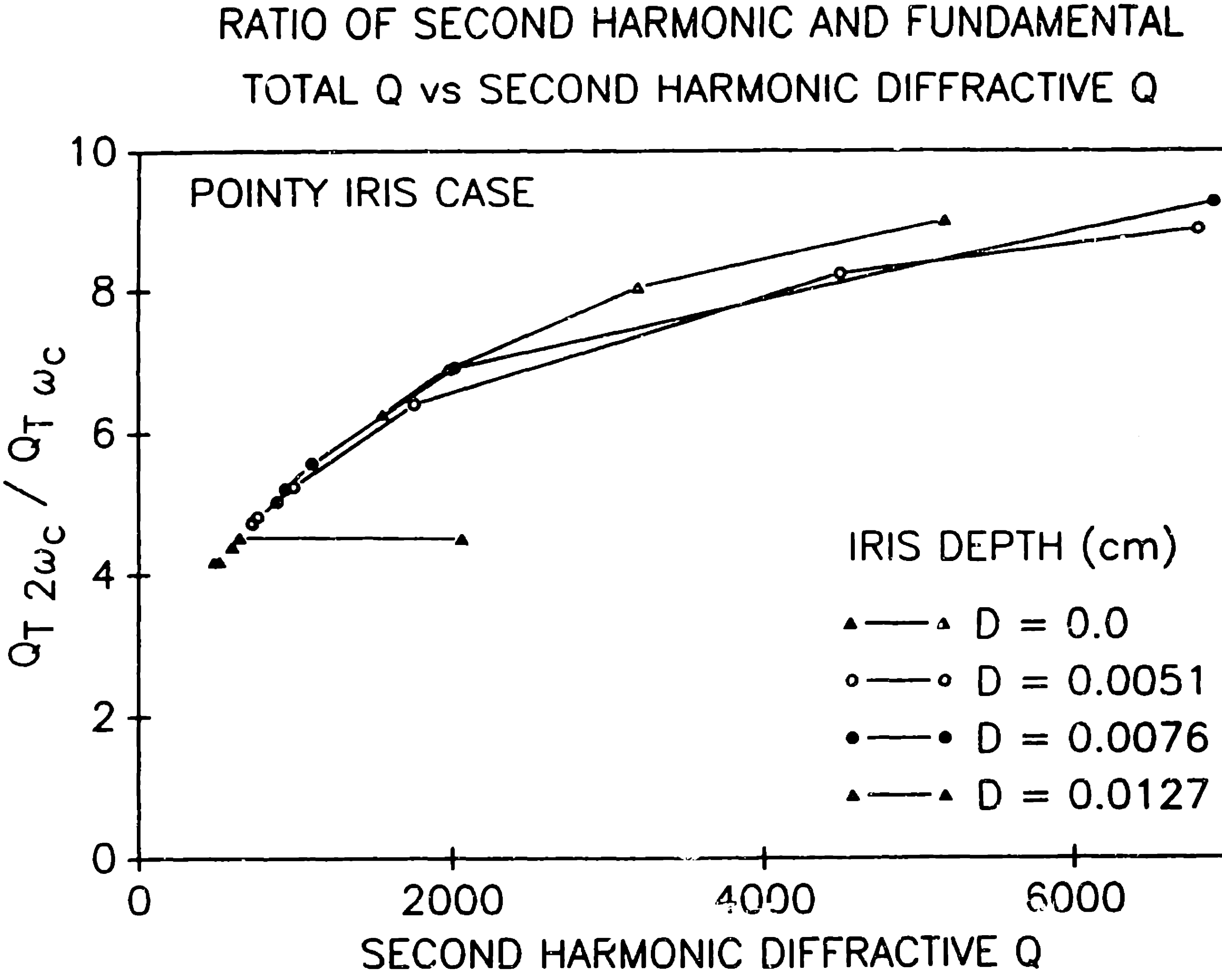

Figure 6.1.5a Ratio of the second harmonic to fundamental total Q as a function of second harmonic diffractive Q for the pointy iris case of the symmetric iris study.

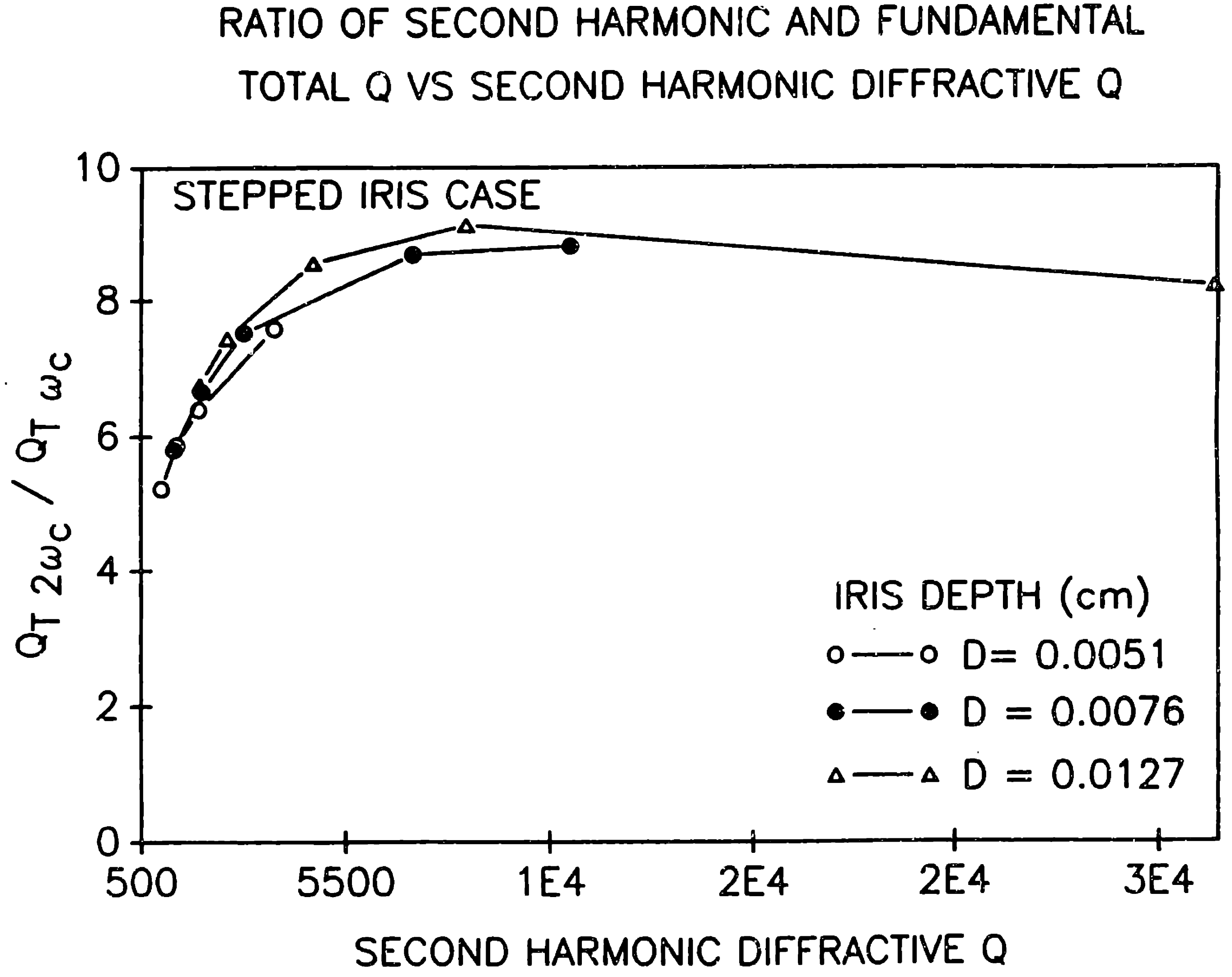

Figure 6.1.5b Ratio of the fundamental to second harmonic total Q as a function of the second harmonic diffractive Q for the stepped iris case of the symmetric iris study.

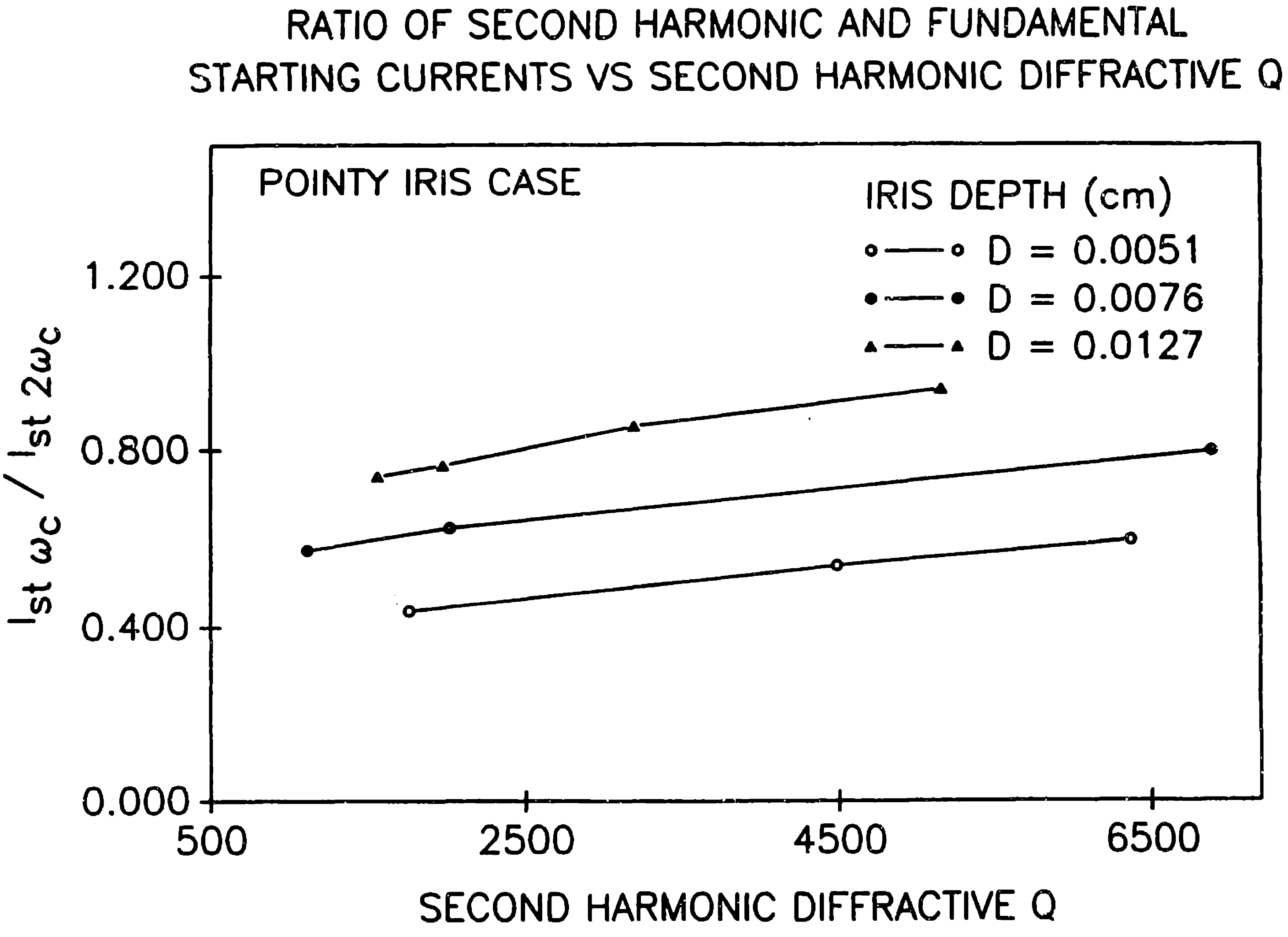

Figure 6.1.6a Fundamental to second harmonic starting current as a function of second harmonic diffractive Q for the pointy iris case of the symmetric iris study.

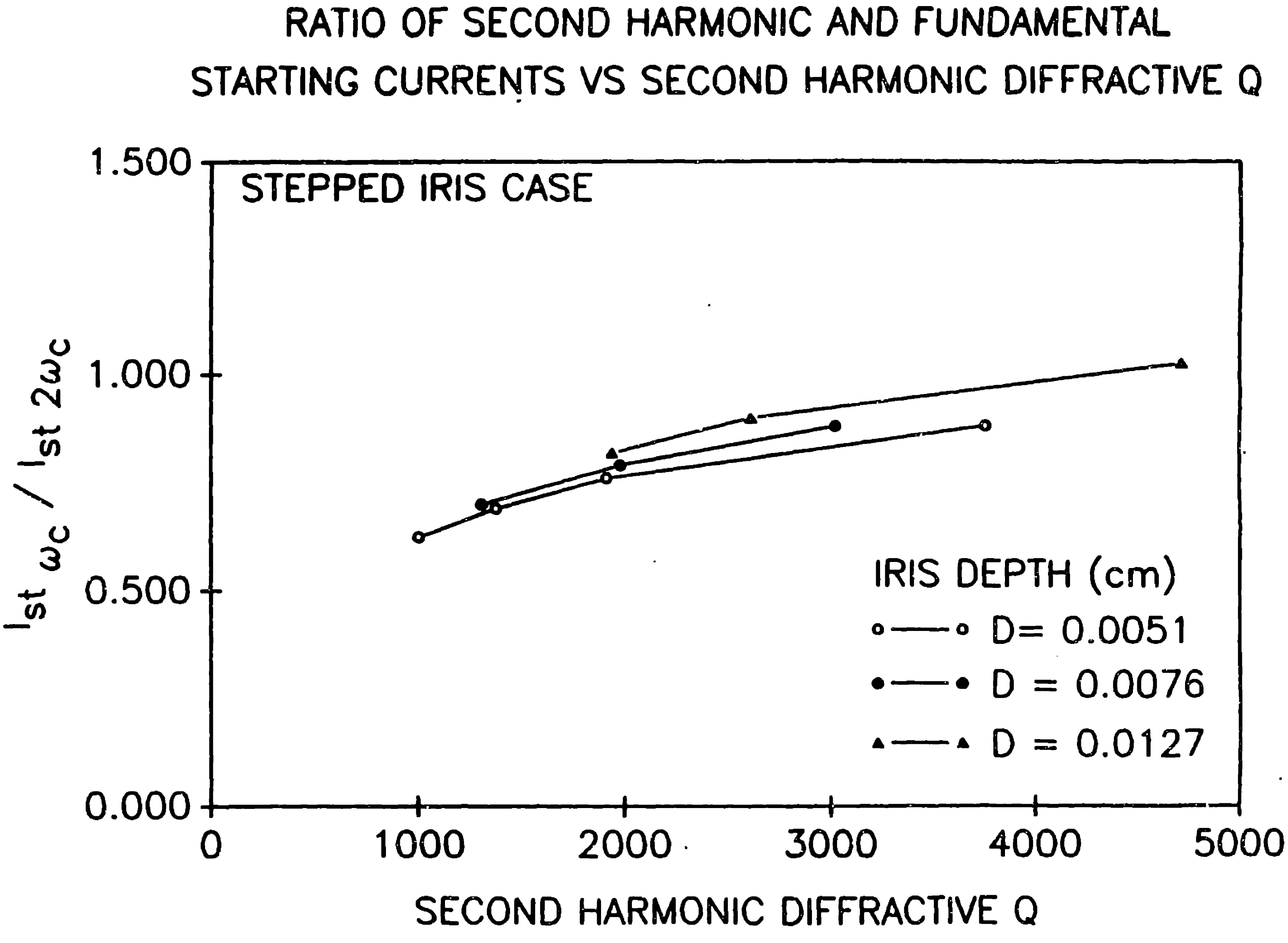

Figure 6.1.6b Ratio of the fundamental to the second harmonic starting currents as a function of the second harmonic diffractive Q for the stepped iris case of the symmetric iris study.

ratio did not increase. If the simple diffraction theory is used, and the minimum Q is used, the total Q is given by $Q_T \simeq Q_{Dmin} = 4\pi(L_{eff}/\lambda)^2$, and therefore $Q_{T2}/Q_{T1} \simeq 4$, which is close to the saturation value for the no iris case. Hence the saturation value of the total Q ratio and therefore the starting current ratio is improved by the iris.

If the optimum value for the total Q ratio is to be increased, a mode with a higher ohmic Q is needed. In Table 6.1.1 are listed the ohmic Q values for second harmonic modes close to the $TE_{13,2,1}$. The frequencies used in calculating the ohmic Q values correspond to the dimensions of the first iris cavity listed in Table 6.2.1. As can be seen in Table 6.1.1, ohmic Q values increase with the axial index, p. We now turn to the question of higher p modes. The starting current is influenced by the coupling coefficient of the mode, $J^2_{m\pm n}(k_\perp R_e)/J^2_m(\nu_{mp})(\nu^2_{mp} - m^2)$. When considered as a function of beam radius it is found that the optimal coupling coefficient occurs on the innermost radial maximum of the mode. Since the beam position determines the maximum value of m, the value of p is increased by operating with a higher mode index, ν_{mp}. However when the mode index is increased, mode competition problems become worse. For example, the $TE_{13,4,1}$ mode at 400 GHz is possible with the existing gun, but for this mode $\nu_{mp} = 27.48$ and the mode density increases with ν_{mp} leading to more severe mode competition problems. Therefore modes with $p > 3$ were not considered. The p=3 modes are only accessible due to beam spread and misalignment effects. Therefore we look for a mode with p = 2 or 3. The p = 3 mode has a slight advantage over a p = 2 mode due to the higher ohmic Q. This can be seen in Figure 6.1.7, where the starting current ratio is plotted as a function of diffractive Q for one p=2 mode and two p=3 modes. Two p=3 modes were selected in order to show that the result was not specific to a particular p=3 mode. Since the diffractive Q ratio is independent of iris shape, we only show the results for the stepped iris case where the effective length ratio had the optimum value for any iris length or depth. The 0.0127 cm deep iris was chosen, and the starting current ratio is plotted as a function of second harmonic diffractive Q which is a monotonically increasing function of iris length. Due to higher ohmic Q values the $TE_{10,3,1}$ and $TE_{12,3,1}$ are seen to saturate at a starting current ratio of

1.3, which is somewhat higher than the the saturation value for the $TE_{13,2,1}$, for which $I_{st1}/I_{st2} = 1.0$.

The upper limit on diffractive Q is also limited by ohmic efficiency considerations. If Q_D is too high the ohmic efficiency will decrease and thus significantly lower the total efficiency. This degradation of the total efficiency can be seen in Figure 6.1.8, which shows the total efficiency as a function of diffractive Q for a $\beta_\perp/\beta_\parallel = 1.5$, with the cavity radius and effective interaction length calculated from the dimensions of the first iris cavity. The value of the interaction length, and therefore μ, is assumed to fixed since $\mu = \pi(\beta_\perp^2/\beta_\parallel)L_{eff}/\lambda$. As the diffractive Q increases, the perpendicular efficiency increases due to increasing RF field amplitude, but this increase is slowed by the decrease in ohmic efficiency. This leads to an almost constant total efficiency for a wide range of diffractive Q. A similar efficiency calculation was also done for the $TE_{10,3,1}$ mode and a similar total efficiency result was obtained with a 1% higher maximum total efficiency of 19.4 %. Again, operating with a p=3 mode has a slight advantage over a p=2 mode.

The diffractive Q is constrained by the length of the straight section, too. By shortening the straight section of the cavity, for a fixed value of diffractive Q, the starting currents of both the second harmonic and fundamental modes are increased due to the fact that $I_{st} \propto L_{eff}^{-2}$. Therefore, a shorter effective length can compensate for a high diffractive Q and prevent the fundamental starting current from having an excessively low value ($\leq$ 1.0 A). If higher fundamental diffractive Q values are tolerable, one can operate with a larger iris which creates a higher second harmonic diffractive Q and thus a higher diffractive Q ratio, Q_{D2}/Q_{D1}. Having a low fundamental starting current, can still allow the second harmonic to be excited first if the resonator has a good Q ratio. However, high power regions, which correspond to higher beam currents, could become unattainable due to accessibility problems from the startup of each shot or mode suppression problems. The fundamental interaction has stronger beam-RF coupling than the second harmonic, and after the fundamental does get excited it can grows strong enough to suppress the harmonic mode. In addition, studies of fundamental mode competition have shown that mode competition increases as the ratio of the operating

TABLE 6.1.1

Ohmic Q Values for the Design Mode and Neighboring Second Harmonic Modes

Frequency (GHz)	Ohmic Q	TE Mode
415.9	3522	$TE_{18,1,1}$
410.5	9200	$TE_{13,2,1}$
417.3	12209	$TE_{10,3,1}$
411.7	14076	$TE_{7,4,1}$

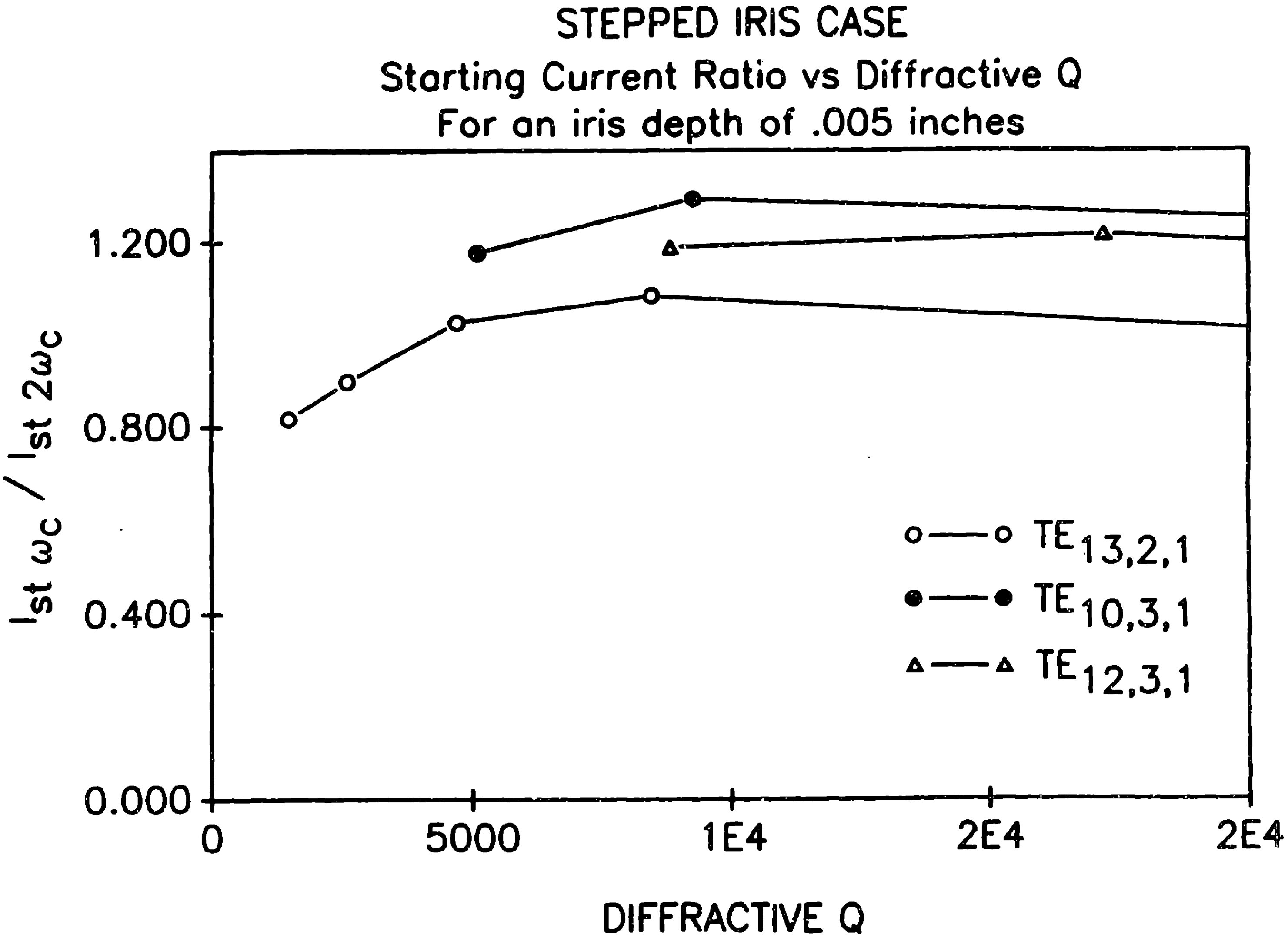

Figure 6.1.7 Ratio of the fundamental to the second harmonic starting currents as a function of diffractive Q for several second harmonic modes using the stepped iris case with a 0.0127 *cm* deep iris of the symmetric iris study.

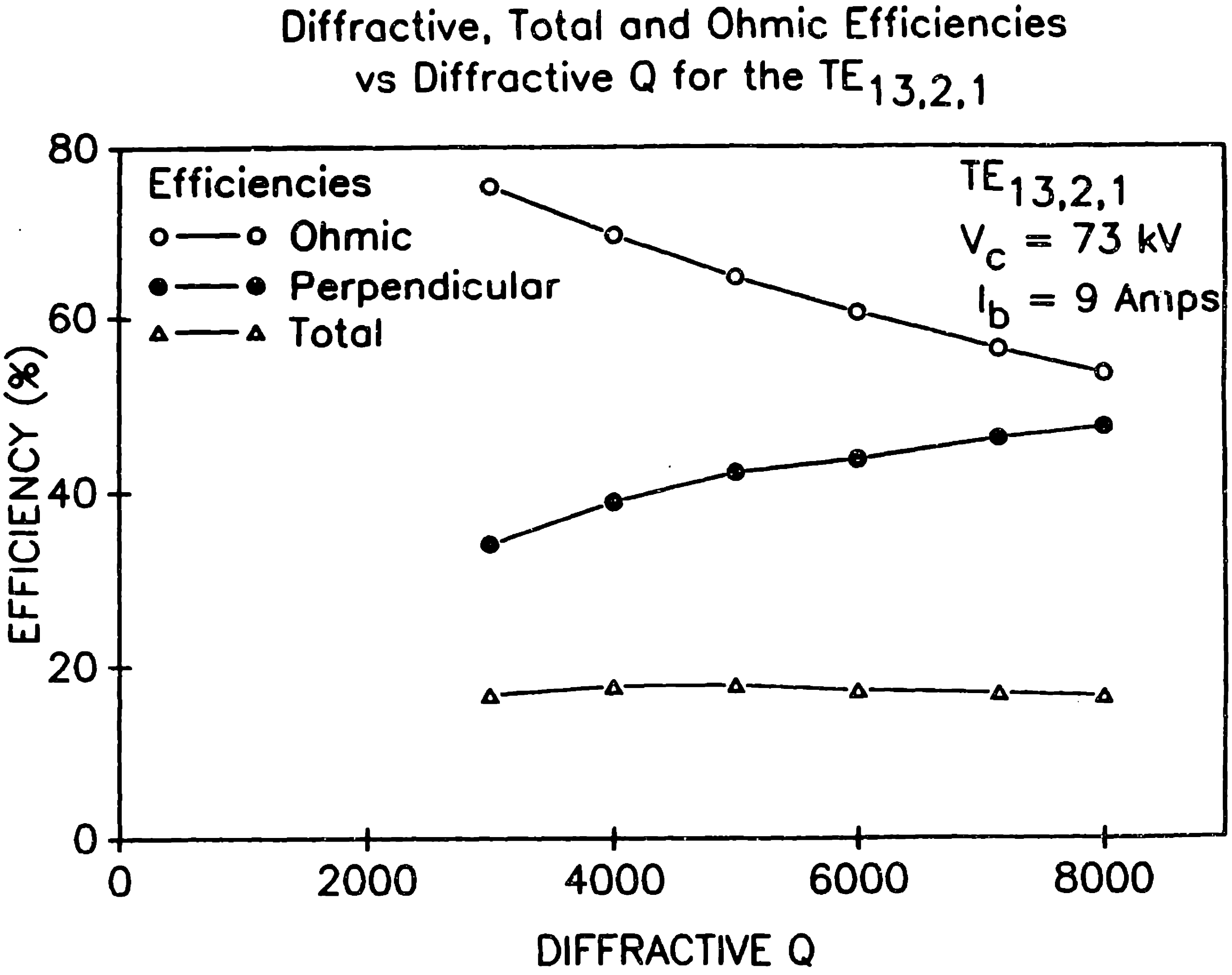

Figure 6.1.8 Efficiency as a function of second harmonic diffractive Q for a fixed value of μ.

beam current to starting current, I_{op}/I_{st} increases (Dumbrajs (1988)). A compromise must be made in increasing the fundamental starting currents (by decreasing L_{eff}) and keeping the the effective interaction length (and μ) long enough to access the high efficiency regions. In Figure 2.3.1, which shows the regions of isoefficiency as a function of normalized RF field strength, F, and normalized effective interaction length, μ, one can see that if L_{eff} and consequently μ is not big enough, as F is increased the maximum perpendicular efficiency attained can be as low as 10 %. So when designing a cavity, one wants the highest Q_{D2} consistent with good ohmic efficiency, a cavity length long enough to access the high power regions, and fundamental starting currents that are not excessively low.

These principles will be used when designing the two resonators discussed in this chapter, the high Q and the low Q iris cavities. The high Q iris cavity was designed with a high diffractive Q to produce a high diffractive Q ratio and therefore improve the starting current ratio. The low Q cavity was designed with a lower diffractive Q ratio, so that the ohmic losses would not be so severe.

6.2 HIGH Q IRIS RESONATOR EXPERIMENTS

The decision to use an existing electron gun imposed a number of constraints on the system. As discussed in Chapter 4, the existing gun has a beam position, $k_\perp R_e \simeq 13.0$ for operation at 400 GHz with a main field around 8 Tesla. The other system constraints are a maximum beam current of 10 Amps at a cathode voltage of 65 kV with a pulselength of 1 - 2 μsec and $\beta_\perp/\beta_\parallel = 1.5$.

Two main criteria were used to select the design mode, strong beam-RF interaction and weak surrounding fundamental modes. The $TE_{13,2,1}$ satisfied the weak surrounding fundamental modes criteria and the beam could be placed at the innermost (and biggest) maximum of the coupling coefficient which corresponded to a beam position, $k_\perp R_e$, of 12.8. The $TE_{13,2,1}$ was chosen because the beam position that maximized the coupling for the $TE_{13,2,1}$ produced low coupling coefficients for $TE_{5,2,1}$ and the $TE_{4,2,1}$, which are the dominant fundamental modes of the system (assuming a thin beam). However, since the electron beam is not thin in practise and misalignment does occur, coupling to the fundamental p=2 modes was rather strong, and as a result the second harmonic p=3 modes which have a slight starting current and efficiency advantage turned out to be the strongest modes of the system.

As discussed in Chapter 4, selecting a mode specifies the cavity radius. Next the cavity length and iris dimensions must be chosen. The determination of iris dimensions and cavity length is governed by the tradeoff between a high starting current ratio, I_{st1}/I_{st2} and high perpendicular and ohmic efficiencies. In this experiment, to ensure that the fundamental mode was not excited too easily, the theoretical starting current of the strongest fundamental mode was required to be above 1 A. When determining the cavity length and iris dimensions only a rough estimate is needed for the input and output tapers, since the effect of changing these dimensions is smaller than that of changing the iris or cavity length. The exact design of the input and output tapers can be designed after the optimization of the cavity length. The tapers must have shallow angles ($\leq 5^\circ$) to minimize mode conversion problems.

The input taper has to be designed so that less than 5% of the second harmonic mode's RF power leaks back toward the gun. This condition is achieved when the front section of the input taper is near or at cutoff for the second harmonic mode. The power leakage was determined by running CAVRF for two cases. The first corresponded to the actual cavity design, with the input taper not at cutoff, and yielded the diffractive Q corresponding to where the mode is not cutoff at the input taper, which we denote by Q_{nc}. Since the mode is not cutoff at the input, we have power diffracting out from the input end back towards the gun, P_{inp}, and power from the output end forward towards the window, P_{out}, and we can write $Q_{nc} \propto \frac{1}{P_{inp}+P_{out}}$. The second case used the same design, except that the input taper had been modified so that the mode was cutoff at the input end. In the cutoff case the diffractive Q, Q_{cut}, is higher, because power is only leaking out from the output end and $Q_{cut} \propto \frac{1}{P_{out}}$. Excessive power leakage from the cavity can damage the gun. However the input taper must be made short enough so that the undesirable higher order axial modes are not cutoff, but are weakened by big leakage losses. After the tapers are optimized, the length and iris dimensions are modified if necessary. Several iterations of optimizing the length and iris and then the tapers may be necessary in order to find the best design.

Table 6.2.1 lists the design parameters for a 100 kW, 410 GHz second harmonic gyrotron operating in the $TE_{13,2,1}$ mode. The resonator was required to produce 100 kW to demonstrate high power operation. The iris was constrained in two ways. The first constraint was that the minimum iris depth was 0.0051 cm, which was the smallest depth the machinist would guarantee. As mentioned earlier, the output taper angle must be 5° or less to avoid mode competition problems. A 0.0051 iris was the deepest iris that would not produce a fundamental starting current that was too low and create severe ohmic losses due to a second harmonic diffractive Q that was too high. A 5° output taper was chosen to make the second harmonic diffractive Q as low as possible and to have as large an effective length ratio as possible, since that ratio increases with output taper angle. A pointy iris configuration was used, since at this point it was thought that 0.0051 cm was the minimum iris depth that could be reliably machined, therefore a short stepped iris would have resulted in a low ohmic efficiency caused by a high diffractive Q. The straight section length was shortened to a length of 0.526 cm, which was the minimum length that theoretically produced 100 kW at 65 kV and 9 Amps. The design current was chosen to be 9 A, since this is the highest current that the gun can be expected to reliably produce. As a result of the second harmonic diffractive Q being very high, the ohmic efficiency has now been reduced to 56.4%. The magnetic field of 8.3 T corresponds to the minimum starting current. In Figure 6.2.1 we show a schematic of the resonators actual dimensions and the RF field profiles of the $TE_{13,2,1}$ and the $TE_{5,2,1}$, which is the strongest fundamental mode. In the diagram it can be seen that the second harmonic mode, represented by the broken line is more trapped than the fundamental mode. The iris contains a 0.0025 cm flat section, because a sharper point could not be reasonably machined.

Figures 6.2.2 a and b show the effect of the iris on fundamental starting currents where no beam spread effects were assumed. The $TE_{4,2,1}$ and the $TE_{5,2,1}$ are the

TABLE 6.2.1

OUTPUT IRIS CAVITY DESIGN PARAMETERS FOR THE HIGH Q RESONATOR

Second Harmonic

Frequency = 410 GHz

Beam Current = 9 Amps

Power = 101 kW

η_T = 17.3 %

Magnetic Field = 8.3 Tesla

Magnetic Field at the Gun = 0.221 Tesla

Cathode Voltage = 65 kV

$\eta_\perp$ = 49.4 %

η_{OH} = 53.7 %

η_{el} = 65.3%

Cavity Radius = 0.2316 cm

$Q_{D2\omega c}$ = 7946

$Q_{D\omega c}$ = 779 ($TE_{5,2,1}$)

$Q_{OH2\omega c}$ = 9200

$Q_{OH\omega c}$ = 9059 ($TE_{5,2,1}$)

$Q_{T2\omega c}$ = 4263

$Q_{T\omega c}$ = 717 ($TE_{5,2,1}$)

$L_{eff2\omega c}$ = 0.537 cm

$L_{eff\omega c}$ = 0.647 cm ($TE_{5,2,1}$)

$I_{ST2\omega c}$ = 1.60 Amps

$I_{ST\omega c}$ = 1.59 Amps ($TE_{5,2,1}$)

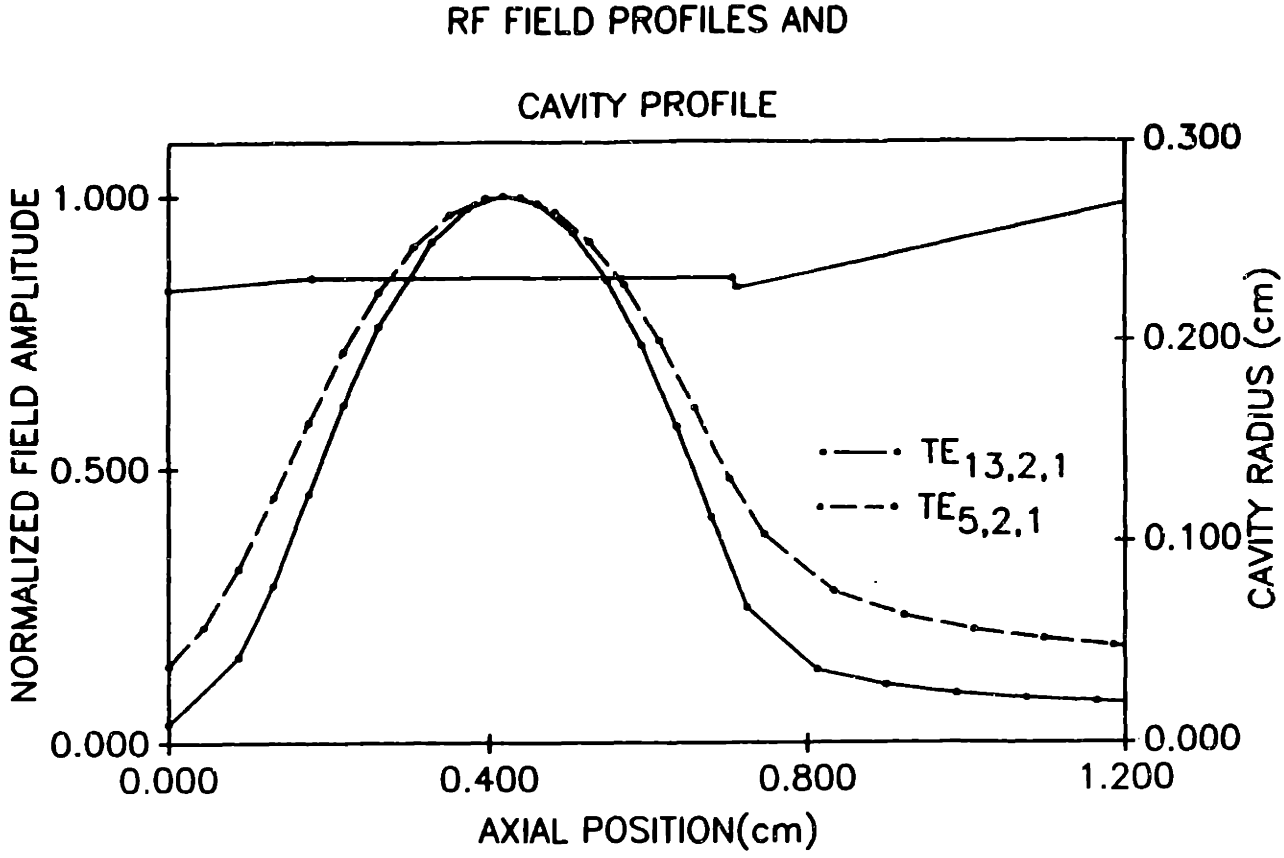

Figure 6.2.1 RF field profiles for the fundamental $TE_{5,2,1}$ mode and the second harmonic $TE_{13,2,1}$ mode as a function of axial position for the high Q output iris cavity.

strongest fundamental modes near the design mode for this resonator radius. Four cases of starting current as a function of magnetic field were calculated. The first two cases used the actual dimensions of the cavity with and without beam spread. Next a resonator without an iris was used to calculate the starting current with and without beam spread effects. The same cavity dimensions were used for the case without the iris where the iris was flattened creating a slightly longer flat section. The beam spread effects were approximated by averaging the term $J_{m\pm n}(k_\perp R_e)^2$ in the coupling coefficient over the width of the beam thickness. The theoretically calculated beam spread (Felch (1982)) is 2 Larmor radii at the magnetic field that the cavity is designed to operate at, 8.3 T for the gun used in this experiment. The beam spread effects result in a 5 % increase in the starting current ratio, I_{st1}/I_{st2} whereas the presence of the iris decreases ratio by a factor of 1.8 to become unity with no beam spread. The starting current ratio was calculated using the minima of the fundamental and second harmonic starting currents. At the magnetic field corresponding to the minimum second harmonic starting current the fundamental will have a higher starting current and the second harmonic mode will get excited first assuming that beam spread effects do not lower the starting current too much. This method of approximating beam spread effects may be an underestimate for the variation of starting current, since misalignment has not been taken into account. The tube can be aligned to within 0.0127 cm at the resonator, which implies that an error of 1.4 r_L (Larmor radii) is possible.

RESULTS

Initially the experiment was run with a cathode voltage of 65 kV. However, when the voltage was increased to 73 kV the harmonic modes became stronger. This can be understood as follows. As the cathode voltage increases, the perpendicular velocity, $\beta_\perp$ increases. A larger $\beta_\perp$ results in higher efficiency and a larger fundamental to second harmonic starting current ratio. The second harmonic modes also became stronger when the mod anode voltage was decreased. This may be a result of the fact that in practice the gun is nonadiabatic and tends to be very sensitive to mod anode voltage. Since

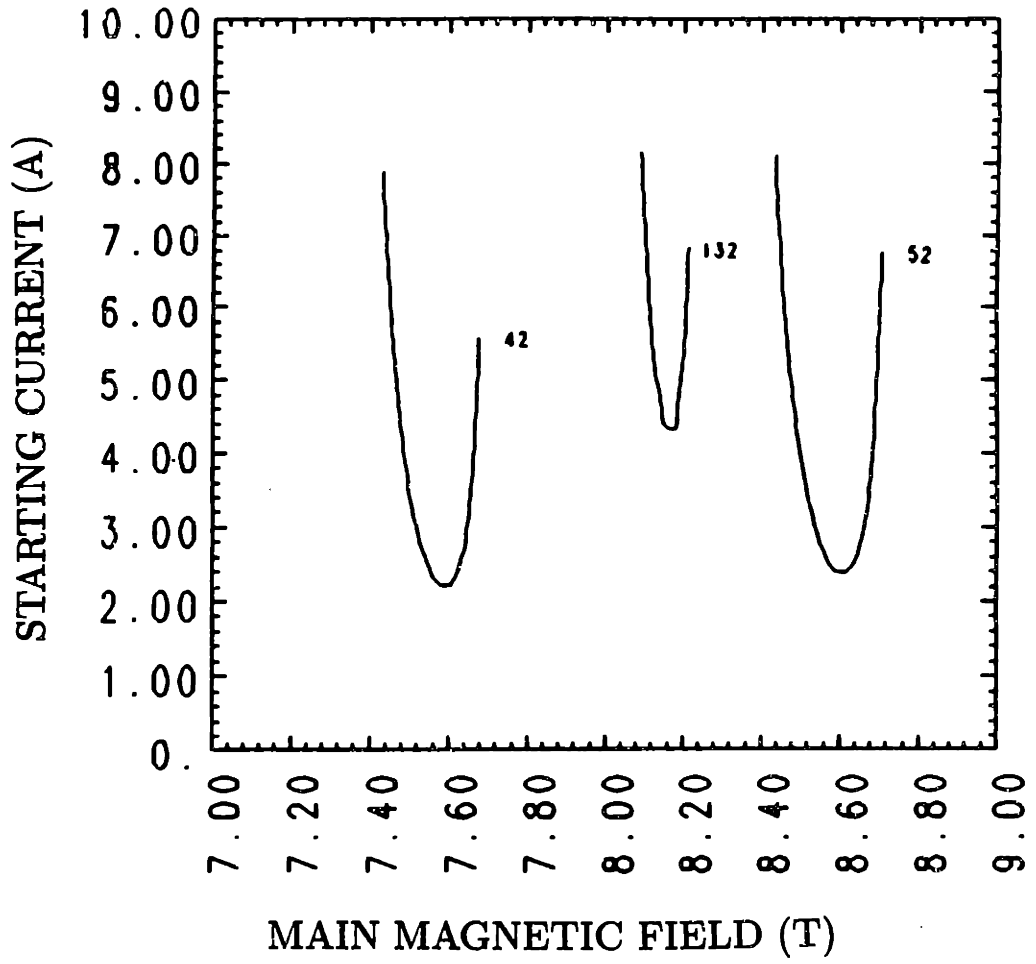

Figure 6.2.2a Starting currents for the second harmonic mode and the two strongest fundamental modes. (No iris case with no beam spread.)

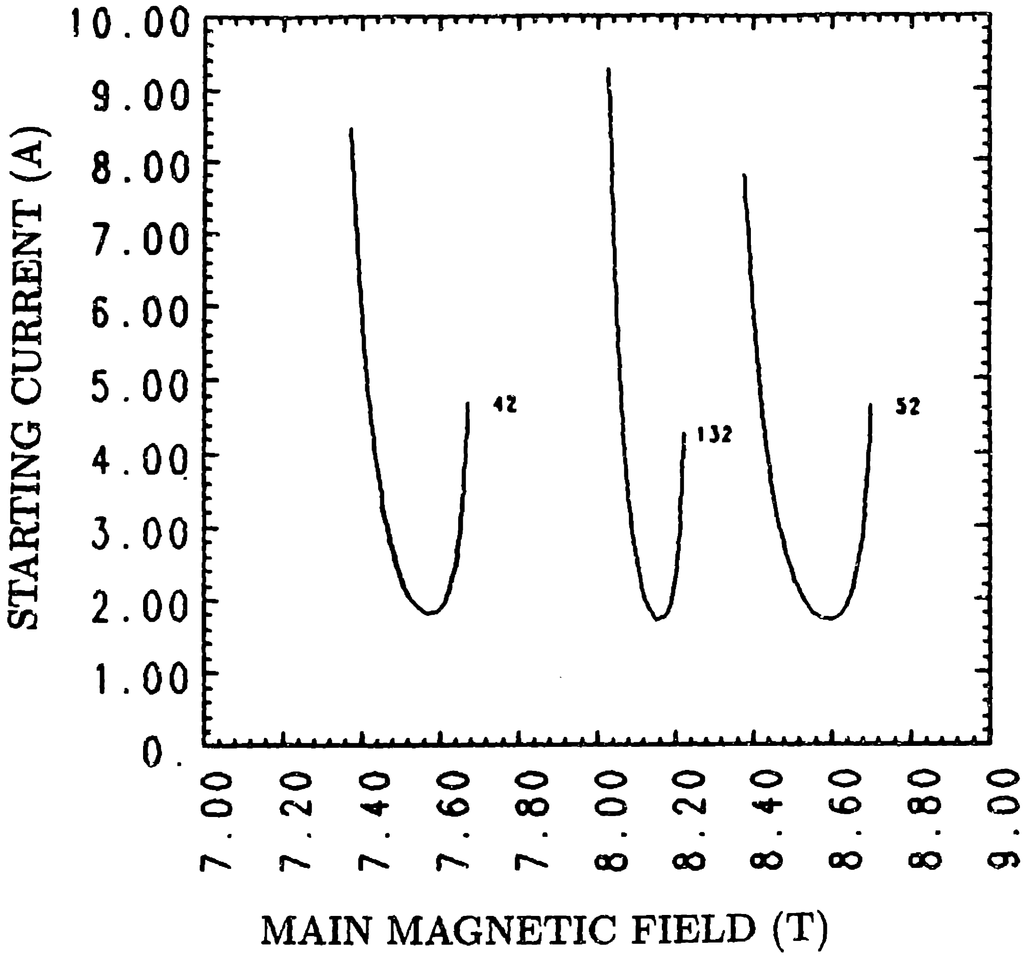

Figure 6.2.2b Starting currents for the second harmonic mode and the two strongest fundamental modes. (Iris case with no beam spread.)

the gun was being run at a higher cathode voltage than it was designed for, lower mod anode voltages may correspond to better beam quality or higher α ($= \beta_\perp/\beta_\parallel$).

Experimentally, twelve second harmonic modes ranging from 301 to 503 GHz were observed and these modes are listed in Table 6.2.2. The power, frequency, and efficiency are given for each of the second harmonic emissions, as well as the theoretical mode that most closely corresponds to the frequency. The power measurements were all taken at a cathode voltage of 73 kV. All of the power measurements, except the ones taken at 417 GHz and 467 GHz, were mixtures of fundamental and second harmonic modes. The method for determining the ratio of fundamental to second harmonic mode present will be discussed in the diagnostics section. In the measurements at 417 GHz and 467 GHz, the emission was believed to be purely second harmonic emission, with no significant fundamental present at the same time. Evidence for this is obtained by using a plexiglass absorber and the calorimeter or video diode. Strong signals are observed in a diode with a filter horn that transmits frequencies above 400 GHz. The signals observed in a fundamental mode diode detector disappear when the plexiglass is inserted in front of the detector. This proves that the radiation is at high frequency (400 - 500 GHz), and not fundamental, low frequency ($\simeq$ 200 GHz) emission. The lack of a fundamental sets an upper limit on the amount of fundamental present at 8% based on the sensitivity of our calorimeter. At 417 GHz, 15 kW of power was measured, which corresponds to a 6% total efficiency. The other modes ranging from 301 GHz to 503 GHz had powers of 3-14.2 kW and efficiencies of 0.6%-5.73%. Measurements with higher current were not possible, because when the beam current increased the fundamental modes get excited and suppress the second harmonic modes. Starting current and power as functions of beam current were measured, and these results will be discussed later in this chapter.

At low frequencies several second harmonic p=1 modes are present, but disappear at higher frequency (higher magnetic fields) as the beam moves away from the cavity wall with increasing compression caused by the higher magnetic fields. As noted previously, the p=3 modes are the highest efficiency modes and, in particular, the $TE_{10,3,1}$ and the $TE_{11,3,1}$ were the highest power modes in this experiment.

TABLE 6.2.2

Second harmonic emission observed in the
high Q output iris cavity with the quartz window

Frequency (GHz)	Magnetic Field (T)	Power (kW)	Efficiency (%)	TE Mode
301.6	6.1	4	1.3	$TE_{3,4,1}$
329.6	6.7	5	2.6	$TE_{14,1,1}$
339.3	6.9	4	2.9	$TE_{10,2,1}$
363.3	7.4	7	2.4	$TE_{11,2,1}$
366.9	7.4	4	1.7	$TE_{8,3,1}$
372.6	7.6	4	1.7	$TE_{16,1,1}$
417.1	8.4	15	6.0	$TE_{10,3,1}$
442.8	8.8	14	5.73	$TE_{11,3,1}$
457.1	9.1	≥ 1		$TE_{15,2,1}$
467.2	9.4	9.7	4.8	$TE_{12,3,1}$
492.0	9.9	1.5	0.6	$TE_{13,3,1}$
503.3	10.1	≥ 1		$TE_{17,2,1}$

Figure 6.2.3 shows the regions of excitation for a fixed cathode voltage of 73 kV, 22.92 kV mod anode voltage, and 3 ampere beam current as a function of magnetic field at the cavity and magnetic field at the cathode. Varying the cathode magnetic field corresponds to changing the ratio of perpendicular to parallel velocity, $v_{\perp}/v_{||}$, which changes the starting current of a given mode. As magnetic field at the gun is decreased, perpendicular velocity increases. This increase is due to the fact that at the gun, electrons experience an $E \times B$ drift and the velocity associated with the drift, $v_{E\times B}$, that generates the perpendicular velocity in the beam, is given by

$$v_{E\times B} = \frac{E \times B}{B^2} \qquad 6.2.1$$

where E is the electric field and B is the magnetic field at the cathode. The graph in Figure 6.2.3, was generated by fixing the main field and continuously varying the field at the gun. The process was repeated for a number of discrete values of the main field. The boundaries of each mode are determined by whether the corresponding frequency is observed by the frequency system. This is done because using just the video diode signal can lead to inaccuracies when more than one fundamental mode is being excited. Each of the regions of second harmonic emission in Figure 6.2.3 corresponds to regions where that second harmonic mode was observed, including areas with a second harmonic and fundamental mixture. In this modemap, the step tunable behavior of the second harmonic emission, similar to that described by Kreischer[8] for the fundamental emission, can be seen. When the harmonic mode is not being suppressed by a strong fundamental mode, the p = 1,2,3 ($TE_{m,p,q}$) sequences are excited. The region of excitation for the $TE_{17,2,1}$ is seen to be smaller than the other second harmonic modes, and above a main field of 10.2 T no second harmonic modes were observed. At higher fields, the fundamental and second harmonic spectra become sparser, since beam compression is increased, and therefore the beam quality is diminished, since velocity and energy spreads increase in more compressed beams. Poorer beam quality (larger energy and pitch angle spreads) and a decrease in the ratio $\beta_{\perp}/\beta_{||}$, result in less of the beam energy coupling to the RF-wave. These effects raise the starting currents and decrease the starting current ratio, which scales like $I_{st1}/I_{st2} \propto 1/\beta_{\perp}^2$.

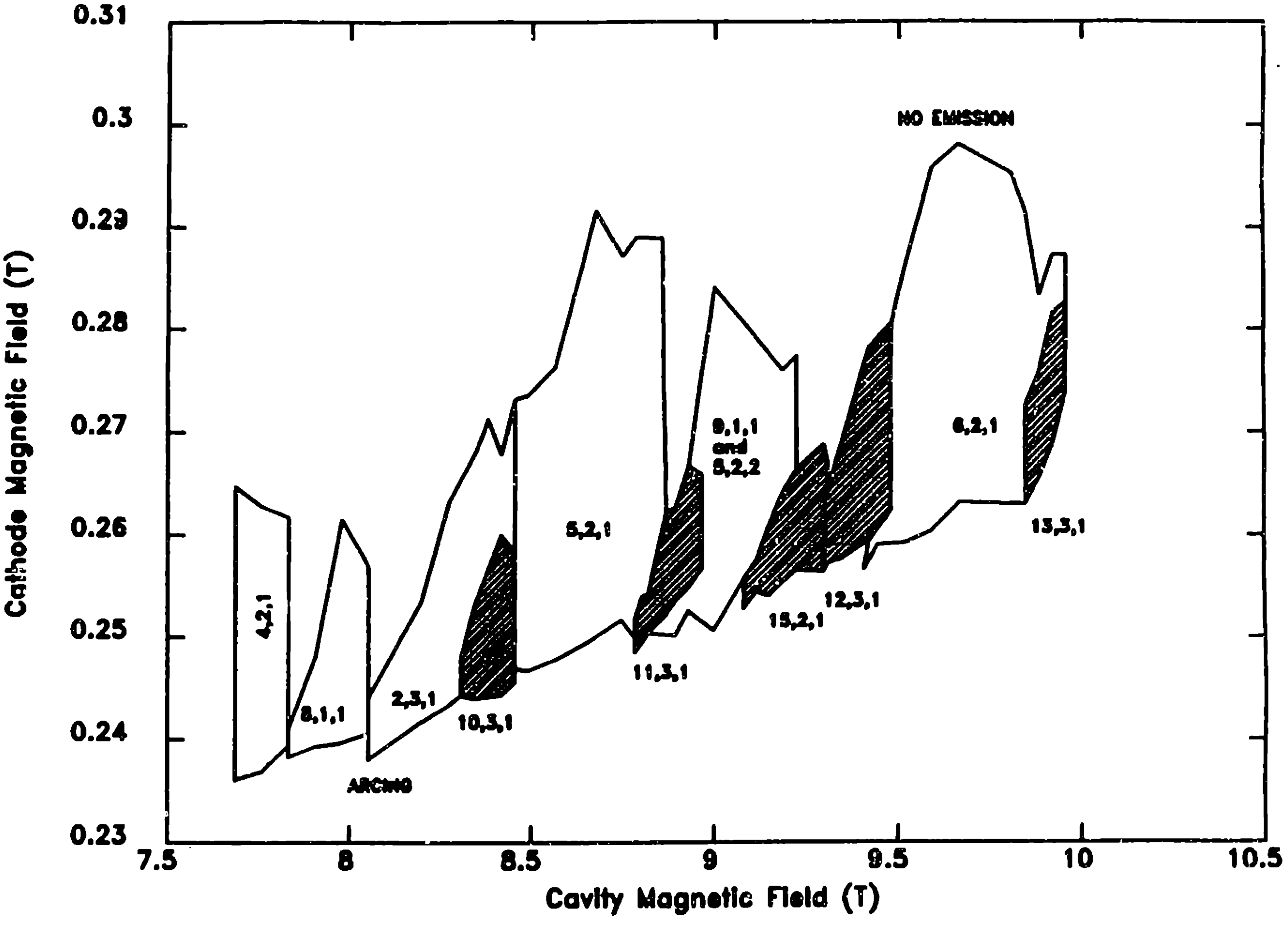

Figure 6.2.3 Mode map for the high Q iris cavity with a 14 T magnet at 3 A and 73 kV with quartz window.

In each of the harmonic regions, at least a small region exists where only second harmonic was observed by the video diodes. As can be seen in Figure 6.2.3, the design second harmonic mode at 410 GHz was not observed. This was because the starting current of the $TE_{13,2,1}$ was too high and the fundamental modes got excited first. Misalignment and beam spread effects can also lower the starting currents of the fundamental modes, if due to these effects the beam is displaced to a position of stronger beam - RF coupling. To excite the $TE_{13,2,1}$ mode, a method must be designed that will selectively reinforce only the second harmonic so that it gets excited before the fundamental modes.

MOTHEYE WINDOW

In this section, another method of reinforcement that was used to supplement the iris's effect will be described. Using a motheye window (Ma (1983)) instead of an ordinary quartz window proved to be very effective, and required only the window mount to be slightly enlarged. A motheye window is fabricated by cutting two perpendicular sets of sawtooth grooves which form pyramidal protuberances on both of the window's surfaces. These protuberances act as a gradation for the refractive index and thereby reduce window reflections for broad band of frequencies as shown in Figure 6.2.4. The window used in this experiment had a transmission coefficient of 0.8 or greater from 100-300 GHz. From 300-400 GHz the transmission coefficient drops to 0.2 and varies from 0 to 0.2 at higher frequencies. The transmission coefficient measurement was made with a broadband source and a spectrometer (Afsar (1984)). Since the transmission characteristics of the window are poor at high frequency, but good at low frequency, only the diffractive Q of the second harmonic is significantly increased.

RESULTS

The effect of the motheye window can be seen in the modemap shown in Figure 6.2.5, where the regions of second harmonic excitation are bigger than those in the modemap shown in Figure 6.2.3, which corresponds to a regular quartz window. It is

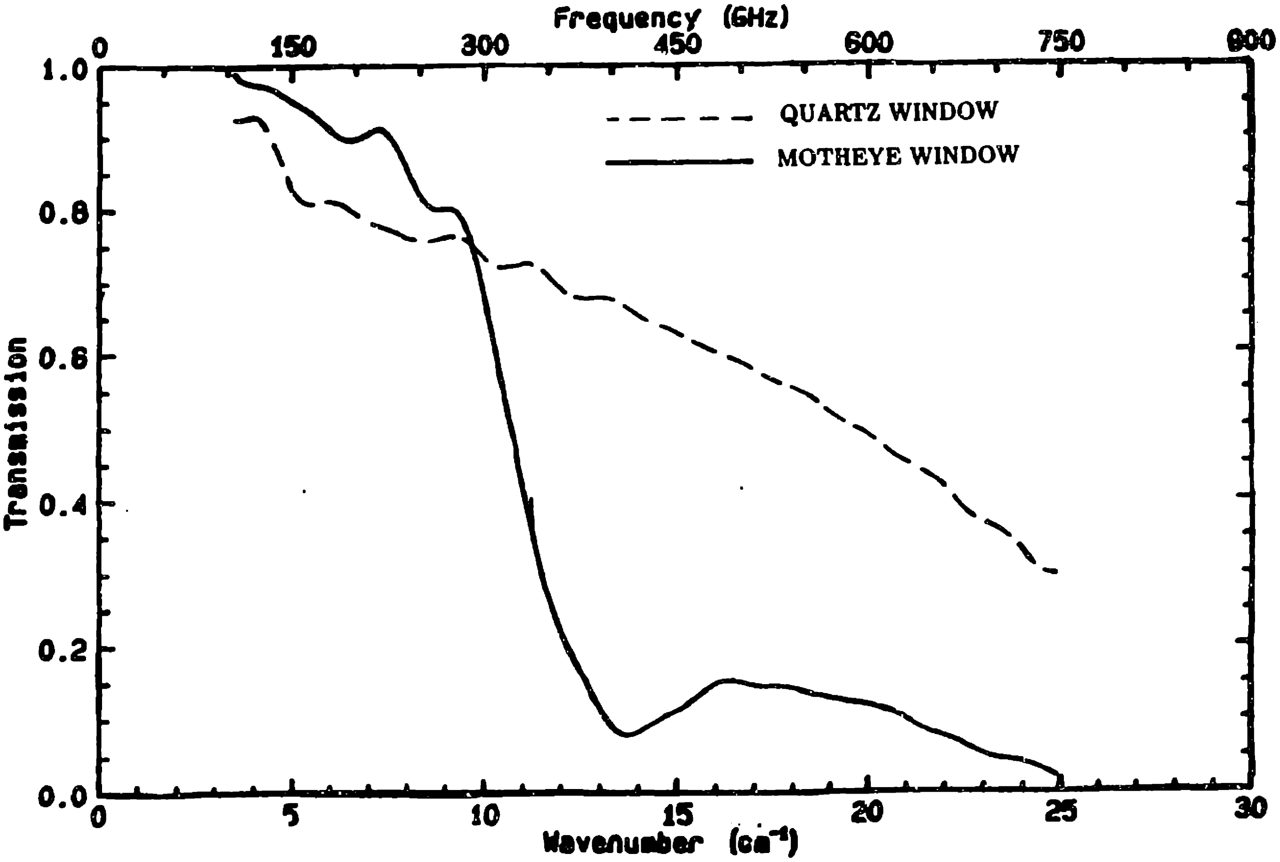

Figure 6.2.4 Transmission curve as a function of frequency for the motheye window (very reflective at high frequency) (Afsar (1988b).

also noticed that the $TE_{13,2,1}$ and $TE_{9,3,1}$ modes were present. The regions of second harmonic emission are significantly larger at higher frequencies, which correspond to low transmission coefficients, than the regions of the second harmonic modes with frequencies less than 390 GHz, such as the $TE_{16,1,1}$, the $TE_{8,3,1}$, or the $TE_{11,2,1}$. This is consistent with the measurement of transmission coefficient as a function of frequency, with the result that the transition region between good and poor transmission is somewhere between 300 and 400 GHz. As mentioned earlier, operation at higher values of the main magnetic field may cause beam degradation. For the second harmonic, this is somewhat counterbalanced by the increase of Q_D due to the motheye window.

In Table 6.2.3 the power, frequency, efficiency and theoretical mode are listed for the observed modes. All of those modes above 339 GHz that were also observed using a quartz window are in that list, except for the $TE_{11,3,1}$ mode, as well as the new modes, the $TE_{9,3,1}$ and the $TE_{13,2,1}$. The $TE_{11,3,1}$ may correspond to a different tube alignment, and therefore was not observed when the motheye window was used. The $TE_{12,3,1}$ and the $TE_{17,2,1}$ modes are stronger when the motheye window is used. The presence of the $TE_{9,3,1}$ and the $TE_{13,2,1}$ as well as the higher power levels observed for the $TE_{17,2,1}$ and the $TE_{12,3,1}$ modes indicate that the motheye window is reinforcing the higher frequency ($>$ 390 GHz) modes. The lower power level of the $TE_{10,3,1}$ mode may have been due to poor alignments with a non-optimal beam position. This can be postulated because in the modemap shown in figure 6.2.5 the region of excitation is larger than when using the quartz window. With more modes present, the step tunable behavior is more pronounced, with an average step size of 10 GHz between modes. If different alignments had been explored, it is quite likely that the $TE_{12,2,1}$, $TE_{14,2,1}$ and the $TE_{16,2,1}$ modes would also have been observed. All of the modes from m=8 to m=13 were observed in the p=3 family of modes, supporting the theory that the p=3 modes are more efficient and have lower starting currents than the p=2 modes.

A comparison between the experimental and theoretical efficiency was also made for both windows. The peak power and efficiency of the $TE_{12,3,1}$ second harmonic mode measured as a function of beam current at a fixed cathode voltage was analysed. Figure

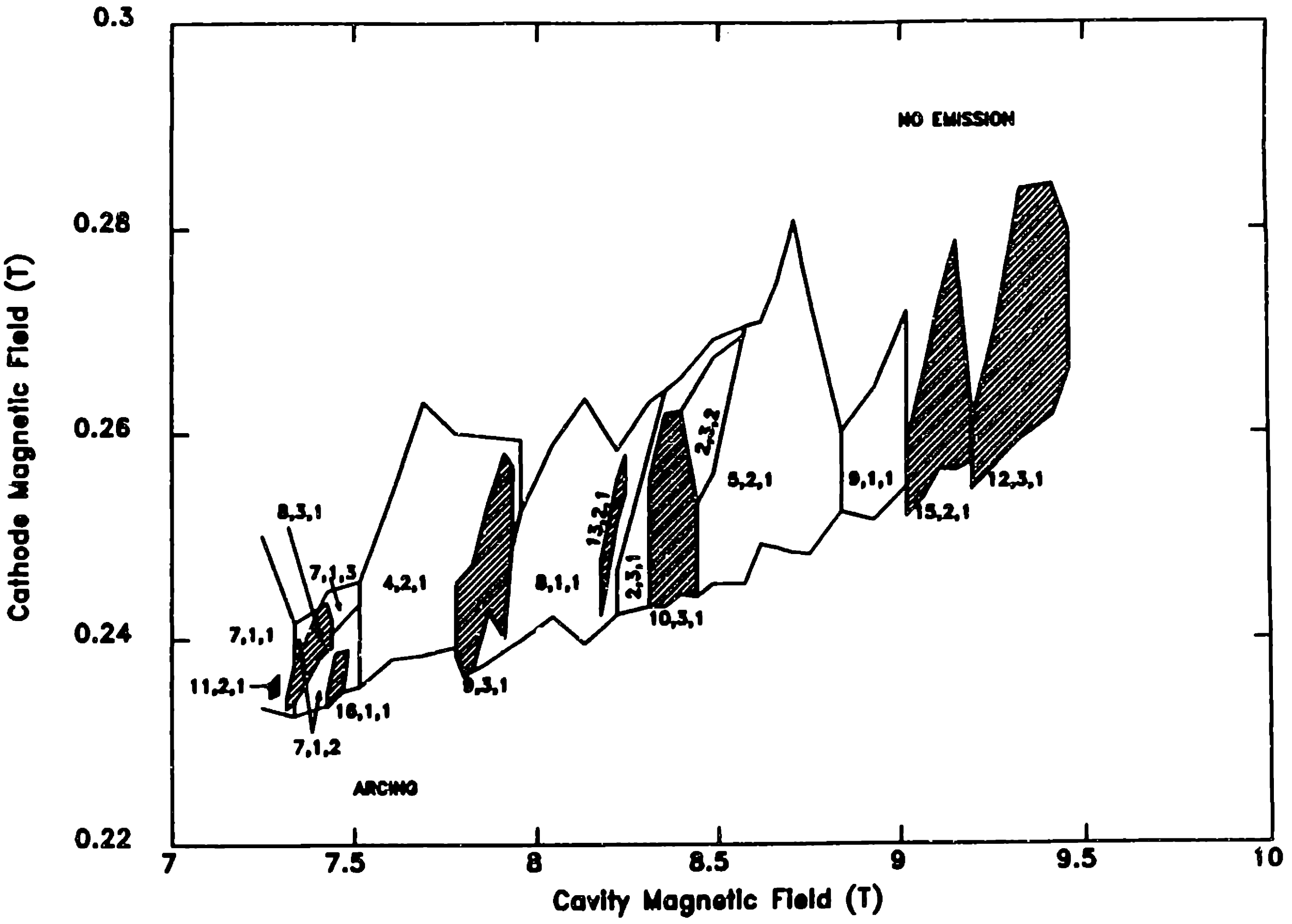

Figure 6.2.5 Modemap for the output iris cavity with the motheye window at $I_B = 3\ A$ and $V_c = 73\ kV$.

TABLE 6.2.3

Second harmonic emission observed in the
high Q output iris cavity with the motheye window

Frequency (GHz)	Magnetic Field (T)	Power (kW)	Efficiency (%)	TE Mode
339.8	6.8	≥ 1		$TE_{10,2,1}$
363.3	7.4	≥ 1		$TE_{11,2,1}$
366.9	7.4	≥ 1		$TE_{8,3,1}$
372.6	7.6	≥ 1		$TE_{16,1,1}$
392.5	7.8	4	1.8	$TE_{9,3,1}$
410.6	8.2	1	0.7	$TE_{13,2,1}$
417.1	8.4	9	4.1	$TE_{10,3,1}$
457.1	9.1	7	2.1	$TE_{15,2,1}$
467.2	9.3	22	3.4	$TE_{12,3,1}$
492.0	9.8	≥ 1		$TE_{13,3,1}$
503.3	10.2	10	5.33	$TE_{17,2,1}$

6.2.6a shows the theoretical efficiency as a function of beam current with the cathode voltage at 73.1 kV (all the power measurements were at this voltage), $\alpha = v_\perp/v_\parallel = 1.5$ assuming a thin beam at beam position corresponding to the 22 kW power measurement. The open circles denote the case with no correction calculated from equation 2.2.1. So far we have assumed that the only losses are the power diffracting out of the cavity and the ohmic losses in the straight section. However losses also occur in the output taper of the resonator, the collector and in the window. From Figure 6.2.4, where the dashed line is the transmission characteristic of a plain quartz window, we can see that at this frequency 40 % of the power will be absorbed in the window. The ohmic losses in the uptaper and the collector are given by (Collin(1966))

$$P_L/P_T = e^{-2\alpha_L Z} \tag{6.2.2}$$

with

$$\alpha_L = \frac{R_m}{RZ_o}\left(1 - \frac{k_{c,mp}^2}{k_o^2}\right)^{-1/2}\left[\frac{k_{c,mp}^2}{k_o^2} + \frac{m^2}{\nu_{mp}^2 - m^2}\right] \tag{6.2.3}$$

$$R_m = \left(\frac{\omega\mu_o}{2\sigma}\right)^{1/2} \tag{6.2.4}$$

where $2\alpha_L$ is the power lost per meter, P_L is the power lost, P_T is the total power, ω is the frequency, Z_o is the impedance of and μ_o the permeability of free space, R is the radius, k_o is the wave number, $k_{c,mp} = \nu_{mp}/R$ is the cutoff wavenumber for a TE_{mpq} mode, and σ is the electrical conductivity of copper. The collector has a fixed radius of 1.1 cm and it is 61 cm long. These parameters give the collector a 97.4% efficiency. Since the output taper starts at a radius of 0.2265 cm and ends up at a radius of 1.1 cm with a linear angle of 5° over a distance of 14.9 cm, equation 6.2.3 must be integrated over R between these two radii. The result is that the uptaper efficiency is 98.1 %. The filled circles represent the results including all of these effects and give the theoretical predictions to which the experimental results are compared.

When a quartz window was used, the power saturated at 7 kW with a peak efficiency of 4.9% and a beam current of 2 amperes, as shown in Figure 6.2.6b. With

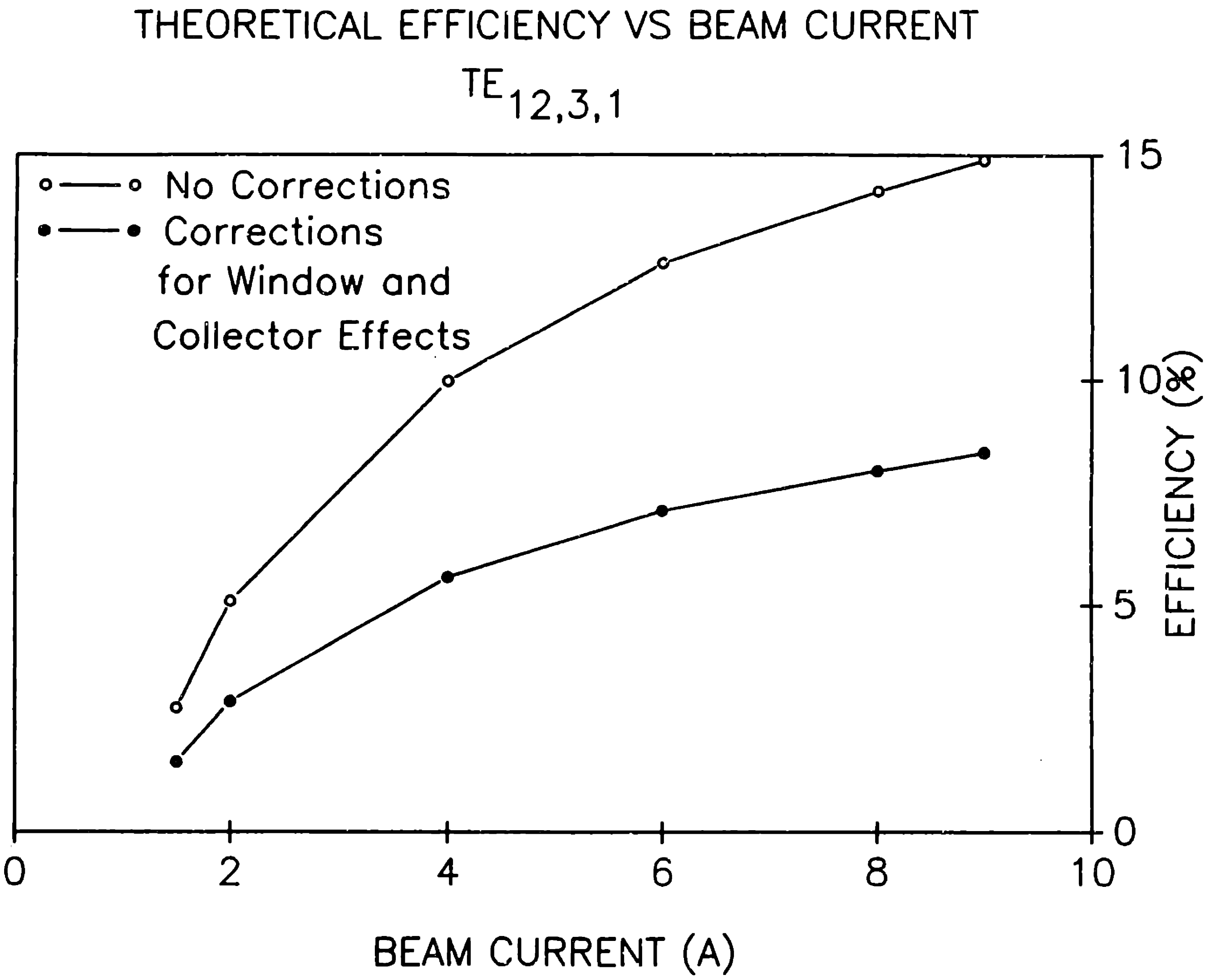

Figure 6.2.6a Theoretical efficiency as a function of beam current for the second harmonic $TE_{12,3,1}$ mode at $V_c = 73\ kV$, $\alpha = 1.5$

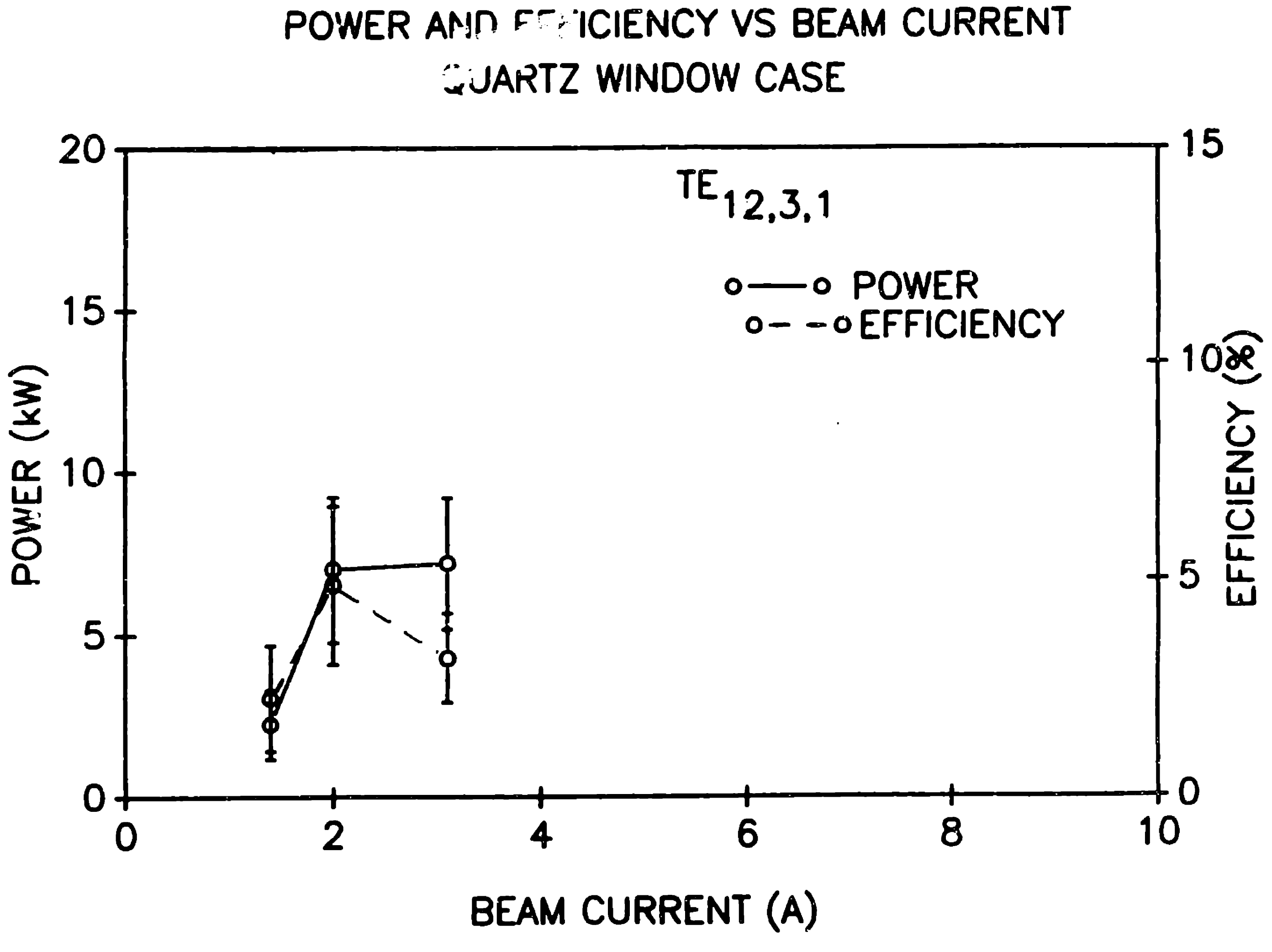

Figure 6.2.6b Experimentally measured power and efficiency as functions of beam current at $V_c = 73\ kV$ for the $TE_{12,3,1}$ mode with a quartz window.

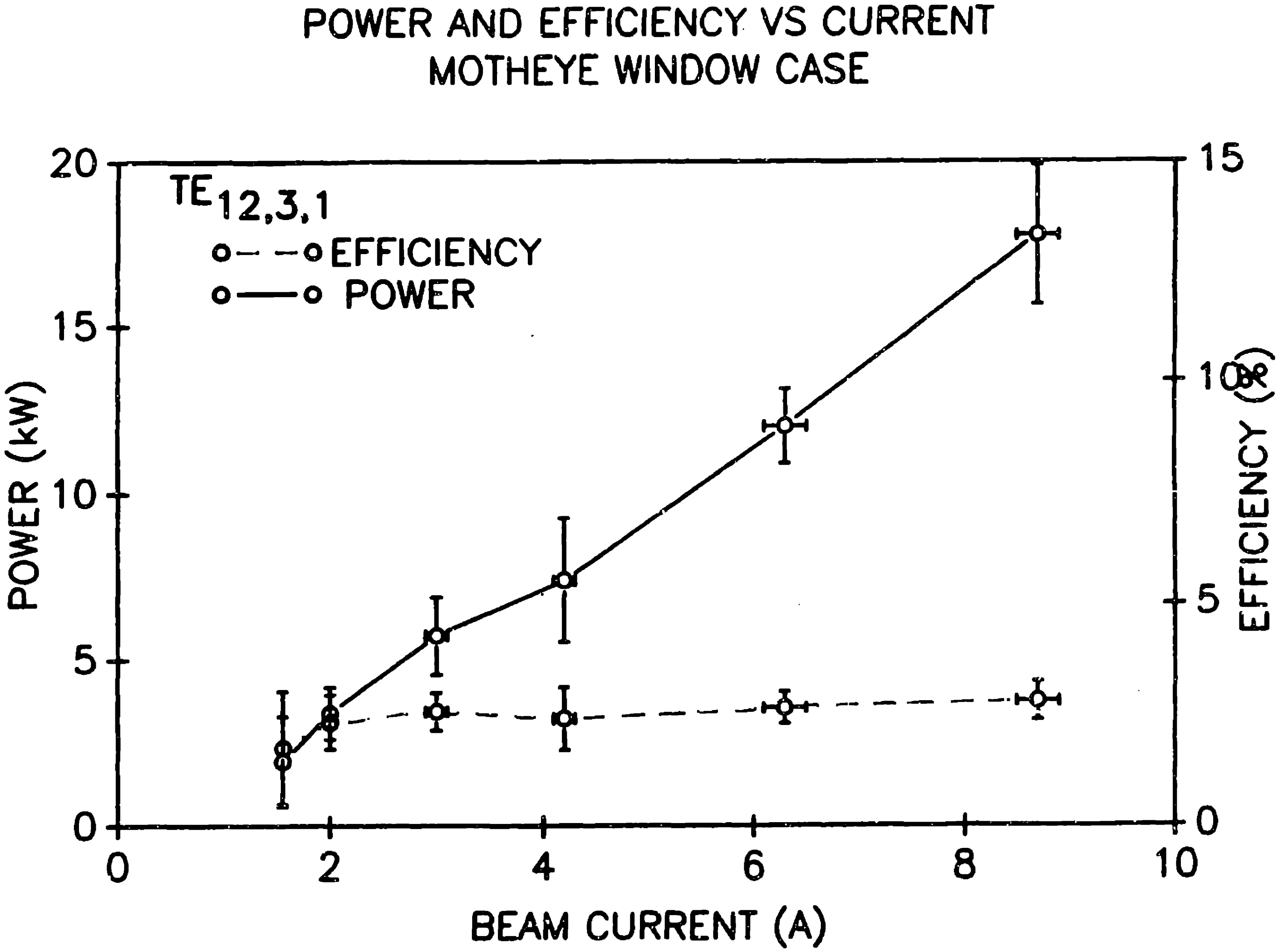

Figure 6.2.6c Experimentally measured power and efficiency as functions of beam current at $V_c = 73\ kV$ for the $TE_{12,3,1}$ mode with a motheye window.

the beam current above 3 amperes it was not possible to find an operating point where the fundamental mode was absent. It is seen that the peak efficiency is higher than predicted by theory. The reason may be the ratio of perpendicular velocity to parallel velocity may be higher than the value of 1.5 quoted in the Varian gun manual. Another reason may be that due to beam spread or a poor alignments the beam may in fact be in a more optimal position, so that the coupling to the $TE_{12,3,1}$ may be better than the value used in the efficiency calculation.

With the motheye window, Figure 6.2.6c, it was possible to observe single mode emission at currents up to 9 amperes and therefore generate higher output power. The highest observed power was 17.8 kW with an efficiency of 2.8 % at a beam current of 7.8 amperes. This suggests that the motheye window significantly reinforces only the second harmonic modes. The discrepancy between the theoretical and experimental efficiencies may be explained by the fact that the data in Figure 6.2.6c was only taken at operating points where no fundamental was observed. Therefore the detuning and value of α in the operating points where the experimental data was taken may not have been as optimal as the values used for the theoretical calculation.

Power as a function of magnetic field was also measured for the $TE_{5,2,1}$, as shown in Figure 6.2.7, which was a strong fundamental mode. The peak power of 79 kW corresponding to an efficiency of 22.4 %, was measured at 4.8 amps. The efficiency peaked at a value of 31 % at 2.7 amps. The high efficiencies attained in this measurement prove that a high quality beam is even possible at 9 Tesla.

Differences can also be seen in the starting current measurements of the $TE_{5,2,1}$ and the $TE_{12,3,1}$ modes taken with the quartz window and with the motheye window. To compare the experimental starting current with the theoretical one we operate at a constant $\beta_\perp$, which requires that the magnetic field at the gun and the cathode voltage must be held constant for each mode. For the quartz window case measurements for the above two modes were taken at a cathode voltage of 73.1 kV, and these will be compared with starting currents observed when using the motheye window at the same cathode voltage. To observe the effect of cathode voltage on starting current, measurements were

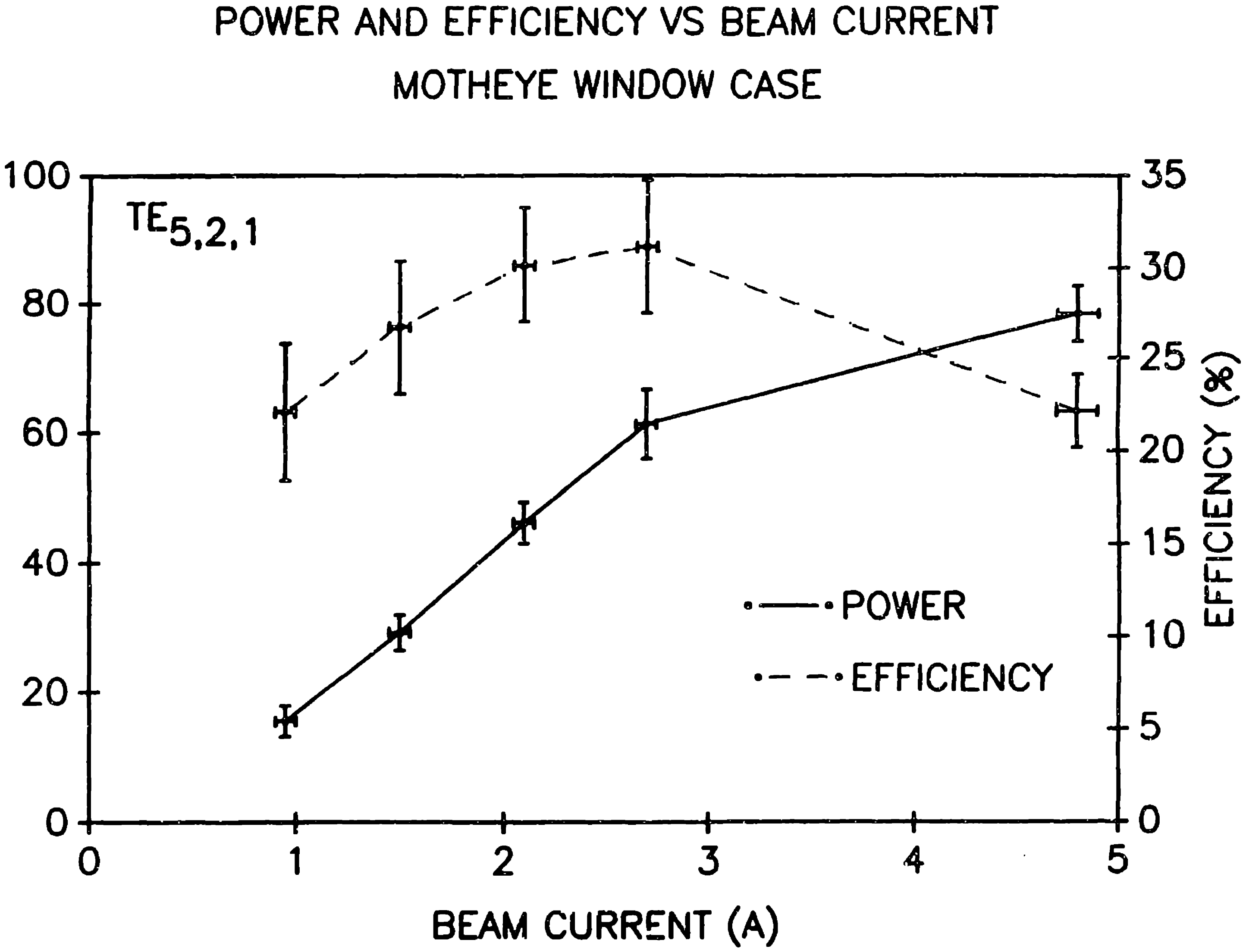

Figure 6.2.7 Experimentally measured power and efficiency as functions of beam current for the fundamental $TE_{5,2,1}$ mode with the motheye window at $V_c = 73\ kV$.

also taken at a cathode voltage of 65 kV for the motheye window case.

Measurements for the $TE_{5,2,1}$ mode were taken at a 0.25 Tesla magnetic field at the cathode. In the quartz window case, shown in Figure 6.2.8a, the $TE_{5,2,1}$ mode has a minimum starting current of 0.25 Amps at a main magnetic field of 8.82 Tesla. When a motheye window is used (Figure 6.2.8b), the minimum starting current is 0.48 amps at a main field of 8.747 tesla. The motheye window affects only the second harmonic modes, and therefore these two measurements should be identical. The variation in these two measurements may have been caused by the different alignments, causing the beam to be in a different position for each measurement. The theoretical starting current curve for the $TE_{5,2,1}$ mode at a cathode voltage of 73.1 kV, represented by filled circles in Figure 6.2.8c, predicts a starting current of 1.44 Amps at a magnetic field of 8.7 Tesla. If $\alpha = 2.0$ is used, the minimum starting current is 0.61 Amperes. Since it was not possible to measure α, the value of α may have been higher than 1.5. Also misalignment may have decreased the minimum starting current. If the beam is assumed to be at the position of maximum coupling, the minimum starting current is 0.45 Amperes. A measurement of the $TE_{5,2,1}$ starting current was also taken at a cathode voltage of 65 kV in the motheye window case. The minimum starting current was found to be 0.74 Amps at a magnetic field of 8.7 Tesla. For a fixed value of α, the ratio of perpendicular to parallel velocity, the theoretical starting current is actually slightly lower for a cathode voltage of 65 kV than at 73.1 kV as seen in the results for the $TE_{5,2,1}$ mode represented by filled triangles in Figure 6.2.8c. If the cathode voltage is decreased for a fixed value of α, the value of $\beta_{\|}$ decreases and the electron spends more time in the cavity, tending to decrease the starting current. However, with a smaller cathode voltage the perpendicular velocity also decreases, as seen from equation 6.1.1, which gives $v_{\perp} \propto E$, where E is the electric field between the cathode and the mod anode (this is for a fixed value of B_{gun}). Using $\alpha = 1.25$, a higher minimum starting current of 2.31 Amps at is obtained at 8.56 Tesla. This shift to a lower magnetic field is caused by the $\beta_{\perp}$ dependence in the detuning parameter, $\Delta = \frac{2}{\beta^2_{\perp o}}\left(1 - \frac{n\omega_{co}}{\omega}\right)$, where $\omega_{co} = eB/\gamma m$. As mentioned in Chapter 2, the minimum starting current for a given mode excited in a cavity of a specified length corresponds to a specific value of Δ. As the voltage decreases, $\beta_\perp$ decreases, with the result that the cyclotron frequency and therefore the magnetic field must decrease to keep Δ constant. Although the magnetic field corresponding to the minimum starting current is almost the same for 65 kV and 73.1 kV, the shape of the starting current curve as a function of magnetic field taken at 65 kV is shifted to a slightly lower field. This magnetic field shift is even more pronounced for the $TE_{12,3,1}$ starting current curves.

The starting current data taken for the $TE_{12,3,1}$ mode has better agreement with theory. With the quartz window, the minimum starting current is 1.2 Amps at 9.44 Tesla. In the case of the motheye window, the minimum starting current was 1.0 Amps at a magnetic field of 9.43 Tesla. The lower $TE_{12,3,1}$ starting current in the motheye window case suggests that the motheye window is reinforcing the second harmonic modes. The magnetic field at the cathode for the $TE_{12,3,1}$ mode measurements was 0.263 Tesla. The theoretical minimum starting current is 1.46 Amps at a magnetic field of 9.42 Tesla, which is close to the measured values with a cathode voltage of 73.1 kV. The shift to lower field at lower values of cathode voltage is more obvious for the $TE_{12,3,1}$ starting current curve than that of the $TE_{5,2,1}$. At 65 kV with the motheye window, the minimum starting current is 1.75 Amps at a magnetic field of 9.37 Tesla. The theoretical minimum starting current for $\alpha = 1.25$ is 2.82 Amps at a magnetic field of 9.28 tesla. The value of α is not known for this setting and may account for the difference between experiment and theory.

Three other starting current measurements were taken using the motheye window for another high frequency fundamental mode and low frequency fundamental and second harmonic modes. The measurement of another high frequency fundamental mode, the $TE_{6,2,1}$, was made because this mode is a strong fundamental mode bordering the $TE_{12,3,1}$. Since both modes operate at almost the same magnetic fields, the beam position and $\beta_\perp$ will be similar for the two modes. Similar beam position and $\beta_\perp$ are useful when comparing starting currents, since for a fixed cathode voltage and cavity profile, these are the only parameters that vary in the expression for the starting current. At 73.1 kV and a magnetic field at the cathode of 0.265 Tesla the minimum starting current

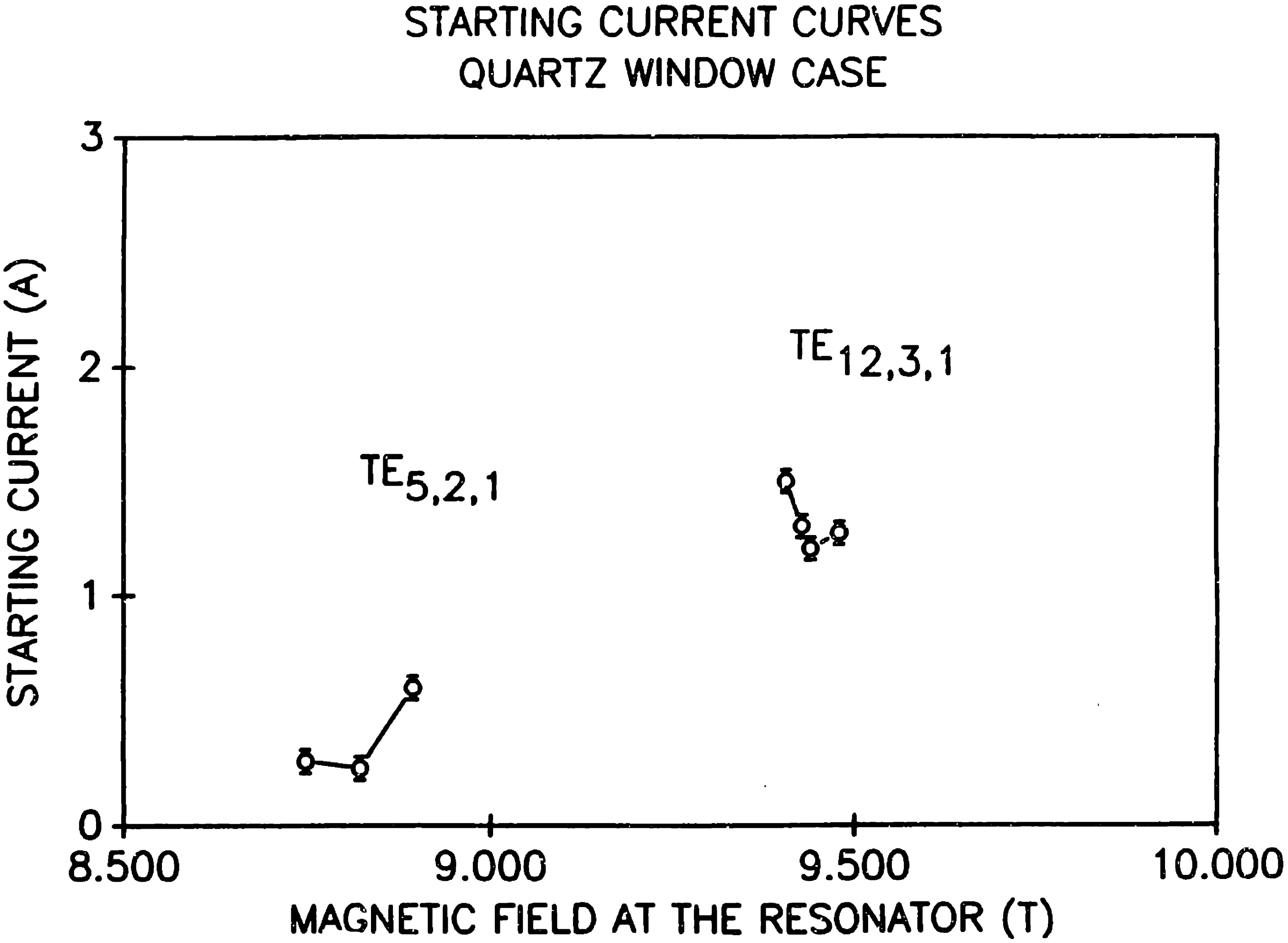

Figure 6.2.8a Experimentally measured starting currents for the strongest high frequency fundamental and second harmonic modes when a quartz window is used at $V_c = 73\ kV$.

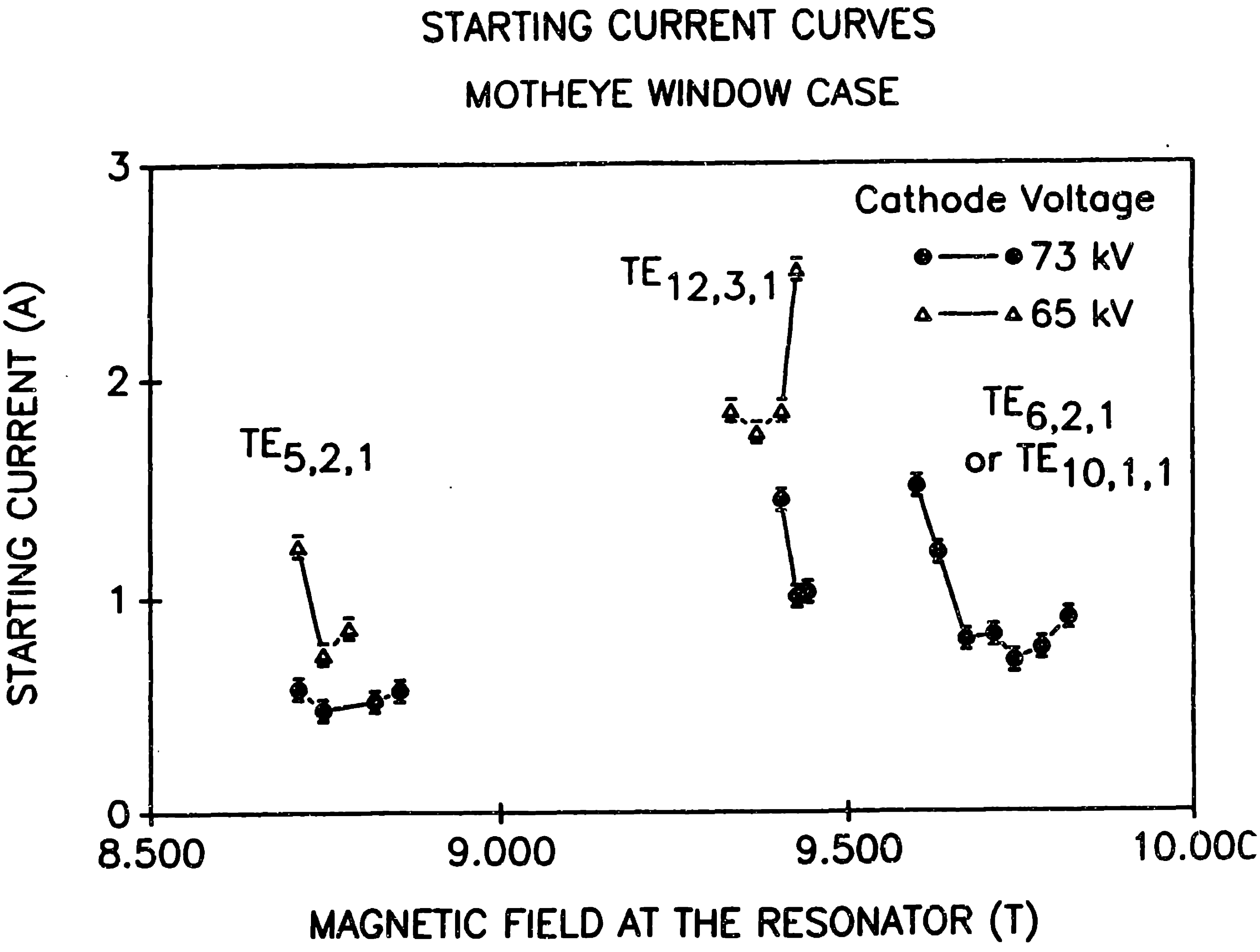

Figure 6.2.8b Experimentally measured starting currents for the strongest high frequency fundamental and second harmonic modes when a moth-eye window is used at $V_c = 73\ kV$.

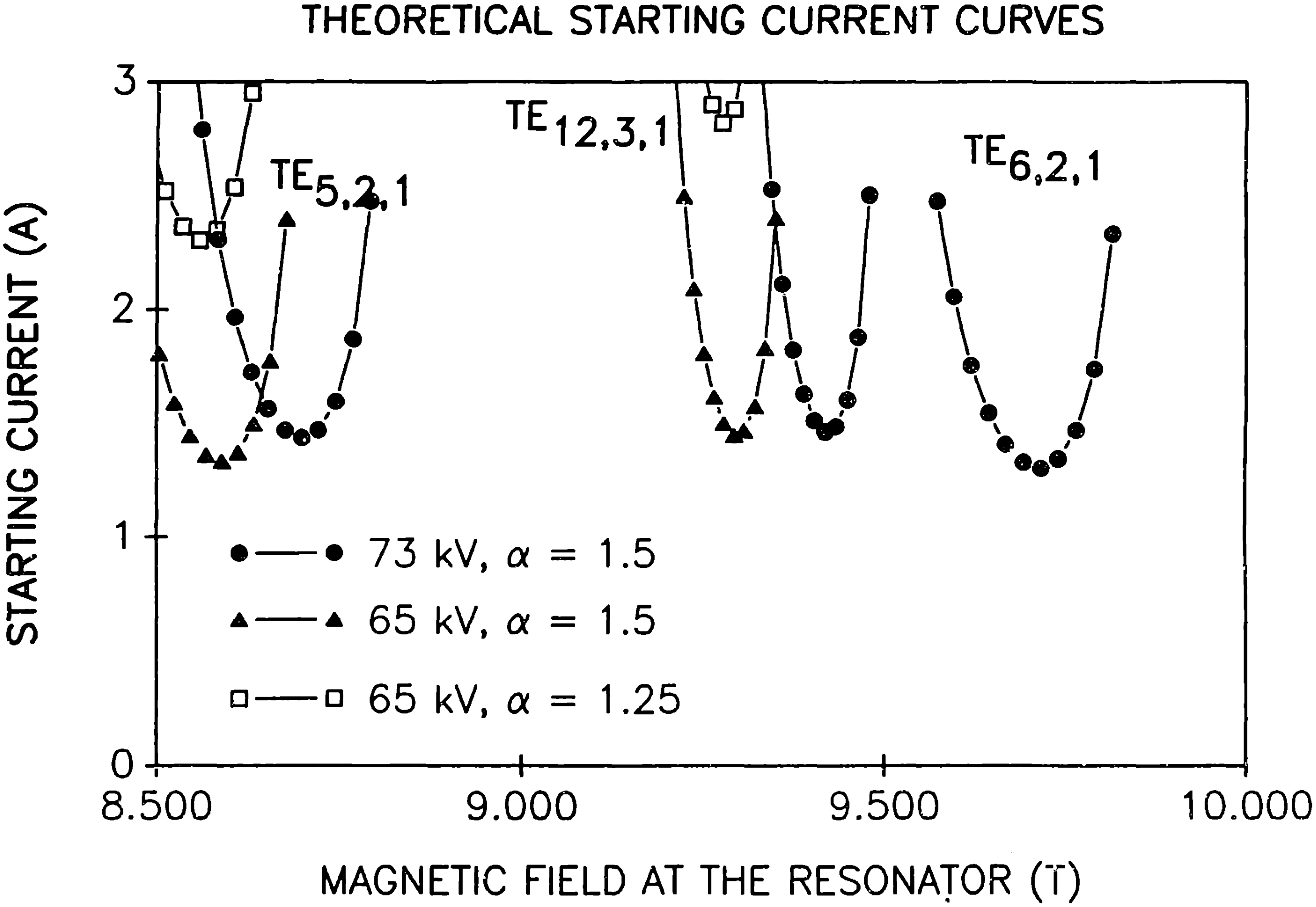

Figure 6.2.8c Theoretical starting currents for two fundamental modes $TE_{5,2,1}$ and $TE_{6,2,1}$ and a second harmonic mode $TE_{12,3,1}$.

of the $TE_{6,2,1}$ was 0.7 Amps at a main field of 9.74 Tesla, shown in Figure 6.2.8c, which has reasonable agreement with the theoretical starting current of 1.30 Amps at a main field of 9.72 Tesla in Figure 6.2.8a. Since the starting currents of the $TE_{6,2,1}$ and the $TE_{5,2,1}$ are similar, the $\beta_\perp$ is roughly the same for these modes.

The behavior of the motheye window below 400 GHz was investigated by measuring the starting current of a low frequency second harmonic mode, the $TE_{10,2,1}$, which oscillates at 339.3 GHz. At this frequency, the transmission coefficient is 40%, so the second harmonic mode is getting some reinforcement, but not as much as a mode above 400 GHz where the transmission coefficient is 10 - 20 %. As mentioned before, we note that the regions of excitation for the second harmonic modes shrink when operating below 390 GHz. This low frequency second harmonic mode is compared with a neighboring low frequency fundamental mode, the $TE_{6,1,1}$ to see if the ratio of fundamental to second harmonic starting currents changes at lower frequency. The minimum starting current of the $TE_{10,2,1}$, as shown in Figure 6.2.9 is 0.3 Amps at 6.89 Tesla. For a cathode voltage of 73.1 kV and a magnetic field at the cathode of 0.231 Tesla, the theory predicts a starting current of 7.02 Amps at 6.82 Tesla. However, if the value of α is increased to 2.0, the minimum starting current is 2.59 Amperes, and in the position of maximum coupling, one gets a starting current of 0.93 Amperes. The starting current for the $TE_{6,1,1}$ was not in good agreement with the theoretical prediction, either. Experimentally, at a magnetic field at the gun of 0.23 Tesla, the minimum starting current was 0.2 Amps at 6.3 Tesla. The theory predicts a starting current of 2.5 Amps at 6.2 Tesla. With $\alpha = 2.0$ the starting current becomes 1.0 Amperes and at the position of maximum coupling the starting current is 0.86 Amperes.

In general, the experimentally measured starting current tends to have better agreement when the beam position is close to the optimal position. If this is not the case, agreement is poor and the disagreement is difficult to analyse because the beam spread and misalignment effects are hard to estimate. Disagreement may also have been caused by assuming too low a value of α for the theoretical starting current, since with $\alpha = 2.0$ the agreement between theory and experiment improved for the $TE_{5,2,1}$, $TE_{6,1,1}$ and

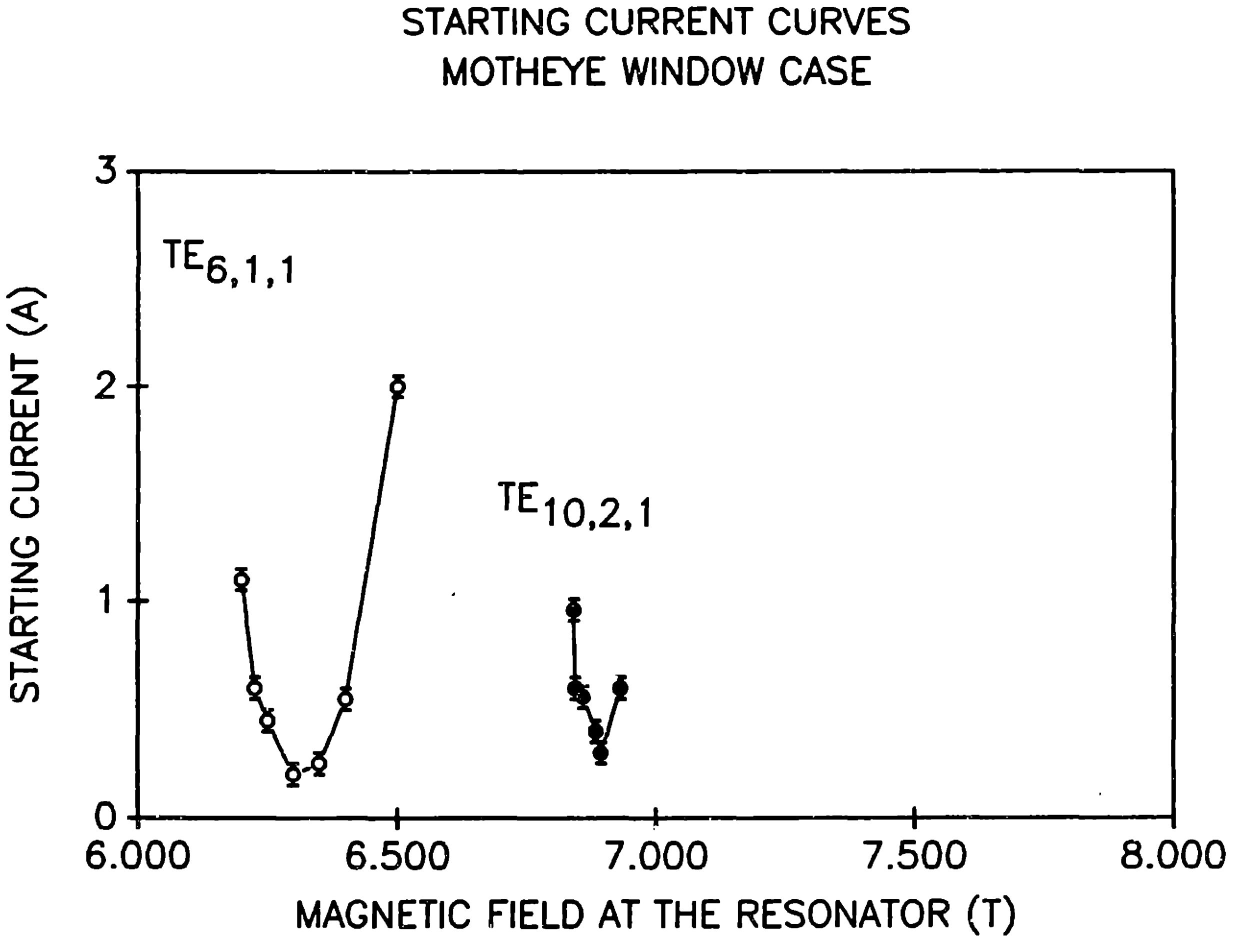

Figure 6.2.9 Experimentally measured low frequency fundamental and second harmonic mode starting currents at $V_c = 73\ kV$ as functions of magnetic field.

the $TE_{10,2,1}$ starting currents.

A search for third harmonic modes was also conducted with this cavity and the motheye window. To observe third harmonic modes, the fundamental and second harmonic modes must be weakened. By operating below 7 Tesla, the motheye only reinforces the third harmonic modes since the frequencies of the second harmonic modes are under 350 GHz. This search was conducted at beam currents of 3 and 5 amps and no third harmonic modes were observed.

6.3 LOW Q IRIS RESONATOR EXPERIMENT

The first iris cavity was only successful in exciting the design mode, the $TE_{13,2,1}$ when the motheye window was used. However, high power operation was not achieved. As the beam current was increased, the $TE_{5,2,1}$ was excited and eventually suppressed the $TE_{13,2,1}$ mode. To attain high power operation, the starting current of the fundamental modes, like the $TE_{5,2,1}$ must be higher. This can be accomplished by decreasing the the fundamental diffractive Q, Q_{D1}, directly, or by decreasing the effective interaction length, which also decreases the diffractive Q. Operating with a smaller iris decreases the reflection coefficient at the output end and directly decreases the diffractive Q. However it is difficult to fabricate an iris that is much smaller than the iris in the first cavity. The other way is to decrease the straight section length and therefore the effective interaction length, which lowers the diffractive Q and also directly raises the starting current, since $I_{st} \propto \left(Q_D L_{eff}^2\right)^{-1}$. This will also decrease the second harmonic diffractive Q and effective interaction length. However since the diffractive of the second harmonic is lower the ohmic effects will be less severe, so the total Q ratio decrease will not be as large as the decrease in the diffractive Q ratio. With less severe ohmic effects the decrease in the perpendicular efficiency is mitigated by an increase in ohmic efficiency.

The effective interaction length can be decreased in another way, as seen in the pointy iris case of the symmetric iris study. When the output taper angle is increased, the reflection coefficient at that junction increases. If a long stepped iris is used the effect is stronger on the fundamental mode which is less attenuated at that point by the iris. In this fashion the fundamental effective interaction length can be selectively shortened while the second harmonic effective interaction length is unperturbed. Unfortunately this is not a large effect, so it is used for fine tuning a design. In summary, this cavity was designed to have a shorter straight section with a shallower but longer iris and a steeper output angle. In this cavity. the straight section length was 0.4562 cm long and the output taper angle was 16°. As a result of operating with a steep output angle, the starting current ratio, $I_{st1}/I_{st2} = 1.15$, which is a 15% improvement over the first cavity. The total Q ratio is slightly lower than in the first cavity, but the effective length ratio is higher and accounts for the increase in the starting current ratio. The design parameters are listed in Table 6.3.1. This cavity was designed to produce 70 kW at 9 Amps at a frequency of 410 GHz, using the $TE_{13,2,1}$ mode.

RESULTS

The data is very limited from this experiment, since the cavity was extensively damaged by beam interception, near the beginning of the experiment. This experiment was conducted using the quartz window. The data is summarized in Table 6.3.2, which lists the theoretical mode, frequency and magnetic field at which the measurement was made. Frequency measurements were made for two of the modes and both frequencies were shifted with respect to the values in the first cavity, by the same amount. The other modes were identified by their magnetic field values.

SUMMARY

In this the iris theory and the iris cavity results were discussed. The advantage gained by using an iris is that the second harmonic modes are reinforced more than the fundamental modes. This means that cavities can be designed where the second harmonic starting currents are equal to or less than the fundamental starting currents. As a result of these low starting currents, 14 different second harmonic modes were observed with frequencies ranging between 300-503 GHz, with 22 kW measured at a frequency of 467 GHz.

TABLE 6.3.1

LOW Q IRIS CAVITY DESIGN PARAMETERS

Second Harmonic

Frequency = 410 GHz

Beam Current = 9 Amps

Power = 70 kW

η_T = 11.84%

Magnetic Field = 8.3 Tesla

Magnetic Field at the Gun = 0.221 Tesla

Cathode Voltage = 65 kV

$\eta_\perp$ = 23.0 %

η_{OH} = 79.2%

η_{el} = 65.3%

Cavity Radius = 0.2316 cm

$Q_{D2\omega c} = 2416$

$Q_{D\omega c} = 358$ ($TE_{5,2,1}$)

$Q_{OH2\omega c} = 9200$

$Q_{OH\omega c} = 9059$ ($TE_{5,2,1}$)

$Q_{T2\omega c} = 1914$

$Q_{T\omega c} = 344$ ($TE_{5,2,1}$)

$L_{eff2\omega c}$ = 0.431 cm

$L_{eff\omega c}$ = 0.474 cm ($TE_{5,2,1}$)

$I_{ST2\omega c}$ = 6.05 Amps

$I_{ST\omega c}$ = 6.95 Amps ($TE_{5,2,1}$)

TABLE 6.3.2

Second harmonic emission observed in the low Q output iris cavity

Frequency (GHz)	Magnetic Field (T)	TE Mode
303.7	6.0	$TE_{3,4,1}$
–	6.7	$TE_{14,1,1}$
413.5	8.2	$TE_{13,2,1}$
–	8.4	$TE_{10,3,1}$

Chapter 7

CONCLUSIONS

In Chapter 2, the linear theory showed that the fundamental modes tend to have lower starting currents than the second harmonic modes. Therefore, the fundamental modes get excited first and suppress the harmonic modes. As a consequence, in order to excite second harmonic modes, fundamental mode suppression techniques are necessary. Five such techniques have been discussed in this thesis.

The first technique exploits the fact that the fundamental mode spectrum is not uniformly distributed. Concentrations of modes around certain mode indices, ν_{mp}, tend to occur. Since each mode is excited over a limited range in magnetic field, it was assumed that the gap in the fundamental spectrum would translate into a region of magnetic field devoid of fundamental modes. A resonator was designed, as discussed in Chapter 4, with a second harmonic mode that existed in the middle of a large gap in the fundamental spectrum. The absence of fundamental modes in the region of magnetic field corresponding to the gap in the fundamental spectrum was not observed. The regions of excitation for the fundamental modes were found to be larger than predicted by theory. It was also discovered that the higher order axial modes filled in the magnetic field region. The harmonic modes were suppressed by the strong fundamental modes in this experiment. The second technique involves placing the beam in a position where the coupling to the fundamental modes is weak. This technique is difficult to implement, since the fundamental mode spectrum is denser at higher frequency, and it is difficult to find a beam position where the coupling to the fundamental modes is weak. Furthermore, finite beam thickness effects and misallignment of the beam can allow the beam to couple to undesired fundamental modes. The combination of the above two techniques, which was implemented in the design of the resonator in the Chapter 2 experiment, is not strong enough to suppress the fundamental modes. Some other techniques are necessary. On such technique is to operate with a higher value of perpendicular velocity, $\beta_\perp$. As discussed in Chapter 2, at higher values of $\beta_\perp$ the ratio of fundamental to second harmonic starting current, I_{st1}/I_{st2} increases. At a high enough value of $\beta_\perp$, the second harmonic mode has a lower starting current and can be excited first. However, since an existing 65 kV gun was used for this experiment, only a limited increase in $\beta_\perp$ was possible, due to the upper limit on the cathode voltage.

The fourth technique for suppressing fundamental modes involves designing a cavity where the ratio of the second harmonic to fundamental total Q, Q_{T2}/Q_{T1} is as large as possible, so that the starting current of the second harmonic mode is as low as possible. This can be accomplished by making an electromagnetic structure that highly perturbs the fundamental modes (thereby lowering the Q) and leaves the second harmonic modes unperturbed or a structure that reinforces (raises the cavity Q) the second harmonic modes more than the fundamental modes. In Chapter 5, the first type of structure was built, by cutting axial slots in the cavity wall at positions corresponding to electric field minima of the second harmonic mode. Unfortunately, the second harmonic modes as well as the fundamental modes had large leakage losses through the slots. However, when a foil sheath was wrapped around the outside of the large slots cavity to decrease the leakage out of the slots, nineteen discrete frequencies were observed in the frequency range from 186.3 - 200.6 GHz. This is a higher density of modes than would be predicted by conventional resonator theory for an unslotted cavity. The larger number of modes may be a result of several effects. Since the cavity configuration resembles a vaned cavity, magnetron effects might be creating a higher density of modes. Also, the slots cut in the cavity wall substantially lower the cavity Q, so the amount of frequency pulling can be quite large. Frequency pulling caused by variation of the magnetic field and variation of the parallel electron velocity, $v_\parallel$ (pitch angle tuning) was observed.

In Chapter 6, a high Q resonator which had an iris at the output end of the straight section was used the reinforce the second harmonic modes. A study was conducted to determine the effect of iris shape (stepped or pointy) on the ratio of the fundamental to second harmonic starting current, I_{st1}/I_{st2}, to determine whether for a given diffractive Q of the second harmonic, an optimal design could be found. The study had two results. The first result was that for a given value of second harmonic diffractive Q, the starting current ratio was independent of iris shape, if the cavity length was not varied. Next, we found that the ratio of second harmonic to fundamental diffractive Q, Q_{D2}/Q_{D1} improved as the second harmonic diffractive Q was increased, corresponding to larger irises. However, the ratio of second harmonic to fundamental total Q, Q_{T2}/Q_{T1} saturated when the second harmonic diffractive Q reached a value of approximately 0.5 Q_{oh}, where Q_{oh} is the ohmic Q. As a result, the best discrimination against the fundamental modes with the highest fundamental mode starting currents, is obtained for a value of second harmonic diffractive Q close to half of the value of the ohmic Q.

When the high Q iris cavity experiment was conducted with an ordinary quartz window, twelve different second harmonic modes were observed with frequencies ranging from 301 to 503 GHz. At 417 GHz, 15 kW of power was measured, which corresponds to a 6 % total efficiency. The other second harmonic modes had power levels of 3 - 14.6 kW and efficiencies of 0.6 - 5.7 %. When a motheye window was used (with the same cavity) to implement the external feedback to the second harmonic mode technique, two new second harmonic modes were observed. At 467 GHz, 22 kW of power was measured with a 3.4 % total efficiency, and the other modes had power levels of 1 - 10 kW and total efficiencies of 0.7 - 5.3 %. A 12 MHz frequency bandwidth was observed for these second harmonic frequencies. The effect of the motheye window was to slightly increase the region of excitation and slightly lower the starting current of the second harmonic modes, thereby allowing two extra second harmonic modes to be excited. In these two iris cavity experiments, step tunable behavior for the second harmonic modes was observed. When the harmonic modes were not being suppressed by the fundamental modes, the p = 1,2,3 ($TE_{m,p,q}$) sequences were excited with an average step size of 10 GHz was noticed.

FUTURE RECOMMENDATIONS

As mentioned earlier, the ratio of second harmonic to fundamental total Q saturates for values of the second harmonic diffractive Q above 0.5 Q_{oh}. If one operates with a mode that has a higher value of ohmic Q, the maximum total Q ratio increases.

Therefore, since the ohmic Q for a given cavity radius increases for higher values of the radial index, it is desirable to operate with a mode that has the highest p possible. The desirability of higher p modes is demonstrated by the fact that the high power modes in the high Q iris cavity experiment in Chapter 6 were the p = 3 modes. However, operating with higher p modes leads to higher values of mode index, ν_{mp} if the same electron gun is used. At higher values of ν_{mp} the mode spectrum is denser and mode competition problems are more severe. If an electron gun is used that has a smaller radius at the cathode, it is possible for the beam to occupy a radial position further away from the cavity wall without changing the magnetic compression needed to increase the perpendicular energy of the beam, so one can access the higher p modes at lower values of ν_{mp}.

It is recommended here that a new gun be designed with a smaller cathode radius and a higher value of $\beta_\perp$. This would allow a better utilization of the third fundamental mode suppression technique (increasing $\beta_\perp$) and a systematic study of the high p modes could be undertaken. Even higher power and efficiencies than achieved in this paper may then be possible.

For work at higher harmonics a system that provides more fundamental mode discrimination is recommended, since no third harmonic emission was observed in the experiments described in this thesis. Complex cavity configurations have been successfully used to excite third harmonic emission in the past (Zapevalov (1983)).

TABLE OF COMMONLY USED SYMBOLS

The subscripts 1 and 2 used in this thesis refer to fundamental and second harmonic mode parameters.

R_o = cavity radius

R_e = electron beam radius

R_k = emitter strip radius

ω_{co} = eB/m

r_L = Larmor radius

ω_c = cyclotron frequency = eB/γm

$k_{||}$ = $||$ component of the wave vector, **k**

$k_\perp$ = $\perp$ component of **k**

ν_{mp} = p^{th} root of $J'_m(k_\perp R_e)$

v = electron velocity

$\beta_\perp = v_\perp/c$ = perpendicular normalized velocity

$\beta_{||} = v_{||}/c$ = parallel normalized velocity

β_k = normalized electron velocity at the cathode

β_o = normalized electron velocity at the resonator

λ = wavelength

L_{eff} = effective interaction length

$\gamma = (1-\beta^2)^{-1/2} = 1 + V_c(kV)/511$

V_c (kV) = cathode voltage in kV

B_o = magnetic field at the cavity

B_g = magnetic field at the gun

m = azimuthal index

p = radial index

q = axial index

n = harmonic number

f(z) = axial field profile

Δ = detuning = $2/\beta_\perp^2\left(1-\frac{n\omega_c}{\omega}\right)$

μ = normalized cavity length

F = normalized rf field strength

Q_D = diffractive Q

Q_{oh} = ohmic Q

Q_T = total Q

η_T = total efficiency

$\eta_\perp$ = perpendicular efficiency

η_{el} = electrical efficiency

η_{oh} = ohmic efficiency

I = normalized beam current

I_A = beam current in amps

L_i = iris length

I_B= beam current

$C_{mp} = \frac{J_{m\pm n}(k_\perp R_e)}{(\nu_{mp}^2 - m^2) J_m^2(\nu_{mp})}$ = coupling coefficient

D_i = iris depth

REFERENCES

M. Abramowitz and I. Stegun, "Handbook of Mathematical functions" (Dover Publications, New York) (1965), p. 319.

M.N. Afsar, IEEE Trans Instrum. and Meas., **IM-36**, (1987), p. 530.

M.N. Afsar, Private communication (1987b)

M.N. Afsar, IEEE Trans. on Microwave Theory and Tech., **MTT-32**, (1984) p. 1598.
M.N. Afsar, Private communication (1984b)

G. Bekefi, A. Dirienzo, C. Liebovitch and B.G. Danly, Appl. Phys. Lett., **54**, No. 14, (1989), p. 1302.

S.V. Benson, J.M.J. Madey, J. Schultz, M. Marc, W. Wadensweiler, G.A. Westenskow, and M. Velghe, Nucl. Instr. Methods Phys. Res. A, **250**, (1986), p. 39.

P. Bhartia and I.J. Bahl, "Millimeter Wave Engineering and Applications", John Wiley and Sons, New York, (1984).

Blaney, T. G., Power measurements at submillimetre wavelengths, Proc. Soc. photo-optical Instrum. Engrs., **234**, (1980), p. 22.

P. Boulanger, P. Charbit, G. Faillon, E. Kammerer and G. Mourier, Int. J. Elect., **53**, No. 6, (1982), p. 523.

I.E. Botvinnik, V.L. Bratman, A.B. Volkov, G.G. Denisov, B.D. Kol'chugin, M.M. Ofitserov, Pis'ma Zh. Eksp. Teor. Fiz., **8**, (1982a), p. 1376.

I.E. Botvinnik, V.L. Bratman, A.B. Volkov, N.S. Ginsburg, G.G. Denisov, B.D. Kol'chugin, M.M. Ofitserov, and M.I. Petelin, Pis'ma Zh. Eksp. Teor. Fiz., **35**, (1982b), p. 418.

J.L. Byerly, B.G. Danly, K.E. Kreischer, R.J. Temkin, W.J. Mulligan, and P. Woskoboinokow, Int. J. Electron., **57**, (1984), p. 1033.

V.L. Bratman, N.S. Ginzburg, G.S. Nusinovich, M.I. Petelin, and P.S. Strelkov, Int. J.

Electron., **51**, (1981), p. 541.

S.C. Chen, Priavate communication (1987).

K.R. Chu and D. Dieletis, Int. J. Infrared and Millimeter Waves, **5**, (1984), p. 37.

K.R. Chu and J.L. Hirshfield, Phys. Fluids, **21**, (1978), p. 461.

R.E. Collin, in "Foundations of Microwave Engineering" (McGraw-Hill Book Company, New York, 1966) p. 110.

R.E. Collin, in "Microwave Magnetrons" (McGraw-Hill Book Company, New York, 1948).

B.G. Danly, K.E. Kreischer, W.J. Mulligan and R.J. Temkin, Trans. Plasma Science, **PS-13**, No. 6 (1985), p. 383.

B.G. Danly and R.J. Temkin, Phys. Fluids, **29**, (1986), p. 561.

A.N. Didenko, A.R. Borisov, G.R. Fomenko, and Yu.G. Shtein, Pis'ma Zh. Tekh. Fiz., **9**, (1983), p. 60.

D. Dieletis and K.R. Chu, IR. and MM. Waves, **7**, (1983), p. 537.

O. Dumbrajs, G.S. Nusinovich, and A.B. Pavelyev, Int. J. Electron., **64**, (1988), p.137.

L.R. Elias, R.J. Hu, and G.J. Ramian, Nucl. Instr. Methods Phys. Res. A, **237**, (1985), p. 203.

S.E. Evangelides Jr., (1989), PhD. Thesis, M. I. T., unpublished.

K. Felch, D. Stone, H. Jory, R. Garcia, G. Wendell, R.J. Temkin, K.E. Kreischer, IEDM Tech. Dig., Paper 14.1, (1982), p. 362.

A.W. Fliflet and J.M. Baird, NRL Contract No. N00173-80-M-4143, (1981).

A.W. Fliflet, M.E. Read, K.R. Chu and R. Seeley, Int J. Electron., **53**, (1982), p. 505.

A.W. Fliflet, R.C. Lee and M.E. Read, NRL Memorandum Report 5881, (1987).

V.A. Flyagin, A.V. Gapanov, M.I. Petelin, and V.K. Yulpatov, IEEE Trans. Microwave Theory Tech., **MTT - 25**, (1977), p. 514.

D.S. Furuno, D.B. Mcdermott, N.C. Luhmann, Jr., P. Vitello, K. Ko, IEEE Trans. Plasma Science, **16**, No. 2, (1988), p. 155.

A.V. Gapanov, V.A. Fliagin, A.L. Goldenberg, G.S. Nusinovich, Sh.E. Tsimring, V.G. Usov, and S.N. Vlasov, Int. J. Electron., **51**, (1981), p. 277.

V.L. Granatstein, I. Alexeff, "High Power Microwave Sources", Artech House, Boston, (1987).

H.Z. Guo, Z.G. Chen, S.C. Zhang, W.U. DeShun, Int. J. Electron., **51**, (1981), p. 485.

M.K. Haldar and A.H. Beck. Electron Lett, **15**, (1979), p. 487.

J.L. Hirshfield, Conf. Dig., Eighth Int. Conf. on Infrared and Millimeter Waves, Miami Beach, Florida (1983).

K.E. Kreischer, R.J. Temkin, H.R. Fetterman, and W.J. Mulligan, Int. J. Electron., **57**, (1984), p. 835.

K.E. Kreischer and R.J. Temkin, Infrared and Millimeter Waves, **7**, (1983), p. 377.

K.E. Kreischer, MIT Plasma Fusion Center Report No. PFC/RR/82-8, (1982).

K.E. Kreischer and R.J. Temkin, Int. J. Infrared and Millimeter Waves, **1**, (1980), p. 195.

M.V. Kuzelev et al., Zh. Eksp. Teor. Fiz., **83**, (1982), p. 1358.

J.Y. Ma and L.C. Robinson, Optica Acta., **30**, (1983), p. 1685.

T.C. Marshall, "Free Electron Lasers", Macmillan Publishing Company, New York, 1985.

E.M. Marshall, P.M. Phillips, and J.E. Walsh, IEEE 16, **2**, (1988), p. 199.

D.B. McDermott, H.B.Cao, and N.C. Luhmann, Jr., Conf. Dig., 13th Int. Conf. on Infrared and Millimeter Waves, Honolulu, Hawaii, (1988), p. 324.

D.B. McDermott, N.C. Luhmann, Jr., D.S. Furuno, A. Kupiszewski, and H.R. Jory, Int. J. of Infrared and Millimeter Waves, **4**, No. 4, (1983), p. 639.

K.K. Mon and A.J. Sievers, Applied Optics, **14**, No. 5, (1975), p. 1054.

W. Namkung, J.Y. Choe, H.S. Uhm, and V. Ayres, IEEE Trans. Plasma Science, **16**, No. 2, (1988), p. 149.

G.S. Nusinovich, and R.E. Erm, Elektronnaya Technika, Ser. 1, Elektronika SVCh, (1972), p. 55.

G.S. Nusinovich, Radio Eng. Electron. Phys, **22**, (1977), p. 151.

T.J. Orzechowski, B.R. Anderson, J.C. Clark, W.M. Fawley, A.C. Paul, D. Prosnitz, E.T. Scharlemann, and S.M. Yarema, Phys. Rev. Lett., **58**, (1986) p. 2172.

J.B. Schutkeker, (1985), Master's Thesis, M. I. T., unpublished.

J.D. Silverstein, R.N. Curnutt, M.E. Read, Sixth Int. Conf. on Infrared and Millimeter Waves, Miami Beach, Florida, (1981).

H. Shirai, J. Bae, T. Nishida, K. Mizuno, Conf. Dig., 13th Int. Conf. on Infrared and Millimeter Waves, Honolulu, Hawaii, (1988), p. 312.

J.F. Shively, K. Felch, and J. Neilson, Twelth Int. Conf. on Infrared and Millimeter Waves, Orlando, Florida, (1987).

W.M. Stacey, "Fusion: An Introduction to the Physics and Technology of Magnetic Confinement", John Wiley and Sons, New York, 1984.

U. Stom, J.R. Hendrickson, R.J. Wagner and P.C. Taylor, Solid State Comm. **15**, (1974), p.1871.

R.J. Temkin, K.E. Kreischer, W. J. Mulligan, S. Macabe, and H. R. Fetterman, International Journal of Infrared and Millimeter Waves, **3**, No. 4, (1982) p. 362.

R.J. Temkin, Int. J. Inf. and MM. Waves, **5**, (1984), p. 103.

T.M. Tran, B.G. Danly, K.E. Kreischer, J.B. Schutkeker and R.J. Temkin, MIT Plasma Fusion Center Report No. PFC/JA-85-8, (1985).

S.N. Vlasov, G.N. Zhislin, I.M. Orlova, M.I. Petelin, and G.G. Rogacheva, Radiophys. Quantum Elect., **12**, (1969), p. 972.

P.P. Woskov, MIT Plasma Fusion Center Report No. PFC/RR/87-16, (1987).

I.G. Zarnitsina and G.S. Nusinovich, Radiophys. Quantum Electron., **17**, (1974), p. 1418.

N.I. Zaytzev, T.B. Pankratova, M.I. Petelin, and V.A. Flyagin, Radio Eng. Electron. Phys., **19**, (1974), p. 103.